Molecular Spectroscopy of Planet-Forming Regions in Circumstellar Disks

Thesis by

Colette V. Salyk

In Partial Fulfillment of the Requirements

for the Degree of

Doctor of Philosophy

California Institute of Technology

Pasadena, California

2009

(Defended May 14, 2009)

To my friends and family, especially to those who are no longer here with me.

Acknowledgements

This thesis would not exist right now if not for my incredible family, friends and mentors.

I would like to thank my many great teachers and mentors at MIT, especially Jim Elliot, who kept pushing me forward, despite years of stubbornness, and without whom I literally would not be at Caltech today. I would also like to thank all of my scientific collaborators here at Caltech, especially Andy, Joanna, Adwin and Klaus, and the great planetary science and GPS staff, especially Leticia, Irma, Mike, Sarah and Dian. And, most importantly, I would like to thank Geoff for believing in me when I didn't believe in myself, and for always encouraging me in my quest for work-life balance, and beautiful Hawaiian hikes.

The number of great friends I've made at Caltech continues to amaze me, and it's to them that I owe my sanity. I want to especially thank my crew of office-mates: Kevin, Kris, Xin, Emma, Sloane, Kaveh, Sonja and Meg (yes, I've been here a long time!), my old roommate Emily — who adopted a good number of us as younger siblings, and others in the 2003 bunch, including Ravi and Carl. And, I want to thank the incredible group of Caltech women who have been my inspiration over the years, including Ashley, Gretchen, Margarita and Amy. And lastly, to Rem, for inspiring me, for always asking the hard questions, and for being my partner in my escape from the world of concrete.

Finally, and most importantly, I would like to thank my whole family, and especially my mom, dad and brother. Growing up in a family that will do anything to further their children's education is a privilege I will forever be grateful for. To my dad, for teaching me about photosynthesis and circuits, multiple times, at 2 AM before exams. To my mom, for buying me math workbooks instead of dolls. And to my brother, for reminding me that, no matter how much success I may have in life, I will still be his dopey little sister.

Abstract

Planets, now known to be common companions of nearby stars, are believed to originate in circumstellar disks—disks of gas and dust that form around collapsing protostars. Because of their small angular size, disks in nearby star-forming regions are difficult to spatially resolve. However, since radial temperature gradients are set up by the luminous central star, the peak wavelength of blackbody emission is a proxy for disk location, and spectroscopic observations can thus be used to study disk structure. In this thesis, I present spectroscopic observations of circumstellar disks obtained with the Keck Near Infrared Spectrograph (NIRSPEC) and the Spitzer Space Telescope Infrared Spectrograph (IRS).

High-resolution (R $\sim$ 25000) M-band spectra have been obtained with NIRSPEC for over 100 circumstellar disks. CO vibrational emission in the M-band is nearly ubiquitous from classical, optically thick disks, and can be used to examine the disks' inner structure and gas content. The emission is consistent with high temperatures and densities, and small emitting areas, suggesting that it originates at small disk radii—a few AU or less. An analysis of CO lineshapes shows that the CO gas is truncated at or near the dust sublimation radius for low and mid-mass stars but at larger radii for more luminous stars. CO emission is also present from many transitional disks—disks in which the inner regions have been depleted of small dust grains—demonstrating that many of their inner disks have significant quantities of gas. Although the formation mechanism for transitional disks is not yet known, gas-rich inner disks are consistent with formation via tidal clearing by a giant planet.

Spitzer-IRS spectra have been obtained for 82 disks, as part of the Cores to Disks (c2d) legacy program and other archived programs, and as part of a targeted IRS GO-5 survey at high S/N. Water vapor and other gaseous molecules, including OH, HCN, C_2H_2, and CO_2, are detected from $\sim 40\%$ of disks. Excitation temperatures for the molecular species of $\sim 500\,\mathrm{K}$ or higher and emitting radii of a few AU suggest an origin in the planet-forming regions of the disks. There are no strong correlations between detection rates or line equivalent widths and stellar or disk parameters. However, molecular detection rates are correlated with each other, and with disk color, suggesting a dependence on disk structure. Unlike for classical disks, transitional disks show no evidence for H_2O, OH, or any organic molecules, perhaps because these molecules are easily photodissociated in the optically thin inner disk.

Contents

List of Figures

List of Tables

Chapter 1

Introduction

How did the solar system form? Are other planetary systems created in the same way? Is our solar system ordinary, or a great cosmic coincidence? These are a few of the overarching questions that have motivated the work in this thesis. Until recently, attempts to answer these questions were based solely on our own solar system. However, with the advent of advanced astronomical techniques in the mid-20th century, it became possible to search for and study the birth of planetary systems besides our own. In particular, a set of young stars was identified with characteristics of 'youth', including high variability, outflow signatures, high lithium abundances, large luminosities, and a physical association with nebulosity (Herbig, 1962). It later became apparent that young stars were commonly surrounded by circumstellar (a.k.a. protoplanetary) disks composed of small dust particles and gas (Cohen et al., 1989; Strom et al., 1989; Beckwith et al., 1990). These so-called T-Tauri (low-mass) or Herbig Ae/Be (mid-mass) stars, and their disks, are the focus of this work.

Circumstellar disks are believed to be the birthplaces of planetary systems, and early solar system analogs. As such, they have become the subject of much study since their discovery. In the past 50 years, as the result of observations across many wavelengths, and with many techniques, a standard sequence of star-formation and planet-formation stages has emerged. Star formation begins via gravitational collapse of dense clouds in the interstellar medium. As a result of angular momentum conservation, they develop circumstellar disks as they collapse. The star and disk enter an extended phase during which mass is transferred from the disk to the star, and is ejected via winds and outflows. Eventually, planets form in the disk, and the disk begins to dissipate, through accretion onto the star and planets, and photoevaporation. Finally, after the primordial disk has dissipated, dusty debris disks can be formed via collisions between planetesimals. This sequence is shown schematically in Figure 1.1. The various stages of star and planet formation can be linked to observational classes, typically identified via spectral energy distributions (SEDs)—shown in Figure 1.2. T-Tauri stars correspond to Class II objects.

Although this simple theoretical progression does a good job of explaining the major evolutionary stages of star formation, the actual process is much more complex. In particular, the great variety of planetary systems that has been discovered to date (Mayor et al., 2004; Marcy et al., 2005) suggest that there are a multitude of outcomes to the planet-formation process. In addition, there may be multiple paths by which circumstellar disks proceed from an optically thick (T-Tauri) stage to a largely optically thin planetary debris-disk stage. Figure 1.3 shows a classical circumstellar disk SED compared to several types of evolved disks. The circumbinary disk has a completely cleared few-AU inner region, the transitional disk has an inner region depleted of small dust grains, the gapped disk has an inner annulus that has been depleted of small grains, and the depleted disk has been depleted of material at all disk radii.

Unfortunately, detailed observations of circumstellar disks remain challenging to obtain, because at a distance of 50–150 pc, even disks in the closest star-forming regions are unresolved with conventional imaging techniques. One solution to this difficulty is to use spectroscopic resolution in lieu of spatial resolution. There are several ways in which spatial information can be obtained from spectra. Circumstellar disks have radial and vertical temperature gradients created by the central star. Thus, each solid particle in the disk emits as a blackbody with temperature directly related to location, and wavelength becomes a proxy for disk location. It is this relationship that is exploited in the interpretation of disk SEDs. In the case of disk gas, each molecular or atomic transition has a unique excitation temperature, such that each transition originates in a unique region of the disk. Also, since the material in the disk is rotating around the central star subject only to Kepler's laws and disk pressure gradients (Lynden-Bell and Pringle, 1974), velocity, and hence, redshift, can also be related to disk location. If several molecules are observed, spatial information can be combined with chemical information to provide even more information about the disk environment. With spectroscopy, therefore, the challenge is to take the wealth of information obtained and relate it back to disk models.

In this work, I will utilize the spectroscopic techniques described above to study the terrestrial-planet-forming regions (within a few AU of the central star) of circumstellar disks. In Chapters 2 and 3, I will discuss high-resolution spectroscopic observations of CO gas from transitional disks—disks with inner clearings that may be caused by the gravitational influence of a young giant planet. In Chapter 4, I will discuss the use of CO lineshapes to study the inner disk structure of both T Tauri and Herbig Ae/Be disks. Data for Chapters 2–4 were obtained with the Near Infrared Spectrograph (NIRSPEC) at Keck Observatory. Finally, in Chapters 5 and 6, I will discuss observations of gaseous H_2O, OH, and organic molecules from inner disks. Data for Chapters 4 and 5 were obtained with NIRSPEC as well as the Spitzer Space Telescope Infrared Spectrograph (IRS).

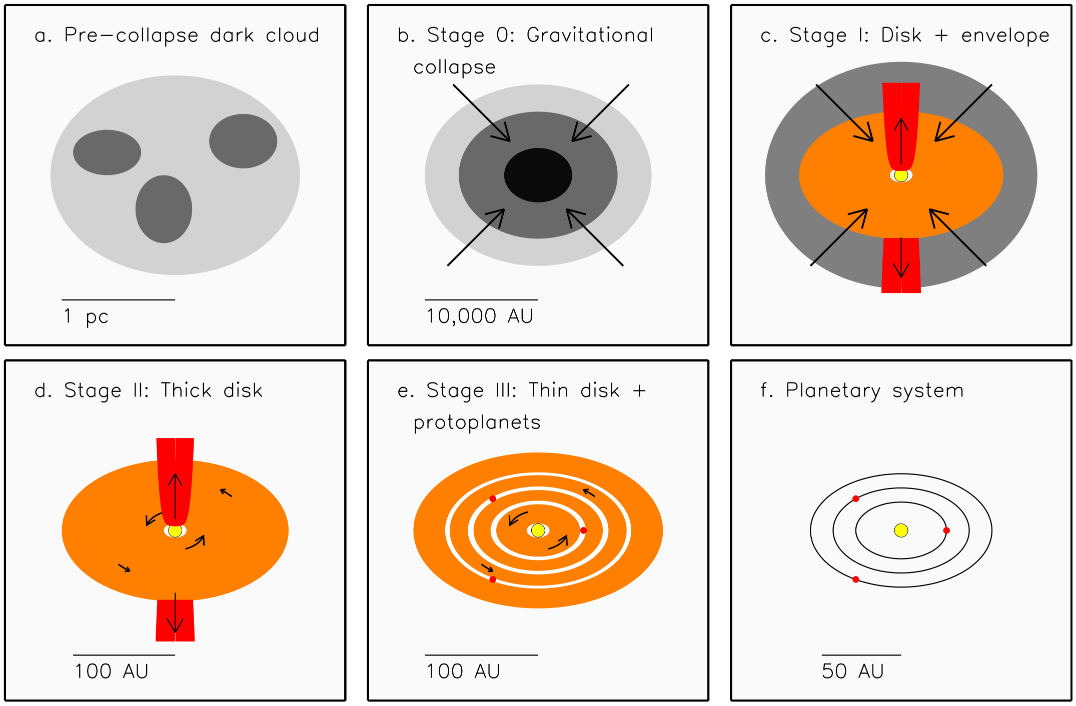

Figure 1.1: A schematic diagram of the major stages of star and planet formation. Panels are not drawn strictly to scale; scale bars provide a rough sense of the size scales involved. Adapted from Greene (2001) and Hogerheijde (1998).

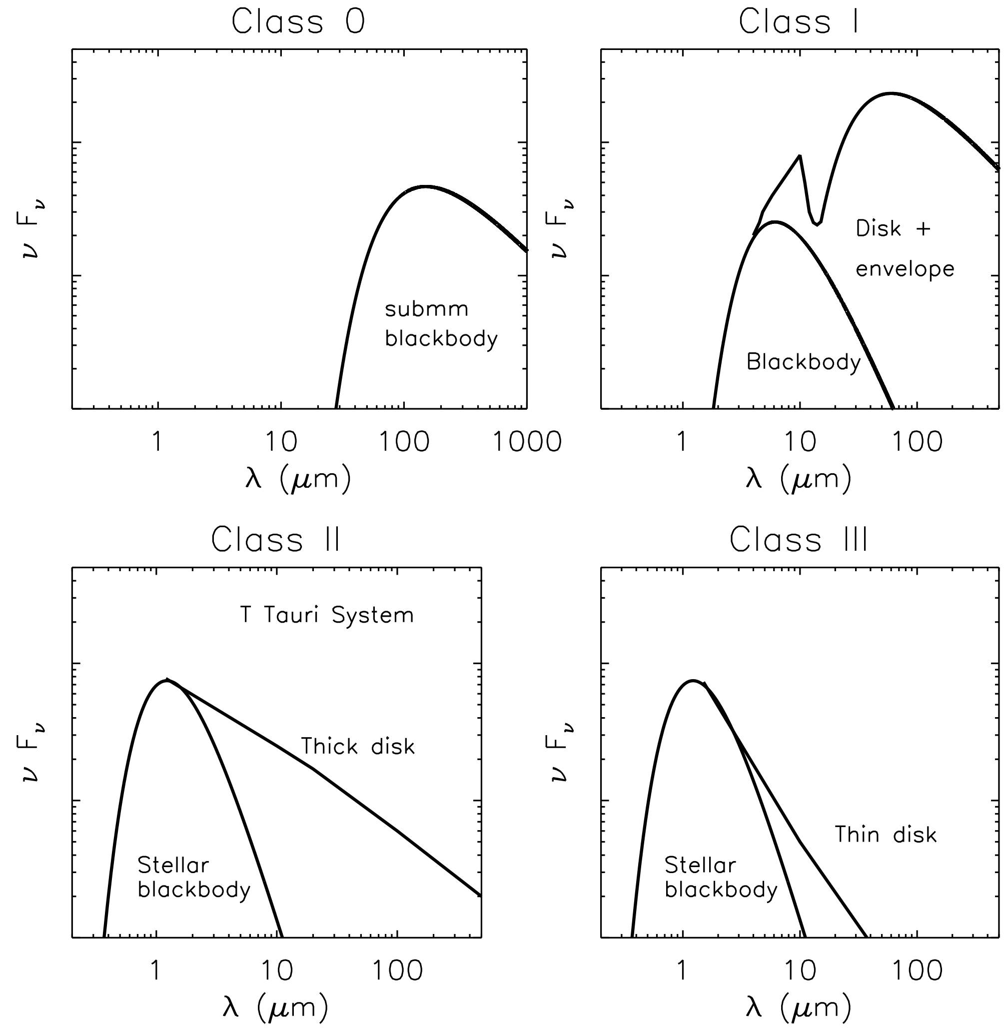

Figure 1.2: Observational classes identified via spectral energy distributions, adapted from André (1994).

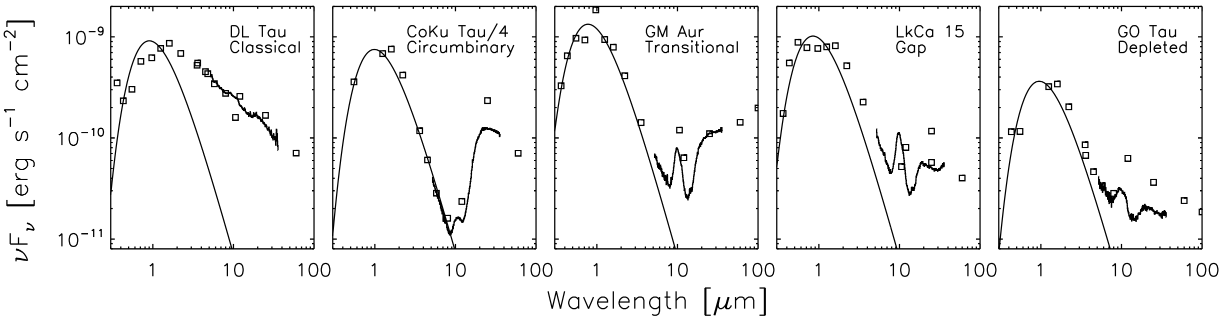

Figure 1.3: Spectral Energy Distributions of a classical circumstellar disk and several types of evolved disks. The solid line is a stellar blackbody, open squares are photometric measurements from the literature, and spectra were obtained with the Spitzer Infrared Spectrograph (data from Furlan et al., 2006).

Chapter 2

Molecular Gas in the Inner 1 AU of the TW Hya and GM Aur Transitional Disks

This chapter, with minor differences, was published in its entirety under the same title with authors C. Salyk, G. A. Blake, A. C. A. Boogert, and J. M. Brown in *The Astrophysical Journal*, 2007, Volume 655, pp. L105–L108.

2.1 Abstract

We report the detection of CO rovibrational emission from the circumstellar disks around TW Hya and GM Aur. These T Tauri stars have significant mid- to far-IR dust emission but a relative deficit in the near-IR, indicating the presence of an optically thick outer disk but a reduced surface density of small dust grains in the inner disk. Kinematic fits to the resolved emission lines yield inner emission radii of $0.2^{+.4}_{-.05}$ AU for TW Hya and $0.3^{+.2}_{-.15}$ AU for GM Aur, thus the CO v=1→0 emission arises from within the tenuous inner disk. By considering the amount of dust necessary to shield CO from dissociation, we demonstrate that these emission radii are consistent with the inner disk dust populations predicted by SED modeling and K-band interferometry. Rotation diagram analyses yield temperatures that are consistent with our kinematic fits, as well as densities that imply dynamically significant amounts of gas in the inner disk and a gas:small-dust-grain ratio in excess of that in dense clouds. Nevertheless, densities are not high enough to maintain current

accretion rates without replenishment for more than a few hundred years, and transfer of gas from the outer to inner disk is therefore likely required.

2.2 Introduction

As the intersection between star and disk processes and the likely location of terrestrial planet formation, the inner regions of circumstellar disks (R $\lesssim$ 5 AU) hold information essential for understanding the evolution of young stars and planetary systems. In particular, inner disk gas controls such varied processes as planetary migration rates (Ward, 1997), orbit circularization (Kominami and Ida, 2002), and accretion (Shu et al., 1994). Because of their small angular scale and proximity to the bright parent star, inner disks are notoriously difficult to image. Recently, however, rovibrational emission lines of species such as H_2O (Carr et al., 2004) and CO have emerged as ideal probes of the near-surface layers of disks. Fundamental CO rovibrational emission (v=1$\rightarrow$0) has been observed from embedded protostars (Pontoppidan et al., 2002), classical T Tauri stars (Najita, Carr, & Mathieu 2003; Rettig et al., 2004), and Herbig Ae/Be stars (Brittain et al., 2003; Blake and Boogert, 2004).

CO v=1$\rightarrow$0 emission can also provide a unique view into the inner regions of so-called transitional disks, whose spectral energy distributions (SEDs) are characterized by nearly photospheric levels of emission in the near-IR but significant excess flux at mid- to far-IR wavelengths. They are thus believed to have optically thin inner disks or gaps caused by grain growth and/or clearing due to dynamical interactions (Lin and Papaloizou, 1979), perhaps due to the presence of a planet (Rice et al., 2003; Calvet et al., 2002). Two prototypical examples of transitional disks are TW Hya [K8V] and GM Aur [K5V], whose SEDs show evidence for significant disk clearing out to $\sim$ 4 AU (Calvet et al., 2002) and $\sim$ 24 AU (Rice et al., 2003), respectively. For TW Hya, SED modeling yields an inner disk dust mass estimate of $\sim 6\times10^{-3}$ $M_\oplus$ (Calvet et al., 2002), while a K-band interferometric study yields values closer to $\sim 5\times10^{-7}$ $M_\oplus$ (Eisner, Chiang, & Hillenbrand 2006). There is an estimated 2.5×10^{-4} $M_\oplus$ of dust encircling GM Aur, confined to within $\sim$ 5 AU from the star (Calvet et al., 2005). Accretion rates for TW Hya and GM Aur are lower than that of average

T Tauri stars: $\sim 4\times10^{-10}$ $M_\odot$yr^{-1} (Muzerolle et al., 2000) and $\sim 10^{-8}$ $M_\odot$yr^{-1} (White and Ghez, 2001).

Observations of CO v=1→0 emission from TW Hya were first reported by Rettig et al. (2004). We expand on these results, reporting NIRSPEC observations of CO emission from TW Hya that cover a larger range of rotational energies, ($E_{\rm up} \sim$ 3000–6000 K versus $\sim$ 3200–4700 K), as well as Phoenix observations for which the emission lines are spectrally resolved. We also report the first observations of CO v=1→0 emission from GM Aur.

2.3 Observations

M-band spectra were obtained with NIRSPEC (McLean et al., 1998) at the Keck II telescope on 2005 April 24–25 and 2005 December 18, 20 for TW Hya, and 2004 December 27, 30 for GM Aur. Echelle mode observations with the $0.43'' \times 24''$ slit (yielding a Gaussian FWHM of $\sim$ 12.5 km s^{-1}, as measured on unresolved CO absorption lines) encompassed the first two R-branch and many P-branch lines [specifically P(1→12) and P(30→40)] of the v=1→0 CO rovibrational band. Further Phoenix (Hinkle et al., 2003) spectra of a few TW Hya lines were obtained at Gemini South on 2006 April 06–07 using the $0.25'' \times 14''$ slit (measured FWHM $\sim$ 5 km s^{-1}).

The 2D echellograms were analyzed with the procedures outlined in Boogert et al. (2002), using nearby standard stars (HR1620 [A7V], HR4313 [A2V], HR4494 [B9V], and, for Gemini data, HR5028 [A2V]) for atmospheric correction and flux calibration. After removal of wavelengths with significant telluric absorption (transmission $\lesssim$ 40–65%), flux calibrated spectra with signal-to-noise ratios approaching the shot noise limit can be obtained. For TW Hya, which was observed twice with Doppler shifts of $\sim$ 12 and $\sim$ 24 km s^{-1}, most line profiles remain complete after the removal of potential telluric interference. For GM Aur, observed only once with a Doppler shift of $\sim$ 11 km s^{-1}, line profiles are incomplete. However, more than half of the profile remains, allowing reasonable constraints on both the height and width of the lines. Although previous results reported line-to-continuum variability by a factor of 10 or more for TW Hya (Rettig et al., 2004), we saw variations consistent with noise, with line-to-continuum ratios varying from 0.6–1 (for the P(5)–P(7) lines).

TW Hya shows CO v=1→0 R(0–1), P(1–12) and P(30–32) lines. GM Aur was observed in one additional setting and its spectrum shows emission out to at least P(14). No ^{13}CO v=1→0 or CO v=2→1 emission is seen. The line and continuum spatial FWHM of $\sim 0.5''$ are consistent with the 0.4–0.7$''$ K-band seeing, and constrain the emission to radii $<$ 10–15 AU for TW Hya and $<$ 30–35 AU for GM Aur. Excerpts of our NIRSPEC M-band spectra are shown in Figure 2.1.

2.4 Results

2.4.1 Line Widths

Because CO v=1→0 emission originates from the inner regions of Keplerian disks, the line shapes depend on the disk inclination and emitting radii (Najita et al., 2003; Blake and Boogert, 2004). For TW Hya's nearly face-on disk, the NIRSPEC data yield only marginally resolved lines, so we instead utilize the R=60,000 Phoenix spectra. A composite lineshape from the P(6)–P(9) transitions is presented as an insert in Figure 2.1. Individual lines were velocity centered, continuum subtracted, normalized, and resampled into $2\,\mathrm{km\ s^{-1}}$ bins.

Inner emission radii are often estimated by measuring the velocity of the Half Width at Zero Intensity (HWZI). This procedure yields an inner radius for TW Hya of $\sim$ 0.04 AU (for $M_\star$=0.6 $M_\odot$ and i=7° ± 1°, Qi et al. 2004), but does not take into account the effect of disk structure or of any non-Keplerian (turbulent) motions, whose line-of-sight projections are especially important for low-inclination disks. A complete 2-D disk model would be difficult to constrain with only the data shown here, and we therefore present a compromise—a disk model consisting of an optically thick dust layer and overlying hotter gas layer, each with T=$T_0\,(r/\mathrm{AU})^\alpha\,(L/L_\odot)$. Based on SED fits using the radiative transfer models of Dullemond et al. (2002), and on matching total line fluxes, we chose the following model parameters: T_0(dust)=345 K, T_0(gas)=$440K$, α=−0.2, and r_{out}=2 AU. Stellar and disk parameters—M and i as above, L=0.25 $L_\odot$ (Thi, van Zadelhoff & van Dishoeck, 2004) — are derived from other studies, and v_{Turb} is parameterized as $0.01v_{\mathrm{Kep}}$. The resultant line shapes were then convolved with the known Phoenix instrument response function (IRF).

The best least-squares fit was achieved with $r_{\rm in}$=0.2 AU. Including all trials within the χ^2 95% confidence interval, with σ defined by the flux variation beyond the line profile wings, inner radii consistent with the data are $r_{\rm in}$=$0.2^{+0.2}_{-0.05}$. Note that this estimate is several times larger than that estimated from the HWZI. An investigation of all of the disk parameters that could influence estimates of $r_{\rm in}$ is not possible with this dataset; nevertheless, we tried to get a feel for the magnitude of the importance of a few key parameters.

For nearly face-on disks such as TW Hya, the turbulent velocity is the most influential parameter at fixed inclination. For example, with $v_{\rm Turb} \sim 0.05 v_{\rm Kep}$ the best-fit radii are $\sim$ 1 AU, but at such distances the disk may be too cool to induce the observed line fluxes. Doppler broadening at the temperatures of interest is unimportant, but the temperature gradient can be significant. Tests with α=-0.44 and -0.05 result in $r_{\rm in}$ up to 0.4 AU. To reflect this uncertainty, true error bars should be larger than the χ^2 estimate by a factor of a few. Because the inclination of TW Hya's outer disk is well-constrained this turns out to be a relatively insignificant source of error, affecting $r_{\rm in}$ by $\lesssim$ 40%, unless the disk is strongly warped.

The CO emission lines from GM Aur have a FWHM of $\sim$ 30 km s^{-1}, and so the NIRSPEC IRF makes a minor contribution to the measured line profile. A composite line was created utilizing P(9)–P(12) and P(14) (see Figure 2.1 insert), and a HWZI estimate yields an inner emission radius of 0.1 AU (with M=0.84 $M_\odot$, i=54° ± 5°; Simon et al. 2001). Utilizing our two-layer disk model with the same parameterization as for TW Hya, with stellar mass and disk inclination as above, and with L=0.74 $L_\odot$, $r_{\rm out}$=5 AU, we find that $r_{\rm in}$=0.3 AU. A χ^2 95% confidence interval metric yields $r_{\rm in}$=$0.3^{+0.2}_{-0.15}$. The turbulent velocity in this case is much less significant, but changes in α can still affect $r_{\rm in}$ by factors of $\sim$ 2. Inclination errors have little effect ($\lesssim$ 15%) on $r_{\rm in}$.

2.4.2 Excitation Diagrams

To estimate the gas temperatures and mass surface densities, we construct excitation diagrams, in which $\ln\left(F_{ji}/(g_j A_{ji} \nu_{ji})\right)$ is plotted against E_j. Here, F_{ji} is the line flux, A_{ji} is the spontaneous emission coefficient, ν_{ji} is the wavenumber of the transition, $g_j (= 2j + 1)$ is the degeneracy of the upper state and E_j is the upper state energy. For optically thin, single-temperature emission the dependence is linear, with a slope of $-1/T$, where T is the excitation temperature that characterizes the rotational manifold, and an intercept that yields the column density. Nonlinear dependencies can indicate temperature gradients or optically thick emission.

Before calculating line fluxes, we first estimate the reduction in observed line fluxes induced by absorption features in the photospheres of TW Hya and GM Aur. Although these photospheres are nearly unobstructed at 1 μm (Edwards et al., 2006), in the M-band veiling appears to dominate. We quantify this effect by assuming that away from the v=1→0 CO lines the spectrum is the sum of a constant veiling term plus a scaled photospheric template, given by NIRSPEC data for the [K7V] star HD 79211 (see Figure 2.1). The veiling and median photospheric contributions are 0.197±0.006, 0.096±0.006 Jy for TW Hya and 0.081±0.002, 0.019±0.002 Jy for GM Aur. Here the error bars reflect only the statistical uncertainties of the fit. Subtraction of the photosphere+veiling model should now yield the "true" disk line fluxes. For TW Hya, R(1)–R(0) and P(1)–P(12) transition fluxes are changed by $\sim$ 6% on average, but P(30)–P(32) fluxes by $\sim$ 30%. For GM Aur, the moderate S/N and the dominance of veiling render flux corrections insignificant. (The model fluctuations are of order 0.001 Jy, while the noise level for GM Aur is $\sim$ 0.01 Jy).

If HD 79211 is not a proper template, or if TW Hya's or GM Aur's photospheric absorption lines are filled in by hot gas from the inner disk or accretion flow, our fits will tend to underestimate the photospheric contribution. Therefore, to provide an upper limit to the possible photospheric impact, we considered the case where the spectra between the CO v=1 → 0 emission lines are assumed to be "veiling free". Specifically, the model photosphere was scaled such that its median matched that of the source spectrum and was then subtracted from the data to derive veiling-free fluxes. Again, the GM Aur line fluxes are not significantly affected because the variations in the reference photosphere ($\sigma \sim$ 0.007 Jy) are smaller than the noise level of the spectrum. TW Hya R and P(1)–P(12) line fluxes are changed by 7%, on average, while P(30)–P(32) fluxes are increased by up to 160%.

The rotation diagram in Figure 2.2 includes fluxes of 17 identifiable emission lines for TW Hya and 12 for GM Aur. Line fluxes are shown in Table 2.1. Raw fluxes are displayed as squares and fluxes corrected by a veiling+photosphere model are displayed as diamonds. Additionally, we show upper limits for GM Aur and veiling-free fluxes for TW Hya. (For clarity, we show only one set of fluxes at low energies). Error bars include two contributions added in quadrature: one derived from the standard deviation of the continuum flux and the other derived from the standard deviation of fit line widths.

The most obvious feature of these plots is that they are nonlinear; therefore, the optically thin, isothermal assumption is invalid. To fully model the line emission, one would need to consider both the gas and dust distributions and temperatures as well as the disk geometry. However, to derive a simpler, more intuitive estimate of conditions, we fit our rotation diagrams with a constant dust continuum plus a single temperature gas whose column density, rotational temperature, and emitting area are free parameters. Gaussian line shapes derived from the data are also provided to the model.

The best fit to TW Hya's veiling+photosphere corrected fluxes can be seen in Figure 2.2. Error bars are defined by the range of models within a 95% χ^2 confidence interval, plus an upper density limit provided by the non-detection of ^{13}CO (see top of Figure 2.2). Note that Area and N tend to covary, and are both anti-correlated with T, such that fits with high T correspond to low N and Area, and vice-versa. The veiling-free fluxes (representing an upper limit) give only a slightly different temperature and area: $\log(N){=}{-}3.7^{+0.5}_{-0.4}\,\mathrm{g\,cm^{-2}}$, $\mathrm{T}{=}950^{+550}_{-300}\,\mathrm{K}$, and $\log(\mathrm{Area}){=}\ {-}2.3^{+0.6}_{-0.6}\,\mathrm{AU}^2$. A lower temperature and density (T=430±40 K, $N{\sim}1{\times}10^{-8}\,\mathrm{g\,cm^{-2}}$) were derived by Rettig et al. (2004), assuming optically thin lines and an emitting area equal to that sampled by NIRSPEC (i.e., out to several tens of AU). However, given the curvature below $\sim$ 3300 K in Figure 2.2 and the high temperatures required to excite the transitions, these assumptions are not appropriate. For graybodies, our fit temperatures correspond to $r{=}0.07^{+0.36}_{-0.05}\,\mathrm{AU}$ and $0.04^{+0.39}_{-0.03}\,\mathrm{AU}$, but warm gas can exist at larger radii in disks with super-heated atmospheres (e.g., Kamp and Dullemond, 2004).

Best fits for GM Aur can also be seen in Figure 2.2. In this case, the χ^2 interval is significantly larger and we used three additional limits to constrain our fits — an upper flux limit based on non-detection of emission at high energies, a density limit imposed by non-detection of ^{13}CO and a requirement that fit models have significant curvature at low energies. The best-fit temperature corresponds to r=$0.53^{+0.94}_{-0.16}$ AU for graybodies.

2.5 Discussion

The molecular emission we observe originates from inside 1 AU—well inside the estimated disk transition radii of $\sim$ 4 and $\sim$ 24 AU for TW Hya and GM Aur. Line profiles yield inner radii of $0.2^{+0.4}_{-0.05}$ and $0.3^{+0.2}_{-0.15}$ AU, and rotational temperatures are consistent with emission radii of r=$0.07^{+0.36}_{-0.05}$ and r=$0.53^{+0.94}_{-0.16}$ AU for equilibrium graybodies. The consistency between the emission radii and inner radii suggests that the CO emitting layer has temperatures similar to those for graybodies in equilibrium with the stellar radiation field.

Although the CO lies inside the optically thick transition radius derived from SEDs, it lies outside the estimated disk truncation and dust destruction radii. For example, Keck interferometry plus IR photometry yield an inner radius of 0.06 ± 0.01 AU for TW Hya's dust disk, which is consistent with an estimate of the magnetic truncation radius (Eisner et al., 2006). GM Aur's inner disk dust is truncated at $0.221^{+0.082}_{-0.085}$ AU, consistent with the dust sublimation radius (Akeson et al., 2005a). In both cases, our measurements put the CO inner radius outside that of the dust. This is expected because the CO must be shielded from photodissociation; at our derived inner radii, radial vacuum-UV ($\lambda \sim 0.1\ \mu$m) optical depths are > 5–10 according to dust ($\kappa = 10^3\,(\nu/\nu_k)\,\mathrm{cm^2 g^{-1}}$) and disk mass surface density ($\Sigma = \Sigma_0\,(R/\mathrm{AU})^{-3/2}$) models analogous to those in Eisner et al. (2006).

Column densities derived from fits to the rotational diagrams allow us to estimate the gas content in the inner disk and the gas-to-dust ratio. The best fit to TW Hya's rotation diagram yields a gas surface density of $\Sigma_{gas} \sim 0.07\,\mathrm{g\,cm^{-2}}$ for an H_2/CO ratio of 5×10^3 (Lacy et al., 1994). (This molecular ratio, observed toward massive protostars, is among the lowest observed in the dense ISM, and thus should provide a reasonable lower limit to the total gas mass.) A comparison with dust column densities derived by Eisner et al. (2006) for TW Hya implies a gas-to-dust ratio of $\sim 10^4$ at $\sim$ 0.2 AU; a comparison with the much higher dust surface density derived from Calvet et al. (2002) implies a gas-to-dust ratio of $\sim$ 20. If we extrapolate our densities to 4 AU with a surface density that scales as $r^{-1.5}$ we predict a total inner disk gas mass of 3×10^{25} g ($0.005\,M_{\oplus}$).

The best fit to GM Aur's CO emission yields a gas surface density of $\Sigma_{gas} \sim 0.1$ g cm^{-2}. Extrapolating to 5 AU yields a total inner disk gas mass of 3×10^{25} g ($0.005\,M_{\oplus}$). Given the total dust mass from Calvet et al. (2005), this implies a gas-to-dust ratio of ~ 70.

The inner disk mass could only sustain the observed accretion rate for tens of years or less without invoking transfer of material from the outer disk. Steady mass transfer across gaps may be caused by an embedded planet (Rice et al., 2003). Interestingly, the derived gas surface densities also approximate those shown to provide significant circularization of the orbits of planetary embryos in the terrestrial planet-forming region (of order 0.1–1 g cm^{-2} at 1 AU; Kominami and Ida, 2002), and so may play an important role in shaping the dynamics of any forming planetesimals.

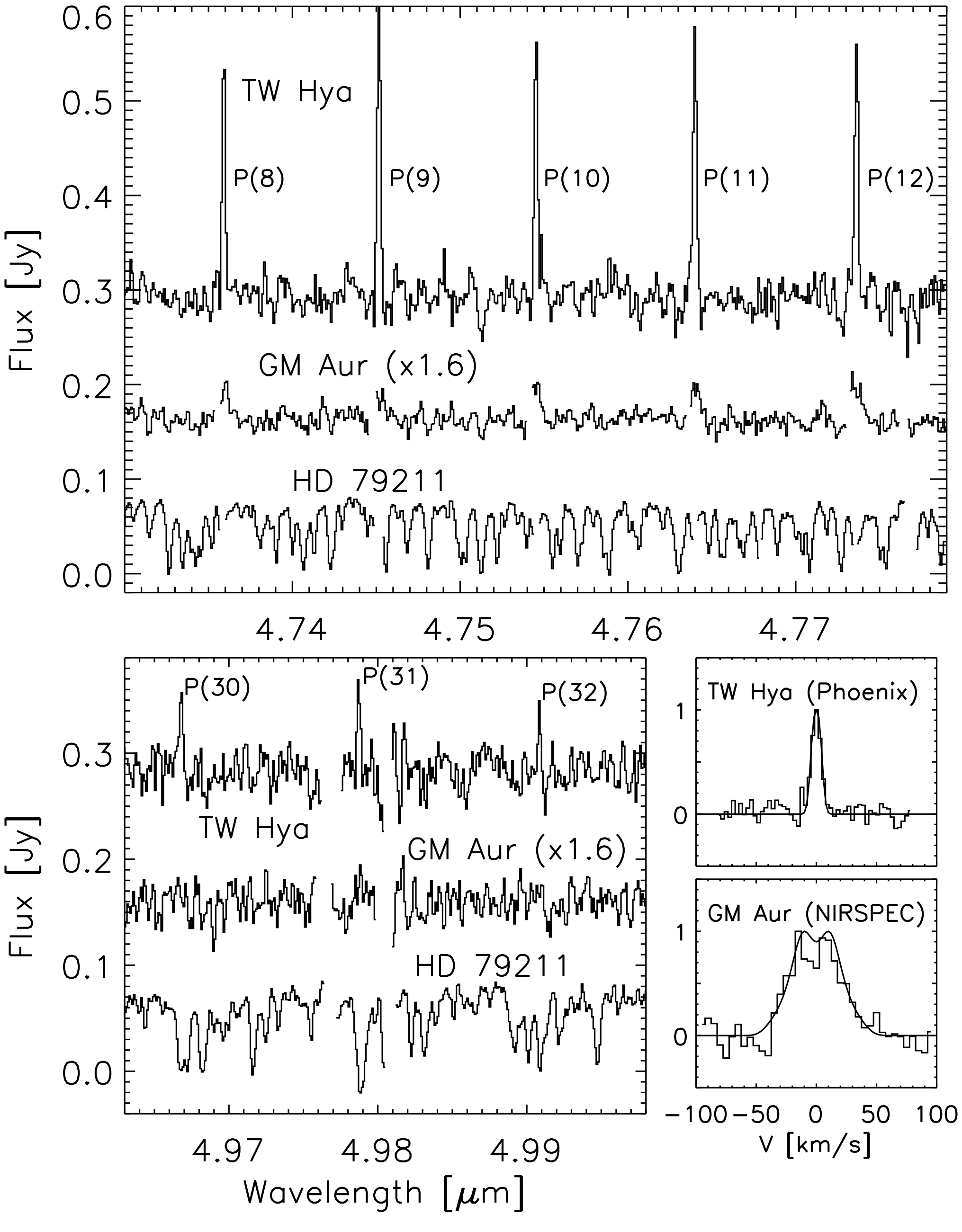

Figure 2.1: Excerpts of the NIRSPEC spectra of TW Hya and GM Aur. The HD 79211 spectrum has been normalized to TW Hya's continuum and offset. Line composites are shown at lower right, with the best two-layer disk model overlain.

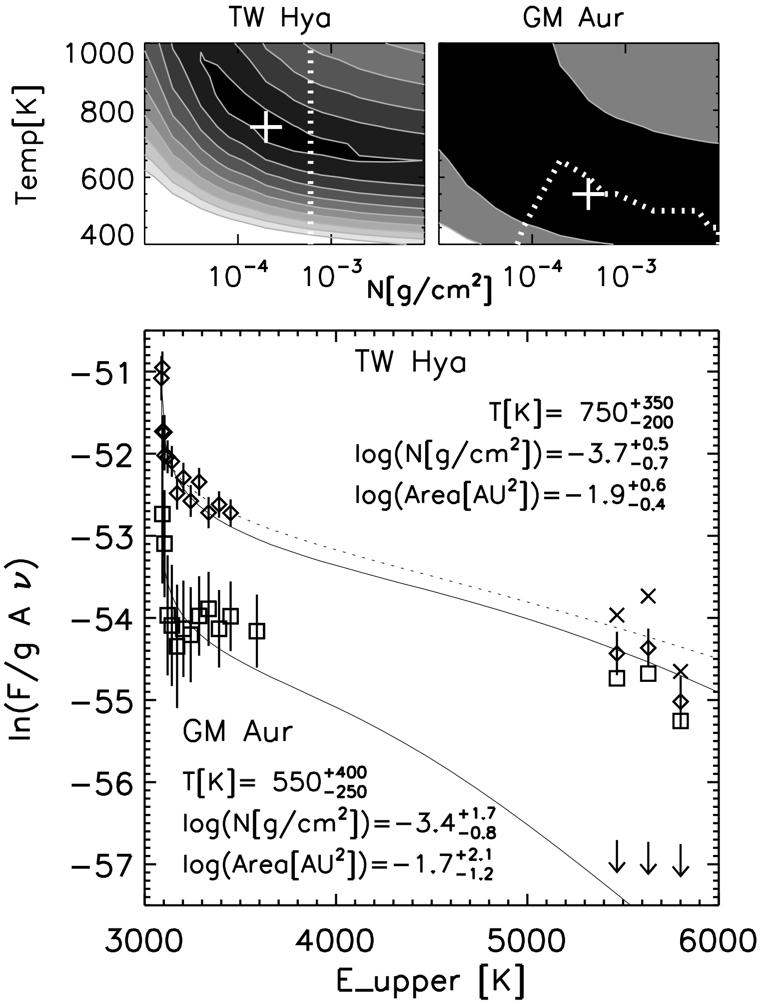

Figure 2.2: Rotation diagrams for TW Hya and GM Aur. Raw data are shown as squares, photospheric plus veiling-corrected fluxes as diamonds, and veiling-free fluxes as crosses. Arrows denote upper limits and best model fits are shown as solid lines (dashed line for veiling-free fluxes). Above we show the fit χ^2 contours for column density and temperature with area fixed at best-fit value. The innermost contour depicts the 95% confidence interval; subsequent contours are integer multiples of this critical χ^2 value. Additional constraints are shown as dotted lines. The quoted limits are the *ranges* of the correlated fit parameters consistent with the data.

Table 2.1. Line Fluxes

	TW Hya						GM Aur	
transition	F_0	FWHM	F_c	FWHM	F_{nv}	FWHM	F_0	FWHM
R(1)	5.0 ± 1.0	14.5	5.1 ± 1.3	14.6	5.4 ± 1.3	15.0	1.3 ± 0.9	22.8
R(0)	5.5 ± 1.1	15.5	5.5 ± 1.3	15.1	5.6 ± 1.4	14.6	0.9 ± 0.8	15.6
P(1)	2.9 ± 0.8	16.8	4.8 ± 1.1	22.8	3.7 ± 1.0	15.0	···	···
P(2)	5.2 ± 1.0	20.7	5.0 ± 1.1	20.8	5.0 ± 1.1	22.2	···	···
P(3)	5.9 ± 1.1	21.0	5.5 ± 1.2	20.3	5.1 ± 1.1	19.5	···	···
P(4)	7.1 ± 1.4	13.5	7.2 ± 1.8	13.6	7.5 ± 1.8	13.9	1.0 ± 0.8	19.6
P(5)	8.3 ± 1.6	14.2	8.4 ± 2.0	14.3	8.5 ± 2.0	14.5	1.1 ± 0.8	18.0
P(6)	6.7 ± 1.3	13.8	6.8 ± 1.7	13.9	7.0 ± 1.7	14.0	1.1 ± 0.8	18.0
P(7)	9.5 ± 1.7	14.5	9.5 ± 2.2	14.7	9.8 ± 2.2	15.2	1.5 ± 0.9	26.9
P(8)	8.3 ± 1.6	13.6	8.1 ± 2.0	13.4	7.9 ± 2.0	13.1	1.6 ± 0.9	25.4
P(9)	11.3 ± 1.9	15.3	11.5 ± 2.5	15.5	11.9 ± 2.5	15.9	2.2 ± 1.1	37.2
P(10)	8.8 ± 1.7	13.8	8.7 ± 2.1	13.7	8.5 ± 2.1	13.4	2.7 ± 1.2	44.6
P(11)	10.6 ± 1.7	16.5	10.5 ± 2.2	16.2	10.3 ± 2.2	15.8	2.3 ± 1.1	35.6
P(12)	9.9 ± 1.7	16.0	10.2 ± 2.1	16.2	10.7 ± 2.2	16.6	2.9 ± 1.2	42.9
P(14)	···	···	···	···	···	···	2.8 ± 1.2	46.3
P(30)	2.9 ± 0.8	18.5	3.9 ± 1.0	21.4	6.3 ± 1.2	26.5	···	···
P(31)	3.1 ± 0.7	15.6	4.3 ± 1.0	18.2	8.1 ± 1.3	27.1	···	···
P(32)	1.8 ± 0.6	11.8	2.3 ± 0.7	12.6	3.3 ± 0.9	14.0	···	···

Notes: All fluxes are in 10^{-18} W m^{-2}. Error bars include two contributions added in quadrature: one derived from the standard deviation of the continuum flux and the other derived from the standard deviation of fit line widths. F_0 is the flux with no photospheric corrections. F_c is photospheric+veiling adjusted flux. F_{nv} is the flux adjusted with a model assuming no veiling contribution. Line FWHMs for each set of fluxes are also given in km s^{-1}.

Chapter 3

High-Resolution 5 μm Spectroscopy of Transitional Disks

This chapter will be published in its entirety under the same title with authors C. Salyk, G. A. Blake, A. C. A. Boogert, and J. M. Brown in a future issue of *The Astrophysical Journal*, 2009.

3.1 Abstract

We present high-resolution M-band ($\sim 5\,\mu$m) spectra of fourteen transitional disks—circumstellar disks with an optically thick outer zone but an inner region significantly depleted of small dust grains—obtained with NIRSPEC on the Keck II telescope. We detect CO emission from nine disks, and show that for the majority of these systems, the emission originates in the depleted inner disk region. We find that the presence of high 5 μm veiling, strong CO emission, and high accretion rates are usually correlated, suggesting that at least two classes of transitional disks exist — those nearly completely cleared, and those only partially depleted—within their transition radius. *Cleared* inner disks are consistent with the presence of a close stellar companion, or with formation by photoevaporation. Of the cleared transitional disks, at least two (HD 98800 B and CoKu Tau/4) are known to be circumbinary with projected binary separations of several AU or less. *Partially depleted* inner disks most often have CO that extends to small ($\lesssim$ 1 AU) radii, but compared to "classical" disks the CO excitation temperature is lower and the emission radii are larger than that expected for dust sublimation. These disks are consistent with the presence of a giant planet, and

inconsistent with having been formed by photoevaporation. Although the inner regions of such disks are vertically optically thin in dust emission, line-of-sight opacities from the star can be large, and the complex physical and chemical processes therein make it difficult to derive a fiducial CO abundance w.r.t. molecular hydrogen. Thus, CO M-band lines are best suited to providing lower bounds as to the total inner disk gas mass. Amongst the partially depleted sources, veiling measurements and CO emission models demonstrate a great diversity of inner disk gas content and gas/dust ratios, suggesting a variety of planet-forming environments.

3.2 Introduction

Planets, now known to be common companions of nearby Sun-like stars, are believed to originate in the disks of gas and dust that form around collapsing protostars as a consequence of angular momentum conservation. Circumstellar disks and planetary systems are both well-studied, and the set of processes that convert one to the other have been fleshed out in some detail (e.g., Ruden, 1999). However, the observational constraints on this process are few. The formation of terrestrial planets and giant planet cores occurs on small scales, which cannot easily be spatially resolved. Additionally, to date, no planet has been conclusively shown to exist inside a gas-rich circumstellar disk, largely because high radial velocity precision is difficult to achieve with highly variable young stars (Setiawan et al., 2008; Huélamo et al., 2008). The potentially $\sim$ Jovian-mass companions to HR 8799 (Marois et al., 2008) and Fomalhaut (Kalas et al., 2008) reside in young debris disks, and extending such results to gas rich systems would provide new laboratories for the study of planetary system formation.

With this background in mind, it is easy to understand the excitement that accompanied the discovery of disks like TW Hya and GM Aur (Koerner et al., 1993; Calvet et al., 2002). The spectral energy distributions (SEDs) of these stars show a deficit of flux in the near-IR that suggests a lack of material close to the star. At the same time, far-IR fluxes are much higher, so the outer disk is still relatively massive. Could these disks represent the transitional phase between classical circumstellar disks and planetary systems like our own? Although this question is still unanswered, GM Aur and

TW Hya are often referred to as ‘transitional disks’.

To date the term transitional disk has been adopted somewhat loosely to describe collections of young stars whose SEDs are depleted relative to classical disks, in one way or another. Although the word ‘transitional’ implies an evolutionary characteristic, these disks are generally defined by observational signatures. One broad definition of transitional disks, as described by Najita et al. (2007), is used for SEDs in which the near- to mid-IR fluxes are below typical classical levels. Another, which is the definition we will adopt here, refers to a subset of these objects—those with lower than typical fluxes in the near-IR but with steep rises in flux toward the far-IR. These peculiar SEDs suggest not just that material has been removed from the disk, but that it has been removed selectively from a gap surrounding the star.

The actual mechanism for clearing out gaps in transitional disks is not yet known, but possibilities include photoevaporation (Hollenbach et al., 1994; Alexander and Armitage, 2007), dynamical clearing by a stellar or planetary-mass companion (Calvet et al., 2002; Rice et al., 2003) and grain growth (Tanaka et al., 2005). However, the discovery of significant quantities of gas in the inner regions of the transitional disks LkCa 15, GM Aur, and TW Hya (Najita et al., 2003; Rettig et al., 2004; Salyk et al., 2007) suggests against photoevaporation for at least some transitional disks. Additionally, recently obtained images of LkHα 330 (Brown et al., 2008) demonstrate a sharp transition between the thin and thick disk regions, which would be difficult to produce with grain growth alone. The exciting possibility thus remains that the characteristics of some transitional disks are most readily explained by the presence of young giant planets.

Transitional disks may not represent a single phenomenon. Although sharing a characteristic SED dip in the near-IR, the class as a whole spans a wide range of other parameters. For example, in the sample presented here, accretion rates range from undetectable (CoKu Tau/4, D’Alessio et al., 2005) to nearly classical (GM Aur, Johns-Krull and Gafford, 2002), disk gap sizes range from 3 AU (DM Tau, Calvet et al., 2005) to 56 AU (UX Tau A, Espaillat et al., 2007), and total disk masses range from 1×10^{-4} to 2×10^{-2} $M_\odot$ (CoKu Tau/4 and DM Tau, respectively, Andrews and Williams, 2005). As suggested by Alexander and Armitage (2007), the class of transitional disks may include both photoevaporated inner disks, as well as systems that harbor giant planets, with the second process being more appropriate for sources with high accretion rates (i.e., TW Hya and GM Aur). Whether the variety amongst transitional disks reflects varied processes, stages of evolution, or population heterogeneity is an important question that remains to be answered.

With these issues in mind, we selected a varied group of fourteen transitional disks to observe in the M-band ($\sim 5\,\mu$m) with NIRSPEC, a high-resolution echelle spectrograph on the Keck II telescope. The M-band region sits within the near-IR SED dip, and thus the M-band excess continuum emission is produced largely by dust within the disk gap. Additionally, the M-band harbors the P- (ΔJ=+1) and R-branch (ΔJ=−1) rovibrational transitions of CO. With upper state (v=1) energies greater than 3000 K, producing these transitions thermally requires temperatures of at least several hundred K, meaning they are a good probe of the region within an AU or so from the host star. Indeed, these transitions appear to originate in a disk atmosphere at distances of $\sim$ 0.1−few AU (Najita et al., 2003; Blake and Boogert, 2004; Pontoppidan et al., 2008a). In this paper we report the detection of CO rovibrational emission originating in nine out of the fourteen observed transitional disks. For those with emission, we discuss the characteristics of the gas and its emitting region and implications for the formation of transitional disks. We also discuss the question of why some disks show emission and some do not, and how this relates to transitional disk diversity.

3.3 Description of Sample

The selection criteria for our sample of transitional disks are shown graphically in Figure 3.1. We were interested in studying those disks with depleted (optically thin) inner regions but optically thick outer disks. Accordingly, these disks tend to have a high 30/13 μm ratio (Brown et al., 2007) as compared to the median SED, but millimeter fluxes similar to classical disks. As selection criteria, we chose to include sources with $F_{30}/F_{13} \gtrsim 3$, and $F_{1.3\mathrm{mm}} \gtrsim 0.0005$, which corresponds approximately to a Neptune mass of material (with $\kappa_{1.3} = 0.02\,\mathrm{cm}^2\,\mathrm{g}^{-1}$ and $T = 30\,\mathrm{K}$). The use of F_{30}/F_{13} as a means of distinguishing transitional disks was introduced by Brown et al. (2007), but is in essence the same as the n_{13-25} criterion used to identify outliers in Furlan et al. (2006).

This set of criteria is simple to apply because it is observationally based and does not require any model-based interpretation. The drawback of this approach is that it does not take into account other factors (such as grain opacity and stellar spectral type) that may determine whether or not the disk truly has an inner depleted region. Nevertheless, this set of criteria does result in the inclusion of those transitional disks with confirmatory images of inner holes—a list that currently includes TW Hya (Hughes et al., 2007), LkHα 330 (Brown et al., 2008), GM Aur (Dutrey et al., 2008), SR 21, and HD 135344 (Brown, (in preparation)—as well as HD 141569 A, which has had its inner hole resolved in CO emission lines (Goto et al., 2006). In addition, it does a fairly good job of excluding younger, optically thick classical disks, and more evolved debris disks. Interestingly, our selection criteria would permit the inclusion of Beta Pictoris, which, at a probable age of only $\sim$ 20 Myr (Di Folco et al., 2004, and references therein), may be transitioning from a primordial to a debris disk phase. The 1.3 mm fluxes were derived from the literature, or extrapolated from the closest known flux value assuming $F_\nu \propto \nu^2$ (Andrews and Williams, 2005), while 30/13 μm flux ratios were calculated using Spitzer Infrared Spectrograph (IRS) spectra derived from Furlan et al. (2006), c2d data releases (Evans et al., 2003) or the Spitzer data archive.

Characteristics of the fourteen selected transitional disks are summarized in Table 3.2. Sources derive from a variety of clusters, including Taurus, TW Hya , Serpens, and Ophiuchus. Additionally, they span spectral types from B9.5 to M1, accretion rates from undetectably low to $10^{-8}\ M_\odot\,\mathrm{yr}^{-1}$, and many orders of magnitude in disk mass. The sample thus represents a decent cross section of the T Tauri star population plus two Herbig Ae/Be stars, although typically with older ages and lower accretion rates than most classical T Tauri stars (cTTSs). Although all of the disks in our sample share the distinctive near/mid-IR SED dip, followed by a subsequent rise in flux out to 20 μm or so (Jayawardhana et al., 1999; Calvet et al., 2002; Furlan et al., 2006; Brown et al., 2007), the location and size of the cleared-out gap, as well as the remaining mass in small dust grains, vary significantly from source to source.

Several of our sources are members of multiple star systems. HD 135344, HR 4796 A, and SR 21 are all in wide binary systems with separations of $20.''4$ (Coulson and Walther, 1995), $7.''7$ (Jura et al., 1993), and 7.″8 (McCabe et al., 2006), respectively. HD 141569 A is a member of a triple system with A-B separation of 7.″5 and B-C separation of 1.″5 (Rossiter, 1943; Weinberger et al., 2001). For all of these sources, the Spitzer spectrum should have included only the primary, and only the primary was observed with NIRSPEC. UX Tau is a quarternary system, with A-B and A-C separations of 5.″86 and 2.″63, respectively, and with B a subarcsecond binary. Thus Spitzer photometry and spectra include two to four of the components, depending on the wavelength band and observing mode (Furlan et al., 2006). While the A component is classified as a cTTS, the B and C components are classified as weak-line T Tauri stars (wTTSs). In addition, the A flux dominates over that from B and C by factors of 7 and 24, respectively, at 3.6 μm (White and Ghez, 2001). Therefore, a circumstellar disk around the A component is the likely source of the emission observed with Spitzer. Our spectra, too, are dominated by only one component, presumably UX Tau A.

HD 98800 B is a member of a quadruple system with an A-B separation of 0.″8 (Koerner et al., 2000). Both components are themselves spectroscopic binaries with separation 23.7 mas ($\sim$ 1 AU) (Boden et al., 2005). For this source, the disk is circumbinary, and the transitional-like SED is a result of tidal truncation due to the binary orbit (Furlan et al., 2007). Similarly, for CoKu Tau/4, a 53 mas ($\sim$ 8 AU) binary, the SED-derived transitional radius is consistent with dynamical clearing from the binary pair (Ireland and Kraus, 2008). Although these disks are circumbinary and so not physically in transition, we explicitly include them here for the purpose of comparison.

The resulting sample encompasses most of the bright transitional disks that have been discussed in the literature and are observable from Mauna Kea. Some notable exceptions include disks with depleted inner disks, but no significant rise out to longer wavelengths—for example, Hen 3-600 A (Uchida et al., 2004) and v819 Tau (Calvet and D'Alessio, 2001). Transitional/debris disks that fit our criteria but are not observable due to their low declination include T Cha (Brown et al., 2007) and β Pic. Further, we are effectively limited to M-band fluxes $\gtrsim$ 0.01–0.1 Jy, and so our set of observations becomes less complete for later-type sources and for more distant clusters. For example, we have not fully investigated the possibly transitional disk-rich IC 348 cluster in Perseus (Lada et al., 2006; Muzerolle et al., 2006). M-band observations were previously reported for at least

4 sources in our sample: LkCa 15 (Najita et al., 2003), HD 141569 A (Brittain et al., 2003; Goto et al., 2006), TW Hya (Rettig et al., 2004; Salyk et al., 2007), and GM Aur (Salyk et al., 2007).

3.4 Observations and Reduction

The fourteen transitional disks in this study were observed over a period of 5 years (from 2002–2008, see Table 3.1) with NIRSPEC (McLean et al., 1998), a high-resolution echelle spectrograph on the Keck II telescope. Spectra were obtained in the M-band region, with a $0.43'' \times 24''$ slit, providing a resolution of R ∼ 25000 (FWHM ∼ 12.5 $\mathrm{km\,s^{-1}}$). Two spectral orders typically spanning 4.65–4.78 and 4.96–5.1 μm were obtained. LkCa 15 and HD 98800 B were observed over a smaller range, while GM Aur, LkHα 330, and TW Hya were observed over a slightly more extended range. These wavelength ranges encompass R(0–1) and P(1–12, 30–40) (or R(0–5) and P(26–43) in the extended cases) of the fundamental ($v=1\rightarrow0$) rovibrational transitions of CO, as well as portions of the $v=2\rightarrow1$ spectrum and ^{13}CO P- and R-branches. Additionally, the spectra encompass two to three H I electronic transitions: Pfβ (4.654 μm), Huε (4.673 μm) and Huδ (5.129 μm).

Spectra were recorded in ABBA sets, with each image acquisition (integration time plus co-adds) limited to one minute, in order to minimize atmospheric changes between the AB pairs. Data were reduced using IDL routines. AB pairs were subtracted to remove thermal noise, linearized, and summed along the slit direction to create 1D spectra. The 1D spectra were then aligned using telluric emission lines, weighted according to S/N and summed. Telluric lines were also used for wavelength calibration, while standard stars served to correct for atmospheric absorption. Stars of type A and earlier were chosen because of their relatively few photospheric features at 5 μm. Nevertheless, the cooler stars do have prominent Pfβ absorption. To correct for this, these stars were divided by a Kurucz model, which was broadened to match the appearance of the Pfβ line. These corrections were all examined manually and are quite successful at removing Pfβ, with any possible remaining structure being less than a few % of the continuum.

After an adjustment for source airmass, source spectra were divided by the standard star spectra. A final alignment of less than one pixel between source and standard was typically required to maximize S/N; this is likely due to small shifts in telluric emission line centers between images due to grating jitter. Flux calibration was performed by comparing sources and standards, along with standard star K magnitudes and spectral types. Flux calibration is not always reliable, because position shifts and changes in seeing can affect the throughput. To minimize this effect, slit positioning was constantly monitored and adjusted while observing and the brightest spectra of standards and sources were chosen (i.e., spectra in which the stars were best centered). Continuum fluxes were compared at regions of low atmospheric absorption. Absolute flux calibration is generally accurate to within $\sim 20\%$, though there is never a guarantee that the discrepancy is not higher for a particular observation.

Data quality is primarily limited by the quality of the atmospheric absorption corrections. For our analysis, we removed spectral regions with very low atmospheric transmission by qualitatively analyzing individual spectra to decide the transmission threshold, which was typically in the range of 40–70%. Since source CO emission will lie near or atop atmospheric CO absorption, it is helpful to observe at significant Doppler shifts. However, it was not always possible to avoid some overlap between source and telluric lines. Thus, spectra were also obtained at multiple Doppler shifts, when possible, to ‘fill in’ a complete spectrum (see Table 3.1). Spectra from different nights were averaged together, after small manual flux adjustments, to create the spectra shown in Figures 3.2 and 3.3. CO emission showed no significant night-to-night variations in line/continuum ratios, but 20% Pfβ flux variations were observed for DoAr 44 and TW Hya. Thus, this analysis uses an averaged version of the Pfβ emission line.

Spectra of TW Hya in a more limited wavelength range, but with significantly higher spectral resolution (measured FWHM$\sim 5\ \mathrm{km\,s^{-1}}$) were obtained with Phoenix (Hinkle et al. 2003) on Gemini South. Spectra were obtained on 2006 April 6–7 using the $0.25'' \times 14''$ slit, and were reduced using the procedures outlined above (Salyk et al., 2007).

3.5 Overview of Spectra

The complete set of reduced transitional source spectra is shown in Figures 3.2 and 3.3. We have also plotted the spectrum of one of our photospheric template stars (discussed further in Section 3.6). Of these disks, nine have detectable CO emission lines: DoAr 44, GM Aur, HD 135344, HD 141569 A, LkCa 15, LkHα 330, SR 21, TW Hya, and UX Tau A. Five disks do not have detectable CO emission at our achieved level of sensitivity: CoKu Tau/4, DM Tau, DoAr 21, HD 98800 B, and HR 4796 A. Note that the line detections for LkCa 15 are weak, but were previously detected across a larger wavelength range by Najita et al. (2003).

In Figure 3.4, we show the number of disks with CO and Pfβ detections, neither CO nor Pfβ, and Pfβ but no CO, separated by accretion rate. The presence of CO emission is very strongly correlated with the presence of H I Pfβ emission, with DM Tau being the only source with Pfβ but no CO. This is consistent with both emission signatures arising from the inner disk. We also show that strong accretors always have Pfβ emission, and usually have CO emission, while only one of two weak accretors have CO emission. Additionally, for the set of sources with a weakly constrained or unknown accretion rate, the presence of CO and Pfβ is correlated with the strength of Hα. Although HD 141569 shows CO emission and has a low accretion rate, its CO emission does not arise from the inner disk, as we will show in Section 3.8.2.

CO-emitting sources tend to have relatively structureless continua, while many non-emission sources have stellar photospheric features. This qualitative grouping is also consistent with IR photometry, with emission sources having significant excess emission at or near 5 μm, while most non-emission sources have little or no 5 μm excess (e.g., Jayawardhana et al., 1999; Calvet et al., 2002; Furlan et al., 2006; Brown et al., 2007). In Figure 3.5, we plot the distance normalized CO line flux against M-band excess flux (discussed in Section 3.6). Note that HD 135344, HD 141569, and HR 4796 A are not included in this plot, for reasons discussed in §3.6. The correlation between these two parameters suggests some coevolution of gas and dust in transitional inner disks.

Note that the CO emission typically peaks shortward of 4.8 μm and is either absent or much weaker in the longer wavelength order. If gas densities are high enough, ^{13}CO emission can be observed; however, only two of our sources (HD 141569 A and SR 21) have detectable ^{13}CO emission. In addition, if temperatures and densities are high enough and/or if nonthermal processes such as UV pumping are important, one may expect to detect hot-band (v=2→1) CO emission. This is observed around HD 141569 A and SR 21 but no other stars in our sample; this is in contrast to classical T Tauri stars, for which strong CO emitting sources have both fundamental and hot-band emission lines (Najita et al., 2003). CO also appears in absorption around SR 21 (for R(0) and R(1), and possibly part of the P-branch). This likely arises from cool foreground material, as SR 21 has a low-inclination (i.e., nearly face-on) disk.

3.6 The 5 μm Continuum

Although transitional sources are defined in part by their low excess flux in the near-IR, even a quick look at their M-band spectra reveals that many are far from photospheric at 5 μm. The infilling of photospheric features is referred to as veiling, and is defined as the ratio of continuum to photospheric flux ($r = F_{\mathrm{cont}}/F_{\mathrm{phot}}$). An understanding of the 5 μm veiling can be important for measurements of CO line fluxes, as well as interesting in its own right. Veiling measurements are crucial for accurately determining the dust content of the inner disk, as infrared excess emission can only be measured precisely if the flux contribution from the stellar photosphere is well characterized. In addition, observations of veiling at several wavelengths can be used to study the source of the excess.

Previous studies of veiling in classical T-Tauri systems at shorter wavelengths (e.g., Hartigan et al., 1989; Folha and Emerson, 1999; Johns-Krull and Valenti, 2001; Muzerolle et al., 2003; Edwards et al., 2006; Eisner et al., 2007) have revealed at least two sources of veiling. These include a hot (several thousand K) component, correlated with various accretion proxies and therefore likely arising in the accretion column, and a cooler component (roughly $\sim$ 1500 K) well fit as emission from a hot inner disk rim located at the dust sublimation radius. To our knowledge, no M-band veiling measurements have previously been published. As we will show, the 5 μm veiling in transitional sources may be consistent with emission from a slightly cooler dust component.

3.6.1 Fitting Method

Determination of veiling has been performed by a number of different methods, including examination of individual lines (e.g., Johns-Krull and Basri, 1997), correlation analysis (Tonry and Davis, 1979; Guenther and Hessman, 1993; Folha and Emerson, 1999), and point-by-point fitting (Hartigan et al., 1989). What all methods have in common is the idea that an observed spectrum consists of a scaled template photosphere and a constant or smoothly varying continuum. Determining the veiling at 5 μm presents a unique challenge because of the relatively lower signal-to-noise ratio (S/N), the apparently large contribution from the continuum in many cases, and the complex nature of the photospheric features. Consequently, the veiling must be determined using a large number of points, and small numbers of outliers (for example, due to poor sky correction) can artificially cause large changes in the results. Except for qualitatively distinguishing the end-member cases, it is difficult to confirm the resulting fits by eye. Therefore, we use a modified version of a standard technique, which helps us characterize the systematic uncertainties in our fits.

We began by removing the CO emission regions from each spectrum and assumed that the remaining spectrum consisted of a scaled photospheric template plus a constant term. Our photospheric templates were taken to be observed M-band spectra of standard stars HD 79210 [M0V], HD 79211 [K7V], HD 107146 [G2V] or ROX 43 A [G5], shifted by a velocity v_{rad} and then convolved with a stellar rotation profile with some $v \sin i$ and a limb-darkening coefficient of 0.6. We rebinned the standard star spectrum so that its wavelength values matched that of the source. We then performed a linear least-squares fit—i.e., we found the coefficients of the equation $y = Ax + b$ where y is the observed spectrum, x is the observed photospheric template, A is a scaling term, and b is a constant continuum. Finally, v_{rad} and $v \sin i$ were varied to minimize the residual sum of squares. Except for the fact that we solved for v_{rad} and $v \sin i$ iteratively, rather than explicitly, our method is equivalent to the correlation method; the scaling term in a linear least-squares fit is directly related to the correlation coefficient R by $A = R \times \sigma_y/\sigma_x$ where σ_x and σ_y are the standard deviation of the x and y values, respectively.

There are several ways in which analyses of this kind can produce slightly incorrect or even spurious results. Problems related to the data themselves include misalignment of flux from different observations or in different orders, improper flat-fielding or non-Gaussian noise (from sky-subtraction, for example). To minimize these effects we split our spectra into four sections at the natural boundaries between observations, performed the fits separately on each component, and then computed a weighted mean. The fits were carefully examined to remove outliers (from bad pixels, cosmic rays, bad sky-subtraction, etc.) This method has the added benefit that the true uncertainty in the parameters is reflected in the variation amongst the four measurements. To determine our final error bars, we computed the ratio of the standard deviation of the four measurements and the statistical uncertainties of the fit parameters and then used this to scale the statistical uncertainty in the weighted mean. In short, this amounted to multiplying the purely statistical error bar in the weighted means by factors of $\sim$ 2–6×.

A more difficult issue to address is the effect of using an improper template, for example with a surface gravity or spectral type different from the source. Unlike with the data-related problems, using an improper template will always act to increase the continuum term, perhaps by as much as 10–15% (Hartigan et al., 1989). To estimate the magnitude of this offset in our own data, we fit one template, HD 79210, with another, HD 79211. This fit produced a continuum term of about 10% of the photospheric flux. A correction at this level is somewhat smaller than the size of our error bars, but should be kept in mind, as it preferentially results in low photospheric fluxes and high continuum fluxes. We also attempted to fit each spectrum with a variety of templates, including those listed in Table 3.4, CoKu Tau/4 and a weak-line T Tauri star TWA 8a. In all cases, we chose the fit with the lowest amount of veiling.

For Herbig Ae/Be stars HD 141569 A and HR 4796 A, a lack of photospheric features at 5 μm made an analysis of this kind impossible. Therefore, these two sources are not included in the analysis. Additionally, we did not observe an F-type standard star, and so there was not an appropriate template star for HD 135344.

Finally, we wanted to derive actual flux values for the photosphere, so that we could compare the veiling results with stellar blackbody estimates. However, as discussed in Section 3.4, absolute flux calibration is not always reliable. Therefore, we used published flux values (see last two columns of Table 3.4) to estimate an M-band flux by linearly interpolating between the two closest measurements. We then scaled both our photospheric and continuum terms so that their sum equaled the interpolated flux value.

3.6.2 Veiling Results

Our veiling fits are summarized in Table 3.4. It is interesting to note that the transitional objects as a group span a large range of M-band veiling values, representing perhaps different 'hole' sizes or different degrees of inner disk clearing/grain-growth. CoKu Tau/4, DM Tau, and HD 98800 B are consistent with having zero excess flux in the M-band.

In Figure 3.6, we compare our veiling-derived excess fluxes with those obtained by subtracting a model photospheric flux from the measured M-band flux. HD 141569 A, HR 4796 A, and HD 135344 have been excluded from this plot. The photospheric models are derived from a grid of Kurucz model atmospheres (Kurucz, 1993), linearly interpolated over $T_{\rm eff}$ and log(g) and adjusted for size and distance according to Table 3.2. We have also corrected for extinction, although corrections are less than 10% for all but SR 21 ($A_{\rm V}$=9; Brown et al. 2007) and DoAr 21 ($A_{\rm V}$=6.2; Chen et al. 1995). Corrections for these sources are 25% and 16%, respectively.

In general, the predicted and observed excesses agree to within the error bars, but for a few sources the M-band veiling is somewhat different than would be predicted from photometry. The most likely explanation for much of this discrepancy is the use of an inappropriate template photosphere. Another possible explanation for the discrepancy could be time variability of the M-band flux. Near-IR variability has frequently been observed (Carpenter et al., 2001; Eiroa et al., 2002) and could extend to the M-band. We have also observed variability of the H I recombination lines Pfβ and Huϵ in our own sample. Additionally, the photospheric fluxes themselves could have been overestimated. This possibility was discussed in Cieza et al. (2005), who showed that T Tauri luminosities are often based on the false assumption of no J-band veiling, which results in an overestimate of luminosity. Further, spectrally resolved K-band interferometry of Herbig Ae stars shows evidence for significant continuum emission from hot gas—perhaps H^- (Eisner et al., 2009)—which would also provide J-band veiling.

A final possible explanation for the observed discrepancy, when fit continua are too high, could be a third emission source that is neither photospheric nor smooth, such as hot molecular gas. Although the details of such a source cannot be constrained by our data, we show in Figure 3.7 that hot molecular gas close to the star can form a pseudo-continuum at some wavelengths. However, it is unlikely to be the dominant source of veiling, since it produces large-scale structure between 4.5 and 5 μm that is not seen in our data.

It is likely that dust in the inner disk is providing most or all of the continuum veiling at 5 μm, and veiling measurements at multiple wavelengths can be used to constrain the dust temperature and thus location. To our knowledge, only three stars in our sample have published veiling measurements at other wavelengths: GM Aur, TW Hya, and LkCa 15. In Figure 3.7, we show the excess flux as a function of wavelength for our measurements and those previously published (Folha and Emerson, 1999; Johns-Krull and Valenti, 2001; Edwards et al., 2006; Espaillat et al., 2008). From the definition of veiling, we assume:

$$F_{\mathrm{excess}} = F_{\mathrm{X}} \times \frac{r_{\mathrm{X}}}{1 + r_{\mathrm{X}}} \tag{3.1}$$

where r_{X} is the veiling measured in filter X, and F_{X} is a published photometric flux in that same filter, or an interpolated flux value based on fluxes in neighboring filters. Y-, J- and K-band flux values are taken from Rucinski and Krautter (1983), Kenyon and Hartmann (1995), Webb et al. (1999), and Hartmann et al. (2005).

For LkCa 15, we show that a 1600 K blackbody—found to provide a good match to a K-band veiling spectrum (Espaillat et al., 2008)—underpredicts the M-band excess, and suggests that an additional emission source may be present. For TW Hya and GM Aur, we show blackbody continua which best fit the M- and K-band veiling, and best-fit 1400 K blackbody emission. Temperatures of ~ 1400 K are characteristic of near-IR continuum emission from cTTs disks (Muzerolle et al., 2003), and correspond well with the expected dust truncation radius, due either to magnetospheric accretion or dust sublimation (Eisner et al., 2007). The excess emission for TW Hya and GM Aur is more consistent with slightly lower temperatures, which could imply that the disk truncation is not due to dust sublimation, but rather to magnetospheric or dynamic truncation. Finally, for TW Hya, we also plot the emission expected from the simple disk model of Eisner et al. (2006); this model predicts slightly lower M-band veiling than is observed, but the results agree to within 2σ.

Since veiling measurements directly measure excess flux, and do not depend strongly on stellar model parameters (as is the case for SED fitting), they can provide strong constraints on the inner disk dust mass. A proper analysis of dust fluxes requires careful modeling combined with measurements at a variety of wavelengths, which is beyond the scope of this paper. However, our data can provide an estimate of the inner disk dust content for very optically thin disks (with $\tau < 1$ along all lines of sight from the star), or a lower limit of the dust content for other disks. We assume the disk is everywhere optically thin to incoming radiation, such that

$$T(r) = \frac{1}{\epsilon^{1/4}} \left(\frac{R_\star}{2r}\right)^{1/2} T_\star, \tag{3.2}$$

where $\epsilon \sim (\lambda/a)^{-\beta}$ is the grain emissivity (Chiang and Goldreich, 1997). For sub-micron sized grains, $\beta \sim 1$ and a is similar to the peak stellar blackbody radiation, so $\epsilon \sim T/T_\star$ and

$$T(r) \approx \left(\frac{R_\star}{2r}\right)^{2/5} T_\star. \tag{3.3}$$

We also assume $\kappa_{5\mu m}$= 440 cm^{2}g^{-1}, $R_{\rm in} = R_{\rm sub}$ (see Equation 3.4), $R_{\rm out}$ from Table 3.3 and $\Sigma = \Sigma_{0,v}\,(r/1\,{\rm AU})^{-3/2}$, where Σ is the dust mass surface density, and derive $\Sigma_{0,v}$—the veiling-derived dust mass surface density at 1 AU. See Table 3.4 for results.

Comparing our estimated inner disk dust contents with those estimated from SED fits (Table 3.3), we find that the results agree reasonably well for some sources (CoKu Tau/4 and the TW Hya result from Eisner, Chiang & Hillenbrand 2006), but in most cases it is an underestimate. Given the $\Sigma_{0,v}$ we derive, only CoKu Tau/4, HD 98800 B and TW Hya have $\tau \lesssim 1$ in the disk midplane, and so for all other disks, $\Sigma_{0,v}$ is a lower limit to the true disk dust content. For the three disks with $\tau \lesssim 1$, we confirm that the disk dust has been significantly depleted relative to a Minimum Mass

Extrasolar Nebula disk with dust mass surface density $\Sigma_0 \sim 22\,\mathrm{g\ cm^{-2}}$ (Kuchner, 2004).

In the analyses that follow, we have utilized our best-fit photospheric templates to correct CO line fluxes for TW Hya. This correction could be underestimated if we have underestimated the photospheric flux contribution. However, even in the extreme case that all 5 μm continuum emission originates in a stellar photosphere, corrections are still modest and will not affect the overall conclusions of our work (Salyk et al., 2007). For all CO emission sources besides TW Hya, photospheric corrections were smaller than the measurement error and so no correction was applied.

3.7 H I Recombination Lines

Emission lines deriving from ionized hydrogen in the spectra of young stars are believed to arise in the magnetospheric interface between star and disk (see Calvet et al., 2000, and references therein). Although the line strength is related to the stellar accretion rate, the complexity of the environment typically precludes defining a simple relationship between the two. As the H I lines are not the main focus of our paper, we include only a qualitative exploration of the relationship between observed H I lines and other spectral diagnostics.

The full spectral region observed for this study included the Pfβ (4.654 μm), Huε (4.673 μm), and Huδ (5.129 μm) transitions. We see no evidence for H I emission in main sequence or weak-line T Tauri stars, and so all H I emission is assumed to derive from the accretion flow. Detection statistics and equivalent widths are shown in Table 3.5.

There is a correspondence between accretion rate and the presence or lack of Pfβ emission. No clear correlation is seen between Pfβ equivalent width (or line luminosity) and accretion rates, although there is a moderate correlation between EW(Pfβ) and EW(Hα) (see Figure 3.8). This may be due to our small number statistics, opacity effects, or other complications. The lines also lack the blue asymmetries sometimes produced by inflow, but such asymmetries are not ubiquitious (see, for example, Muzerolle et al., 1998). Finally, line widths range from $\sim$ 80–170 km s^{-1}—values typical for H I lines originating in the magnetospheric inflow (Muzerolle et al., 2003).

As discussed in Section 3.5, we find a very strong correspondence between the presence of CO emission and Pfβ emission, with DM Tau as a possible exception. There is also a positive correlation between EW(Pfβ) and EW(CO), as seen in Figure 3.8. This is not too surprising, given that the inner gas disk is the reservoir for accreting material.

3.8 CO Emission Line Shapes

Spectrally resolved emission lines provide information about the velocity distribution of the gas from which they arise, as velocity along the line of sight causes Doppler broadening. The dominant velocity component for disks is from Keplerian motion (except for very face-on disks, where thermal or turbulent broadening can become important), and line shapes can be used to determine the inner extent of CO emission, $R_{\rm CO}$. To extract spatial information from the line profiles, it was first important to confirm that they are spectrally resolved. NIRSPEC provides $\sim 12.5\,{\rm km\,s^{-1}}$ sampling in the echelle mode, and average line widths for the six CO emitting sources are shown in Table 3.6. Errors are $\sim$ 1–3 km s^{-1}. Since TW Hya's lines appeared only marginally resolved with NIRSPEC, additional spectra were obtained with Phoenix (FWHM $\sim 5\,{\rm km\,s^{-1}}$) on Gemini South. Details of the Phoenix observations are described in (Salyk et al., 2007).

3.8.1 Constructing Line Composites

In order to increase emission line S/N and to fill-in incomplete emission lines, we created line composites for each star. Although all lines should originate from the same approximate disk region, lower energy lines will be excited at somewhat lower temperatures. This preferentially increases the amount of low-velocity flux contributing to the lower energy emission line, making the line appear narrower. However, for most disks, we were unable to detect differences between lines of different energy, or between ^{12}CO, ^{13}CO, and overtone lines. For DoAr 44, there is a systematic increase in line width with excitation temperature, but no noticeable change in line shape. Therefore, we selected all clean, uncontaminated emission lines to create a single composite for each disk.

The following procedure was followed to construct the emission line composites. Firstly, lines were extracted, centered using theoretical centers from the HITRAN database (Rothman et al., 2005), and converted to a velocity coordinate system. Then, lines were interpolated onto a 5 $\mathrm{km\,s^{-1}}$ grid (except for Phoenix lines, which were interpolated at a resolution of 2 $\mathrm{km\,s^{-1}}$), and added together. Finally, lines were continuum-subtracted, and normalized to height 1. Note that this is slightly different from the procedure used in Salyk et al. (2007), in which lines were first normalized, then combined, and, finally, interpolated. This new procedure provides more weight for stronger (lower-excitation) lines. The complete set of line composites is shown in Figure 3.9.

3.8.2 Inner Radii

The CO emission line width is primarily determined by disk inclination and the inner radial extent of emitting CO molecules, but is also influenced by the disk density and temperature structure, as well as by any non-Keplerian motion in the disk. We have fit the emission with a simple disk model, in which the line emission originates in a disk surface with power-law temperature given by $T = 300(R/\mathrm{AU})^{-\alpha}$ K, and the inner (R_{CO}) and outer (R_{out}) radii are specified. We assume the gas is everywhere optically thin and normalize the peak flux to 1. We also set R_{out} to 50 AU. Radii beyond $\sim$ 10 AU no longer contribute significant flux to the CO emission line, and so the model is insensitive to the exact value of R_{out}. Finally, we set α=0.4, the exponent expected for dust in a passive disk with sub-micron-sized grains (Chiang and Goldreich, 1997). For DoAr 44 and GM Aur, however, models with α=0.4 were more double-peaked than the data, but α=0.2 was found to yield a good fit.

Results are shown in Table 3.6 and Figure 3.9. Error bars represent the range of values in a 95% confidence interval, assuming a reduced χ^2 of 1 for the best-fit model. Note that the error bars do not include additional uncertainties in inclination and stellar mass. Also, the choice of α can have a substantial impact on the derived inner radius, with larger values of α corresponding to larger R_{CO}.

In Figure 3.10, we compare R_{CO} to other relevant disk radii: R_{sub}—the sublimation radius, R_{corot}—the stellar corotation radius, R_{dust}—the inner radius of the dust disk, R_{SA}—the CO inner radius derived from spectroastrometry, and R_{trans}—the radius of transition to an optically thick disk. R_{corot} is only provided for sources with published disk inclination and stellar $v \sin i$ (Clarke and Bouvier, 2000; de la Reza and Pinzón, 2004). $R_{\rm sub}$ is calculated assuming blackbody grains in a thin disk, with sublimation temperature 1500 K, but multiplied by a factor of 1.5 to account for grain properties (see Akeson et al., 2005a, for a discussion of how this factor varies amongst studies in the literature):

$$R_{\rm sub} = 1.5 \times 0.035 \times \left(\frac{L}{L_\odot}\right)^{1/2} \left(\frac{T_{\rm sub}}{1500.}\right)^{-2}. \tag{3.4}$$

$R_{\rm dust}$ was measured via IR interferometry for GM Aur (Akeson et al., 2005a) and TW Hya (Eisner et al., 2006). $R_{\rm trans}$ is taken from Table 3.3. For the purpose of comparison, we include all disks in our sample—even those from which no CO was observed. Note that sublimation radii are always much smaller than the transition radii, and so all disks are theoretically capable of harboring CO in the inner region. Also, there are no obvious structural differences between those disks with and without inner disk CO.

Our results are consistent with spectroastrometric results for SR 21 and TW Hya but slightly overestimated for HD 135344 (Pontoppidan et al., 2008a), as well as for HD 141569 (11 ± 2 AU; Goto et al., 2006). $R_{\rm CO}$ is usually well within the transition radius, $R_{\rm trans}$, except for HD 141569 A and SR 21, where the two radii are similar. Therefore, for most but not all disks, the CO emission originates from well within the optically thin disk gap. $R_{\rm CO}$ should intuitively be similar to, or slightly larger than $R_{\rm dust}$, since the dust provides protection from UV dissociation. However, $R_{\rm CO}$ is often many times larger than $R_{\rm sub}$, in contrast to previous studies of cTTSs and Herbig Ae/Be (HAeBe) stars. For example, Najita et al. (2003) found that $R_{\rm CO}$ was within 0.5–1$\times R_{\rm corot}$. And, Monnier et al. (2005) found strong correlations between dust inner radii and sublimation radii for HAeBe stars. Eisner et al. (2006) calculated that the magnetic truncation radius is actually a few times larger than $R_{\rm corot}$, and suggested that this may explain the relatively large inner radius of GM Aur's dust disk. However, it is also possible that an entirely different mechanism may set the inner radius of transitional disks.

3.9 Rotation Diagrams

The strength of an emission line depends on both the temperature and amount of emitting gas, so variations in line flux with excitation energy are used to break this degeneracy. A convenient way to visualize this variation is with a rotation diagram, a plot of the log of the line flux—normalized by the state's degeneracy, Einstein A-coefficient, and frequency—against the upper state energy. In the optically thin limit they define a line with a slope of $-1/T_{\mathrm{rot}}$, where T_{rot} is defined as the rotational temperature, and an intercept proportional to $\ln(N\Omega)$, where N is the gas column density, and Ω is the solid angle subtended by the gas. T_{rot} is equivalent to the actual temperature of the gas if it is characterized by a single temperature and if the state populations are in thermal equilibrium. Deviations from linearity in rotation diagrams can result if the transitions are not optically thin, if the temperature is not constant throughout the material, or if there is nonthermal excitation of transitions—any of which can be true when considering emission from a circumstellar disk.

Rotation diagrams for eight of the nine CO emission sources are shown in Figure 3.11. LkCa 15 was not included in this analysis because too few lines were observed. The diagrams were constructed with the following procedure. First, all lines were fit with Gaussian distributions. An average line width was computed, and combined with Gaussian heights to compute a total line flux for each line. In all cases, we assumed a constant continuum flux underlying the lines. Error bars were derived by adding the standard deviations of the line width and continuum flux in quadrature. Upper limits were computed for the ^{12}CO P(29) line (the lowest-energy observable transition in the 2nd M-band order) if no transitions were observed beyond $\lambda \sim 4.95\ \mu$m. They are shown as downward-pointing triangles in Figure 3.11. A prominent feature of all of the rotation diagrams is curvature at low energy, which may indicate temperature gradients, nonthermal excitations, or high optical depths.

The idea of explaining rovibrational fluxes as emission from optically thin gas components with different temperatures, or with a significant temperature gradient, has been discussed by Najita et al. (2003), Brittain et al. (2003), and others. In this case, the high excitation energy transitions would originate from a higher-temperature gas and the lower excitation energy transitions from a lower-temperature gas, producing steeper slopes at low excitation. However, given the steep dependence of flux on temperature, there must be a much larger mass of lower-temperature molecules compared to higher-temperature molecules in order to increase the flux in lower-energy transitions significantly. This difference in mass required is not consistent with the structure of circumstellar disks. We attempted to fit the rotation diagram with a power-law distribution of molecules ($N \propto T^{-q}$), as seen in circumstellar disks (Andrews and Williams, 2007a), but find that power-laws cannot produce the sharp kink seen at $\sim$ 3200 K. We find, rather, that a reasonable fit can be obtained with two components at $T = 900$ K and and $T = 50$ K (see Figure 3.11). However, to produce enough 50 K flux, the ratio of numbers of molecules of the two components (cold/hot) must be 10^{24}. In contrast, in a disk with $\Sigma \propto r^{-1}$, the relative amounts of mass from, say 0.05 to 0.1 AU as compared to that from 0.1 to 100 AU is only about 2000. Therefore, it seems unlikely that a typical circumstellar disk, in which mass is a decreasing function of radius, could produce significant rotation diagram curvature yet largely constant line profiles with upper state energy if emission lines are thermally excited and the gas is optically thin.

The curvature could also be caused by nonthermal processes, such as by resonant scattering. This possibility is discussed in the context of HAeBe stars by Brittain et al. (2003) and Blake and Boogert (2004). We will show that, with the exception of HD 141569 A and SR 21, the line fluxes in our sample are well-fit by a single temperature slab of moderate optical depth, in which the lower energy lines are optically thick but the higher energy lines are optically thin. For our analysis, we will assume the simplest case—that transitions are excited in a single temperature slab—as this allows for a qualitative understanding of the line emission. For our observations, the lowest energy transitions are optically thick, while the highest energy transitions are optically thin. For those transitions that are optically thick, the ordinate in the diagram is determined primarily by the inverse of the degeneracy (g=2J+1), causing significant curvature at low energies. The fluxes in the optically thick transitions depend on emitting area and temperature, while the optically thin transitions depend on column density and temperature. Thus if the transitions represent a variety of optical depths, the temperature, column density, and solid angle can all be constrained.

3.9.1 Model Description

In our simple slab model for CO emission, the gas sits in a flat disk with a single temperature T, column density N and solid angle Ω (or Area, if a distance is assumed). We assumed the local line broadening to be Gaussian with $\sigma = 2\,\mathrm{km\,s^{-1}}$—the sound speed for H_2 at 1000 K. (Note that this is different from Salyk et al. 2007, where the local line shape was assumed to be the same as the observed line shape. As a result, our current fits tend toward lower column densities). We varied N, T and Ω in order to fit the features of the rotation diagram, minimizing χ^2 to achieve the best fit. Our grid spacing for temperature was $\Delta T = 25$ K. For Area, the gridding was $\Delta\log(\mathrm{Area[AU^2]}) = 0.08$ and for column density, the spacing was $\Delta\log(N[\mathrm{cm^{-2}}]) = 0.23$.

Multiple solutions exist for any given rotation diagram, due to degeneracies between parameters (Najita et al., 2003; Salyk et al., 2007). To narrow the potential parameter space, we utilized a few additional constraints. One constraint is a column density upper limit imposed by the non-detection of ^{13}CO. To compute this limit, we assumed that ^{13}CO lines could be detected at the 2σ level above the background continuum. We then computed the $^{13}\mathrm{CO}/^{12}\mathrm{CO}$ line strength ratio at which the lines would be detectable, assuming an abundance ratio of 80/1. The line strength ratio is almost completely determined by the column density of the gas (with only a weak dependence on temperature), and so we determined a density limit. We also introduced a limit based on the assumption that the curvature at low rotational energies is real, and due to optical depth effects. χ^2 minimizations do not care about the order of the points, and therefore can allow fits that are clearly inappropriate when examined by eye. Our 'curvature' limit required that the ordinate values for R(1) and P(13) differ by at least 1, thereby excluding very optically thin fits. A final limit was introduced for those sources with no detectable emission at P(29) or higher.

3.9.2 Model Fits

In general, a range of model fit parameters was allowed by the data, with low T fits corresponding to large N and large Area, and vice versa. Best fit Ts ranged from 250–800 K, with a 95% confidence interval including T as high as ~ 1100 K for some sources, while best fit Ns ranged from $10^{17} - 10^{20}$

cm^{-2}. Best fit areas ranged from as small as 0.02 AU^2, to as large as 78 AU^2 for sources with no detectable emission at P(29) or higher. We show the complete range of acceptable parameters, assuming a 95% confidence interval and the limits described in Section 3.9.1, in the top portion of Table 3.7. Note that the change in procedure as compared to Salyk et al. (2007) (as discussed in Section 3.9.1) results in slightly larger derived column densities, and a larger allowed range of parameters. The previously derived log(N) of 18.9 and 18.6 for GM Aur and TW Hya, respectively, lie within the ranges given in Table 3.7. Similarly, the previously derived temperatures of 550 and 750 K lie within the ranges derived here. However, the differences between various model fits underline the degeneracy of model parameters and the need for additional model constraints. Best-fit models are shown as black lines in Figure 3.11.

For future analyses, constraints on gas emission could be improved with more observations at higher excitation temperatures, or by constraining the emitting area with well-resolved lineshapes. To allow some comparative analysis between transitional disks, we present here best model fits with Area fixed at 0.23 AU^2—the best-fit area for LkHα 330, and an area for which most of the disks had acceptable fits. This small area was not compatible with the rotation diagrams for HD 141569 A and SR 21, and so for these two sources we instead fixed the area to the best fit value. Best-fit parameters are shown in the middle portion of Table 3.7 and are plotted as gray lines in Figure 3.11. χ^2 contours are shown in Figure 3.12.

For those disks from which no CO emission was observed, we calculated upper limits to the CO column density. We assumed $T = 400$ K, which is near the low end of the observed excitation temperatures, and emitting areas of 0.23 AU^2. We also assumed a 2σ detection threshold. For LkCa 15, we did not have enough data to constrain all model parameters, and so we fixed T and Area for this source as well, to derive N.

3.9.3 The Special Case of HD 141569 A and SR 21

Neither HD 141569 A nor SR 21 were well-fit by the isothermal model, and best model fits required unusually large emitting areas. Both of these disks have significant emission in higher vibrational states, and yet no $v = 1 \rightarrow 0$ emission in the 2nd M-band order (J$\geq$29), making an isothermal fit difficult. As discussed by Brittain et al. (2003) for HD 141569 A, this is indicative of UV pumping, in which electronic excitation of CO by stellar UV is followed by relaxation to vibrationally excited states. This effect also explains the characteristics of OH rovibrational emission from intermediate-mass stars (Mandell et al., 2008). With sufficient UV radiation from the accretion column, this may also explain the CO emission from SR 21. UV excitation is also consistent with our finding that the CO emission arises at or near the transition radius—much further out in the disk than for the other stars in our sample.

Using a UV-excitation model, Brittain et al. (2007) derive a CO column of 10^{15} cm^{-2}, four orders of magnitude less than is found in our best isothermal fit. A factor of 100 can be accounted for by our smaller assumed emitting area, but the isothermal fit still overestimates the column density by two orders of magnitude, because it uses ^{13}CO/^{12}CO ratios as a density constraint. Therefore, the column density for SR 21 has also likely been overestimated by the isothermal fit.

3.9.4 Discussion of Rotation Diagram Results

Rotational temperatures are consistently higher than 250 K, and possibly as high as $\sim$ 1000 K. These temperatures are consistent with dust grain temperatures in the disk surface of planet-forming regions ($\lesssim$10 AU) around T Tauri stars. However, gas temperatures decouple from dust temperatures in the disk atmosphere, and may reach temperatures as high as $\sim$ 5000 K even at 20 AU (Kamp and Dullemond, 2004), for a 4000 K star. However, since CO inner radii are also consistent with planet forming distances (a few AU or less), this suggests that the CO and dust temperatures are similar, and that the emission does not originate far above the gas/dust coupling boundary ($\sim \tau = 1$). Collectively, the excitation temperatures for transitional disks are considerably lower than those found toward T Tauri ($\sim$1200–1500 K, Najita et al., 2003) or Herbig Ae ($\sim$ 800–1000 K, Blake and Boogert, 2004) stars, in accordance with the larger emitting radii inferred from the line profiles.

In Table 3.7, we show CO/dust column density ratios computed using Σ_0 (the dust column density at 1 AU) derived from SED fitting, and $\Sigma_{0,v}$ derived from 5 μm veiling measurements.

Because $\Sigma_{\rm CO}$ is a measure of hot gas, it represents a lower limit to the gas present. Nevertheless, using a fractional gas mass of $\sim 10^{-3}$ for CO, we see that GM Aur, and possibly, TW Hya, have gas/dust ratios that must be higher than the canonical 100/1 assumed for classical circumstellar disks. HD 135344 and LkHα 330, on the other hand, have significantly lower gas/dust ratios, with LkHα 330 in particular having the thinnest gas layer, and yet appearing heavily veiled. These results suggest that whatever the clearing mechanism for transitional disks may be, it does not affect all inner disks in the same way.

In Figure 3.13, we plot CO column densities against the total disk mass as derived from the mm-wave flux (leaving out HD 141569 A and SR 21, for the reasons discussed in Section 3.9.3) . We do not see a correlation between the 1.3 mm flux and CO column, which would have suggested interaction between the inner and outer disk, or else a retention of information about initial conditions in the inner disk. However, we do see that the disks with no CO emission tend to have lower total disk masses. This suggests either that the disks with and without inner disk CO represent two different classes of disks, or else that the process which has depleted the inner disk of gas has also affected the outer disk. It is interesting to note that two of the disks with no CO detections, HD 98800 B and CoKu Tau/4, are known close binaries, which, as a class, have lower disk masses (Andrews and Williams, 2005).

The inner disk gas content can potentially be used to distinguish between different gap-opening mechanisms. For example, a disk with an inner optically thin region may be susceptible to the magneto-rotational instability (MRI) transport, which predicts the following relationship between H_2 column density and accretion rate:

$$N \approx 5 \times 10^{24} \left(\frac{\dot{M}}{10^{-9} M_{\odot} {\rm yr}^{-1}} \right)^{3/4} \left(\frac{a}{\rm AU} \right)^{-3/4} \times \qquad (3.5)$$

$$\left(\frac{\alpha}{0.02} \right)^{-1} \hat{T}^{-1} \ {\rm cm}^{-}2, \qquad (3.6)$$

where $\hat{T}$ is a constant > 1 that represents the super-heating of disk gas over equilibrium blackbody temperatures (Chiang and Murray-Clay, 2007). A standard α-disk model, in which the disk evolves through viscous dissipation, predicts (Pringle, 1981)

$$\Sigma = \frac{\dot{M}}{3\pi\alpha\Omega H^2} \ . \tag{3.7}$$

A photoevaporating disk may potentially follow either of these relationships for radii inside of the critical radius for photoevaporative escape. However, such disks are also subject to the constraint that $\dot{M}$ be no higher than $\sim 10^{-10} M_{\odot}\mathrm{yr}^{-1}$ (Alexander and Armitage, 2007). In Figure 3.14, we show these relationships, as well as known values of $\dot{M}$, and Σ as derived from our CO column densities. We do not include HD 141569 A and SR 21, for the reasons discussed in Section 3.9.3. For simplicity, we assume a distance from the central star, a, of 1 AU (the approximate location of our CO emission) and a scale height, H, of 0.05 AU, and consider α ranging from $10^{-3} - 10^{-2}$. In addition, we assume a constant fractional abundance of CO (x_{CO}) of 2×10^{-4} w.r.t. H_2. Note that in Salyk et al. (2007) we assumed the same x_{CO}, but mistakenly treated it as a mass ratio, and so the estimated gas mass densities given in our earlier paper should be reduced by a factor of 14.

The column densities we derive are significantly lower than that predicted by any of the equations described above. Because most of the inner disks are horizontally optically thick, CO emission probes only the upper disk atmosphere, and not the bulk of the disk gas. Furthermore, at low column densities the CO abundance is inversely related to the total column, and rather lower than the value assumed here (van Dishoeck and Black, 1988). Thus, the gas columns and gas/dust ratios we derive are lower limits, and the actual range in Σ for these disks is likely to be smaller than that shown in Figure 3.14. Nevertheless, all sources with CO emission originating from well within the transition radius (i.e., all emitting sources besides HD 141569 A and SR 21) have CO column densities and accretion rates inconsistent with photoevaporative clearing of the inner disk.

3.10 Discussion

We obtained 5 μm spectra of fourteen transitional disks, selected to have high 30/13 μm ratios but ‘classical’ disk masses. Of these disks, nine have detectable CO emission. By measuring the

M-band veiling and CO emission features, we have investigated both the gas and dust components of the disk. Based on characteristic temperatures and emission radii, the CO emission appears to arise from well inside the transition radius for most disks, but at or near the transition radius for HD 141569 A and SR 21. The disks with CO emission inside their transition radii appear to differ in many ways from the disks without CO emission, and we suggest that they may represent two distinct classes of transitional disks. Disks with inner disk CO tend to have observable accretion rates and Pfβ emission, a high degree of veiling, as well as higher disk masses. A possible exception is DM Tau, with a high accretion rate, detectable H I recombination lines, and a high degree of veiling, but no detectable CO emission, to within our detection limits. Thus, many of the disks we observe have significant quantities of gas and dust within the transition radius and are actively accreting, while others have little or no detectable material in the inner disk. Of the class of 'cleared' inner disks, two are known to be close binaries with circumbinary disks. If others turn out to be close binaries, searching for the presence of inner disk material, especially gas, may help distinguish between transitional SEDs formed by close stellar binaries versus planetary-mass companions.

Amongst those sources with CO emission, there is a great variety of CO line strengths and hence column densities. In addition, CO/dust mass ratios in the regions we probe vary greatly from disk to disk, suggesting a variety of inner disk environments. In our sample, a few disks especially stand out. LkHα 330 is heavily veiled, but has a CO column density one to two orders of magnitude lower than the other disks. It also has a relatively large CO inner radius. Has gas been preferentially removed by photoevaporation, or by accretion onto a gas giant? HD 141569 A and SR 21 are also interesting. They are the only two sources with ^{13}CO and CO 2→1 emission, are not well-explained by a thermal emission model, and have large CO inner radii ($\sim$ 10 AU). Why has the CO been cleared to such large radii in these disks, but not in most of the others?

All of the CO emission sources with good available photospheric templates have significantly veiled photospheres at 5 μm. Since 5 μm corresponds to the peak of a $\sim$ 600 K blackbody, the high degree of veiling suggests the presence of dust inside the transition radius. For three disks, GM Aur, LkCa 15, and TW Hya, veiling measurements have been made at other wavelengths. The dust emission is roughly consistent with an origin near the inner dust rim, though M-band excess flux may be somewhat higher than expected. Veiling measurements at several wavelengths thus provide constraints on the dust truncation radius that would otherwise require extremely high resolution measurements, such as those provided by optical or IR interferometry. Using additional veiling measurements, it would be interesting to see if dust truncation radii are different for transitional disks than for classical T Tauri or Herbig Ae/Be disks, and to see if dust truncation radii differ greatly from disk to disk for stars of a given spectral type.

Do the inner disk gas and dust masses provide constraints on the formation mechanism for transitional disks? Disks with low-mass companions will not completely clear their inner regions of gas and dust (Artymowicz and Lubow, 1996; Lubow et al., 1999), and so 'partially depleted' transitional disks may be the best candidates for disks that harbor giant planets. Conversely, photoevaporation is expected to clear the inner disk on the viscous timescale, making observations of filled inner disks unlikely (Alexander and Armitage, 2007). For those disks with nearly cleared inner regions, then, photoevaporation is a possible formation mechanism. However, two of the cleared inner disks observed in this study—CoKu Tau/4 and HD 98800 B—are binary pairs with circumbinary disks. The remaining cleared disks—HR 4796 A, DoAr 21 and possibly HD 141569 A—may still be potential candidates for photoevaporating transitional disks, or may also turn out to be circumbinary.

Unfortunately, it may prove difficult to distinguish between close stellar and planetary mass companions in transitional disks, as binaries display a variety of SEDs and accretion rates (e.g., Mathieu, 1994). CoKu Tau/4 and CS Cha, with projected separations of several AU (Ireland and Kraus, 2008; Guenther et al., 2007), have transitonal SEDs, with little or no near-IR excess (though CS Cha has an estimated accretion rate of $1.2 \times 10^{-8}\ M_{\odot}\ \mathrm{yr}^{-1}$; Espaillat et al. 2007a). DF Tau and GN Tau, on the other hand, have similar projected separations (~ 12 and ~ 6 AU, respectively; Ghez et al. 1993; Simon et al. 1995) and yet have significant accretion rates or Hα equivalent widths (Mathieu, 1994) and nontransitional SEDs (Furlan et al., 2006). Nevertheless, thus far it seems that a cleared inner disk is a good predictor for a close binary with a circumbinary disk.

For those partially cleared transitional disks that may harbor giant planets, high-resolution spectroscopy will be instrumental for understanding disk/planet interactions, and exploring the complexity and seeming diversity of planet-forming environments. However, the challenge will be to relate what is observed in the upper disk atmosphere to the bulk properties of the inner disk. We have shown that even a simple single-temperature slab model cannot be well-constrained by emission fluxes alone. To properly relate CO emission to column density, we will need to incorporate CO line production into a model that includes gas heating/cooling processes and CO dissociation. With these procedures in place, CO emission could provide key constraints on gap opening mechanisms and inner disk physics. More generally, high resolution spectroscopy of additional atomic and molecular tracers should move us towards a better understanding of both the physics and chemistry in planet-forming regions of circumstellar disks.

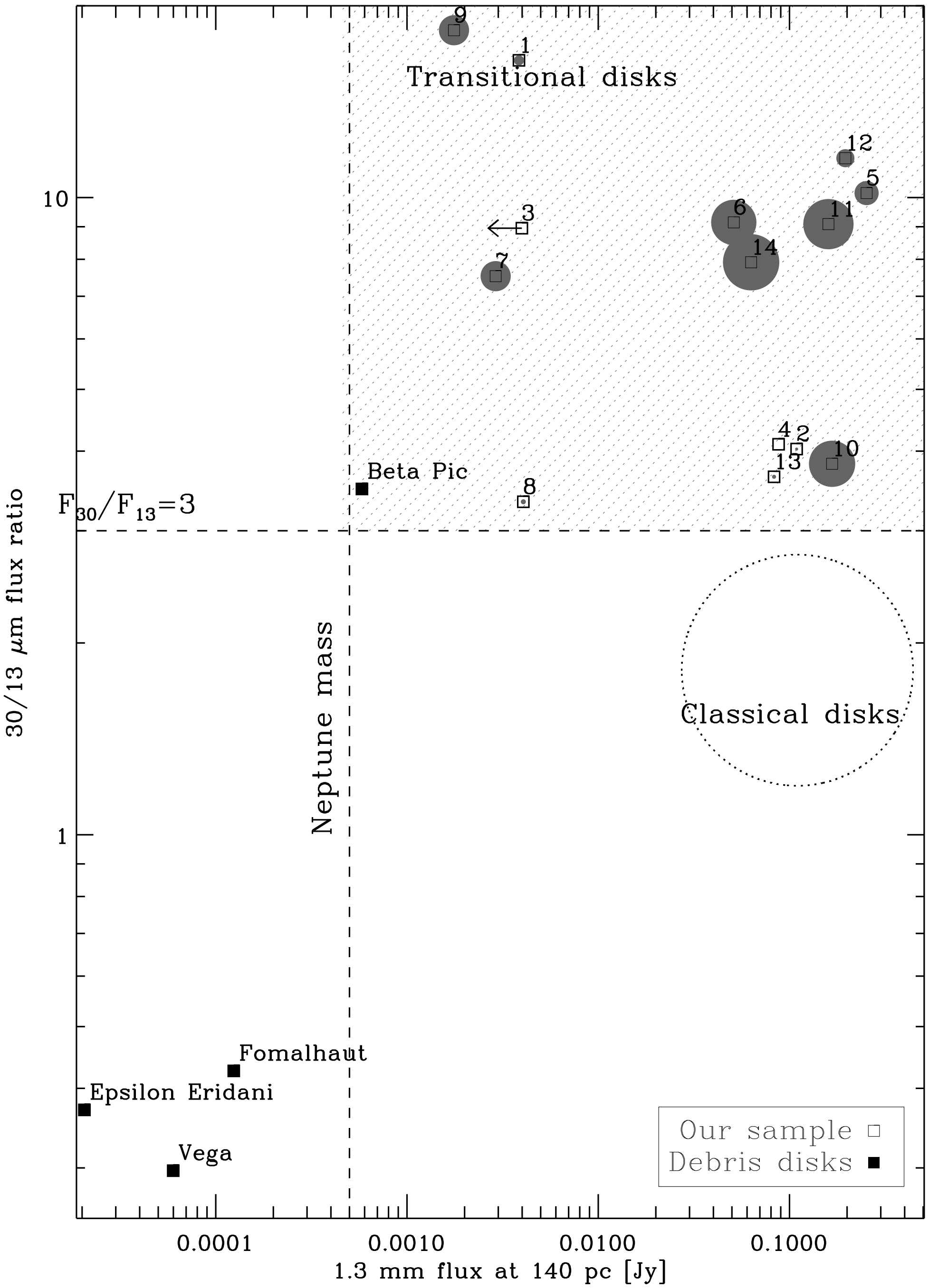

Figure 3.1: 30/13 μm flux ratios and distance-normalized 1.3 mm fluxes for the disks in our sample, as well as for four canonical debris disks. Filled gray circles have radii proportional to the size of the disk transition radius, if known. A dashed circle shows the typical fluxes and flux ratios for classical disks in Taurus. Dashed lines and hatched region delineate our selection criteria for transitional disks in this analysis. Flux corresponding to a Neptune mass disk assumes $\kappa_{1.3} = 0.02\,\mathrm{cm}^2\,\mathrm{g}^{-1}$ and T=30 K.

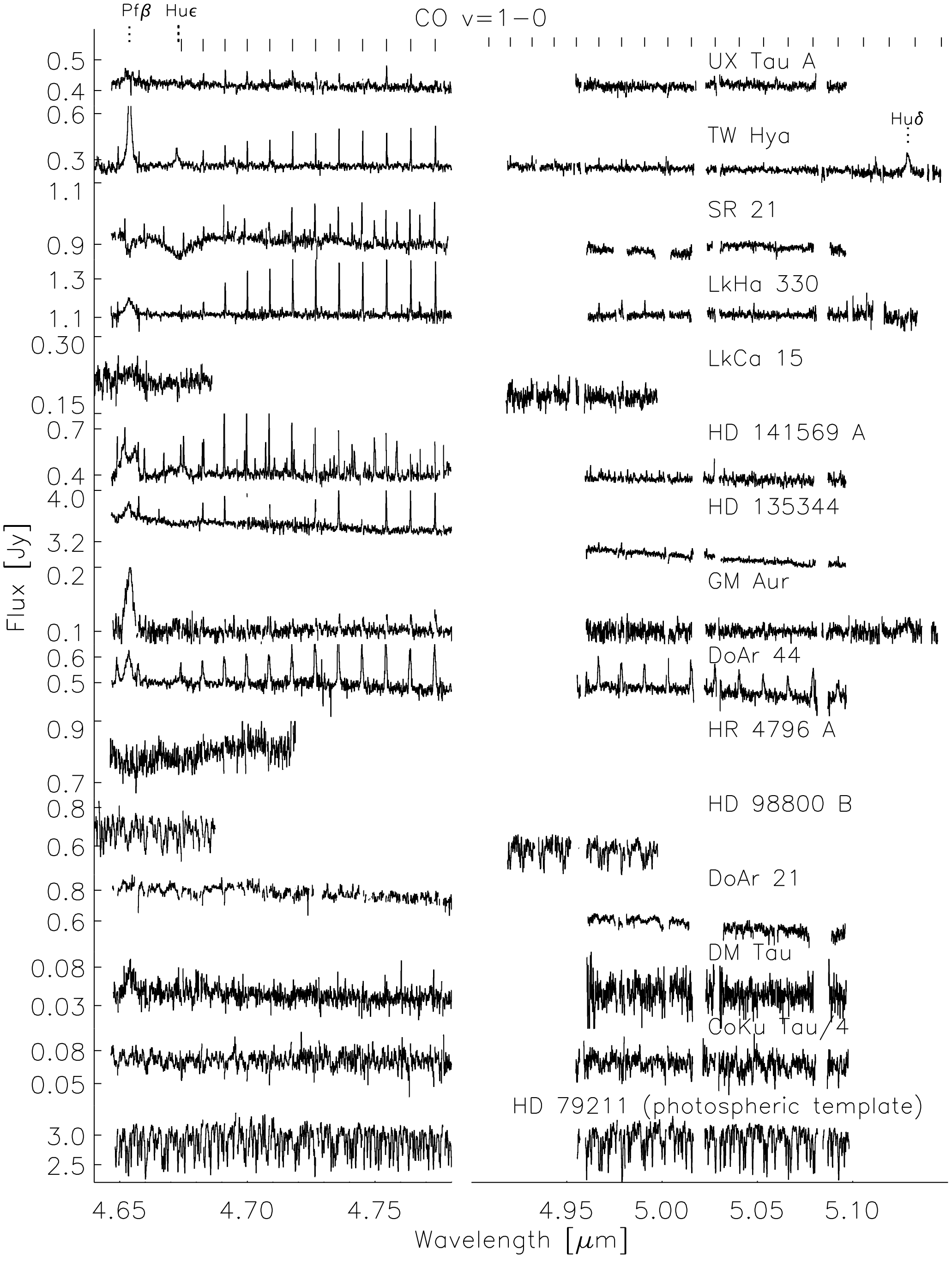

Figure 3.2: Spectra of the fourteen transitional disks in our sample, plus one of our photospheric standards, in the 1st M-band order. CO $v = 1 \rightarrow 0$ emission lines are indicated above. ^{13}CO lines and v=2→1 lines are also present in the spectra of SR 21 and HD 141569 A. H I recombination lines Pfβ, Huδ, and Huε are also labeled.

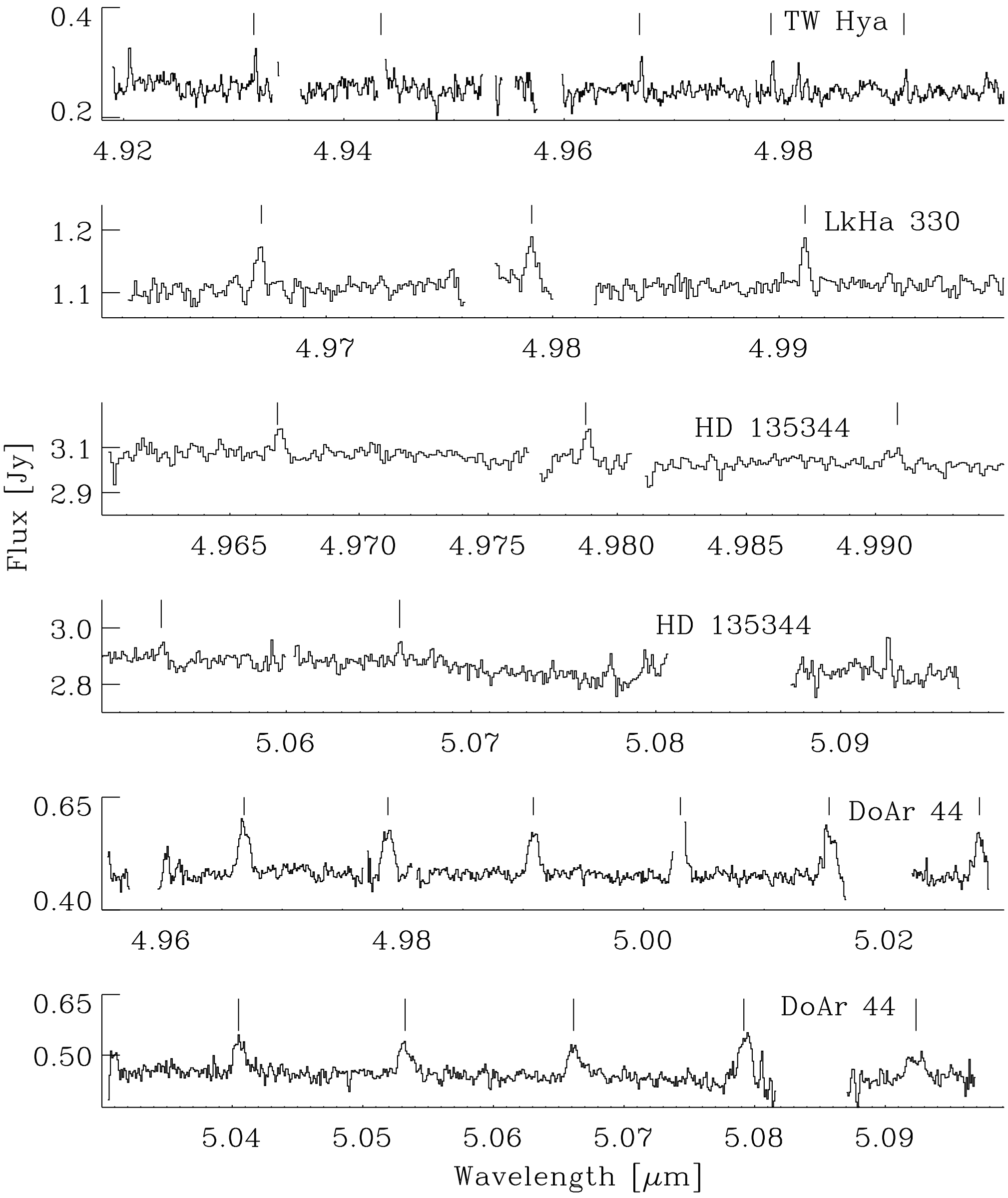

Figure 3.3: A close-up of CO lines longward of P(25). Note the different plot ranges for each source.

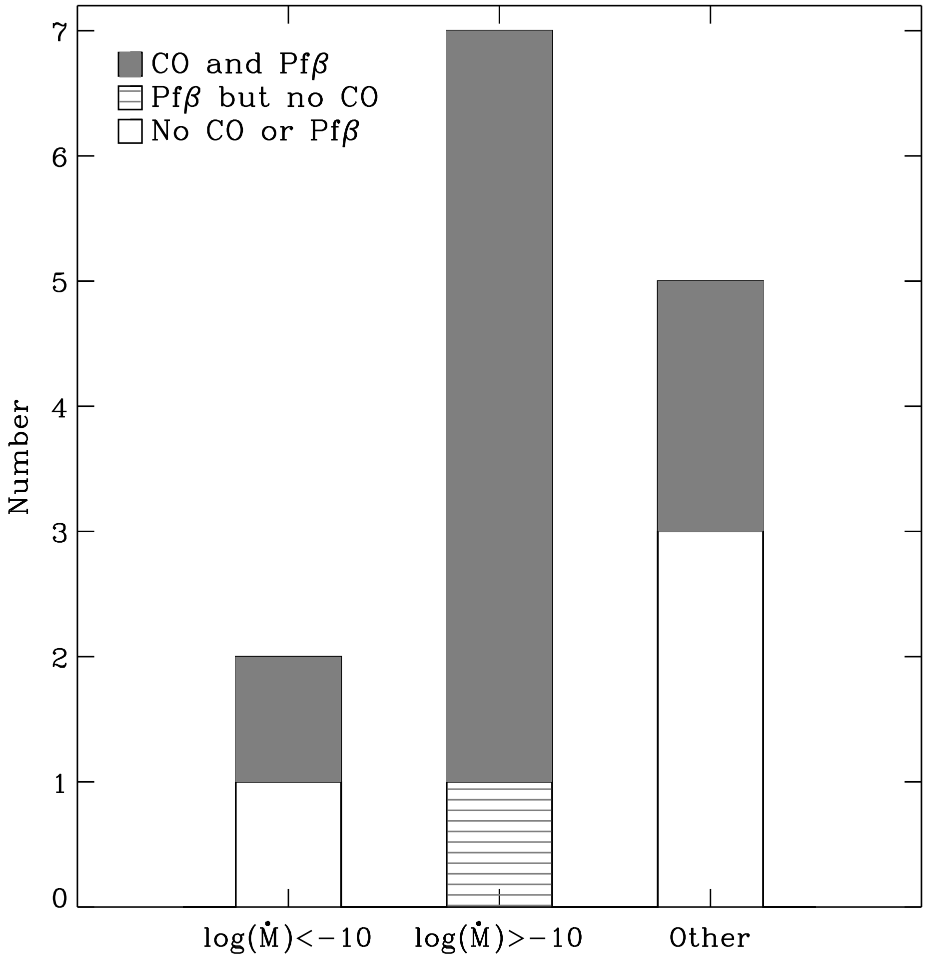

Figure 3.4: A histogram showing the numbers of disks with CO and Pfβ detections, neither CO nor Pfβ detected, or Pfβ but no CO. The three columns show low and high $\dot{M}$ sources ($[\dot{M}]=M_{\odot}$/yr), respectively, followed by those for which $\dot{M}$ is either unknown or has only weak upper limits.

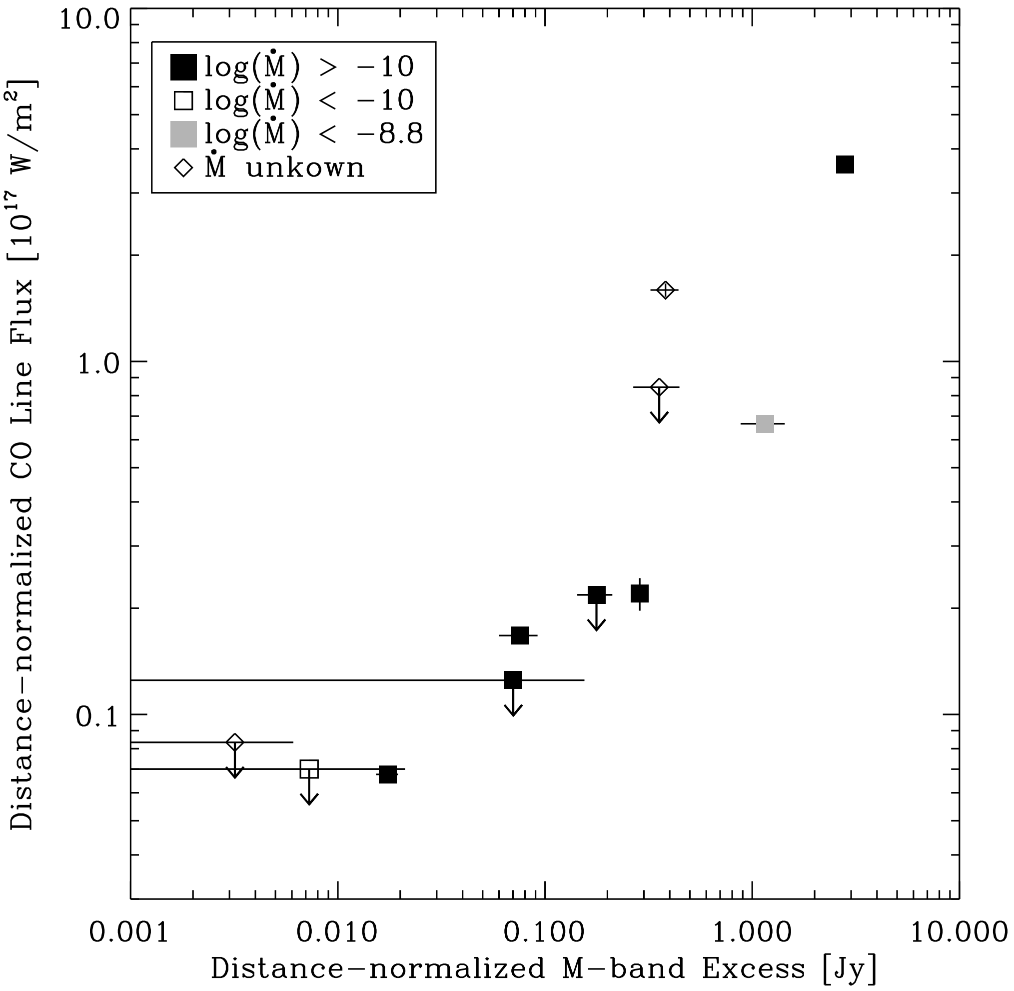

Figure 3.5: A comparison between CO line flux and M-band continuum excess, with both normalized to a distance of 140 parsecs. M-band continuum fluxes and error bars are taken from Table 3.4. CO line fluxes are the mean of P(6)–P(12), and error bars represent the standard error of the mean. Upper limits are shown for sources with no CO emission, assuming a 3σ detection limit and a linewidth (FWHM) of 15 km s^{-1}.

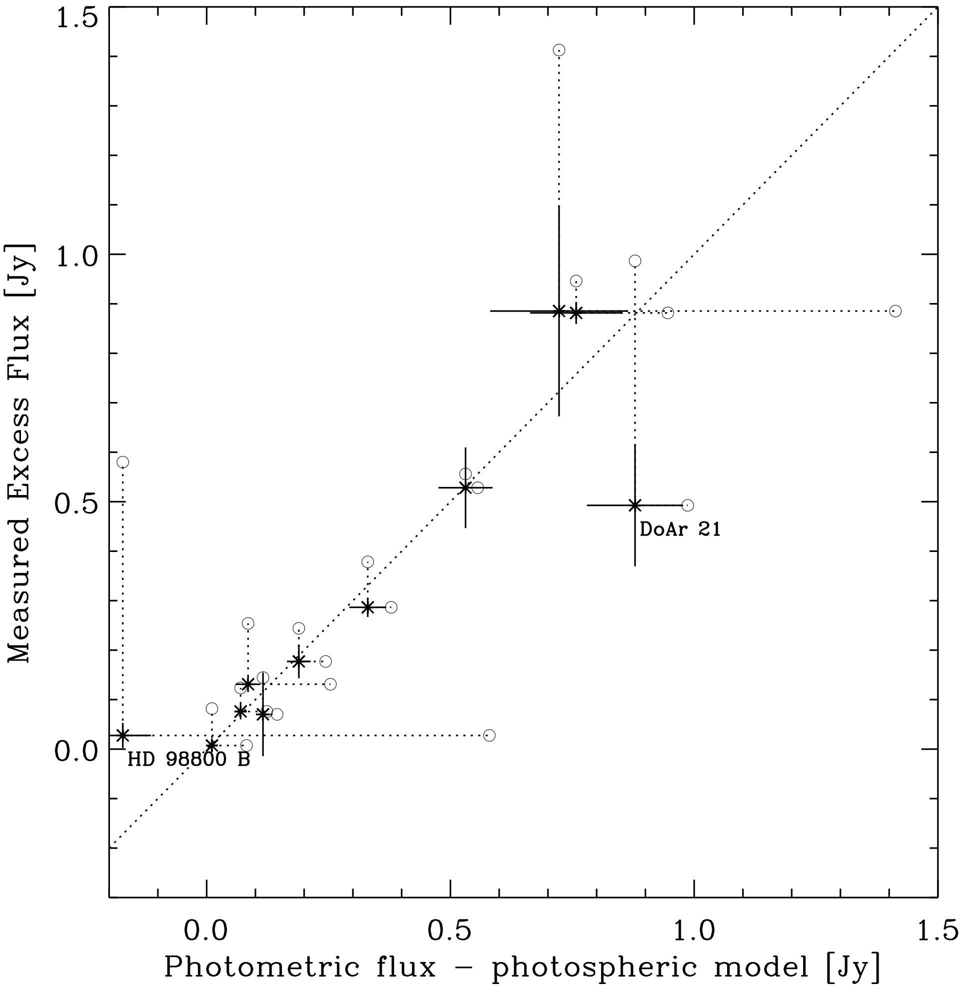

Figure 3.6: Comparison of veiling-derived excess flux (Equation 3.1) and that derived from both photometry and stellar models (based on the parameters in Table 3.2). Veiling error bars are described in the text; photometric error bars are assumed to be 10%. The dashed line shows a 1:1 correspondence. Excess fluxes are by definition less than or equal to the total measured fluxes, which are shown as open circles at the end of dotted lines. Outliers from the 1:1 line are labeled for reference.

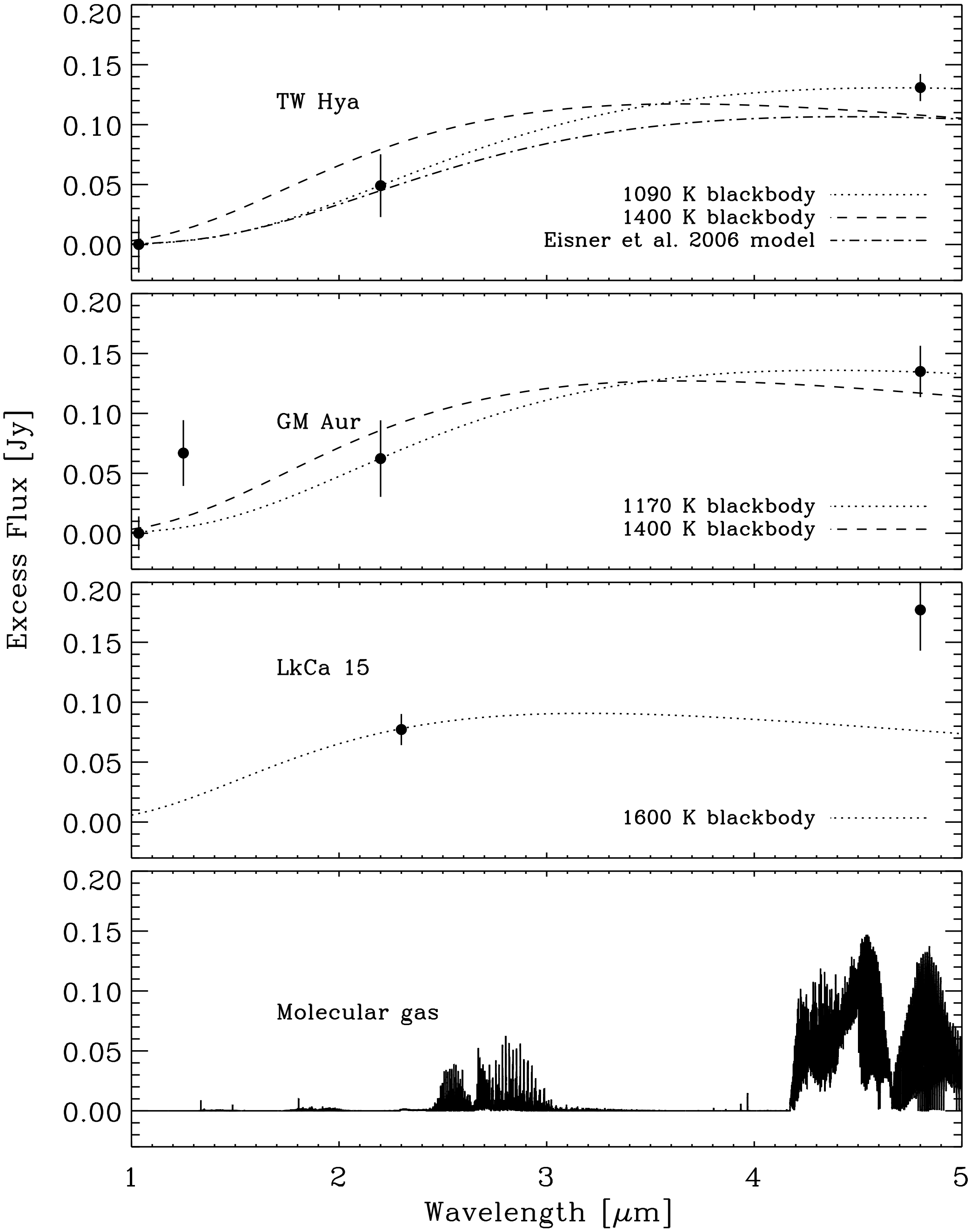

Figure 3.7: Excess fluxes and disk models for LkCa 15, GM Aur and TW Hya. The top three panels show excess flux in the M- (our work), Y-, J-, and K- bands (Folha and Emerson, 1999; Johns-Krull and Valenti, 2001; Edwards et al., 2006; Espaillat et al., 2008), calculated with Equation 3.1. For LkCa 15, we plot the 1600 K blackbody found to fit the K-band continuum (Espaillat et al., 2008). For TW Hya and GM Aur, we plot blackbody continua that simultaneously fit the M- and K-band veiling measurements, as well as the best-fit 1400 K blackbody. For TW Hya, we additionally plot the emission expected from the simple disk model presented in Eisner et al. (2006). The bottom panel shows the emission expected from a gas consisting of CO (and ^{13}CO), H_2O, and CO_2 in the ratio 30:30:1. The temperature was set at 1500 K, emitting area at 1 AU^2 and column density of CO at $4 \times 10^{20}\,\mathrm{cm}^{-2}$. Line shapes were taken to be 200 $\mathrm{km\,s}^{-1}$—velocities comparable to Keplerian velocities near the surface of the star.

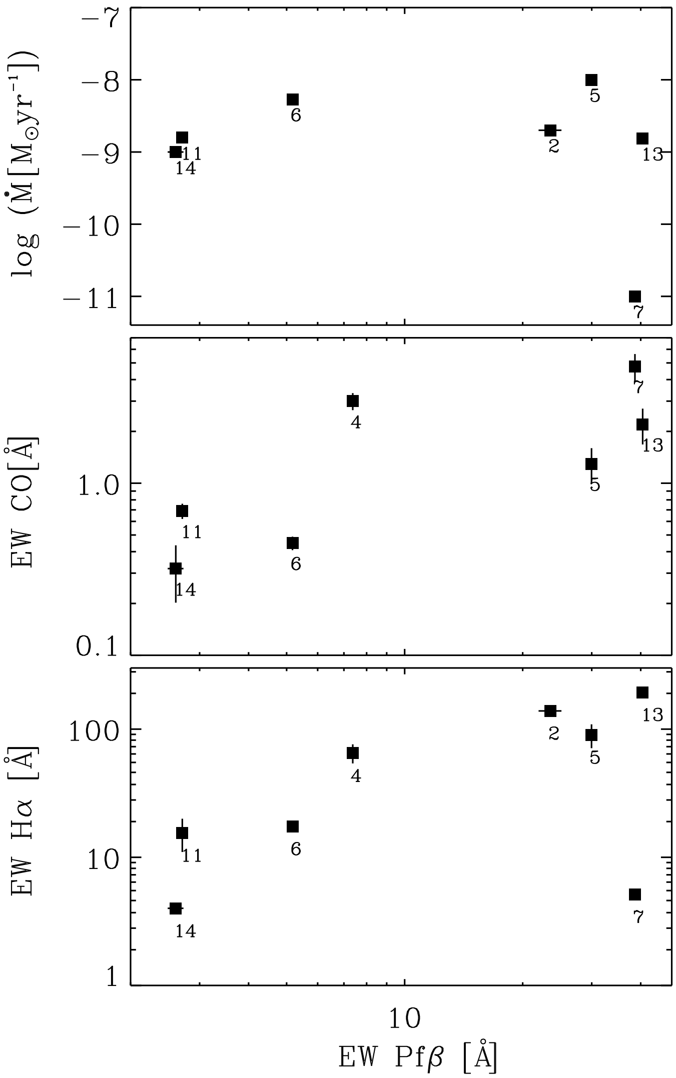

Figure 3.8: Pfβ equivalent width compared to accretion rate (top), equivalent width of the CO v=1 → 0 P(6) line (middle), and Hα equivalent width (bottom).

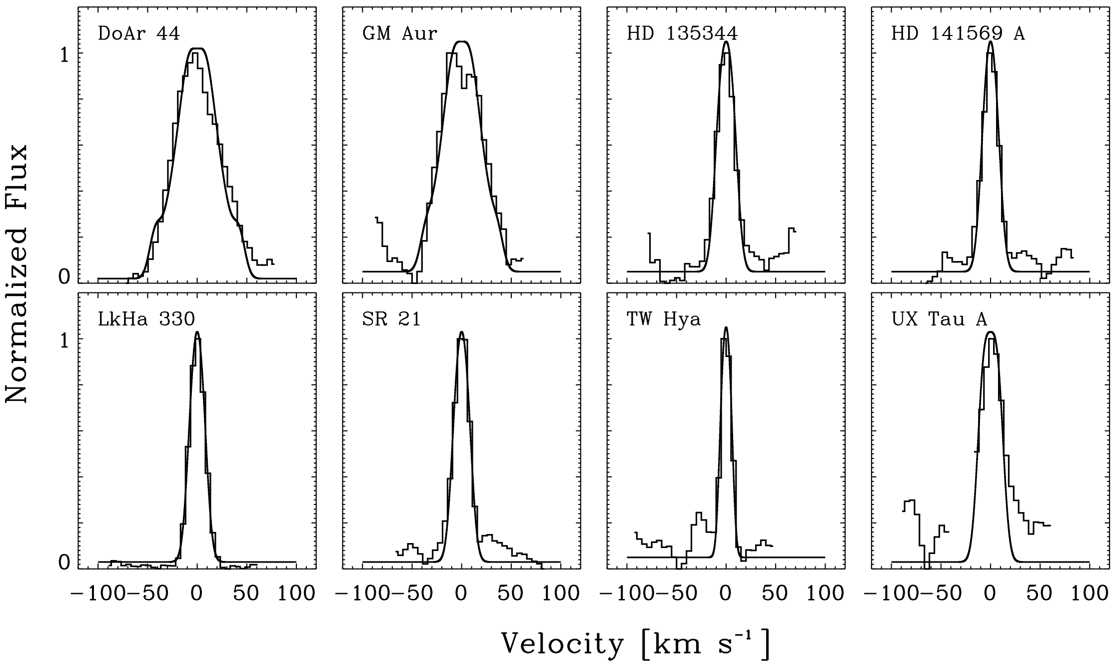

Figure 3.9: CO emission line composites. Fluxes have been continuum-subtracted and divided by their peak value. Solid curves show best-fit disk models used for the calculation of $R_{\rm CO}$.

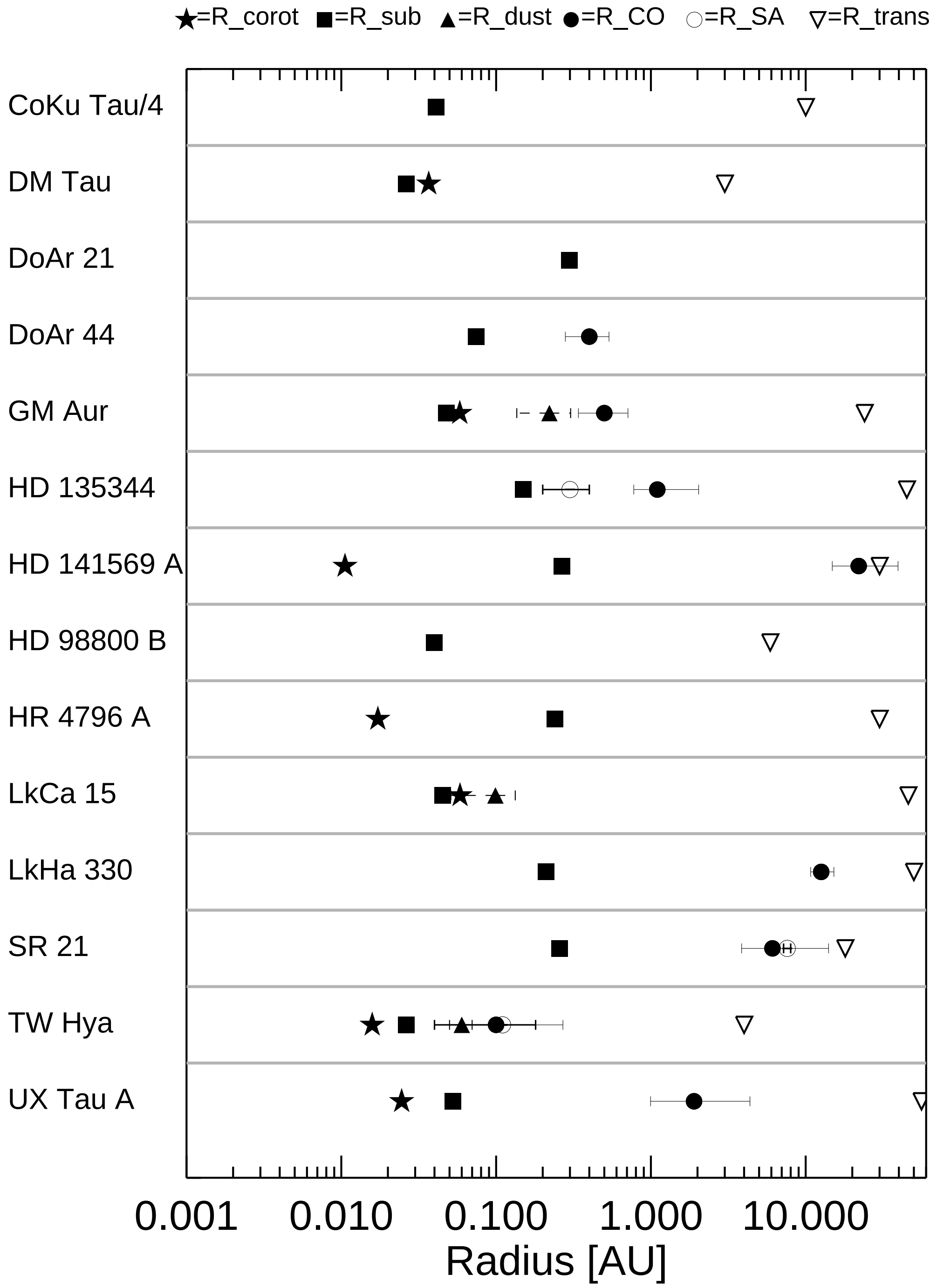

Figure 3.10: A comparison of several relevant disk radii: R_{corot}, R_{sub}, R_{dust}, R_{CO}, R_{SA}, and R_{trans} (details discussed in text).

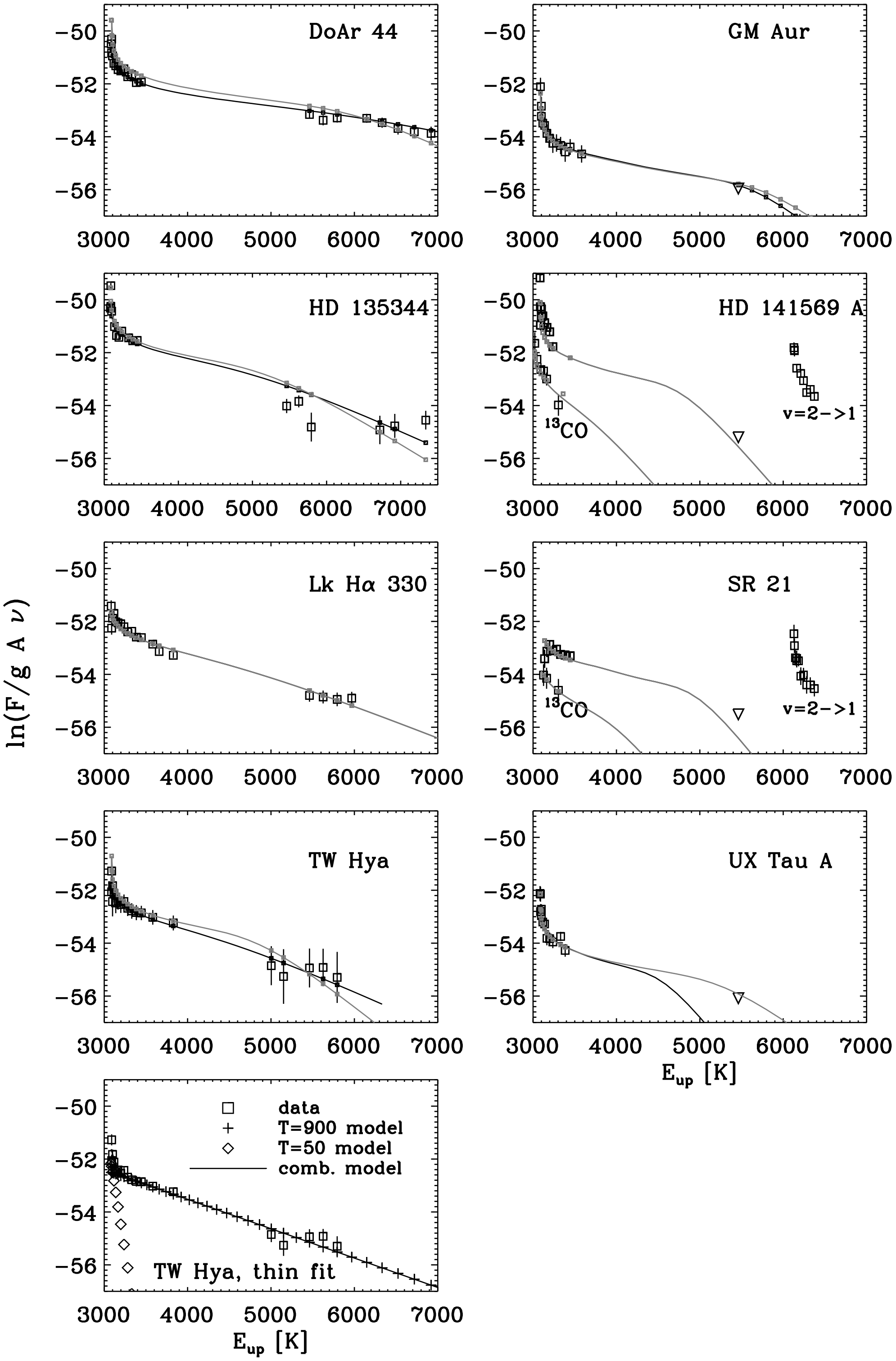

Figure 3.11: Rotation diagrams for the CO emission sources. The data points are usually nonlinear, which is indicative of large optical depths. Measured fluxes are shown as open boxes with error bars. Triangles are upper limits. Small, filled squares connected by solid lines are our best-fit models. Black is the overall best fit; gray is the best fit with fixed emitting area. The bottom left panel shows the rotation diagram for TW Hya fit with two optically thin components at different temperatures. The fit requires 10^{24} times as many cold molecules as hot.

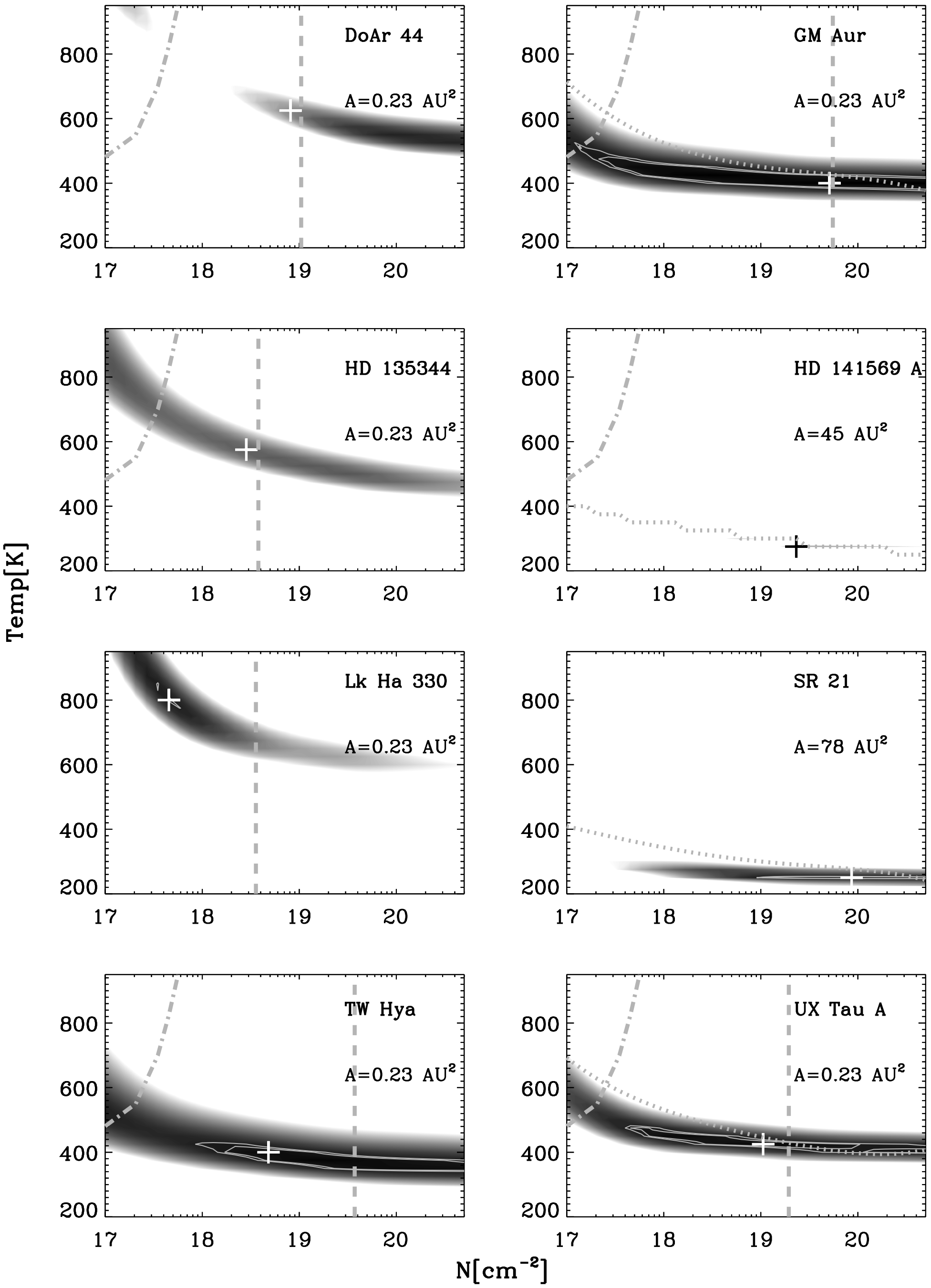

Figure 3.12: χ^2 plots of temperature and column density in our rotation diagram fits. Outlined contours are 95 and 99% confidence intervals. Dashed vertical lines represent density upper limits imposed by the non-detection of ^{13}CO. Dotted lines represent restrictions imposed by a non-detection of transitions at high rotational energy (P(29) or higher). Dash-dotted lines are restrictions imposed by the assumption that the curvature at low energy is real and due to optical depth effects. Note the tilt in the χ^2 contours, caused by the degeneracy of temperature and density.

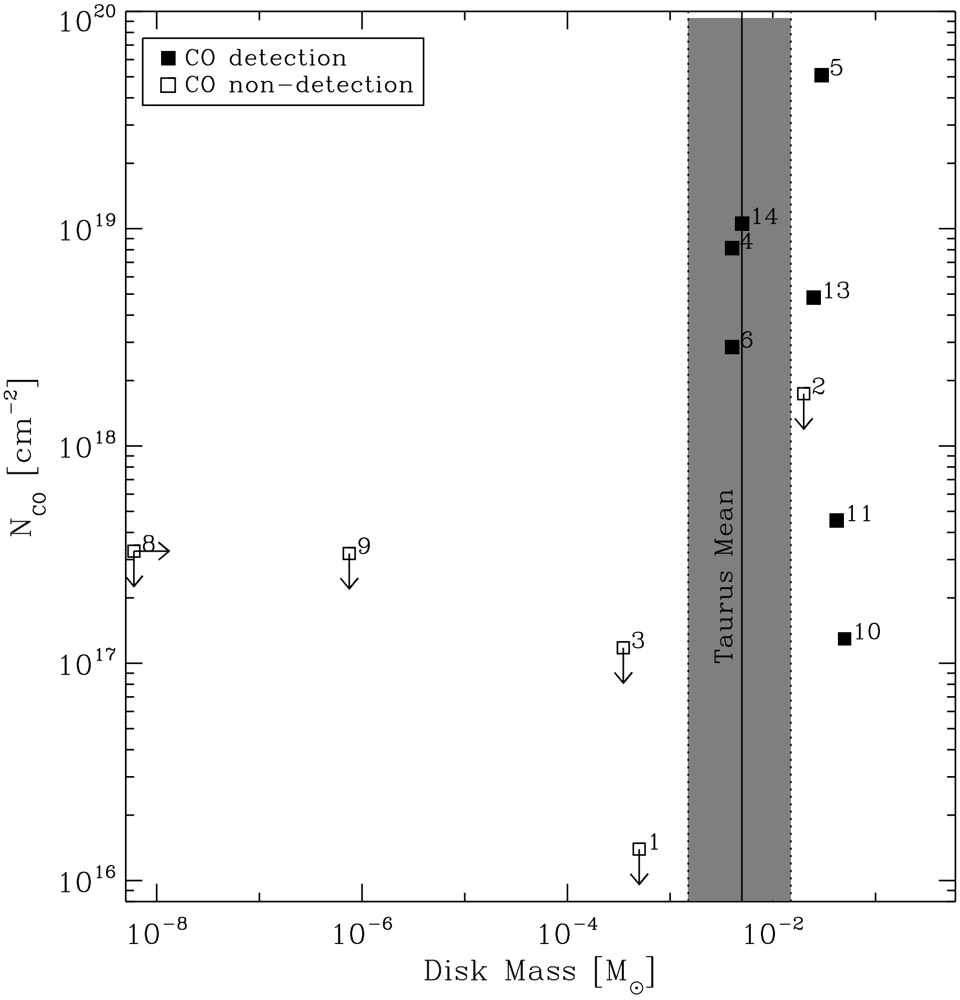

Figure 3.13: $M_{\rm disk}$ against N_{CO}. N_{CO} was derived from our rotation diagram fits. The Taurus mean disk mass and dispersion are shown by the shaded region (Andrews and Williams, 2005). See Table 3.2 to find the source name corresponding to each index.

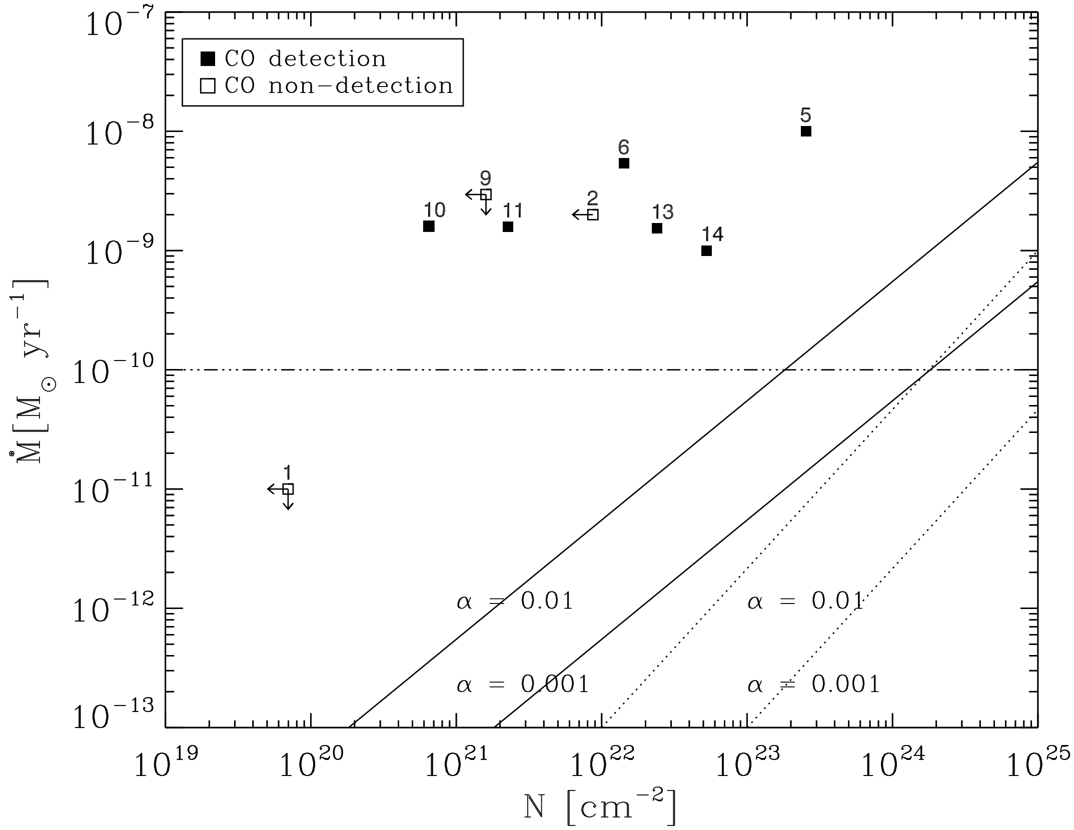

Figure 3.14: $\dot{M}$ against N—the gas column density. N is derived from our excitation diagram fits, assuming a CO abundance of 2×10^{-4}. Solid lines show the relationship expected for an α-viscosity disk model (Equation 3.7); dotted lines show the prediction for MRI-driven accretion (Chiang and Murray-Clay, 2007, Equation 3.5). We show two different values of α, as labeled. The dash-dotted line shows the limit above which the accretion rate is too high to be consistent with photoevaporative clearing.

Table 3.1. Summary of Observations

Star	Dates ($V_\oplus$)[a]	Standards
CoKu Tau/4	2002 Dec (6), 2004 Dec (13), 2005 Dec (7), 2006 Dec (12)	HR 1620 [A7V]
DM Tau	2003 Nov (-14), 2005 Dec (9), 2006 Oct (-24), 2007 Mar (30)	HR 1620 [A7V], HR 1251 [A1V]
DoAr 21	2004 July (23)	HR 6175 [O9V]
DoAr 44	2004 July (23), 2005 April (-17)	HR 6175 [O9V], HR 6070 [A0V]
GM Aur	2004 Dec (11)	HR 1620 [A7V]
HD 135344	2005 Apr (-11), 2006 July (20)	HR 5712 [B4V], HR 5812 [B2.5V]
HD 141569 A	2002 Apr (-13), 2008 Jul (22)	HR 6175 [O9V], HR 5685 [B8V]
HD 98800	2001 Jan (-21)	HR 4635 [A1V]
HR 4796 A	2002 Apr (+2)	HR 4313 [A2V]
LkCa 15	2001 Jan (26)	HR 1620 [A7V]
LkHα 330	2002 Dec (11), 2003 Nov (-11), 2004 Dec (17)	HR 1177 [A3V], HR 1620 [A7V]
SR 21	2002 Apr (-19), 2006 Jul (17), 2007 Mar (-30)	HR 6175 [O9V], HR 5812 [B2.5V]
TW Hya	2001 Jan (-19), 2002 Apr (11), 2002 Dec (-24), 2005 Apr (12), 2004 Dec (-24), 2005 Dec (-24), 2006 May[b](6)	HR 4313 [A2V], HR 4494 [B9V], HR 1620 [A7V], HR 2714 [A2V], HR 5028 [A2V]
UX Tau A	2006 Dec (14), 2007 Oct (-16)	HR 1620 [A7V]

[a] Earth-induced Doppler shift in km s^{-1}. Add heliocentric Doppler shift of source to get shift between source and Earth's atmosphere. Measured heliocentric shifts: DoAr 44 (-2), GM Aur (20), HD 135344 (4), HD 141569 A (-17), LkHα 330 (15), SR 21 (-8),TW Hya (0), UX Tau A (15)

[b] Observed with Phoenix

Table 3.2. Our Sample: Stellar and Disk Properties

Star	SpT	dist [pc]	$M_\star$ $[M_\odot]$	$R_\star$ $[R_\odot]$	$L_\star$ $[L_\odot]$	$T_\star$ [K]	i_d [°]	EW(Hα) [Å]	$\log \dot{\mathrm{M}}$ $[M_\odot \mathrm{yr}^{-1}]$	$\log m_{\mathrm{d}}$ $[M_\odot]$	Index
CoKu Tau/4 ^{a}	M1 ^{20}	140^{b}	0.5 ^{39}	1.9^{c}	0.61 ^{39}	3720 ^{39}	$\cdots$	1.8-2.8 ^{27}	<-11 ^{14,k}	-3.3 ^{3}	1
DM Tau	M1 ^{20}	140	0.65 ^{39}	1.2	0.25 ^{39}	3720 ^{39}	32 ± 1 ^{41}	138.7 ^{12}	-8.7 ^{47}	-1.7 ^{3}	2
DoAr 21	K1 ^{6}	119 ^{30}	1.3	1.6	32 ^{9}	5080	$\cdots$	0.8 ^{6}	$\cdots$	-3.5 ^{2,d,i}	3
DoAr 44	K3 ^{4}	119 ^{30}	1.2	0.8	2 ^{9}	4730	60 ^{4}	54-76.1 ^{40,9}	$\cdots$	-2.4 ^{4}	4
GM Aur	K3 ^{20}	140	1.2 ^{39}	1.4	0.83 ^{39}	4730 ^{39}	56 ± 2 ^{41}	71-109 ^{28,16}	-8.0 ^{25}	-1.5 ^{3}	5
HD 135344	F4 ^{44}	84 ^{10}	1.6 ^{44}	2.5	8.1 ^{44}	6592 ^{44}	14 ± 4 ^{36}	17.4 ^{27}	-8.27 ^{21}	-2.4 ^{11}	6
HD 141569 A	B9.5 ^{31}	108 ^{31}	2.00 ^{31}	1.7	25.77 ^{31}	10000 ^{31}	51 ± 3 ^{46}	5.12 ^{5}	-11 ^{31}	-3.2 ^{31}	7
HD 98800 B^{a}	K5 ^{34}	47.6 ^{18}	1.6 ^{34}	2.00 ^{34}	0.58 ^{34}	4000 ^{34}	66.8 ± 3.2 ^{8}	0.19 ^{15}	$\cdots$	-8.2 ^{34,h}	8
HR 4796 A ^{c}	A0 ^{26}	67.1 ^{26}	2.4 ^{21}	1.7 ^{26}	21 ^{26}	9500 ^{26}	$72\ ^{+6}_{-9}$ ^{29}	$\cdots$	<-8.53 ^{21}	-6.1 ^{22}	9
LkCa 15	K7 ^{42}	140	1.05 ^{1}	1.5	0.74 ^{1}	4350 ^{1}	57 ± 10 ^{42}	13–23.1 ^{28,27}	-8.8 ^{47}	-1.3 ^{3}	10
LkHα 330	G3 ^{10}	250 ^{10}	2.5 ^{10}	4.0	16. ^{10}	5800 ^{10}	30^{+10}_{-10} ^{10,e}	11-20 ^{27}	-8.8 ^{19,f}	-1.4 ^{11}	11
SR 21	G2.5 ^{10}	160 ^{10}	2.5 ^{10}	4.9	24. ^{10}	5800 ^{10}	22^{+4}_{-4} ^{36}	0.54 ^{27,g}	<-8.84 ^{33}	-1.3 ^{11}	12
TW Hya	K7 ^{45}	51 ^{17}	0.6 ^{35}	1.0	0.25 ^{42}	4060	4.3 ± 1.0 ^{36}	194. ^{37}	-8.8 ^{23}	-1.6 ^{43,j}	13
UX Tau A	K5 ^{20}	140	1.1 ^{24}	1.4 ^{24}	1.0 ^{24}	4350	29 ^{11}	4 ^{7}	-9.0 ^{32}	-2.3 ^{3}	14

References. — (1) Akeson et al. 2005 (2) Andre et al. 1994 (3) Andrews & Williams 2005 (4) Andrews & Williams 2007 (5) Andrillat et al. 1990 (6) Bary et al. 2003 (7) Beckwith et al. 1990 (8) Boden et al. 2005 (9) Bouvier & Appenzeller 1992 (10) Brown et al. 2007 (11) Brown 2007 (12) Cohen & Kuhi 1979 (13) Dent, Greaves & Coulson 2005 (14) D'Alessio et al. 2005 (15) Dunkin et al. 1997 (16) Edwards et al. 1994 (17) Eisner et al. 2006 (18) Favata et al. 1998 (19) Fernandez et al. 1995 (20) Furlan et al. 2006 (21) Garcia-Lopez et al. 2006 (22) Greaves 2000 (23) Herczeg & Hillenbrand 2008 (24) Johns-Krull, Valenti & Linsky 1998 (25) Johns-Krull & Gafford 2002 (26) Jura et al. 1998 (27) Kessler-Silacci et al. 2006 (28) Kitamura et al. 2002 (29) Koerner et al. 1998 (30) Lombardi et al. 2008 (31) Merín et al. 2004 (32) Najita, Strom & Muzerolle 2007 (33) Natta, Testi & Randich 2006 (34) Prato et al. 2001 (35) Qi et al. 2004 (36) Pontoppidan et al. 2008 (37) Reipurth et al. 1996 (38) de la Reza & Pinzon 2004 (39) Sargent et al. 2006 (40) Shevchenko & Herbst 1998 (41) Simon et al. 2001 (42) Thi et al. 2004 (43) Trilling et al. 2001 (44) vanBoekel et al. 2005 (45) Webb et al. 1999 (46) Weinberger et al. 1999 (47) White & Ghez 2001

[a] Binary—properties for combined system

[b] Taurus distances are taken to be 140 pc.

[c] Stellar parameters without references are calculated from other parameters.

[d] Upper limit

[e] Adopted for SED fitting; not well constrained

[f] Estimated from full width of Hα at 10% level and equation 1 of Natta et al. (2004).

[g] Absorption

[h] Lower limit

[i] Assuming $\kappa_{1.3\,\mathrm{mm}} = 0.02\,\mathrm{cm}^2\,\mathrm{g}^{-1}$ and $T = 30\,\mathrm{K}$.

[j] Corrected for distance

[k] Estimated upper limit based on Muzerolle et al. 2000.

Table 3.3. Summary of SED Fitting: Results from the Literature

Star	$M_{\rm in}$ [$M_{☾}$]	$R_{\rm thin,out}$ [a] [AU]	$R_{\rm wall,in}$ [b] [AU]	Σ_0 [c] [g cm^{-2}]	Ref.
CoKu Tau/4	0.0007[d]	10	10	6×10^{-6}	4
DM Tau	0.0007[d]	3	3	1×10^{-5}	3
DoAr 21	···	···	···	···	···
DoAr 44	···	···	···	···	···
GM Aur	0.02	5	24	3×10^{-4}	3
HD 135344	0.10	0.45	45	1×10^{-2}	1
HD 141569 A	···	···	30	···	9
HD 98800 B [e]	···	2	5.9	···	7
HR 4796 A	···	···	∼30	···	8
LkCa 15 [f]	0.001[g]	5	46	1×10^{-5}	6
LkHα 330	0.24	0.8	50	1×10^{-2}	1
SR 21	0.10	0.45	18	2×10^{-2}	1
TW Hya	0.5	4, 0.8	4, 0.8	7×10^{-3}, 6×10^{-7}, 9×10^{-7}	2, 5, 10
UX Tau A [h]	···	···	56	···	6

[a] Outer edge of optically thin disk

[b] Inner edge of optically thick disk

[c] Σ_0 is estimated dust surface density at 1 AU assuming $\Sigma = \Sigma_0 (r/\mathrm{AU})^{-3/2}$, inner radius equal to the sublimation radius (Equation 3.4), and outer radius as given in column 3. For LkCa 15, the inner radius is instead taken to be 0.15 AU. For TW Hya, the last two values of Σ_0 are obtained directly from listed references.

[d] Upper limit

[e] The model for HD 98800 B contains an optically thin ring between 1.5 and 2 AU.

[f] The model for LkCa 15 also contains an optically thick ring between 0.12 and < 0.15 AU.

[g] Optically thin region.

[h] The model for UX Tau A contains an optically thick region from 0.16 to < 0.18 AU containing a maximum of 216 $M_{☾}$.

References. — (1) Brown et al. 2007 (2) Calvet et al. 2002 (3) Calvet et al. 2005 (4) D'Alessio et al. 2005 (5) Eisner, Chiang & Hillenbrand 2006 (6) Espaillat et al. 2007b (7) Furlan et al. 2007 (8) Jura et al. 1998 (9) Marsh et al. 2002 (10) Ratzka et al. 2007

Table 3.4. Veiling Results

Star	Phot. Flux [Jy] [a]	Cont. Flux [Jy]	r_M	$\Sigma_{0,v}$ [g cm^{-2}][b]	Template	Ref. flux [Jy]	Ref
CoKu Tau/4	0.07 ± 0.01	0.01 ± 0.01	0.1 ± 0.2	$\mathbf{(1^{+2}_{-1}) \times 10^{-7}}$	HD 79210	0.08	2
DM Tau	0.08 ± 0.08	0.07 ± 0.08	1 ± 2	$(2 \pm 2) \times 10^{-6}$	HD 79210	0.14	3
DoAr 21	0.3 ± 0.1	0.5 ± 0.1	1.6 ± 0.7	$(2.0 \pm 0.5) \times 10^{-5}$ [d]	HD 79210	0.85	1
DoAr 44	0.0 ± 0.1	0.5 ± 0.1	$\cdots$	$(1.9 \pm 0.3) \times 10^{-5}$ [d]	HD 79210	0.53	1
GM Aur	0.04 ± 0.02	0.08 ± 0.02	1.8 ± 0.8	$(1.8 \pm 0.4) \times 10^{-6}$	HD 79211	0.12	2
HD 135344[c]	0.00 ± 0.05	2.25 ± 0.05	$\cdots$	$(4.7 \pm 0.1) \times 10^{-6}$	HD 79211	2.26	4
HD 98800 B	0.52 ± 0.04	0.03 ± 0.03	0.05 ± 0.05	$\mathbf{(4 \pm 4) \times 10^{-8}}$	HD 79210	0.58	5
LkCa 15	0.05 ± 0.01	0.18 ± 0.03	3 ± 1	$(9 \pm 2) \times 10^{-6}$	HD 79210	0.24	3
LkHα 330	0.02 ± 0.03	0.88 ± 0.02	40 ± 40	$(1.79 \pm 0.05) \times 10^{-5}$	ROX 43 A	0.90	1
SR 21	0.2 ± 0.9	0.9 ± 0.2	3 ± 13	$(7 \pm 2) \times 10^{-6}$	ROX 43 A	1.13	1
TW Hya	0.11 ± 0.02	0.13 ± 0.01	1.1 ± 0.2	$\mathbf{(3.5 \pm 0.4) \times 10^{-7}}$	HD 79211	0.25	2
UX Tau A	0.09 ± 0.02	0.29 ± 0.02	3.3 ± 0.8	$(5.8 \pm 0.4) \times 10^{-6}$	HD 107146	0.37	3

[a] Median of Ax where x is the photospheric template and A is the scaling term. Error bars here and elsewhere are 1 σ and do not account for template mismatches.

[b] Column density of dust at 1 AU, assuming optically thin emission, $T = T_\star \, (R_\star/2r)^{2/5}$, $\Sigma = \Sigma_d (r/\mathrm{AU})^{-3/2}$, R_{in} is the dust sublimation radius with T=1500 K, R_{out} is taken from Table 3.3 and $\kappa_{5\mu m} = 440\,\mathrm{cm}^2\mathrm{g}^{-1}$. Bolded values are the actual dust column (because $\tau < 1$), while non-bolded values are lower limits.

[c] No proper template available, so measurement may be unreliable.

[d] Outer radius taken to be 3 AU.

Spectral types of templates are: HD 79210: M0V, HD 79211: K7V, HD 107146: G2V, ROX 43 A: G5.

References. — (1) Evans et al. 2003 (2) Hartmann et al. 2005 (3) Kenyon & Hartmann 1995 (4) Malfait et al. 1998 (5) Prato et al. 2001

Table 3.5. H I Recombination Equivalent Widths

Source	Pfβ [Å]	Huε [Å]	Huδ [Å]
CoKu Tau/4	U	U	⋯
DM Tau	24 ± 2	U	⋯
DoAr 21	M	U	⋯
DoAr 44	7.4 ± 0.1	M	⋯
GM Aur	30.0 ± 0.6	M	M
HD 135344	5.2 ± 0.1	M	⋯
HD 141569 A	39.7 ± 0.3	15.4 ± 0.3	⋯
HD 98800 B	U	U	⋯
HR 4796 A	U	U	⋯
LkCa 15	M	U	⋯
Lk Hα 330	2.7 ± 0.1	M	⋯
SR 21	A	A	⋯
TW Hya	40 ± 0.4	8.0 ± 0.3	12.4 ± 0.4
UX Tau A	2.6 ± 0.1	U	⋯

An ellipsis means the wavelength of the transition was not observed. U means the region was observed, but no emission was detected. An M refers to a marginal detection. A means the line is in absorption.

Table 3.6. CO Inner Radii

Source	FWHM [a] [km s^{-1}]	$R_{\rm CO}$ [b] [AU]
DoAr 44	56	0.4 ± 0.1
GM Aur	42	0.5 ± 0.2
HD 135344	21	$1.1^{+0.9}_{-0.3}$
HD 141569 A	19	22^{+17}_{-7}
LkHα 330	19	13^{+3}_{-2}
SR 21	18	6^{+8}_{-2}
TW Hya	10	$0.1^{+0.2}_{-0.04}$
UX Tau A	31	2^{+2}_{-1}

[a] Before instrumental deconvolution

[b] Models assume $R_{\rm out} = 50$ AU. Error bars represent a 95% confidence interval.

Table 3.7. Excitation Diagram Fit Results

Star	Temp [K]	$\log(N_{\mathrm{CO}})$ [cm^{-2}]	Area[a] [AU^2]		
DoAr 44	875–1325	18.0–18.9	0.012-0.037		
GM Aur	225–1125	16.6–19.7	0.002–94		
HD 135344 [b]	775	18.0	0.064		
HD 141569 A [b]	275	19.3	45.3		
LkHα 330 [b]	800	17.7	0.23		
SR 21	250–350	18.8–20.5	2.0–94		
TW Hya	350–1200	17.3–18.7	0.002–0.68		
UX Tau A	250–700	17.3–19.3	0.021–94		
Best fits (Area fixed)				$\log(\Sigma_{CO}/\Sigma_0)$[c]	$\log(\Sigma_{CO}/\Sigma_{0,v})$[d]
DoAr 44	625	18.9	0.23	$\cdots$	1.3
GM Aur	400	19.7	0.23	1.0	3.1
HD 135344	575	18.5	0.23	-1.8	1.4
HD 141569 A	275	19.4	45	$\cdots$	3.0
LkHα 330	800	17.7	0.23	-2.8	0.1
SR 21	250	19.9	78	-0.6	2.8
TW Hya	400	18.7	0.23	-1.5, 2.6, 2.4	2.8
UX Tau A	425	19.0	0.23	$\cdots$	1.9
Upper limits [e](T, Area fixed)					
CoKu Tau/4	400	16.1	0.23	-1.0	0.7
DM Tau	400	18.2	0.23	0.8	1.7
DoAr 21	400	17.1	0.23	$\cdots$	-0.6
HD 98800 B	400	17.5	0.23	$\cdots$	2.6
HR 4796 A	400	17.5	0.23	$\cdots$	1.0
LkCa 15	400	17.1	0.23	-0.3	-0.2

[a] Assuming distances in Table 3.2

[b] No acceptable fits in a 95% confidence interval. Table entries are for best fit.

[c] Σ_0 from Table 3.3—SED results

[d] $\Sigma_{0,v}$ from Table 3.4—veiling results

[e] For LkCa 15, this is an estimate, not an upper limit

Chapter 4

CO Rovibrational Emission: A Probe of Inner Disk Structure

This chapter will be submitted to *The Astrophysical Journal* with authors C. Salyk, G. A. Blake, A. C. A. Boogert, and J. M. Brown.

4.1 Abstract

We present observations of CO rovibrational emission from a collection of T Tauri and HAe/Be stars and an analysis of emission line shapes and widths. Line shapes are consistent with an origin in a circumstellar disk atmosphere within a few AU from the parent star, although line asymmetry from some sources may be indicative of an additional inflow or outflow origin. With knowledge of disk inclination, line widths yield the inner extent of CO in the disk. We show that CO inner radii correlate well with dust inner radii and an approximate $r \propto L_\star^{1/2}$ relationship for most stars confirms that inner radii are set by dust sublimation. However, a number of stars appear to have unusually small CO inner radii, perhaps because of non-Keplerian line broadening. Additionally, high-mass HAe and Be stars have unusually large CO inner radii, which may indicate a transition in disk structure at $\sim 11\,L_\odot$. Transitional disks also have unusually large dust and CO inner radii, consistent with the idea that these disks have been dynamically cleared and may represent an advanced state of disk evolution. However, using accretion rates as a proxy for age, we find no additional correlation between CO disk radii and age.

4.2 Introduction

Observations of the inner regions ($\lesssim$ 5 AU) of circumstellar disks are essential for obtaining a complete understanding of star and planet formation. The inner disk interacts with the central star, thereby controlling the accretion and ejection of material and setting the timescale for star formation and disk evolution. In addition, inner disks are the likely birthplace of terrestrial planets. Unfortunately, however, conventional telescopes cannot resolve these regions at the distance of known star-forming clouds.

Recently, significant advancements in our understanding of inner disks have been made with two complementary techniques: IR interferometry and high-resolution spectroscopy. IR interferometry is capable of observing thermal emission from the dusty component of disks with resolutions of a few mas (probing size scales down to a few hundredths of an AU) (Millan-Gabet et al., 1999; Eisner et al., 2003; Akeson et al., 2005b; Monnier et al., 2005). High-resolution spectroscopy, on the other hand, has been used to study vibrational emission from hot gaseous molecules, specifically H_2O and CO (Najita et al., 2003; Blake and Boogert, 2004; Carr et al., 2004; Rettig et al., 2004; Brittain et al., 2003). Vibrational emission requires high temperatures and densities, which are preferentially found in inner disks, and thus allows for a focused look at these regions. In addition, observations at high spectral resolution provide spatial information because line profiles are constructed of emission from a rotating Keplerian disk. Both IR interferometry and high-resolution spectroscopy have resulted in successful observations of both T Tauri and Herbig Ae/Be stars with a range of masses, luminosities, and characteristics.

As a result of the extensive and varied IR interferometric studies, a number of patterns have emerged that have improved our understanding of inner disk structure. Firstly, it was noticed that standard, optically thick accretion disk models (such as outlined by Hillenbrand et al. (1992)) fail to simultaneously fit SEDs and visibilities (Millan-Gabet et al., 2001; Akeson et al., 2002)). SEDs utilizing the standard disk model tend to underestimate the radius of the dust-free inner disk. Better fits to visibilities were obtained using simple geometric Gaussian or ring models. Although these models are not physically derived, the ring model may correspond to an optically thin inner gas disk plus a hot, puffed-up wall of dust at the sublimation radius, as suggested by Natta et al. (2001) and Dullemond et al. (2001). Once the correct disk model is taken into account, the inner radius is consistent with the radius at which disk temperatures reach silicate grain sublimation temperatures, although a precise temperature can not be pinned down due to significant scatter in the data points (Monnier et al., 2005). Interestingly, this trend persists down to the lowest mass T Tauri stars observed, suggesting that the dust disk must truncate significantly further out than the gas disk, which is expected to extend inwards to about the stellar corotation radius (Eisner et al., 2005).

In addition to effecting this significant shift in our theoretical picture of inner disk structure, IR interferometry has suggested a few other trends. For example, as noted by Eisner et al. (2003) and Monnier and Millan-Gabet (2002), disks around the earliest-type Be stars in their samples (stars with L$\gtrsim$1000 L$_\odot$) are actually best fit by the standard accretion disk model, consistent with an optically thick inner gas disk. This could signify a transition in the mode of accretion at about 1000 $L_\odot$. In addition, Akeson et al. (2005b) found that for some sources, models required significant gas emission from within the dust disk inner radius, a contribution not often considered in SED modeling. Finally, Akeson et al. (2005a) noted a possible anti-correlation between the ratio of accretion to stellar luminosity ($L_{\rm acc}/L_\star$) and the ratio of inner radius to dust sublimation radius. If the luminosity ratio is a proxy for age, this would suggest a clearing of the inner disk with time.

CO v=1→0 emission is readily produced by the high temperatures and densities found in inner disks around young stars and thereby presents a complementary view of these regions. Although a few regions close to the central star are capable of producing molecular emission, the required temperatures, characteristic velocities, symmetric shapes and a noticeable correlation between emission line shape and inclination (Blake and Boogert, 2004) suggest an origin in the circumstellar disk (Najita et al., 2003). Because temperatures of at least a few 100 K are required to populate the $v = 1$ level, CO v=1→0 emission is restricted to regions within $\sim$ 1 AU, the same area probed by IR interferometry.

We present observations of CO v=1→0 emission around a total of 15 T Tauri and Herbig Ae/Be stars which have also been observed via IR interferometry. We are prompted by the interferometric studies to consider the inner extent of CO emission (which we will refer to as the CO inner radius), which can be determined by calculating the width of the CO emission lines and correcting for inclination effects. We investigate the relationship of CO inner radii with stellar luminosities and accretion rates, as well as to published dust inner radii, with the hope of obtaining further insight into the structure and processes of inner disks.

4.3 Observations and Reduction

Most of our spectra were obtained with NIRSPEC (McLean et al., 1998), a high-resolution (R$\sim$ 25000, FWHM$\sim$ 12.5 km s^{-1}) spectrometer on the Keck II telescope. The data were taken in the M-band in echelle mode with a $0.43''\times24''$ slit. Each source was observed in at least two grating settings, thereby encompassing wavelengths between $\sim$ 4.65 and 5.15 μm, with the exception of a hole between orders at $\sim$ 4.8–4.95 μm. This wavelength range covers the first two R-branch lines and the low/mid P-branch (J=1–12 and J=30–40) of the v=1→0 CO rovibrational spectrum, as well as the H I Pf β and Hu ε transitions.

Our NIRSPEC observations are derived from several observing runs spanning the years 2001–2005. A summary of the observations is presented in Table 4.1. TW Hya's CO emission lines were not resolved with NIRSPEC and this source was therefore observed with Phoenix (Hinkle et al., 2003) on Gemini South. It was observed on 07 and 08 Apr. 2006 using the $0.35''\times14''$ slit. With its significantly higher resolution ($R\sim 60000$; FWHM $\sim$ 5 km s^{-1}), Phoenix provided us with resolved emission lines from P(6) to P(9).

Objects were observed in nod pairs and then differenced to reduce thermal noise on the chip. Wavelengths were calibrated using atmospheric emission lines. Nearby standard stars were observed for additional atmospheric correction. A and B stars with few features in the near IR region were chosen, although H I lines were present and therefore fitted by Kurucz models before division. Standard stars were also utilized for flux calibration, using M-band fluxes estimated from 2MASS K-band photometry (Skrutskie et al., 2006) and spectral type. Wavelengths were also shifted to correct for Earth's motion.

4.4 Sources and Spectra

The dataset included in this article consists of the 20 T Tauri stars (TTSs) and Herbig Ae/Be (HAe/Be) stars listed in Table 4.1. These represent a small subset of our complete M-band survey, chosen because they showed CO v=1→0 in emission and had measured masses, luminosities, and disk inclinations. Although our complete survey includes YSOs spanning a large range of evolutionary states, the sources with CO v=1→0 emission tend to be class II TTSs and their HAe/Be counterparts (for example, those with Type I SEDs in Hillenbrand et al. (1992)). Less-evolved embedded sources often show CO v=1←0 absorption instead, and more evolved sources are much less likely to show any CO emission or absorption signatures. This is consistent with the current belief that the CO emission arises from the surfaces of circumstellar disks; in less evolved sources, the disks are obscured by foreground material and in more evolved sources, the CO does not exist at high enough densities and temperatures to be visible.

We show two example spectra in Figure 2.1—one for T Tauri star DR Tau and one for HAe/Be star AB Aur. The most apparent feature is a set of v=1→0 emission lines extending from R(2)–P(40). Other features include the prominent, wide HI Pf β and Hu ε lines, a dust plus photosphere continuum, and, for DR Tau, ^{13}CO v=1→0 and CO v=2→1 emission. Spectra line shapes may be nearly-Gaussian, double-peaked, flat-topped, or occasionally asymmetric (discussed in more detail in Section 4.5). Except for line widths and shapes, which we discuss in Section 4.5, most of the spectral features are not obviously correlated with stellar or disk parameters and are therefore not easy to predict. However, this may not be too surprising given the complex environment that gives rise to the emission; the spectrum depends on the radial and vertical temperature and density distributions of the disk gas and dust, the viewing geometry of the disk, and properties of the stellar photosphere and any foreground material.

4.5 Emission Line Structure

CO v=1→0 emission is believed to originate from the inner regions of Keplerian disks, because of the conditions required for its production (high densities and temperatures, and significant vertical gradients) and because line shapes are fairly symmetric and dependent on disk inclination (Najita et al., 2003; Blake and Boogert, 2004). With the assumption that the emission lines originate in a circumstellar disk, one can in principle correct for disk inclination and derive the inner extent of CO emission (hereafter the CO inner radius) from the line widths.

One needs to be cautious when determining the CO inner radius, however, because the line shape also depends on the gas and dust temperature and density profiles as well as the degree of non-Keplerian broadening. Ideally, analysis would be performed with a 2D disk model that generates both SEDs and emission lines. However, we focus in this article on a much simpler approach to approximately determine the CO inner radius. We begin by compiling emission line composites from the emission lines that are least contaminated by other CO lines or telluric features. Then, we utilize Gaussian fits to the composite lines and assume that the wings of the profile represent emission from the inner edge of the CO disk. Precisely defining the CO inner radius based on these fits is not entirely straightforward, and we describe our procedure in more detail in Section 4.5.2.

We begin this section by discussing the process of constructing the line composites. Then, we discuss the major emission line features seen in our sources. Finally, we discuss in detail our fitting methods and our estimation of the CO inner radius.

4.5.1 Constructing Line Composites

To investigate emission line shapes and widths, we created normalized, continuum-subtracted composite lines from our spectra. We used only P-branch lines to construct the composites, because R(0) and R(1) lie on top of the HI emission lines. When emission lines were present in both M-band orders, we created a composite for each order, to preserve any differences between low and high energy line shapes. One composite is constructed from emission lines up to P(18) and the other from emission lines P(30) and up. For some stars one of the orders was not observed or was lacking

CO emission, and in these cases only one composite emission line was created. For each composite, we only utilized emission lines that were easily identifiable above the continuum level, that had fairly complete velocity coverage after the removal of telluric contamination, and that were not too entangled with other emission lines (such as CO v=2→1 or ^{13}CO). The P-coefficients of the lines used to construct each composite are listed in Table 4.2.

To construct composites, lines were isolated, continuum subtracted, and normalized to a height of 1. Then, each line was centered according to its wavelength in the HITRAN database (Rothman et al., 1992), wavelengths were converted to velocities, and lines were overlapped. Contamination from nearby lines was removed by eye. Finally, composite lines were constructed using linear interpolation, with a bin size set such that each bin contained approximately five data points. (An exception was made for TW Hya for which this criterion yielded insufficient points for a proper fit). Bin sizes ranged from 2–10 km s^{-1}.

4.5.2 Emission Line Features

The complete set of composite lines used in this study is shown in Figure 4.2. A variety of line shapes is apparent, including nearly Gaussian, double-peaked, flat-topped, and emission plus absorption. This is in general agreement with emission shapes expected from a Keplerian ring of hot gas, plus cooler foreground gas, for different disk geometries. A disk origin for the CO emission is also consistent with the observation that, for most sources, the $P > 29$ emission line composite is somewhat wider than the $P < 19$ composite. Due to radial temperature gradients and any resonance fluoresence, the high-P composite should have proportionally more flux coming from closer to the star, where Keplerian velocities are higher; this will tend to puff up the wings of the emission profile, making it appear broader.

Asymmetric lines are derived for AA Tau, DO Tau, HD 163296, VV Ser, and RY Tau. Asymmetry could either be the result of physical phenomena or the result of improper atmospheric correction, since atmospheric and object lines are offset due to Doppler shifts. For AA Tau, DO Tau, and HD 163296, velocity coverage is not complete and line features vary somewhat when atmospheric removal criteria are varied. Therefore, we should be cautious about attributing these features to physical phenomena. On the other hand, VV Ser and RY Tau were both observed on several occasions and at a variety of Doppler shifts, and the asymmetry is a robust feature of their emission lines. Interestingly, for four out of the five stars, and for three stars observed by Najita et al. (2003), the blue peak is higher than the red peak. Absorption by infalling gas has been suggested as an explanation for this asymmetry (Najita et al., 2003), although we caution that we see no correlation between the presence of asymmetry and accretion rate and/or inclination.

4.5.3 Deriving Inner Radii

Our procedure for deriving CO inner radii was the following. Firstly, we fit each emission line with a simple mathematical model: either one or two Gaussians, depending on its shape, as plotted in Figure 4.2. For the two-Gaussian fits, there were often several minima, so we restricted the solutions to those with a wide positive plus narrower negative Gaussian. The negative Gaussian may represent a dip due to the double-peaked nature of inclined, ring-like emission, or it may represent absorption due to foreground emission. The FWHMs of the positive Gaussians are listed in Table 4.2. We also include in our analysis the FWHMs derived for several additional T Tauri stars by Najita et al. (2003) (see Tables 4.3 and 4.2).

It is important to carefully choose a reference point on the Gaussian curve to represent the CO inner radius. Previous researchers have generally used the velocity corresponding to half width at zero intensity (HWZI) as a convenient estimate (Brittain et al., 2005; Najita et al., 2003). However, non-Keplerian motion can also be important in widening emission lines, so the velocity at HWZI is better seen as a lower limit to the inner radius. Our own 2-layer disk models for TW Hya and GM Aur (Salyk et al., 2007) yielded inner radii of $0.2^{+0.4}_{-0.05}$ and $0.3^{+0.2}_{-0.15}$ AU, respectively, which correspond to approximately 1.5 × HWHM and 2.2 × HWHM. In contrast, the HWZI corresponds to roughly 2.5×HWHM for most stars in our sample. For our analysis, we utilize the velocity at 1.85×HWHM as a best estimate of the inner radius. (These velocities are indicated as solid lines in Figure 4.2). As a lower limit, we utilize 2.5×HWHM, corresponding approximately to the HWZI.

The upper limits to the inner radii in Salyk et al. (2007) are 0.6 AU for TW Hya and 0.5 AU for GM Aur; these correspond to velocities at 0.9 and 1.65×HWHM. As a conservative estimate of the upper limit, therefore, we utilize 0.9×HWHM. These radii are smaller than, and therefore consistent with, the outer emission radii estimated by Najita et al. (2003).

As mentioned in Section 4.5.1, high-P and low-P line composites differ slightly in character and width. Whenever possible, we utilized the high-P line composites to estimate the inner radii used in our analysis, because they are less likely to be contaminated by telluric or foreground CO. A clear demonstration of this choice can be seen with DO Tau, for which the low-P composite appears narrow and oddly asymmetric. These features are apparently due to telluric contamination, or to a combination of telluric and foreground absorption. The high-P composite shows no evidence for such contamination; it is symmetric and much wider. Whenever there was only a low-P composite, however, we utilized this composite instead.

We used the stellar and disk parameters listed in Table 4.3 to convert velocities to inner radii, with the assumption that the emission comes from a Keplerian disk. Note that we will generally assume that the CO inner radius is equivalent to the inner extent of CO in the disk, although in a well-mixed region of the disk in which there is no significant vertical temperature gradient, CO may exist yet not appear in emission. To determine error bars, we added (in quadrature) uncertainties based on the limits discussed above and uncertainties in system inclination. When inclinations were published without error bars, we used a default error of ±10°. Calculated CO inner radii are shown in Table 4.2.

4.6 Results

For low-mass/low-luminosity T Tauri stars (stars with luminosities below $\approx 5\mathbf{L}_\odot$), the CO inner radius is consistent with the corotation radius. For higher-mass stars, the two radii are not consistent.

For a sample of five T Tauri stars observed by Najita et al. (2003), CO inner radii were found to be in the range $\sim$ 0.5–1 times the corotation radius. The corotation radius is defined as the radius at which the disk's Keplerian angular velocity is the same as that at the stellar surface, and is given by:

$$R_c = \frac{GM_\star R_\star^2 \sin^2(i)}{(\mathrm{v}\sin(i))^2}. \tag{4.1}$$

This radius is in turn approximately equal to the magnetic truncation radius, within which disk material is expected to have been cleared by magnetospheric accretion (Shu et al., 1994). With this previous result in mind, we have compared CO inner radii and corotation radii in Figure 4.4 for the stars in our sample and the stars observed by Najita et al. (2003) (with the exception of three stars for which no velocity data were available).

For convenience, we have assumed that $i_\star = i_{\rm disk}$, although the two need not be exactly the same, and in fact are offset by about 6° in our own solar system. In Figure 4.4, symbol sizes are proportional to stellar mass, and we differentiate between TTSs and HAe/Be stars. The solid line is a 1:1 corresondence between the two parameters. It is apparent that many of the lower-mass TTSs have CO inner radii similar to or some fraction of their corotation radius. However, for the higher-mass TTSs and all HAe/Be stars, the CO inner radius is quite a bit larger than the corotation radius, so that CO inner radius is not set by magnetic interactions between the star and disk.

For most low–medium mass stars in our sample, CO inner radii are consistent with dust sublimation radii.

As a result of interferometric observations of inner disks, it has become apparent that dust inner radii are set by sublimation, rather than magnetospheric effects such that $R_{\rm dust} \propto L_\star^{1/2}$. A similar trend could be expected for CO inner radii because of an important connection between CO and dust—dust shielding is required for the protection of molecular CO against dissociation by stellar UV (van Dishoeck and Black, 1988). We therefore plot CO inner radius as a function of stellar luminosity in Figure 4.5 and overplot theoretical curves for the dust sublimation radius as a function of luminosity. The curves are derived from the formula for blackbody grains in an optically thin disk:

$$T_{\rm sub} = \left(\frac{L_\star}{16\sigma\pi r_{\rm sub}^2}\right)^{1/4}. \tag{4.2}$$

This formula neglects grain properties and effects such as disk backscatter, but differs from the results of more in-depth analyses (e.g., Monnier and Millan-Gabet, 2002) by a constant of order unity. (A more complete discussion of various physical models and their differences can be found in Akeson et al., 2005a). We plot curves for three different grain sublimation temperatures—1000, 1500 and 2000 K. Because luminosities are generally published without error estimates, we adopt an error bar of 10%, which is consistent with the errors found by Monnier et al. (2005), which range between a few % and $\sim 50\%$. Up to luminosities of $\sim 11\,L_\star$ CO inner radii for most stars are consistent with the dust sublimation radius.

If inner radii were instead set by the stellar corotation radius (R_c), the slope of radius versus luminosity would be shallower. For example, an empirical fit to our dataset yields $R_c = 0.0001(L_\star/L_\odot) + 0.045$ AU ≈ 0.045 AU. We include R_c and $0.5R_c$ in Figure 4.5 for comparison. Note that at low luminosities, sublimation radii and corotation radii are similar, so it is not possible to decide the physical cause of the CO disk truncation. However, at higher luminosities, it is clear that radii are not consistent with being set by magnetospheric accretion.

CO inner radii are correlated with measured dust inner radii. However, for lower mass stars the tendency is for $\mathbf{R}_{\rm CO} < \mathbf{R}_{\rm dust}$, while for higher mass stars, it's more common that $\mathbf{R}_{\rm CO} > \mathbf{R}_{\rm dust}$.

Because we expect CO inner radii to be determined by the availability of dust to act as a UV shield, we plot CO inner radii against dust inner radii (hereafter referred to as $R_{\rm dust}$) in Figure 4.6. Values and error bars for dust inner radii are taken from the references found in Table 4.3. Error bars for the CO inner radii are the same as in Figure 4.5. The dashed line is a 1:1 correspondence between the two radii.

We were surprised to find a number of low–mid-mass stars for which $R_{\rm CO} < R_{\rm dust}$. We suggest two possibilities for the existence of such sources. The first possibility is that the timescale for mass replenishment via accretion could be shorter than that of CO removal by UV dissociation. In this scenario, the CO inner radius would be set at a point inside the dust inner radius where the radiation field was strong enough for mass removal by dissociation to dominate. This effect would also conveniently explain why we find $R_{\mathrm{CO}} < R_{\mathrm{dust}}$ for only lower mass stars, as it would be seen preferentially around stars with low UV luminosities. To obtain a rough measure of the two timescales, we consider a 4000 K, $2R_{\odot}$ star and compare the dissociation lifetime at 0.05 AU with the time required to fill a gap between 0.05 AU and 0.1 AU by accretion. Utilizing the CO dissociation rates found in van Dishoeck et al. (2008) and assuming no dust shielding, we derive a lifetime for molecular CO at 0.05 AU of $\sim$ 5 yr. (For comparison, the lifetime for CO sitting 0.05 AU from a 10000 K blackbody is 0.05 s.) On the other hand, with an accretion rate of $10^{-7}\,M_{\odot}/\mathrm{yr}$, a gap between 0.05 and 0.1 AU can be filled to a surface density of $10^{-4}\,\mathrm{g\ cm^{-2}}$ in only 0.01 yr. However, this is not the whole story, as UV fluxes are greatly enhanced for accreting protostars. For example, at 0.1 μm, the wavelength primarily responsible for the dissociation of CO (van Dishoeck and Black, 1988), Bergin et al. (2003) estimate that a typical TTS has a flux of $\sim 5 \times 10^{-4}\,\mathrm{erg\ cm^{-2}s^{-1}A^{-1}}$ at 100 AU—an enhancement of nearly 8 orders of magnitude over the reference 4000 K blackbody considered above. With UV fluxes this high, destruction of CO by dissociation is by far the dominant process, and CO inner radii would not be expected to lie within dust radii. The balance of processes for any individual T Tauri star could potentially lie somewhere between these two cases and therefore mass replenishment by CO may be the cause of small CO inner radii for some sources. However, given the large number of such sources, it does not seem the most likely explanation.

The large number of sources with $R_{\mathrm{CO}} < R_{\mathrm{dust}}$ may alternatively be explained by the presence of non-Keplerian motion in the inner disk (turbulence, inflow, or outflow). As discussed in Salyk et al. (2007), the degree of turbulence can be a crucial parameter when fitting emission lines with disk models if the emitting disks have low inclinations. We have assumed only low levels ($v_{\mathrm{th}} = 0.05\,v_{\mathrm{Kep}}$) of turbulent motion when estimating CO inner radii and thus if significant non-Keplerian motion exists, we would falsely attribute it to faster Keplerian motion at smaller radii. However, this is a testable hypothesis, since the percent discrepancy due to thermal motion would be dependent on disk inclination. If we assume $v_{\mathrm{th}} = \alpha v_{\mathrm{Kep}}$, and that v_{th} is isotropic, then the percent discrepancy in radius is given by $\alpha/\sin i$, where α is likely a few percent. If we assume $R_{\mathrm{actual}} \sim R_{\mathrm{dust}}$ then the percent discrepancy in radius should be given by $(R_{\mathrm{dust}} - R_{\mathrm{obs}})/R_{\mathrm{obs}}$. Our dataset, however, demonstrates no correlation between radius discrepancy and $\alpha/\sin i$. Some other form of non-Keplerian motion could also cause the discrepancy although a key signature of inflow and outflow—line asymmetry—is not prevalent amongst the CO lines in our dataset. This is especially true of the subset for which $R_{\rm CO} < R_{\rm dust}$, amongst which only one star (RY Tau) displays line asymmetry.

In short, underestimation of CO inner radii seems a likely explanation for why measured CO inner radii appear to lie inside dust inner radii, although we have not found a satisfying physical explanation for this effect.

We discuss a number of high-mass sources for which $R_{\rm dust} < R_{\rm CO}$ in our next point.

For HAe/Be stars with $\mathbf{L \gtrsim 11\,L_\odot}$, CO inner radii are significantly larger than dust sublimation radii and measured dust inner radii.

In order to visualize all of the various theoretical and measured radii, we have included Figure 4.7. In this figure, we have plotted theoretical dust sublimation radii, corotation radii calculated via Equation 4.1 and measured dust and CO inner radii for each star. Stars are organized in order of luminosity, with higher luminosity sources towards the bottom.

With the exception of HD 144432, for all sources with $L \gtrsim 11\,L_\odot$, measured dust inner radii appear consistent with theoretical dust sublimation radii. However, CO inner radii are much larger than sublimation radii, with the ratio $R_{\rm CO}/R_{\rm sub}$ ranging from 2–13. This could be indicative of differences in disk geometry between T Tauri/low-mass Herbig Ae stars and higher-mass Herbig Ae/Be stars. Indeed, inteferometric observations have suggested a boundary at $\sim 1000\ L_\odot$ between disks with optically thin inner regions and hot inner rims, which tend to have larger inner radii, and disks with optically thick inner regions, which tend to have smaller inner radii (Akeson et al., 2005b). Additionally, results from Hα spectropolarimetry have suggested different inner disk geometries for T Tauri/Herbig Ae stars as opposed to Herbig Be stars (Vink et al., 2002). However, these results both suggest a partition at a higher luminosity ($\sim 1000\ L_\odot$) than we observe in our dataset. In addition, they suggest that higher mass sources have something closer to the 'classical' thin disk, with an optically thick inner disk and hence a *smaller* sublimation radius. Therefore, this particular geometric effect does not explain our results.

Another geometric effect that could cause an increase in the observed CO inner radius is self-shadowing. We consider the self-shadowed disk model from Dullemond et al. (2001), for which stellar parameters are quite similar to the HAe stars in our sample. In this model, the disk region within ~ 1 AU has virtually no vertical temperature gradient, so that it is unlikely to show molecular emission, even if molecules are present. Between 1–2 AU vertical temperature gradients emerge, and disk surface temperatures approach those capable of inducing vibrational transitions. This distance corresponds well with the CO inner radii of HAe stars in our sample. However, if this effect is to explain our results, we should see a correlation between SED type and $R_{\rm CO} - R_{\rm sub}$, but this appears not to be the case. Six of our sample stars have had their SEDs classified as I (flared) or II (self-shadowed) by Meeus et al. (2001) and Acke et al. (2004). Of these six, one (AB Aur) has been classified as type I, although it has a CO inner radius slightly larger than the dust sublimation radius. The remaining five (HD 141569, HD 144432, HD 163296, MWC 480, and VV Ser) have all been classified as type II and most have unusually large CO inner radii, although one (MWC 480) actually has a CO inner radius well inside the sublimation radius. Thus, there is no conclusive evidence that self-shadowing effects can explain our results, although with the small number of sources considered, it cannot be ruled out.

Another possibility one might propose to explain why $R_{\rm CO} > R_{\rm sub}$ for high-luminosity sources is that their high UV flux penetrates a significant distance into the dust disk to dissociate CO. To test this hypothesis, we must determine whether the penetration depth of UV radiation is similar to $R_{CO} - R_{dust}$. We define the penetration depth as the depth at which the dissociation rate equals the rate of replenishment via accretion. Considering a ring from 0.5 to 1 AU, which is the typical ring between R_{CO} and R_{sub} for the HAe stars in our sample, an accretion rate of $10^{-7}\,M_{\odot}$/yr and a surface density of dust $\Sigma = 22 \times (r/AU)^{-1.5}$ g cm^{-2}, the replenishment timescale is ~ 80000 yr. According to the dissociation rates given in van Dishoeck et al. (2008) for a 10000 K blackbody, 80000 years is the dissociation timescale at $\tau \sim 8$. This optical depth is reached in a very short distance along the disk midplane, but we are concerned with the existence of CO in a disk atmosphere, where densities are significantly lower. In this case, the amount of extinction for a light ray depends quite sensitively on the vertical height of the CO emitting region. With a simple disk density prescription, as described in Ruden (1999), and with opacity as defined in Eisner et al. (2006), we estimate that optical depths of ~ 8 are equivalent with $R_{CO} = 1$ and $R_{dust} = 0.5$ if $z/r \sim 0.5$, where z is the height of the emitting layer. This is quite high and implies CO densities of order $10^{-7}\,\mathrm{g\ cm^{-2}}$—orders of magnitude lower than that found by Salyk et al. (2007). In addition, given this setup, one would expect large $R_{CO} - R_{dust}$ to correspond to low densities and, hence, lower line fluxes. However, we do not see evidence for such a correlation. Therefore, UV penetration into the dust disk is not a likely explanation for the large CO inner radii.

In short, the preponderance of high-mass HAe/Be stars for which $R_{CO} > R_{sub}$ and $R_{CO} > R_{sub}$ suggests a transition in disk geometry at $\sim 11\,L_{\odot}$, although the exact nature of the transition is not yet understood.

Amongst the T Tauri stars, there are three notable outliers for which $\mathbf{R_{CO} \gg R_{sub}}$: TW Hya, GM Aur and DR Tau.

TW Hya, GM Aur, and DR Tau have inner radii that lie significantly above the curves for dust sublimation or corotation. It is interesting to note that two of the three sources, TW Hya and GM Aur, are prototypical examples of transitional disks—disks with large inner regions of low opacity within an otherwise optically thick disk, perhaps due to the presence of a planet (Rice et al., 2003; Calvet et al., 2002). For such disks, one might expect the CO inner radius to correspond not with the dust sublimation radius, but instead with the edge of the optically thick outer disk. However, this does not appear to be the case. Although the inner disks of transitional objects are relatively free of dust, they are not entirely so and in fact dust was detected at radii of 0.06 AU (Eisner et al., 2006) and 0.221 AU (Akeson et al., 2005b) for TW Hya and GM Aur, respectively. According to Figures 4.6 and 4.7, the CO inner radii lie just outside of these dust inner radii (see also Salyk et al. (2007)). Since the inner dust disks are optically thin, R_{CO} must be slightly greater than R_{dust} to provide significant UV shielding. Interestingly, the dust inner radii themselves are larger than the expected dust sublimation or corotation radii by factors of $\sim$ 3–5, suggesting that perhaps there has been dynamical clearing of the inner disk.

DR Tau is another notable outlier according to Figures 4.5 and 4.6. We first note that the lower error bar is quite large due to large uncertainties in the system inclination, and that may be the explanation for DR Tau's apparent outlier status. However, there is another physical reason why DR Tau may appear to be an outlier—accretion rates for DR Tau are at least an order of magnitude above those of typical T Tauri stars (Hessman and Guenther, 1997). In Figure 4.5, we plotted stellar luminosity as the abscissa, but the energy from accretion luminosity is also available for heating of the disk, and hence for sublimating grains. For most stars in our sample, the stellar luminosity dominates. However, for two sources, DR Tau and HL Tau, the accretion luminosity may be a magnitude or two larger. If we use the relationship of Hartmann et al. (1998) to estimate accretion luminosity,

$$L_{\rm acc} = 0.8\, G\dot{M}_{\rm acc} M_\star / R_\star, \tag{4.3}$$

and mass accretion rates from Johns-Krull and Gafford (2002), we find that DR Tau's accretion luminosity is $\sim 32\ L_\odot$ (using an average of the accretion rates in Johns-Krull and Gafford (2002)). If placed in Figure 4.5 according to this enhanced luminosity, its CO inner radius becomes consistent with the dust sublimation curve. It is interesting to note that HL Tau, with a $L_{\rm acc} : L_\star$ ratio of about 11, does not appear to be an outlier, and by using the total luminosity, we find that CO inner radius lies somewhat inside of the $T = 2000\,{\rm K}$ sublimation radius. For both sources, it is important to keep in mind that these simple analytical calculations are not taking into account the time variability of T Tauri phenomena. Indeed, DR Tau is known for displaying a high degree of veiling, which is variable on both short and long timescales (Hessman and Guenther, 1997), and HL Tau has an active outflow and shows evidence for periodic large outbursts (Close et al., 1997).

Our results do not indicate an anti-correlation between the ratio of CO inner radius to predicted sublimation radius and the ratio of accretion luminosity to total luminosity.

Based on dust inner radii measurements for 8 T Tauri stars, Akeson et al. (2005a) noted an apparent anti-correlation between the ratio of measured dust inner radius to theoretical sublimation radius and the ratio of accretion to stellar luminosity. This makes intuitive sense; as a star evolves, accretion rates tend to decrease and inner disks should be cleared by some combination of accretion, photo-evaporation, and planetesimal formation. If the dust inner radius increases with age, the CO inner radius should also increase, and this could potentially explain some of the scatter in Figure 4.5.

With this physical motivation in mind, we plot the ratio of $R_{\mathrm{CO}}/R_{\mathrm{sub}}$ against the ratio $L_{acc}/L_{\star}$ in Figure 4.8. To provide a consistent estimate of accretion luminosity, we use Equation 4.3. We calculate the sublimation radius using Equation 4.2, with $T_{\mathrm{sub}} = 1500\ K$. For DR Tau and HL Tau, we use L_{acc} in place of $L_{\star}$ when calculating the sublimation radius.

It is apparent that TW Hya and GM Aur have significantly higher radius ratios than the other TTSs in our sample—a point easily inferred from Figure 4.5. The presence of these two outliers gives a slight downward trend to the dataset, but, a linear fit to the radius ratio against the luminosity ratio yields a just slightly negative slope, with an associated p-value of 95%. Therefore, the dataset is consistent with the two ratios being uncorrelated. This raises some interesting ideas. One possibility for a lack of correlation may be that the luminosity ratio is not a predictive age indicator—intrinsic population heterogeneity could hide any existing age trends. Another possibility is that GM Aur and TW Hya are simply a different breed—i.e., perhaps the formation of inner disk gaps is not a typical evolutionary stage but may occur or not, depending on the particulars of the young stellar system.

4.7 Conclusion

We have detected CO rovibrational emission lines from a variety of young stars with disks, including classical T Tauri stars, transitional objects, and HAe/Be stars encompassing a wide range of luminosities, accretion rates, and disk characteristics. An analysis of line shapes shows that they are consistent with originating from an inner disk atmosphere, although line asymmetries in some sources suggest additional emission from regions of gas inflow or outflow. If asymmetries are due to inflow or outflow, this would imply accretion is occurring well outside the corotation radius.

An analysis of line widths suggests that the inner extent of emission in disks is well correlated with dust inner radii and as well as dust sublimation radii. This result is consistent with the models suggested by IR interferometry, in which the inner gas disk is optically thin. Thus CO rovibrational emission provides a convenient validation of the assumptions made in interferometric analyses and provides an extension to the stellar population available for testing theories of inner disk structure.

Deviations from the $r_{CO} = r_{sub}$ trend also tell an interesting story. A number of T Tauri stars have unusually small CO inner radii, compared to the dust inner radius, even though the CO must be exposed to a significant amount of dissociating UV radiation. If UV excess is small and accretion rates are high, replenishment rates could potentially outdo dissociation rates, but given typical UV excesses for T Tauri stars, this does not seem likely. Another possibility is that non-Keplerian motion is broadening the line shapes, and we are simply underestimating the inner radius by assuming Keplerian motion only.

Transitional objects have unusually large CO inner radii as well. This is primarily due to the fact the dust inner radii are themselves quite large compared to the dust sublimation radius, possibly due to dynamical clearing or grain growth in the inner disk. However, CO inner radii are also significantly larger than dust inner radii, so perhaps the UV radiation is able to dissociate CO some distance into these relatively thin dust disks.

High mass HAe and the single HBe star in our sample also demonstrate unusually large CO inner radii, compared to both the dust inner radii and sublimation radii, which are themselves quite similar. This interesting discrepancy appears only for those stars with $L \gtrsim 11\,L_\odot$, which does not, to our knowledge, correspond to any known transitions in disk or stellar structure. We have considered a few ways in which disk geometry might cause enlarged CO inner radii; although none seem to securely explain our results, one possibility may be a transition between self-shadowing and flared disks.

We have also investigated the relationship between R_{CO}/R_{sub} and $L_{acc}/L_\star$, with the theory that radii may increase with age (and hence decrease with accretion rate) because of inner disk clearing. We note that the transitional disks, TW Hya and GM Aur, have higher R_{CO}/R_{sub} than all other sources, and also a relatively low $L_{acc}/L_\star$. However, there is no general trend between the two variables. This may simply be because accretion luminosity is not an exact proxy for age, or it may indicate that TW Hya and GM Aur are unique and do not represent a common phase of disk evolution.

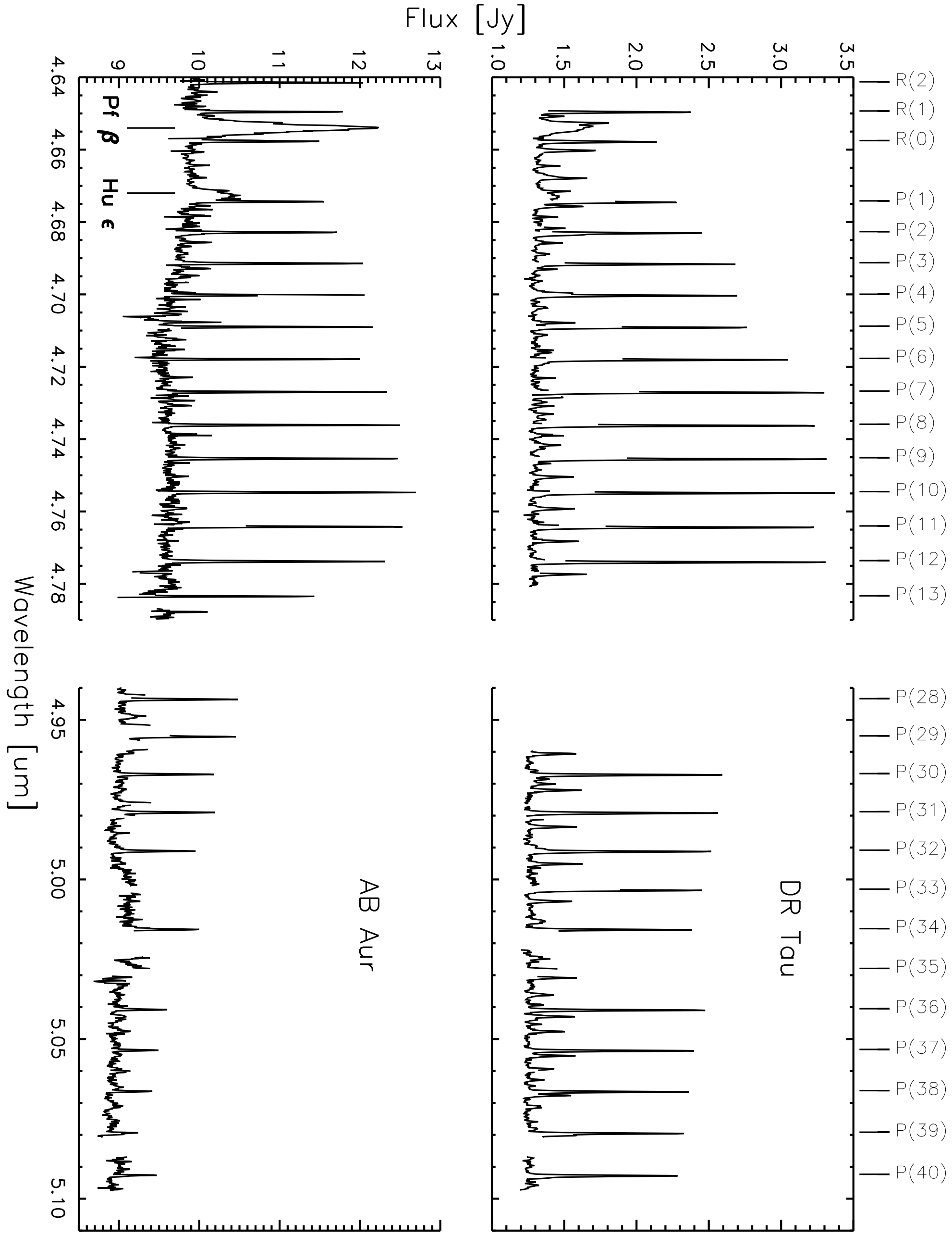

Figure 4.1: NIRSPEC spectra of T Tauri star DR Tau and Herbig Ae star AB Aur. CO v=1→0 transitions are labeled above, and H Pfβ and Huε transitions are labeled below. CO v=2→1 and ^{13}CO transitions are also visible in the spectrum of DR Tau.

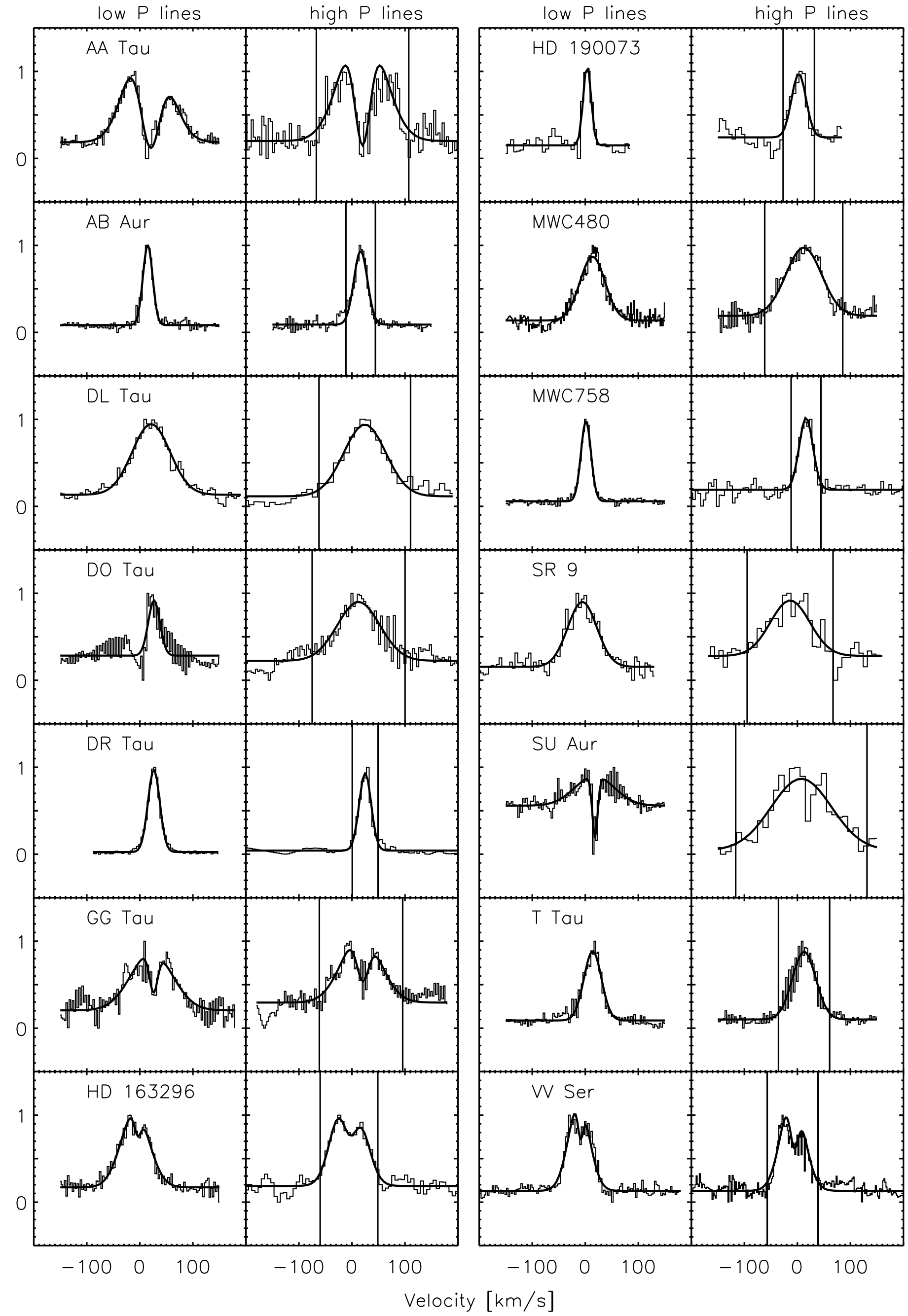

Figure 4.2: Composite emission lines, with one- or two-Gaussian fits. Vertical lines mark the velocity taken to represent the CO inner radius.

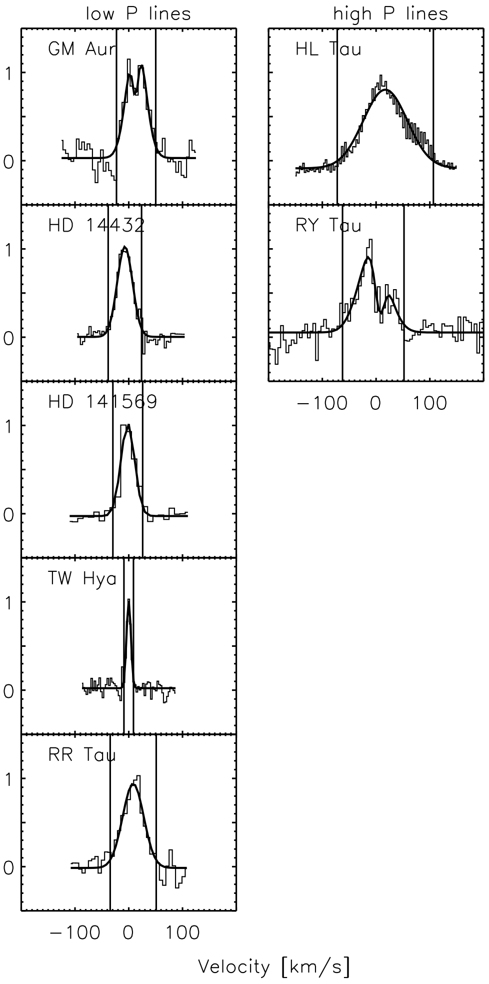

Figure 4.3: Composite emission lines for sources in which only one of the M-band orders was observed with CO v=1 → 0 emission.

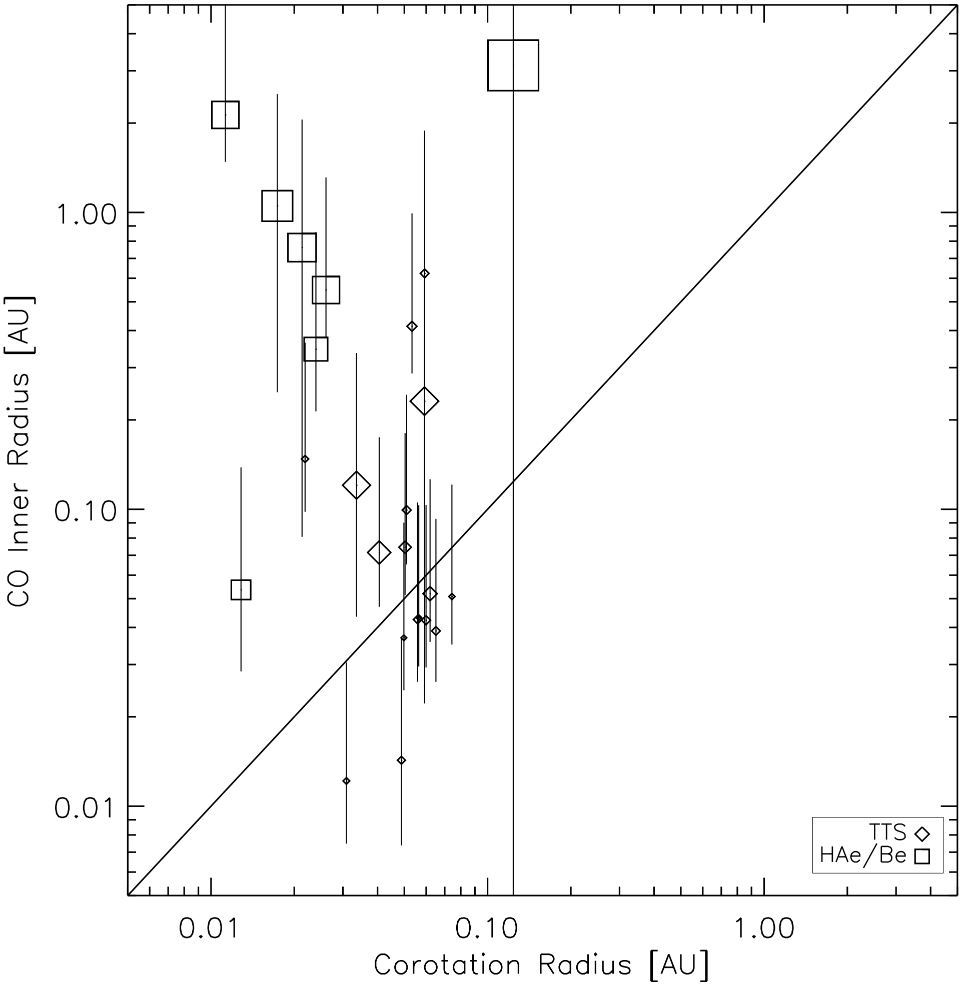

Figure 4.4: CO inner radius against corotation radius. T Tauri stars are represented as diamonds and HAe/Be stars as squares. The size of the symbol is proportional to the stellar mass. The solid line shows a 1:1 correspondence.

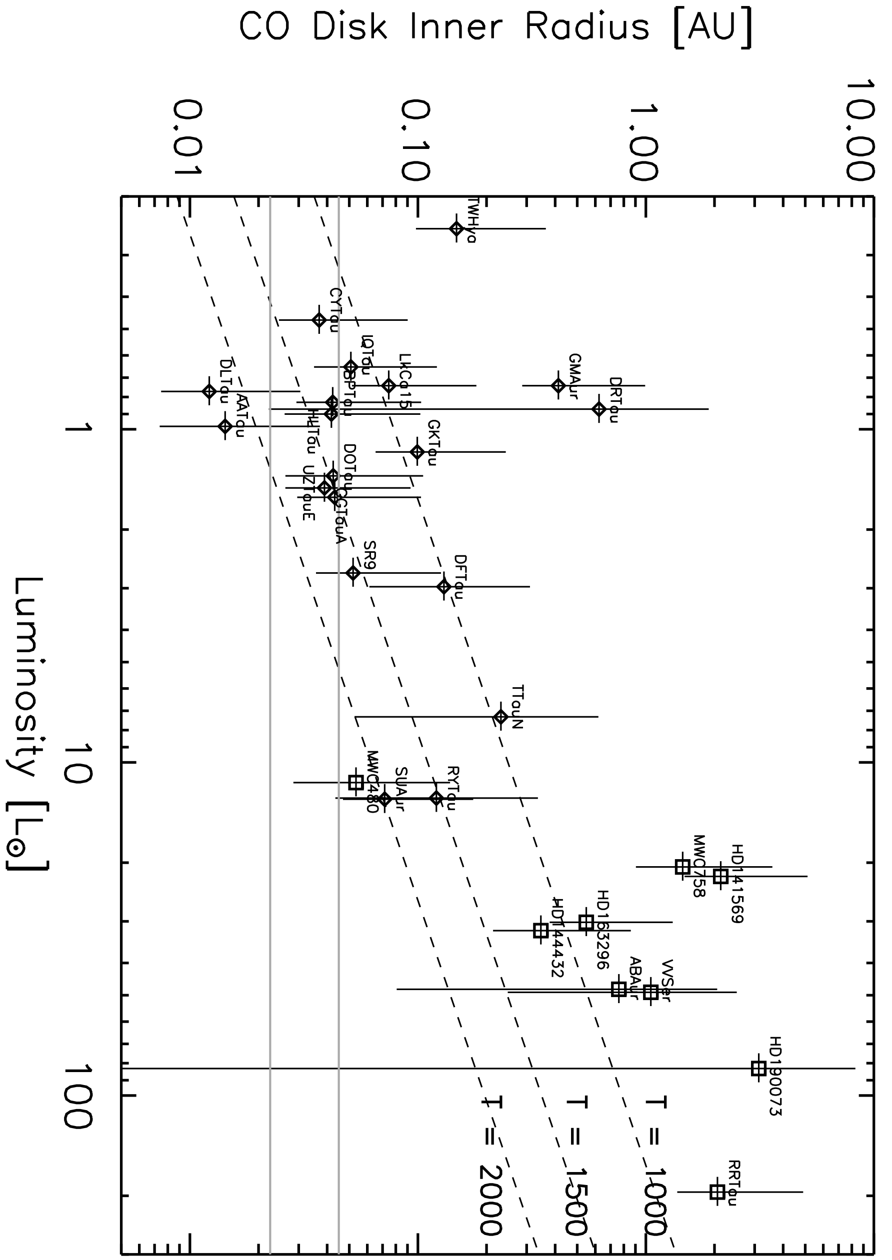

Figure 4.5: CO inner radius against luminosity. Diamonds are T Tauri stars and squares are HAe/Be stars. Dashed lines show theoretical curves for dust sublimation radius as a function of luminosity. Gray lines represent estimates of 0.5 and 1 corotation radii, based on an empirical fit to our dataset.

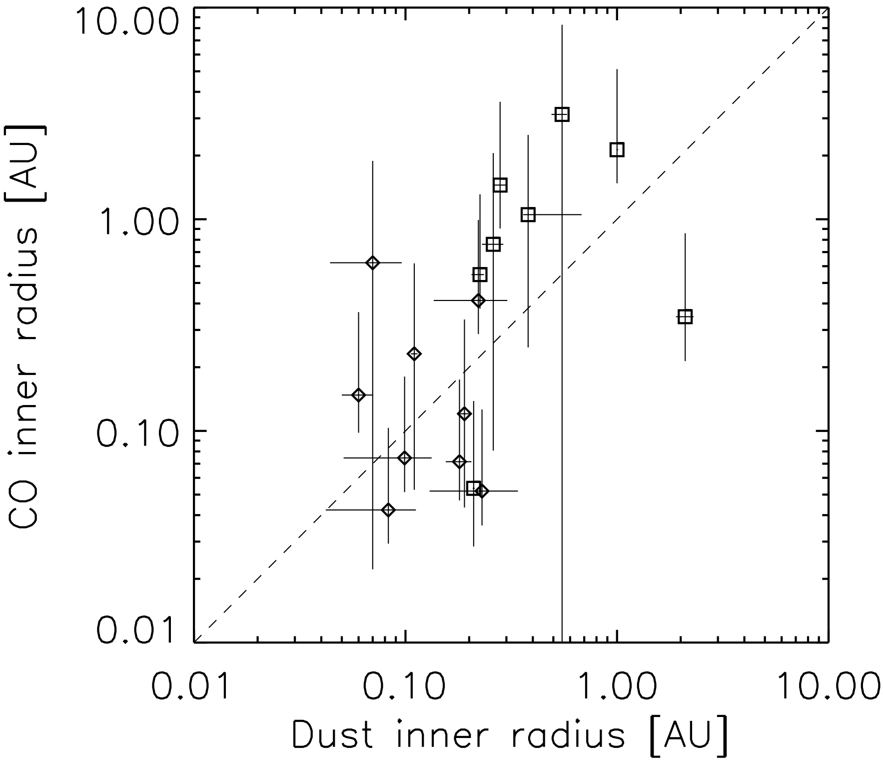

Figure 4.6: CO inner radius against dust inner radius. Diamonds are T Tauri stars and squares are HAe/Be stars. Dust inner radii are derived from IR interferometry results. A dashed line shows a 1:1 correspondence.

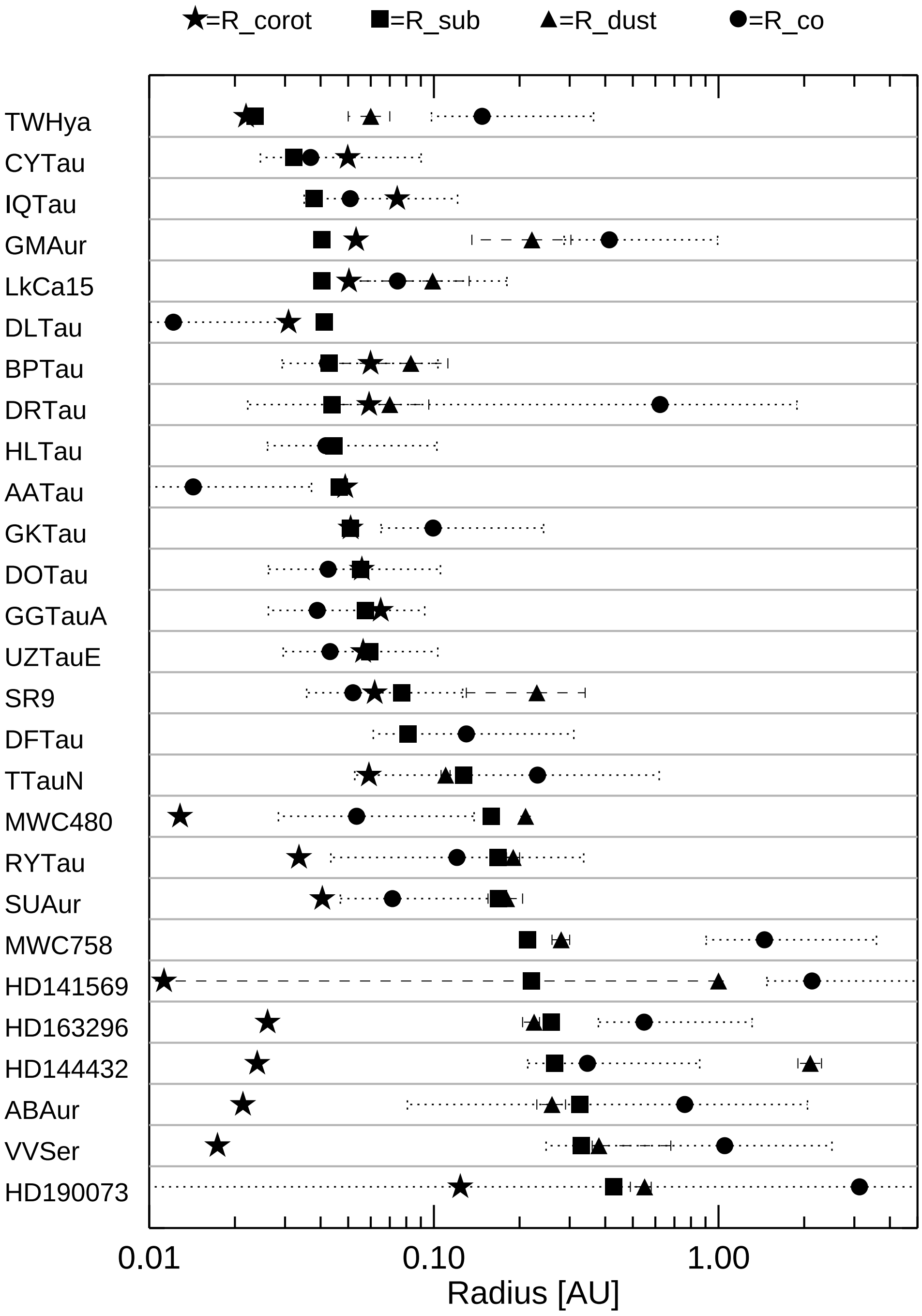

Figure 4.7: Relationships between all relevant disk radii: the disk corotation radius, the dust sublimation radius (with $T = 1500$ K), the dust inner radius (from interferometry, see Table 4.3) and the CO inner radius.Error bars for dust and CO inner radii are shown as dotted and dashed lines, respectively. Stars are arranged from top to bottom in order of luminosity.

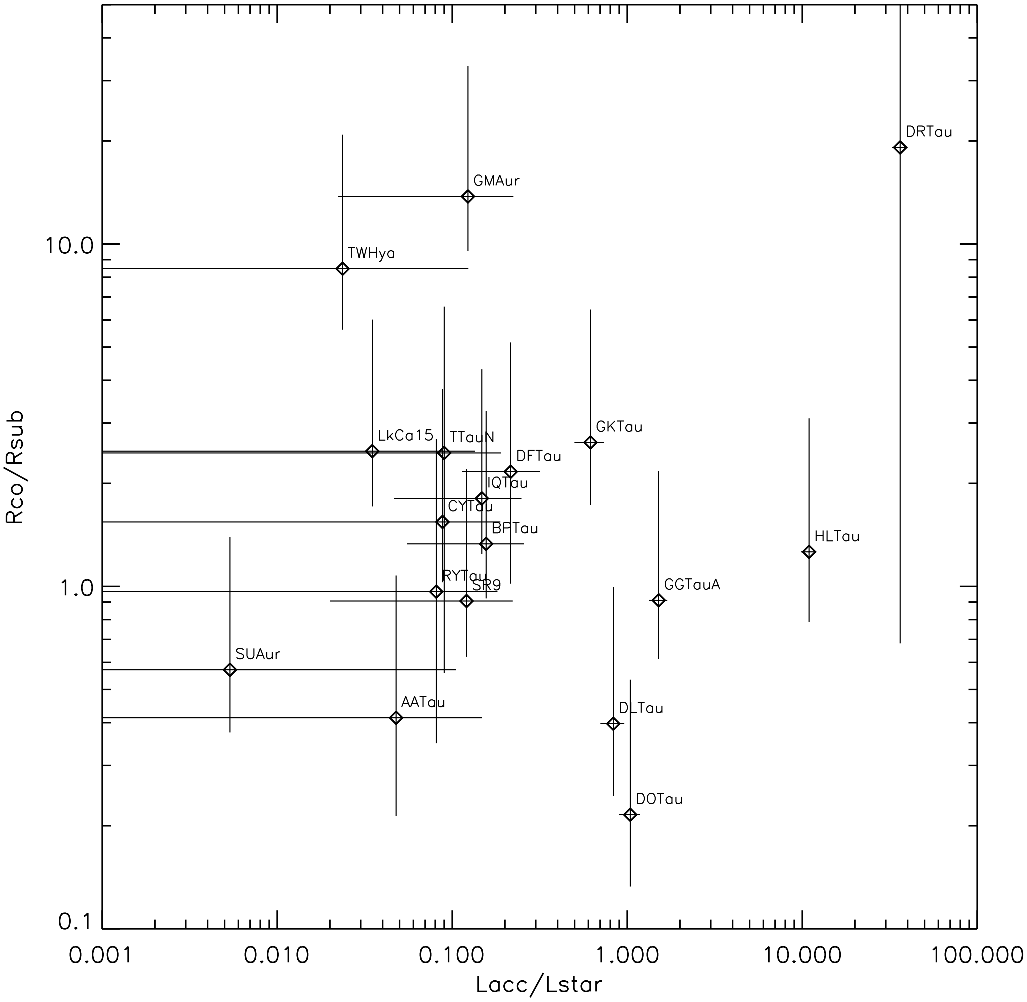

Figure 4.8: $R_{\rm CO}/R_{\rm sub}$ against $L_{\rm acc}/L_\star$. Diamonds are T Tauri stars and squares are HAe/Be stars.

Table 4.1: Summary of Observations

Star	Dates (mth/yr)	^{12}CO $1 \rightarrow 0$	$2 \rightarrow 1$	^{13}CO $1 \rightarrow 0$
AA Tau	11/03,12/04	✓	···	···
AB Aur	1/01,8/01,1/02,12/02	✓	···	✓
DL Tau	11/03	✓	✓	···
DO Tau	12/05	✓	✓	✓
DR Tau	12/02,12/05	✓	✓	✓
GG Tau A	1/02,12/02,1/02	✓	···	···
GM Aur	12/04	✓	···	···
HD 141569	4/02	✓	✓	✓
HD 144432	7/02,4/05	✓	···	···
HD 163296	8/01,4/02,7/02	✓	···	···
HD 190073	7/02,9/05	✓	···	···
HL Tau	10/01,12/02	✓	✓	···
MWC 480	1/01,8/01,1/02,12/02	✓	···	···
MWC 758	4/01,12/02	✓	···	···
RR Tau	12/02, 12/05	✓	✓	···
RY Tau	12/02	✓	···	···
SR 9	7/04	✓	···	···
SU Aur	12/02,11/03	✓	···	···
T Tau N	1/02,12/02,12/04	✓	···	···
TW Hya	1/01,4/02,12/02 12/04,4/05,12/05,5/06[a]	✓	···	···
VV Ser	8/01,7/03,7/04	✓	···	···

---

[a] observed with Phoenix

Table 4.2: Line Widths (FWHM)

Star	low J [km s^{-1}]	P coefficients	highJ [km s^{-1}]	P coefficients	R$_{\rm in}$ [AU]
AA Tau	84	1-12	94	30-32, 36-40	$0.01^{+0.02}_{-0.01}$
AB Aur	22	1-12,14-15	30	26-32, 24, 36-40	$0.73^{+0.92}_{-0.70}$
DL Tau	84	2-6	93	30-32	$0.01^{+0.01}_{-0.01}$
DO Tau	26	1-12	95	30-33,36-40	$0.04^{+0.05}_{-0.02}$
DR Tau	26	1-12	26	30-34,36-40	$0.59^{+0.91}_{-0.60}$
GG Tau A	92	1-12	85	30-34,36-40	$0.04^{+0.04}_{-0.02}$
GM Aur	40	9-12,14	···	···	$0.41^{+0.42}_{-0.17}$
HD 141569	30	3-6	···	···	$2.05^{+2.12}_{-0.88}$
HD 144432	34	1-12	···	···	$1.07^{+1.15}_{-0.57}$
HD 163296	63	2-12,15	55	27-28,30-32,37	$0.54^{+0.56}_{-0.23}$
HD 190073	17	2-3,5-6,8-12	32	30-32,34,36-38	$3.03^{+3.68}_{-3.27}$
HL Tau	···	1-8	97	27,30-34,36-40	$0.04^{+0.04}_{-0.02}$
MWC 480	56	2-4,6-12	80	26-32,36-38,40	$0.05^{+0.06}_{-0.03}$
MWC 758	22	1-12	30	30-33,36-38	$1.4^{+1.5}_{-0.73}$
RR Tau	46	8-12	···	···	$2.1^{+2.8}_{-0.7}$
RY Tau	···	···	62	30-32,34,36,38	$0.12^{+0.16}_{-0.09}$
SR 9	65	4,6,8-12	88	30-32,37	$0.05^{+0.05}_{-0.02}$
SU Aur	88	2-4,6-11	134	30-32	$0.07^{+0.08}_{-0.04}$
T Tau N	39	2-15,17	52	30-34,36-41,43	$0.23^{+0.28}_{-0.20}$
TW Hya	10	6-9	···	···	$0.14^{+0.15}_{-0.07}$
VV Ser	47	6-12	52	27-28,30-42	$1.04^{+1.07}_{-0.88}$

Table 4.3. Stellar Parameters

Star	Type [i]	$M_\star$ [$M_\odot$]	$R_\star$ [$R_\odot$]	$L_\star$ [$L_\odot$]	i [°]	R_{dust} [AU]	$\dot{M}$ [10^{-8} $M_\odot$/yr]	v sin(i) [km s^{-1}]	refs
AA Tau	T	0.67	2.5	0.98	25 ± 7	···	0.71	11	10,11,26,28
AB Aur	HA	2.4	2.5	48	28^{+10}_{-18}	0.26 ± 0.01	···	80	9,38,38
DL Tau	T	0.56	2	0.77	25 ± 5	···	9.3	16	10,14,26,28
DO Tau	T	0.72	1.78	1.38	45	···	14.42	11.1	10,14,22,27
DR Tau	T	0.74	1.9	2.5	40 ± 30	0.07 ± 0.026	329.2	10^{c}	7, 14,26,28
GG Tau A	T	0.73	2.4	1.5	37 ± 1	···	30.31	10.2	14,26,39
GM Aur	T	0.84	1.6	0.74	54 ± 5	$0.221^{+0.082}_{-0.085}$	1.23	12.4	8,14,26,39
HD 141569	HB	2.3	1.7	22.	53 ± 5	1^{b}	236	···	9,31,32,33
HD 144432	HA	2.	2.0	32.	45	2.1 ± 0.2	···	74	9,29
HD 163296	HA	2.30	2.8	30.2	60 ± 5	$0.23^{+0.01}_{-0.02}$	···	120	9,21,25,33
HD 190073	HA	4.3	3	83	50^{+30}_{-50}	$0.55^{+0.03}_{-0.06}$	···	15	15,18,35
HL Tau	T	0.55	2.2	0.9	55 ± 13	···	160	···	10,23,28
MWC 480	HA	1.65	1.6	11.5	26 ± 7	0.21 ± 0.002	···	85	39, 35
MWC 758	HA	2	2.1	20.6	46	0.28 ± 0.02	···	···	30,33
RR Tau	HA	2.7	···	65	90	···	···	···	24
RY Tau	T	2.37	3.6	7.6	25	0.19 ± 0.01	6.4-9.1	52.2	7,13,14,28
SR 9	T	1.2	2.9	2.7	34 ± 4^{a}	$0.23^{+0.11}_{-0.10}$	3.2	15.8	11,19
Su Aur	wT	1.97	3.5	10.7	52 ± 10	0.18 ± 0.025	0.5-0.6	65	7,13,14
T Tau N	T	2.41	2.8	8.91	29^{+10}_{-15}	0.11 ± 0.004	3.1-5.7	20.1	6,13,14
TW Hya	T	1.0	1	0.25	7 ± 1	0.06 ± 0.01	0.04	4	40,20,34,37,16
VV Ser	HA	2.6	2.4	49	81^{+9}_{-51}	$0.25^{0.30}_{-0.02}$	···	229	25,36,36
BP Tau	T	1.24	1.9	0.93	30^{+4}_{-2}	$0.083^{+0.029}_{-0.041}$	2.10	7.8	8,26,14,39
CY Tau	T	0.48	1.6	0.47	47^{+8}_{-8}	0.032	0.56	10	14,26,28,39
DF Tau	T	0.53	3.6	2.97	78^{+12}_{-35}	···	17.69	···	10, 11, 22
GK Tau	T	0.75	2.3	1.17	53^{a}	···	8.99	18.7	12,14, 26
IQ Tau	wT	0.52	2.4	0.65	79	0.045	1.8	11.5	14,28
LkCa 15	T	1.10	0.74	0.74	42 ± 5	$0.099^{+0.034}_{-0.048}$	0.10	12.5	8,14,26,39
UZ Tau E	T	0.47	2.8	1.6	54^{+3}_{-3}	···	···	15.9	14, 39

[i] T:T Tauri Star; wT: weak-line T Tauri star; HA/HB: HAe/Be Star

[a] $i_\star$ from stellar rotation data

[b] Upper limit

[c] Lower limit

[d] UX Orionis star; we assume $i > 80°$.

References. — (6) Akeson et al. 2002 (7) Akeson et al. 2005a (8) Akeson et al. 2005b (9) van den Ancker et al. 1998 (10) Beckwith et al. 1990 (11) Bouvier 1990 (12) Bouvier 1995 (13) Calvet et al. 2004 (14) Clarke & Bouvier 2000 (15) Cuttela & Ringuelet 1990 (16) de la Reza & Pinzon 2004 (17) Eisner et al. 2003 (18) Eisner et al. 2004 (19) Eisner et al. 2005 (20) Eisner et al. 2006 (21) Grady et al. 2000 (22) Gullbring et al. 1998 (23) Hayashi et al. 1993 (24) Hernandez et al. 2004 (25) Hillenbrand et al. 1992 (26) Johns-Krull 2002 (27) Koerner & Sargent 1995 (28) Kitamura et al. 2002 (29) Leinert et al. 2004 (30) Mannings & Sargent 2000 (31) Marsh et al. 2002 (32) Merin et al. 2004 (33) Monnier et al. 2005 (34) Muzerolle et al. 2000 (35) Pogodin et al. 2005 (36) Pontoppidan et al. (in prep) (37) Qi et al. 2004 (38) Semenov et al. 2005 (39) Simon et al. 2001 (40) Thi et al. 2004

Chapter 5

H_2O and OH Gas in the Terrestrial Planet-Forming Zones of Protoplanetary Disks

This chapter, with minor differences, was published in its entirety with authors C. Salyk, K. M. Pontoppidan, G. A. Blake, F. Lahuis, E. F. van Dishoeck, and N. J. Evans II in *The Astrophysical Journal*, 2008, Volume 676, pp. L49–L52.

5.1 Abstract

We present detections of numerous 10–20 μm H_2O emission lines from two protoplanetary disks around the T Tauri stars AS 205A and DR Tau, obtained using the InfraRed Spectrograph on the Spitzer Space Telescope. Follow-up 3–5 μm Keck-NIRSPEC data confirm the presence of abundant water and spectrally resolve the lines. We also detect the P4.5 (2.934 μm) and P9.5 (3.179 μm) doublets of OH and ^{12}CO/^{13}CO v=1→0 emission in both sources. Line shapes and LTE models suggest that the emission from all three molecules originates between $\sim$ 0.5 and 5 AU, and so will provide a new window for understanding the chemical environment during terrestrial planet formation. LTE models also imply significant columns of H_2O and OH in the inner disk atmospheres, suggesting physical transport of volatile ices either vertically or radially; while the significant radial extent of the emission stresses the importance of a more complete understanding of nonthermal excitation processes.

5.2 Introduction

One of the most intriguing questions in the study of the formation of planets, and of terrestrial planets in particular, is how water is transported to their surfaces, and whether or not water is a common ingredient during their formation and early evolution. Spatially and spectrally resolved observations of water in extrasolar planetary systems and protoplanetary disks would be instrumental in resolving these questions. Unfortunately, detecting water in extrasolar planetary systems remains difficult (Ehrenreich et al., 2007) and water in protoplanetary disks has been elusive, with only a few definitive ice (Malfait et al., 1998; Terada et al., 2007) and vapor (Carr et al., 2004) detections. Recently, however, the Spitzer InfraRed Spectrograph (IRS) has begun to reveal warm water vapor emission lines from disks around classical T Tauri stars (cTTs, Carr & Najita 2008).

In this chapter, we present high-resolution spectroscopy of numerous water vapor emission lines from protoplanetary disks around two cTTs: DR Tau and AS 205A. Spectra were obtained using both the Spitzer-IRS and NIRSPEC (McLean et al., 1998) at the Keck II telescope. Accretion rates onto these stars are high, which causes the inner disks to be significantly hotter than in more quiescent systems. DR Tau is known to have variable mass accretion, with measured rates between 0.3 and $79 \times 10^{-7}\, M_{\odot}\, \mathrm{yr}^{-1}$ (Gullbring et al., 2000; Johns-Krull and Gafford, 2002). AS 205A has an accretion rate of $7.2 \times 10^{-7}\, M_{\odot}\, \mathrm{yr}^{-1}$ and is the primary component of a 1.3" triple system, with the secondary being a spectroscopic binary (Eisner et al., 2005). However, it is likely that the physical separation of AS 205A and B is significantly larger than the projected separation and that, therefore, AS 205B does not affect the (inner) disk of AS 205A (Andrews and Williams, 2007a).

5.3 Observations

The Spitzer IRS Short-High (SH) module spectrum of AS 205A was taken as part of the "cores to disks" (c2d) legacy program (Evans et al., 2003; Kessler-Silacci et al., 2006), while the spectrum of DR Tau, observed as part of the guaranteed time observations (Houck et al., 2004), was obtained from the Spitzer archive. The 2-D basic calibrated data images were reduced using the c2d pipeline as described in Lahuis and Kessler-Silacci (2006).

To confirm the detections as well as measure the gas emission line profiles, we obtained high resolution ($\lambda/\Delta\lambda$=25000) L-band spectra using NIRSPEC in a single grating setting, of which two orders, centered at 2.92 μm and 3.16 μm, respectively, have identifiable H_2O and OH emission features. We also collected CO v=1→0 M-band spectra ($\sim 5\,\mu$m) as part of an on-going survey (see Blake and Boogert, 2004; Salyk et al., 2007). The data were reduced in a standard way. Division by the spectra of standard stars (HR 1620 (A7V) for DR Tau; HR 5993 (B1V) for AS 205A) was used to correct for telluric absorption, which can be poor when the absorption is high. Thus, regions of the spectrum with $< 70\%$ atmospheric transmission were removed. Fluxes were calibrated using the photometry and spectral types of the standards, and are generally accurate to $\lesssim 20\%$.

The NIRSPEC lines are narrow (FWHM $\lesssim$ 35 km s^{-1}), spatially unresolved, and centered at the stellar v_{LSR} (Herbig and Bell, 1988; Thi et al., 2001) to within our uncertainty (a few km s^{-1})—all consistent with disk emission. Because the disks are optically thick and heated from above, the line emission likely arises from the upper disk atmosphere (Najita et al., 2003).

5.4 Results

5.4.1 Spitzer-IRS

The IRS spectra of AS 205A and DR Tau show a large number of water emission lines (see Figure 5.1), the vast majority pure rotational transitions with quantum numbers in the range 20–50. The R=600 resolution of the SH module results in unresolved, and significantly blended, lines. Consequently, the identification with water is achieved via a simple, isothermal LTE ring model computed using the HITRAN 2004 database (Rothman et al., 2005). The ring model consists of a single temperature (T) and column density (N) gas in Keplerian rotation. Model parameters include T, N, solid angle (Ω), stellar mass ($M_\star$), inclination (i) and characteristic radius (r). In addition, the local line broadening is assumed to be Gaussian, with specified width (σ). $M_\star$ and i were fixed to values taken from the literature (Clarke and Bouvier, 2000; Kitamura et al., 2002; Eisner et al., 2005; Andrews and

Williams, 2007a). The spectrally unresolved IRS data cannot completely constrain the remaining model parameters, but do require high T ($T \gtrsim 500$ K) and N ($N \gtrsim 10^{17}$ cm^{-2} for $\sigma \sim 2$ km s^{-1}). Figure 5.1 compares the IRS spectra with a model in which T and N are constrained using the NIRSPEC data described below, but where Ω has been increased by a factor of 2.

The addition of CO_2 (and, for AS 205A, OH) improves our fits, as shown by the AS 205A model in Figure 5.1. With T and Ω fixed, we find H_2O:CO_2=40 for DR Tau and 20 for AS 205. Detections of these and other molecules will be discussed in detail elsewhere.

5.4.2 NIRSPEC

While tropospheric water vapor blocks significant portions of incoming radiation near 3 μm, there are a handful of rovibrational lines that are optically thin in the atmosphere but readily excited at temperatures typical of the inner ~ 1 AU of circumstellar disks. This is illustrated in Figure 5.2, in which spectral regions with $< 70\%$ atmospheric transmission have been removed, yet many prominent (line-to-continuum $\sim$ 5–10%) H_2O emission features remain. These are primarily $\nu_3 = 1 \rightarrow 0$ lines, with upper level energies of $\sim$ 5,000–10,000 K. A few weaker (line-to-continuum $\sim 1\%$) features are nominally detected from 3.13–3.18 μm and are used as model constraints. We also detect the P4.5 (2.9344 μm; $T_{\rm up} \sim 5400$ K) and P9.5 (3.1788 μm; $T_{\rm up} \sim 7500$ K) OH doublets. The M-band spectra include portions of the ^{12}CO/^{13}CO v=1→0 and ^{12}CO v=2→1 P- and R-branches (Figure 5.3).

We fit all spectra with the ring models described in §5.4.1. Because the CO lines span a large range of excitation energies, across which they transition from optically thick to optically thin, N, T, and Ω can be determined uniquely. Also, a constraint on $N_{\rm CO}$ is provided by the ^{13}CO lines (assuming a ^{12}CO:^{13}CO ratio, here fixed at 77, see Blake and Boogert, 2004). Thus, we began by fitting the CO emission by comparison with an excitation diagram of the v=1→0 transitions (Figure 5.3), as described in Salyk et al. (2007). For our nominal H_2O and OH fits, we then fixed Ω and T to the CO-derived values to determine N—a reasonable, though not ideal, assumption, given the similarity in line shapes (see Figure 5.3).

Our nominal ring model is shown in Figure 5.2, with best-fit parameters in Table 5.1, and uncertainties of order $\Delta N \sim 30\%$, $\Delta T \sim 15\%$ and $\Delta\Omega \sim 10\%$. We have fixed $r = 3$ AU to roughly match the emission profiles since the lineshape does not affect the integrated flux; we discuss lineshapes below. Ω corresponds to areas of 0.2 and 0.4 AU^2 for DR Tau and AS 205, respectively, at distances of 140 and 120 pc. Uncertainties in the nominal H_2O and OH fits are linked to CO uncertainties, but if T is instead allowed to vary, the H_2O spectra are consistent with $T\sim$ 900–1200/900–1100 K for DR Tau/AS 205A and ranges in N of about 1 order of magnitude. For OH, we can only constrain $T \gtrsim$900 K.

The model results depend crucially on the assumed local line width (σ), which is unknown. For our nominal model, we have adopted $\sigma = 2\,\mathrm{km\ s^{-1}}$—the sound speed for H_2 at 1000 K. However, we have also tested values between ~ 0.3 and 10 km s^{-1}. We find that the opacity needs to remain similar from fit to fit, so that a change in σ^2 requires a proportional change in N. To maintain the flux level, the total number of molecules must remain similar, so an increase in σ implies a decrease in Ω. Accordingly, the CO:H_2O ratio changes by no more than a factor of ~ 2 between models. (If T_{H_2O} is not fixed, however, this ratio may change.) In addition, T is only weakly affected by σ, since it is set by the overall shape of the spectrum, rather than by the absolute flux levels.

NIRSPEC spectrally resolves the molecular emission, allowing an investigation of the disk gas kinematics. In Figure 5.3 we compare the unblended H_2O transition at 2.931 μm with a CO line composite constructed from an average of all v=1→0 lines. In general, Keplerian disks should produce double-peaked emission profiles, with peak separation set by the inner and outer emission radii (r_{in}, r_{out}), as well as the temperature gradient (Horne and Marsh, 1986). The CO and H_2O line profiles, however, are more Gaussian, or even Lorentzian in shape, with relatively wide wings and a narrow peak. The narrow core could be produced by a ring with a very large r_{in} (>10 AU) if the peak-to-peak separation is equal to the NIRSPEC resolution (given the $M_\star$ and i in Table 5.1). However, this is difficult to reconcile with the high T derived from the model fits and the observed line wings.

Another way to produce a single peak would be to have the line emission extend to significant radii (r_{out} of order 7 AU, for a temperature profile that is constant with radius), such that the contribution from low-velocity portions of the disk infills the center of the line profile. However, this model produces too much flux to match observations. Additionally, passive disk models predict a steep temperature decline with radius. A more promising solution may be that some flux is produced via fluorescence, in which molecules in the flared outer disk (typically out to $\sim$ 5 AU) intercept and re-radiate inner disk IR continuum, thus filling in the line profiles at low velocity (Blake and Boogert, 2004). With canonical disk flaring and temperature structure, we find that a resonance fluorescence model with 100% scattering efficiency can indeed produce fluxes comparable to those of thermal emission; a more thorough investigation is left as future work.

In any case, the amount of flux in the line profile wings is consistent with emission arising in a Keplerian disk with a small inner radius. With this assumption, the line wing velocity can be used to estimate $r_{\rm in}$. Because turbulent motion and disk structure can both have non-negligible effects on the line shapes, we adopt here the velocity, $v_{\rm in}$, at 2.2 times the Half Width at Half Maximum—a value found to be appropriate for the moderate-inclination disk around GM Aur (Salyk et al., 2007). To compute $v_{\rm in}$ we use Gaussian fits to the CO and H_2O lines discussed above, as well as the average of two-Gaussian fits to the OH emission doublets, deconvolved with the NIRSPEC instrument response function. If turbulent velocities are low, radii associated with $v_{\rm in}$ will be overestimates, and so we also compute v at 3σ, which should represent a lower limit to $r_{\rm in}$ (see Table 5.1).

5.5 Discussion

We have convincingly detected H_2O emission in the 10–20 μm region with Spitzer-IRS as well as H_2O and OH emission near 3 μm with NIRSPEC, arising from the disk atmospheres surrounding two cTTs. By combining these data with constraints from spectrally resolved CO v=1$\rightarrow$0 emission, we find that the excitation temperatures are typical of terrestrial planet-forming regions ($\sim$ 1000 K). Additionally, line wing velocities imply inner emission radii no larger than 1 AU for all molecules. Therefore, further observations and analyses of these species may provide a new window into terrestrial planet-forming regions.

Observations of H_2O in disks may also provide constraints on disk evolution and water transport.

In a disk in which water vapor transport is controlled by diffusion, the presence of a condensation front ('snow line') can potentially dry out an inner disk in as little as 10^5 yr, for typical disk viscosities (Stevenson and Lunine, 1988). The snow line for the early solar system is estimated to be near 3 AU, but would be further out for these high-accretion-rate stars (Lecar et al., 2006). Therefore, the presence of significant water vapor inside 1 AU may be evidence for inward radial migration, or upward mixing, of icy solids, followed by evaporation. With both solid migration and diffusion controlling water transport, water vapor concentrations become sensitive to an array of parameters, including disk viscosity and planetesimal growth rates, and water concentrations may trace disk evolution (Ciesla and Cuzzi, 2006).

The detection of strong OH emission is also interesting, for OH is known to be an important ingredient to the chemistry in the inner regions of protoplanetary disks. It also acts as a coolant near the disk surface (e.g., Dullemond et al., 2007), and photolysis of OH to O(^{1}D) has been invoked to explain the observed strengths of the 6300 Å O I line (Acke et al., 2005). Detections of OH in these and other disks will be discussed in greater detail in Mandell et al. (in prep).

An understanding of the local line broadening in disks will be crucial for obtaining accurate absolute column densities of molecular species, as smaller local line widths require lower column densities and vice versa. Nevertheless, we find that molecular ratios are more robust, and remain similar when utilizing different disk models, with the nominal fits having CO:H_2O $\sim$ 9–10 and H_2O:OH $\sim$ 3–4, provided $T_{\mathrm{H_2O}} = T_{\mathrm{OH}} = T_{\mathrm{CO}}$. Stronger constraints on both T and N will require high line-to-continuum observations across a wider wavelength range, but the available data reveal that H_2O:CO is similar to, or slightly higher than that in the dense clouds out of which disks form (Boogert et al., 2004). Vertically integrated H_2O:OH ratios have been predicted to be much higher ($> 10^5$) near 1 AU (Markwick et al., 2002), but significant OH abundances are expected near the C^+/C/CO transition zone at large scale heights (Kamp and Dullemond, 2004). Also, it is important to keep in mind that disk transport is not included in current chemical models.

Our analysis of the L- and M-band spectra thus far has assumed thermal excitation of the vibrationally excited states, but this need not be the case. Δv=1 emission can also be driven by the stellar UV output or by the absorption of IR photons from the star or disk, followed by fluorescence (dello Russo et al., 2004; Blake and Boogert, 2004). For OH, vibrationally excited emission can also result from the (photo)dissociation of H_2O followed by prompt emission (Bonev et al., 2006). In fact, fluorescence may be necessary to explain observed line profile shapes (see Section 5.4.2), and could explain the surprisingly strong OH emission. A better understanding of these processes may therefore prove essential for relating observed line fluxes to disk column densities.

If emission in the line wings truly represents emission from the disk inner radius, relatively large inner emission radii are implied for CO, OH, and H_2O. Both DR Tau and AS 205A have had their dust inner rim sizes measured with the Keck Interferometer. At 0.11 ± 0.03 and 0.07 ± 0.01 AU, respectively, they are consistent with the location of dust sublimation (Akeson et al., 2005b; Eisner et al., 2005), while the inner emission radii we derive are at least 3 times larger. Perhaps these high accretion-rate stars can stir up the inner disk enough to erase the vertical temperature gradients necessary for formation of emission lines. Another possibility may be that replenishment rates cannot keep up with photo-dissociation at the disk surface.

The ease with which H_2O and OH are now detected in the terrestrial planet-forming zones of certain disks holds the promise of more extensive and detailed studies. Although the ground-based echelle observations presented here probe only the inner disk atmospheres, future high-spectral-resolution follow-up studies of Spitzer-detected water emission from protoplanetary disks will provide constraints at a variety of disk radii and vertical depths. Additionally, spectro-astrometric observations are being used to directly constrain emitting location and structure of the molecular gas (Pontoppidan et al., 2008a). Eventually, a suite of constraints combined with non-LTE radiative transfer models will allow us to rigorously address such far-reaching questions as: How does the water vapor abundance vary within and between disks? What constraints can be put on models for the chemistry and transport of volatiles in disks, and what implications will these have for the early evolution of the Solar System?

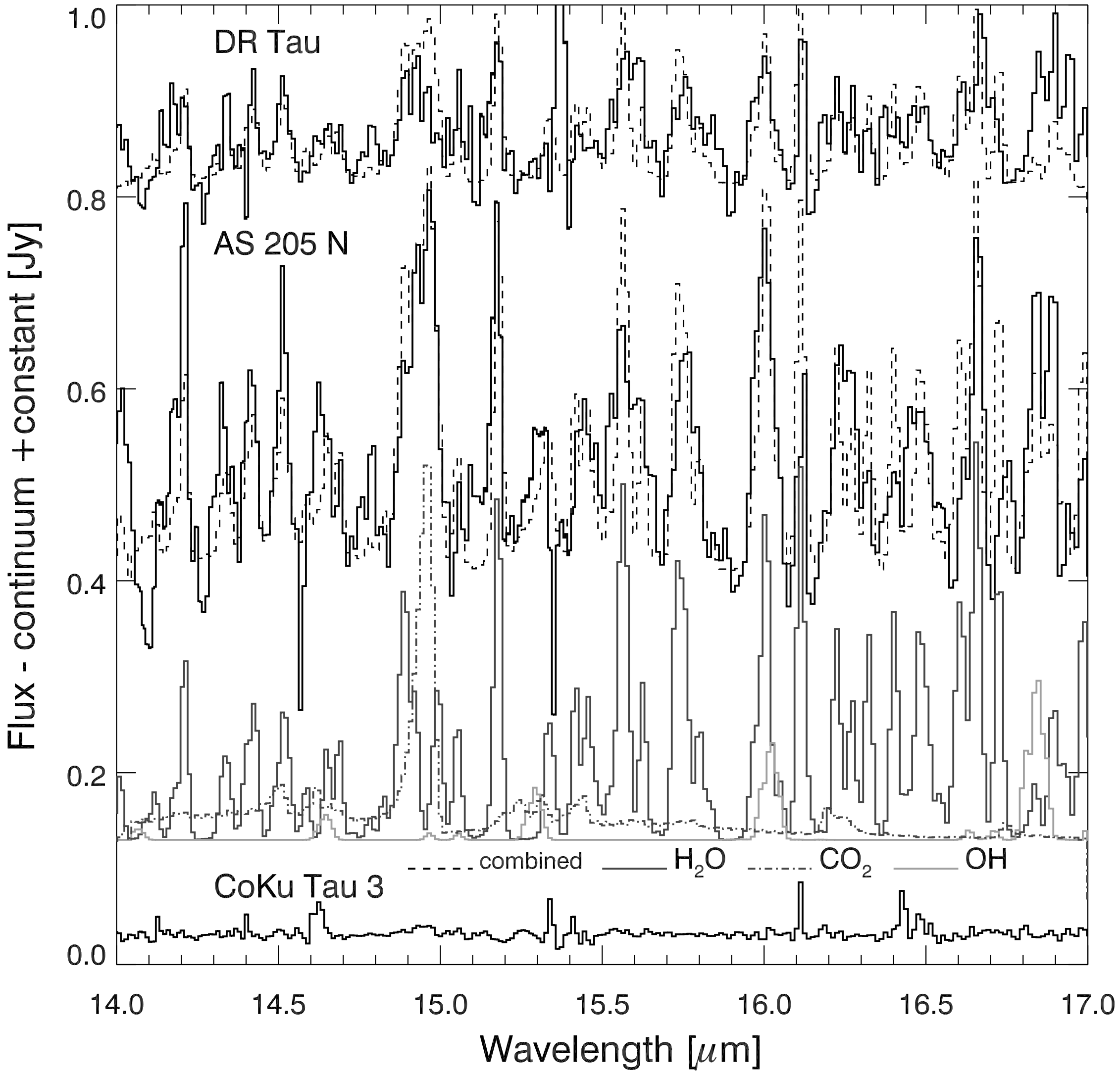

Figure 5.1: Spitzer-IRS spectra of DR Tau and AS 205 A. A portion of the Spitzer-IRS data (in black) and molecular emission models (dashed). The three components of the AS 205A model are shown below, in gray. The largely featureless spectrum of CoKu Tau/3 is included to demonstrate the dynamic range achievable by the IRS and the level of systematics, such as residuals from the de-fringing process. For both spectra, splines have been used to remove broad continuum features from silicates. Line-to-continuum excesses are ~ 5–10%.

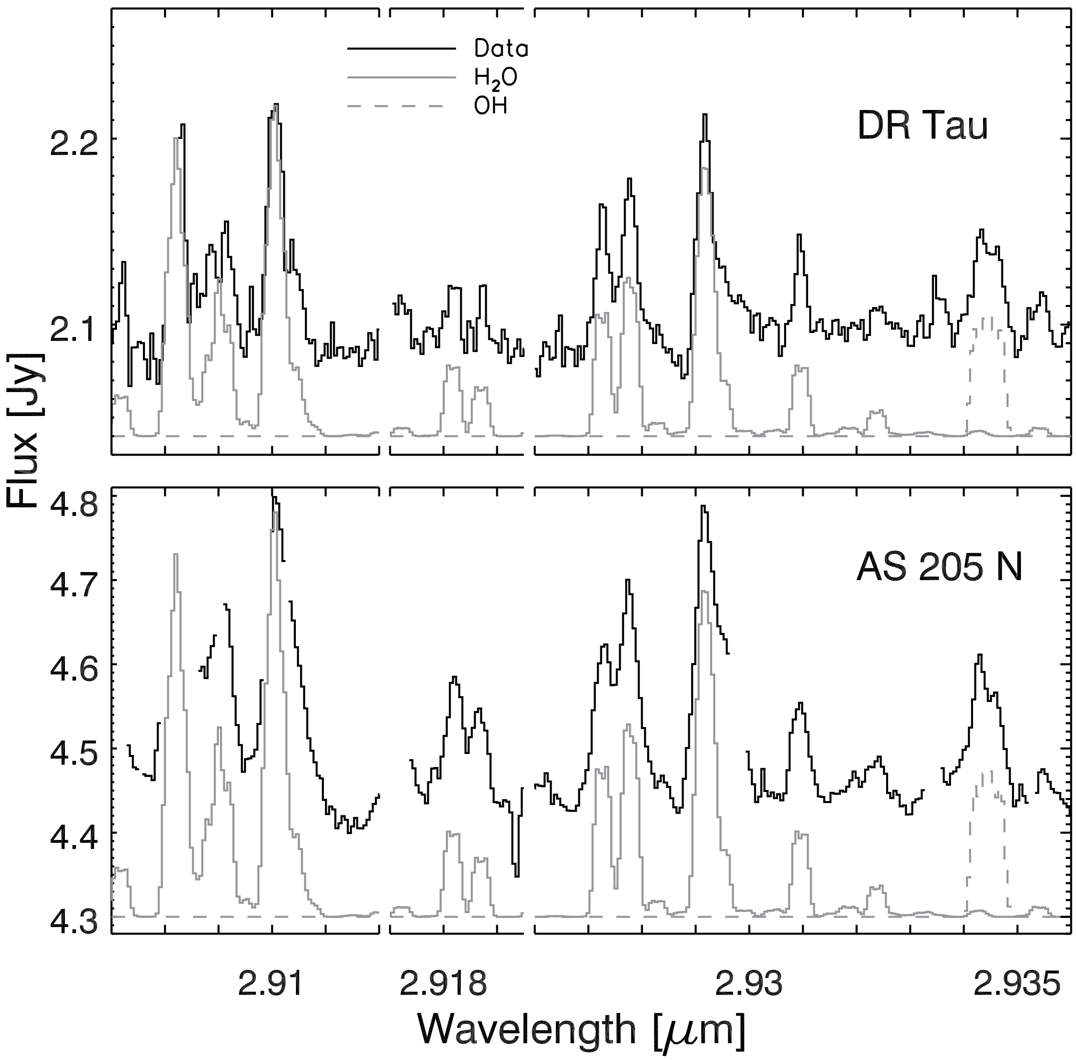

Figure 5.2: NIRSPEC L-band spectra of DR Tau and AS 205 A. Comparison between portions of the NIRSPEC L-band data and best-fit H_2O/OH disk models (offset).

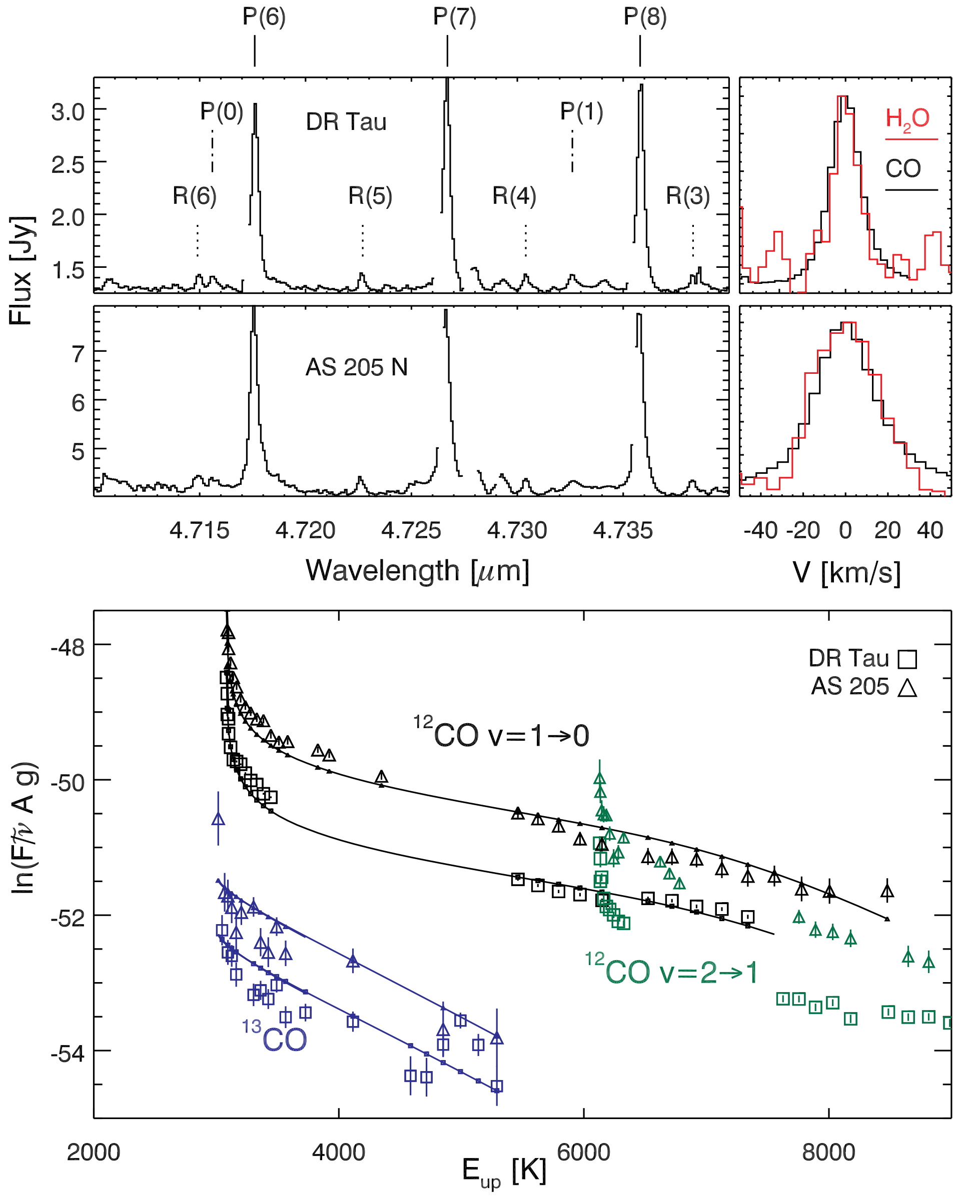

Figure 5.3: NIRSPEC CO emission spectra and rotation diagrams for DR Tau and AS 205 A. Top, left: a portion of the NIRSPEC M-band spectra. ^{12}CO/^{13}CO v=1→0 transitions are marked with solid and dashed lines, respectively. ^{12}CO v=2→1 transitions are marked with dot-dashed lines. Top, right: CO and H_2O emission lines are overplotted. Bottom: an excitation diagram with 1σ error bars and best-fit models to the v=1→0 transitions, with F in W m^{-2} and $\tilde{\nu}$ in cm^{-1}.

Table 5.1. Fits to NIRSPEC Data

	DR Tau	AS 205 A
CO $v_{\rm in}$, $v_{3\sigma}$ [$\rm km\,s^{-1}$]	27, 32	35, 40
CO $r_{\rm in}$, $r_{3\sigma}$ [AU]	0.8, 0.6	0.5, 0.4
H_2O $v_{\rm in}$, $v_{3\sigma}$ [$\rm km\,s^{-1}$]	24, 28	36, 42
H_2O $r_{\rm in}$, $r_{3\sigma}$ [AU]	1.0, 0.7	0.4, 0.3
OH $v_{\rm in}$, $v_{3\sigma}$ [$\rm km\,s^{-1}$]	28, 32	34, 39
OH $r_{\rm in}$, $r_{3\sigma}$ [AU]	0.7, 0.5	0.5, 0.4
r[AU] [a]	3	3 [b]
σ [km $\rm s^{-1}$] [a]	2	2
$M_\star$ [$M_\odot$] [a]	0.76	1.2
i[°][a]	67	47
$\Omega_{\rm CO,H_2O,OH}$ [sr]	2×10^{-16}	6×10^{-16}
$T_{\rm CO,H_2O,OH}$ [K]	1000	1000
$N_{\rm CO}$ [$\rm cm^{-2}$]	7×10^{18}	6×10^{18}
$N_{\rm H_2O}$ [$\rm cm^{-2}$]	8×10^{17}	6×10^{17}
$N_{\rm OH}$ [$\rm cm^{-2}$]	2×10^{17}	2×10^{17}

[a] Fixed

[b] Chosen to approximately match line shapes

Chapter 6

Spitzer-IRS Spectroscopy of Protoplanetary Disks: H_2O, OH, and Organics

Portions of this chapter will be submitted to *The Astrophysical Journal* with authors C. Salyk et al.

6.1 Abstract

We report spectral observations of 82 disks obtained with the Spitzer Space Telescope Infrared Spectrograph (IRS). Molecular emission from H_2O, OH, HCN, C_2H_2, CO_2, and H_2 is common, with detection rates for all species of $\sim$ 30–50%. Atomic emission features are also common, including H I, [Ne II], and [Ar III]. Excitation temperatures for the molecular species of $\sim$ 500 K and emitting radii of a few AU suggest an origin in the planet-forming regions of the disks. There are no strong correlations between detection rates or line equivalent widths and stellar or disk parameters. However, molecular detection rates are correlated with each other, and with disk color, in the sense that higher n_{13-30} and n_{6-13} implies fewer detections, suggesting a dependence on disk structure. Transitional disks, which, by definition, have anomalously high n_{13-30} colors, show no evidence for H_2O, OH, or organic molecules, perhaps because these molecules are easily photodissociated in the optically thin inner disk.

6.2 Introduction

The chemistry of protoplanetary disks plays a pivotal role in the development of planetary systems, of habitable planets, and of life. However, our understanding of the chemical conditions in protoplanetary disks—especially in the inner few AU where terrestrial planets form—is far from complete. In particular, there are many uncertainties about the role of water, which not only plays a crucial role in the formation of life as we know it, but also in many other processes that affect the formation and evolution of planets. For example, the location of water-ice sublimation, the so-called 'ice-line', may define a boundary within which planetary cores do not grow large enough to become gas giants. Whether or not a terrestrial planet has water may also have a significant effect on its geology, as water facilitates volcanism and plate tectonics (e.g., Regenauer-Lieb et al., 2001). And, water ice makes up the bulk of many outer solar system bodies, including Kuiper belt objects and outer-planet satellites.

For many years, the detection of water in protoplanetary disks remained elusive, with only a few definitive examples of ice (Malfait et al., 1998; Terada et al., 2007) and vapor (Carr et al., 2004) detections. Recently, however, Carr and Najita (2008) and Salyk et al. (2008) reported detections of numerous emission lines of water in high-resolution spectra from the Spitzer Space Telescope InfraRed Spectrograph (IRS) and the Keck Near Infrared Spectrograph (NIRSPEC). Based on emitting temperatures and line shapes, these lines appeared to originate in the disk atmospheres over terrestrial-planet forming radii.

The robust detections of water in protoplanetary disks, made possible largely by optimized high dynamic range observing strategies and data reduction routines (Carr and Najita, 2008), mark a turning point in our ability to study water's role in the early solar system. However, because water is involved in many complex chemical and physical processes in the disk, water emission can also be used to probe other disk processes. For example, water is destroyed by photodissociation and by high levels of ionization (Jonkheid et al. 2006, 2007), and so water abundances may reflect the disk irradiation environment. Because water condenses at relatively small disk radii ($\sim$ a few AU for Sun-like stars), water vapor may be driven outward by vapor pressure differences, while water ice is carried inwards by planetesimals. Hence, water abundances may reflect radial transport and planet formation timescales. Finally, the strength of water emission lines depends upon the disk structure as a whole, including the gas temperature structure, vertical transport timescales, and the degree of dust settling/grain growth.

One way to disentangle the many factors that effect water abundances and water line emission strengths is to observe a large sample of disks, and look for trends predicted by the processes described above. Here we report characteristics of disks observed during a focused high S/N program 'Water & Organics in Disks' (PI: John Carr, PID: 50641), that builds upon earlier programs, now available in the Spitzer archive, including the c2d legacy program (Evans et al., 2003) and programs P20363 (PI: J. Carr) and 30300 (PI: J. Najita). Information about the c2d program can be found in Evans et al. (2003). Program 50641 was designed to study water and organics in disks at high S/N ($\gtrsim$ 300 for most disks) across a large range of disk and stellar parameters, and includes disks in the Serpens, Perseus, Taurus, Chameleon, Lupus and Ophiuchus clouds. The observed spectra included water emission, as well as solid-state features, atomic transitions, and emission from several other molecules (including C_2H_2, CO_2, and HCN). Below we report detection statistics for water and other spectral features in our disk sample, and discuss implications for disk structure and evolution.

6.3 Observations

The complete list of targets included in this study can be found in Tables 6.1 and 6.2. Information about the c2d IRS observations can be found in the c2d Spectroscopy Explanatory Supplement (Lahuis and Kessler-Silacci, 2006). Program 50641 targets were observed in 2008 in standard IRS Staring mode, with a minimum of 10 cycles on target. Dedicated sky exposures in an off-position were also obtained to remove hot pixels and properly subtract background noise. Most targets were observed in both the Short-High (SH) and Long-High (LH) modules. Exceptions are RY Tau, IQ Tau, AS 205, and RNO 91, which were only observed in LH, as high S/N SH data had already been obtained. Exposure times varied with the goal of achieving S/N $\sim$ 300.

6.4 Data Reduction

Data were reduced with our own IDL routines, along with the IRSFRINGE package (Lahuis et al., 2007), using a procedure similar to that described in Carr and Najita (2008). We began with IRS droop-corrected, non-flat-fielded basic calibrated data (BCD) from the Spitzer Science Center IRS pipeline. We created average on and off frames, subtracted off from on, and then divided by a flat field. In order to reduce noise caused by edge-effects, pipeline flat-fields were first divided by a low-order polynomial fit in the spectral and spatial directions. Pixel values were excluded from the average if they deviated from the mean value for that pixel by more than 5 times the standard deviation. Noisy or bad pixels (with noise greater than 2 times the average noise) were also removed from the averaged frame via interpolation. Spectra were then extracted from the 2D data frames using value-weighted centering and a 3 pixel aperture, and wavelength-calibrated using an IRS wavelength map.

Science target spectra were divided by standard star spectra taken from the IRS calibration program, and reduced in the same manner. Division by a standard star helps to remove some fringing from the science spectrum, but its efficacy varies due to pointing differences between the source and standards. Using a suite of standards, we identified the frames that produced the best results. Some residual fringing remained after this step, and was carefully removed using the IRSFRINGE package. Orders were then combined, using noise values to weight overlap regions. Finally, the set of complete science/standard pairs that produce the best results were averaged together to produce the final spectrum.

For most of the analyses presented in this work, we used continuum-subtracted spectra. Proper removal of continuum emission (and solid-state features) can be difficult, because the noise is not easily distinguishable from the ubiquitous molecular emission features for data such as these in which the spectral lines are unresolved. We adopted the following procedure, which deals well with complex spectra, and consistently yields a good by-eye match to the continuum. We began with a SH or LH spectrum, and identify a smooth part of the spectrum. Using this section, we subtracted a second-order polynomial fit, and then calculated an outlier-free standard deviation (SD) for all points less than 4 standard deviations from the mean. We then smoothed the entire spectrum over 60 pixels, and subtracted 2.5 times the SD. If strong crystalline silicate emission or ice absorption was present, we smoothed the spectra in the vicinity of the features over only 5 pixels. Finally, SH and LH orders were combined. For disks in the high S/N program, no order overlap corrections were necessary. For a few disks with obvious order overlap issues from the c2d program, we adjusted according to the median value of the spectra near the overlap.

Example continuum determinations are plotted in Figure 6.1.

6.5 Results

6.5.1 Overview and Detection Statistics

The continuum-subtracted spectra contain a variety of emission features from H_2O and other gaseous molecules, as well as several atomic emission lines. In Figure 6.2, we show the complete spectrum of GQ Lup—a source which displays emission from H_2O, OH, HCN, C_2H_2, [Ar III] (21.832 μm), and H I ($n = 7 \rightarrow 6$; 12.372 μm)—along with a molecular emission model (discussed in Section 6.5.4). In Figure 6.3, we show spectra from 7 disks in the 13.5–19 μm range, showing the range of line strengths observed. The great majority of the emission features are from H_2O. Each feature is typically a blend of 2 or more transitions, and lineshapes are not spectrally resolved at R=600. Additional prominent emission features in many of the spectra are [Ne II] (12.814 μm) and H_2 (S(2); 12.279 μm). Other emission features are seen with less frequency in some spectra, but analysis of additional lines will be left for future work. In this work, we focus on H_2O, OH, and organics and only briefly discuss emission from H I, [Ar III], [Ne II] and H_2, in the context of their relationship to the other molecules.

There is significant variety in the occurrence of emission features from source to source. In Figure 6.2, one can see the contrast between a source with many molecular features (GQ Lup) and one with no detectable molecular features (CS Cha). In Figure 6.4 we show H_2O detections and non-detections as a function of signal-to-noise ratios (S/N) in the Short-High and Long-High modules, and demonstrate that these detections are not limited by S/N, except, perhaps for S/N<30. (Note that these S/N estimates are computed empirically from the spectra and will be underestimates of the true S/N if the spectra have real structure.) This result also holds true for the other molecular and atomic detections.

A summary of detection rates can be found in Table 6.3. Detection rates for H_2O, OH, and organics range from 35–49% for the sample as a whole. In Figure 6.5 we show the detection rates as a function of spectral type. We find that molecular emission is more common from disks around G, K and M stars than from B and A stars, but that the differences are only marginally statistically significant, because of the small number of early-type stars in our sample. It has been previously reported from analyses of low-resolution spectra that HCN is more common around *sun-like* (K1–M5) stars than *cool* (M5–M9) stars (Pascucci et al., 2009). With only two cool stars in our sample, we can not reliably confirm or disprove this hypothesis. Neither HCN nor C_2H_2 are detected in our cool sample, which is consistent with the low detection rates of both species found by Pascucci et al. (2009). However, we find significantly higher detection rates of HCN and C_2H_2 in our sun-like star sample than was reported in Pascucci et al. (2009), suggesting that either our samples are different, or that low-resolution spectra can result in underestimates of HCN occurrence by a factor of ~ 2, and C_2H_2(generally the weaker feature) by a factor of ~ 5.

Our sample includes eight transitional disks—disks in which an inner gap has been significantly depleted of small dust grains (Koerner et al., 1993; Calvet et al., 2002). It has been shown that many transitional inner disks contain significant amounts of gas in the form of CO (Najita et al., 2003; Rettig et al., 2004; Salyk et al., 1999, (in press), with the group of gas-rich inner disks including at least four in our sample—GM Aur, HD 135344, LkHα 330, and UX Tau A. However, we see no H_2O, OH, or organics in any transitional disk. In Table 6.3 we compare detection rates between transitional and nontransitional disks, and also calculate the probability of getting the observed transitional detection rate in a sample of eight disks, assuming they are picked at random from the non-transitional-disk population. There is a reasonable probability of obtaining the observed detection rates for H I, [Ne II], and H_2, so the two samples do not have significantly different detection rates of these species. However, for H_2O, OH, and organics, the transitional disk sample is not consistent with the non-transitional sample.

Using the results presented in Table 6.4, we search for relationships amongst detected species, and between detected species and stellar and disk parameters. In the upper-right quadrant, we show the p-value associated with the slope of a linear regression of the two parameters. In the lower left quadrant, we show the p-value for obtaining a χ^2 value at least as high as is observed, using the following procedure: We assume the actual detection rates of the two species (X and Y) are given by their observed detection rates. We then compute the expected number of matching pairs (X detected:Y detected or X not detected:Y not detected), the expected number of nonmatching pairs, and compute χ^2 using these values and the observed numbers of matching and nonmatching pairs. In both cases, a low probability implies that the relationship between the two species (or the species and stellar/disk parameter) is stronger than would be predicted by chance alone.

We find only two possible correlations between stellar/disk parameters and line detections. Not surprisingly, the H I feature in our spectra correlates with the strength of Hα, most likely because both of these features, like other hydrogen recombination lines, are created in magnetospheric accretion columns (e.g., Hartmann et al., 1994). There is also a possible relationship between stellar mass and the presence of C_2H_2. In contrast, the detection rates are strongly related to each other, in many cases. H_2 may also be correlated with some species, including H_2O, HCN, C_2H_2, and [Ar III]. The strongest correlations are found for the presence of H_2O, OH, HCN, C_2H_2, CO_2, and [Ar III]. Note, however, that there is significant overlap between one H_2O feature and the [Ar III] line. Although the feature has been classified as [Ar III] only when it noticeably exceeds the slab-model expectation for H_2O emission, it is possible that the contribution from H_2O is greater when non-LTE effects are taken into account. This could potentially remove the correlation between H_2O and [Ar III].

6.5.2 Colors

The shape of an SED is affected by disk structure and geometry. Disk colors are a simple way to parameterize the major features of the SED, and can be used to look for relationships between emission characteristics and disk structure. In this work, we calculate disk colors following procedures similar to those described in Furlan et al. (2006), except that we utilize fluxes at 30μm instead of 24 μm, to avoid the 23 μm silicate emission feature. Flux densities are calculated at 13 and 30 μm by integrating over the 12.5–14 and 29–31 μm regions, respectively, and then dividing by the width of the region. At 6 μm, we adopt 5.8 μm IRAC fluxes from the literature (see Table 6.5). We then use the flux densities to calculate spectral indices n_{6-13}, n_{6-30}, and n_{13-30}, where

$$n = \log\left(\frac{\lambda_2 F_{\lambda_2}}{\lambda_1 F_{\lambda_1}}\right) / \log(\frac{\lambda_2}{\lambda_1}).$$

When 6 μm fluxes are unavailable, we use spectral indices from Furlan et al. (2006) and Watson et al. (2009). The colors for our entire sample are shown in Table 6.5.

We do not find any strong correlations between single disk colors and any species detection rates. However, in the top panel of Figure 6.6, we show a possible trend for detection rates on a two-color diagram. Towards the top and right of the figure, detections are much less common. In Table 6.6 we show that the detection rates inside and outside the outlined region are indeed different in a statistically significant sense. Although we show in this figure the detections and nondetections for H_2O, the differences are also apparent for OH, the organic molecules and [Ar III], as these detections are all correlated with each other.

Low n_{13-30} values are associated with a large amount of small dust grains in the upper disk layers, while high n_{13-30} values are associated with depletion of small grains in the upper layers—either due to overall removal, or settling of small grains to the midplane (e.g., Furlan et al., 2006). In this case, the high n_{13-30} sources in the top left and top center are transitional disks, so the high n_{13-30} results from an overall depletion of disk dust grains. However, even after accounting for the transitional disks, there is a difference between Region 1 and Region 2 detection rates. Both n_{13-30} and n_{6-13} increase as disk inclination increases, so this trend could represent a relationship between detectability and disk inclination, with low inclinations being easier to detect. However, we do not see a direct relationship between disk inclination in detectability, according to Table 6.4. Another possibility is that the trend could be attributed to accretion rate, which is negatively correlated with the n_{6-13} ratio (Furlan et al., 2006). Molecular detections may correlate with accretion rate because disk atmospheres are hotter, and can more easily excite the observed transitions.

6.5.3 Equivalent Widths

In addition to studying line emission occurrences, we investigate trends associated with the strength of the emission features. In Table 6.7, we show equivalent widths calculated for all detected emission features. Equivalent widths are calculated by integrating over the following wavelength regions (in μm): H I (12.330–12.430); H_2O(12.325–12.427 and 32.907–33.102); OH (18.755–18.909); HCN (13.957–14.065); C_2H_2(13.687–13.719); CO_2 (14.923–14.994); [Ne II] (12.780–12.845); [Ar III] (21.820–21.850); H_2 (12.230–12.305). To compute error bars, we use the standard deviation of the flux in a quiescent region—usually between 10.263 and 10.644 μm in the short-high module, and between 24 and 24.3 or 26.1 and 26.4 μm in the long-high module. Prior to computing equivalent widths for all molecules besides H_2O, we first subtract a best-fit H_2O emission model (described in Section 6.5.4).

In Table 6.8 we show the relationships between stellar and disk parameters and equivalent widths, as well as between equivalent widths of different emission features. In this table, values above the diagonal are the correlation coefficient, R, between the two parameters. Values below the diagonal are the p-value associated with a linear regression of the two parameters. We have bolded both numbers if $\mathrm{p} \leq 0.02$. We find only two correlations between disk parameters and line equivalent widths—anti-correlations between $\log \dot{M}$ and both H_2 and C_2H_2. This relationship can be accounted for entirely by the fact that the equivalent widths of both molecules are strongly anti-correlated with the continuum flux level. Once this is accounted for, the relationship disappears; there is no relationship between line *strength* and $\log \dot{M}$.

Several correlations exist between different molecular equivalent widths. These are roughly in agreement with the detection correlations: H_2O, OH, HCN, C_2H_2, [Ne II], and [Ar III] are, to some extent inter-related. Correlations with [Ne II] may be determined by the continuum level, as [Ne II] equivalent widths are strongly anti-correlated with the continuum. Strong correlations between [Ne II] and both H I and H_2 are the result of transitional disks, for which both lines have stronger than average equivalent widths when present.

In Table 6.9, we show possible relationships between disk colors and equivalent widths. Table inputs are p-values for the slope of a linear regression of the two parameters. Strong (positive) correlations with n_{13-30} are seen for H I and [Ne II]. In both cases, this is due to the fact that transitional disks have large H I and [Ne II] equivalent widths, as well as high n_{13-30}. In Figure 6.7, we plot [Ne II] against n_{13-30}, and label the transitional disks. There is no apparent trend once these sources are removed. In Figure 6.7, we show that the relationship between [Ne II] equivalent width n_{13-30} is due to the strong [Ne II] equivalent widths for transitional disks. This, in turn, is mostly, if not entirely, due to the reduced continuum at $\sim$13 μm.

6.5.4 Models

6.5.4.1 Description of Model

To obtain a better physical understanding of the source of the disk emission, we fit the molecular emission with emission models. In this work, we use an isothermal slab approximation, in which area A, temperature T, and column density N are all free parameters. These models are the same as those utilized in Salyk et al. (2008), and assume a Gaussian local line shape with width, $\sigma = 2$ km s^{-1}. Note that the lines are not spectrally resolved, and so the true line shape is unknown.

There are many limitations to using this simple slab model. The actual disk environment is quite complex, with densities and temperatures that depend on both height and radius. The observed emission almost certainly arises from only the upper disk atmosphere (except, possibly, in the case of the transitional disks), and so the best-fit model parameters represent the flux-weighted average parameters of the upper disk atmosphere at a variety of radii. In addition, the molecular emission may not actually arise from a thermalized gas, in which case the derived column densities can be quite different from those actually present. Finally, the local turbulent velocity is unknown, yet can significantly affect the derived fit parameters (Salyk et al., 2008).

Many of the more complex issues related to line excitation and disk structure are being pursued with more complexing radiative transfer modeling (Meijerink et al., in prep). Here, we use the slab models to understand the bulk properties of the emitting atmospheres, to investigate the variety of emission observed, and to estimate molecular abundance ratios. By focusing on abundance ratios, rather than abundances, we may be less sensitive to some of the limitations mentioned above.

6.5.4.2 H_2O Models

We fit the H_2O emission spectra by iterating over a grid of T, A, and N. T ranges from 200–1200 K with 100 K spacing, A ranges from $4 \times 10^{-4} - 4 \times 10^{2}$ AU^2 with log spacing of ~ 0.6, and N ranges from 10^{16}–10^{22} cm^{-2} with log spacing of ~ 0.3. Best fit models were chosen to minimize the sum of squared residuals between data and model.

Best-fit model parameters are listed in Table 6.10 and shown graphically in Figures 6.8 and 6.9. Typical allowed ranges for the fit parameters are $\sim$ 300 K in temperature, a factor of $\sim$ 100 in density, and a factor $\sim$ 3 in area, assuming the reduced χ^2 of the best model is 1, and using a 95% confidence interval. However, these error ranges are larger than the true uncertainties, as can be seen in the histograms of Figure 6.8. This may be because the parameters are not independent, but instead correlated with each other, as can be seen in Figure 6.9. True error bars are likely about a factor of 2 smaller.

In general, H_2O emission models are consistent with temperatures of $\sim$ 500 K, densities of $\sim 5 \times 10^{18}$ cm^{-2}, and emitting areas of a few AU^2. These results suggest that the emission arises in the warm, inner few-AU region of the disk. Peak optical depths for the strongest lines in the model exceed $\sim$ 1000, which implies that $H_2{}^{18}O$ may be detectable, and therefore accessible for studies of isotopic fractionation in disks.

6.5.5 Other Molecular Models

In addition to H_2O we have fit emission from OH, C_2H_2, CO_2, and HCN. For all molecular fits, we first subtracted the best-fit H_2O emission model, if H_2O was present. To fit the OH emission, we use the same procedure as was used for H_2O. For C_2H_2 and CO_2, it was not possible to simultaneously fit the three model parameters, because there is only a single Q-branch feature detectable at the resolution of the Spitzer IRS, and both density and temperature affect the model in similar ways (see Figure 6.11). It may be possible to distinguish the effects of temperature and density differences for HCN, but we leave this as future work. Therefore, for all molecules besides OH, we assumed the same emitting area and temperature as for H_2O, and fit only for column density.

The results of these model fits are shown in Table 6.10. Model fits typically yield densities of 5×10^{15} for CO_2, and $10^{16}\,\mathrm{cm}^{-2}$ for HCN. C_2H_2 densities range from $\sim 10^{15}$–$10^{16}\,\mathrm{cm}^{-2}$. However, in many cases, the best-fit model appears, by eye, to have overestimated the strength of the emission feature (see Figure 6.2). This is due to the fact that the Q-branches are actually too broad to be properly fit by the constrained values of temperature and density. Therefore, either the model temperatures or the model densities would need to be increased, and model areas would need to be reduced accordingly. Nevertheless, we show ratios of molecular column densities relative to H_2O are in Figure 6.10, and compare to both previous results (Carr and Najita, 2008), disk models (Markwick et al., 2002) and ices (Gerakines et al., 1999; Whittet et al., 2007; Pontoppidan et al., 2008a). Error bars show the standard deviation of the entire sample. Note that the large difference in density ratios between previous results for AA Tau (Carr and Najita, 2008) and this work (which includes AA Tau in the sample) can be primarily attributed to the fact that the areas in the previous work were allowed to vary, and found to be smaller than for H_2O by factors of 3–10 for CO_2, HCN, and C_2H_2. Differences for OH arise from differences in best-fit temperatures. This issue is being investigated further, and will be addressed in more detail in future work. Our results appear nearly consistent with disk models at 1 AU, but are significantly lower than ratios found in YSO and cloud ices.

OH model-fitting results are shown in Figure 6.8. The OH emission appears to be best-fit with very high emitting temperatures—in the range of 600–1200 K. 1200 K is the upper end of our temperature grid, so emitting temperatures may be even higher. Densities are typically $\sim 10^{15}$, 3–4 orders of magnitude lower than that of H_2O, while emitting areas are typically factors of ~ 5 larger than for H_2O. The need for both large emitting areas (i.e., large radii) and high temperatures is inconsistent with disk structure, in which temperatures drop with radius. This may mean that the OH we observe is not in thermodynamic equilibrium. Mechanisms for non-LTE excitation of OH include UV-pumping by the central star and the photodissociation of H_2O followed by 'prompt' emission (Bonev et al., 2006).

6.6 Discussion

When observed at sufficient spectral resolution and with high S/N, emission lines from H_2O, OH, and organics are seen with high frequency around young low mass (G,K, and M) stars. Detection rates for all molecules are typically $\sim 40\%$, and detections and strengths of each species are correlated with each other. Because the molecules do not share a common chemical origin, the prominence of emission lines may be more strongly influenced by the disk environment than by the rates of production and destruction.

Because H_2O condenses at only a few AU, the H_2O content of the inner disk can potentially be affected by the rates of outward vapor diffusion and inward ice migration followed by sublimation (Ciesla and Cuzzi, 2006). The fact that H_2O emission does not appear unique in any way suggests that the H_2O emission lines are not significantly affected by this process.

Unfortunately, there are few obvious trends between detection rates or line strengths and stellar or disk parameters, although we will continue to investigate this issue. There is, however, a trend of decreasing detectability of most molecular species with increasing n_{6-13} and n_{13-30}, which could be due to inclination effects, settling, accretion luminosity, or some combination of these.

One the most unambiguous results of this study is a notable difference in the spectra from classical and transitional disks. No H_2O, OH, or organics are detected in our observations of transitional disks, although the presence of CO and [Ne II] in many transitional disks means that their inner regions do contain significant quantities of gas. A possible reason for the lack of emission may be that because the disk is optically thin, the molecules are not well shielded from the strong radiation field of the central star. CO (and H_2) on the other hand, can self-shield.

Simple slab models, with temperature, emitting area, and column density as free parameters, do a reasonable job of reproducing the major features of the observed spectra. These models suggest that the emission arises from within a few AU of the central star, consistent with both the best-fit emitting areas and temperatures. Molecular ratios are roughly consistent with those predicted by disk chemical models, and lower than those found in YSO and cloud ices, but differences between this work and previous studies highlights potential systematic uncertainties in model parameters.

Two important limitations to studies utilizing slab models include the degeneracy of parameters, and the unknown local velocity. Both of these issues could be resolved with higher-resolution data; line shapes depend on both the local line broadening and the area of origin for the emission. A survey of 3μm H_2O and OH emission from disks at higher resolution (R$\sim$25000) is currently being pursued with NIRSPEC on the Keck II telescope (Salyk et al., in prep).

There are other apparent limitations to the slab models. The H_2O models do not reproduce well the short-wavelength emission lines, below ~ 14 μm, and do not always produce the correct flux for all lines. In addition, OH emission is consistent with very high temperatures and large emitting areas, which could suggest that these features are not thermally excited. A disk model including radiative transfer and nonthermal excitation mechanisms fits much better the emission features (Meijerink et al., in prep). The relationship between the fit parameters in the slab and in a full disk model is not known, but is currently being investigated.

The set of spectra presented in this work represents a rich new dataset to explore disk structure and chemistry. As it was designed for studies of disk gas, it provides an important complement to the many studies that have been made of the solid-state components of disks. First results show that molecular emission is common, and may be related to disk structure. H_2O emission shows no evidence of the effects of radial transfer, and OH emission suggests that an understanding of nonthermal excitation could be important for the intepretation of disk emission. Future work will explore particular species in more detail, and include searches for additional atomic and molecular emission. In addition, radiative transfer models are currently being created to investigate in more detail the origin of the emission lines, and the conditions in disk atmospheres, including turbulent broadening and non-LTE gas heating.

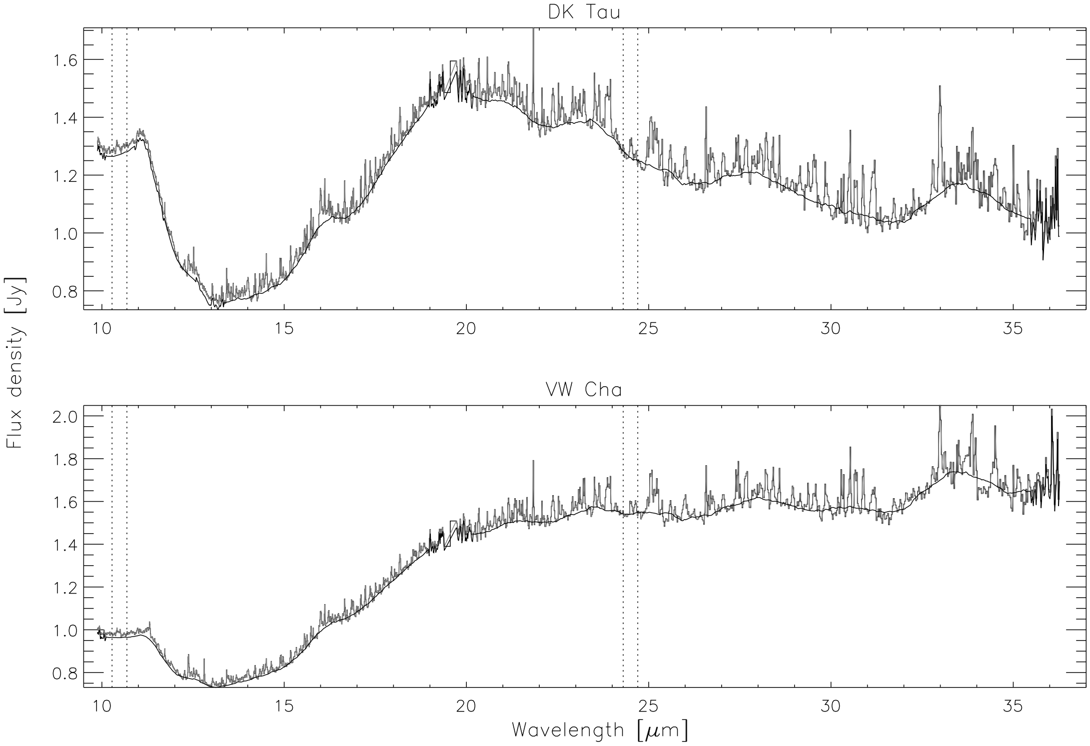

Figure 6.1: Continuum determination for two disks. Samples of continuum determination for two disks. Data are shown in gray, and continuum (described in text) in black. Regions between the dotted lines show where the standard deviation was calculated.

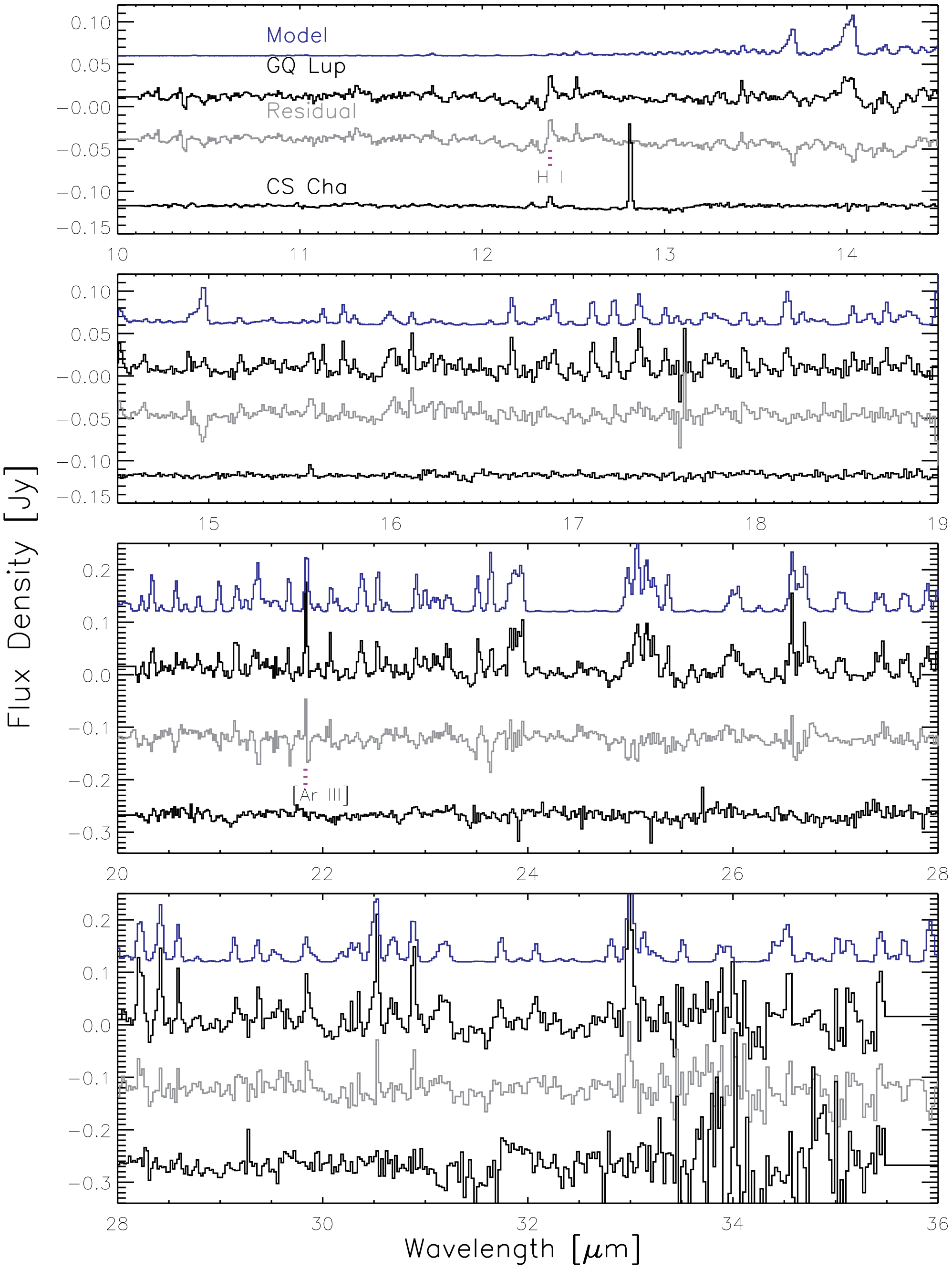

Figure 6.2: Data, best-fit molecular models, and residuals.

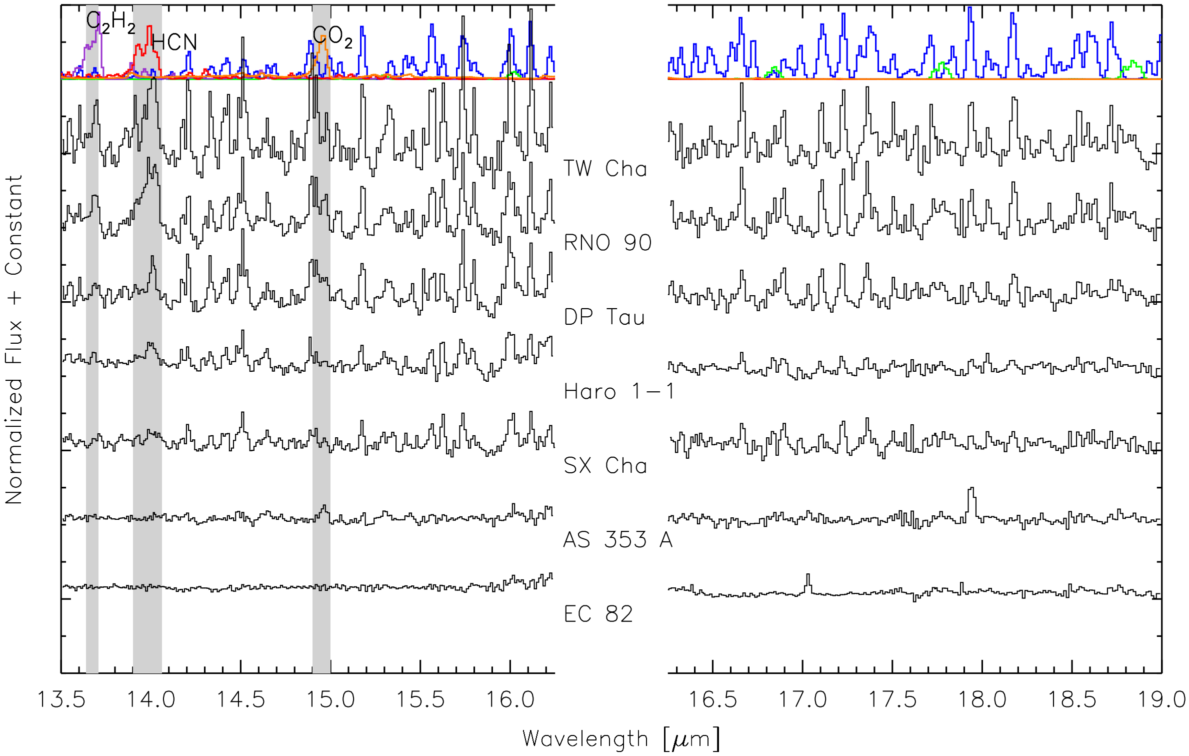

Figure 6.3: Spectra for 7 disks in our sample, showing a variety of emission line strengths. Plotted above are emission spectra expected for H_2O, HCN, CO_2, and C_2H_2.

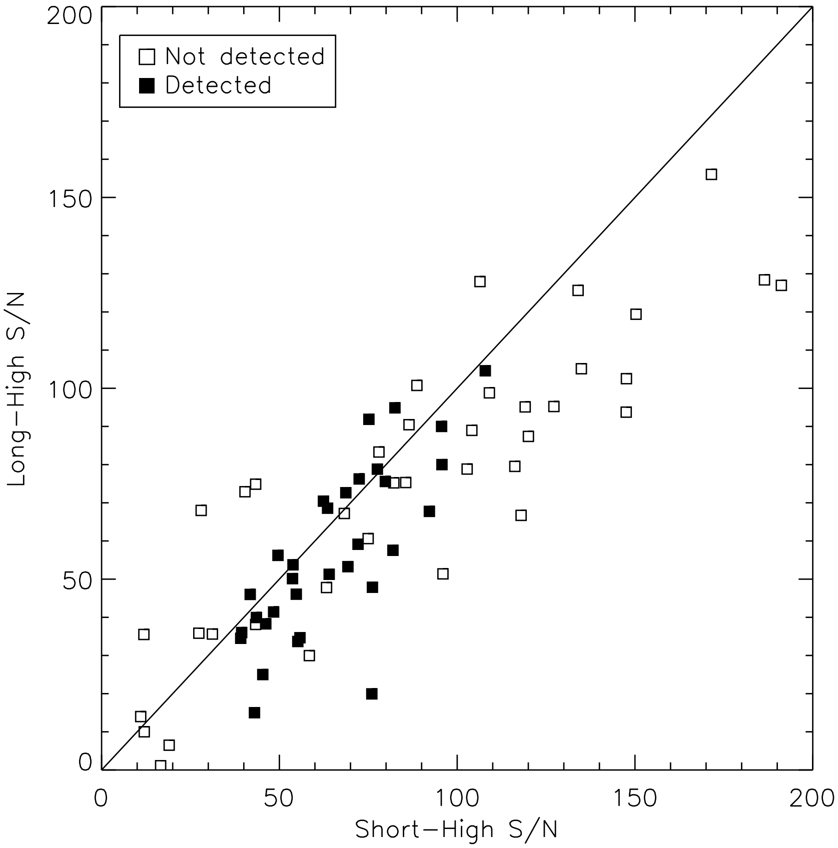

Figure 6.4: Detections and non-detections as a function of S/N in the Short-High and Long-High modules. S/N ratios are taken as Median/σ. σ is computed after subtraction of a best-fit H_2O model.

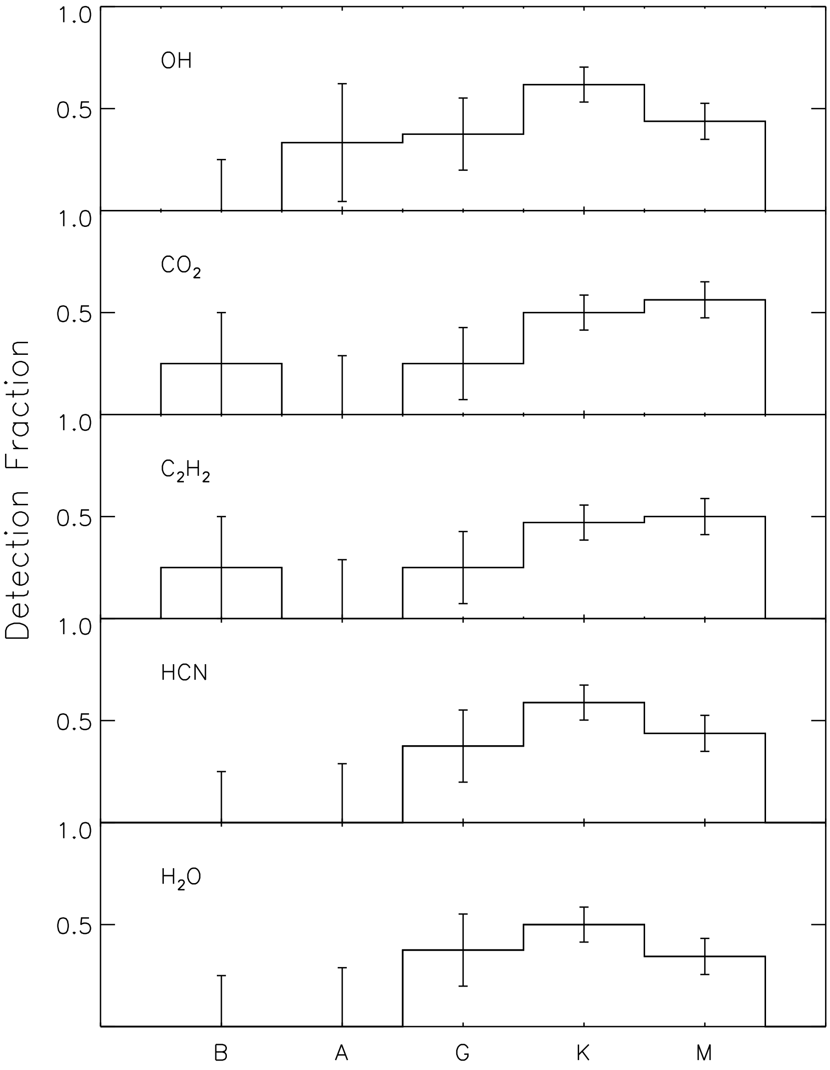

Figure 6.5: Detection fractions as a function of spectral type.

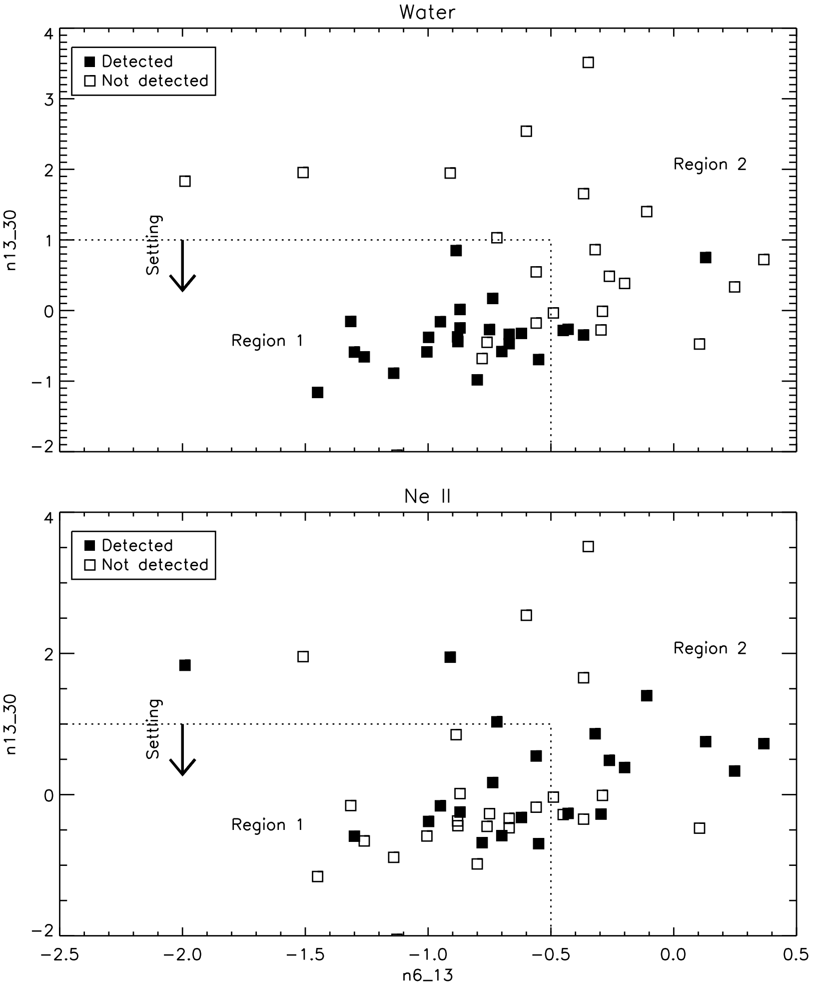

Figure 6.6: Detections and non-detections of H_2O and [Ne II] on a color-color diagram. A two-color plot showing detections and non-detections of H_2O and [Ne II]. Note that settled sources are more likely to have H_2O emission, but are not more likely to have Ne II emission.

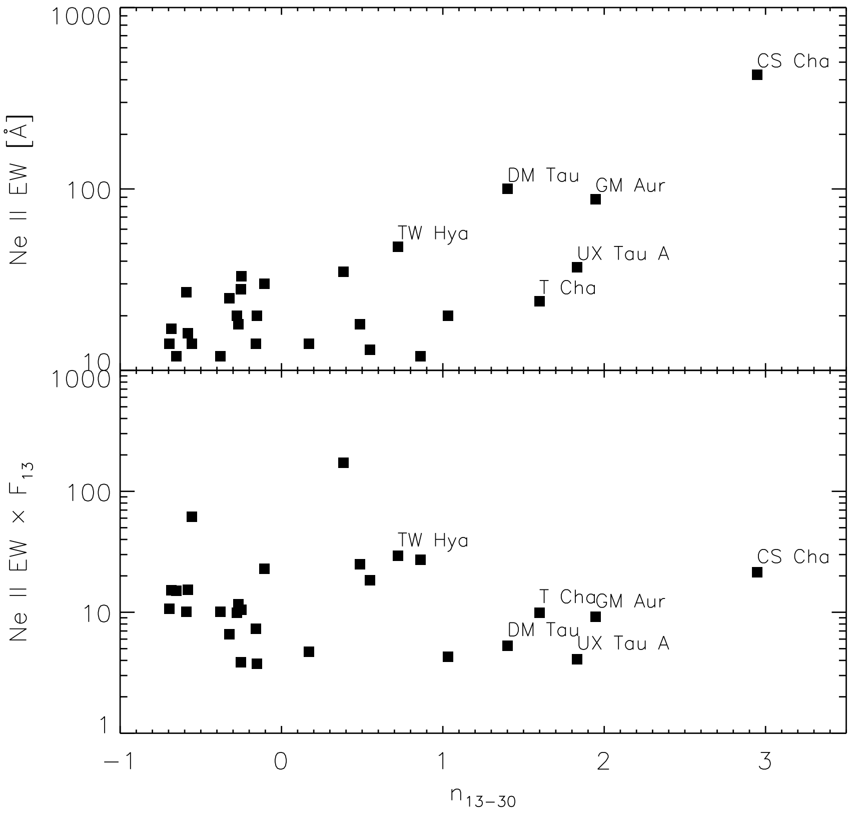

Figure 6.7: Ne II equivalent width versus n_{13-30} color. Sources at the extreme upper right are labeled. Note that the majority of these are transitional disks.

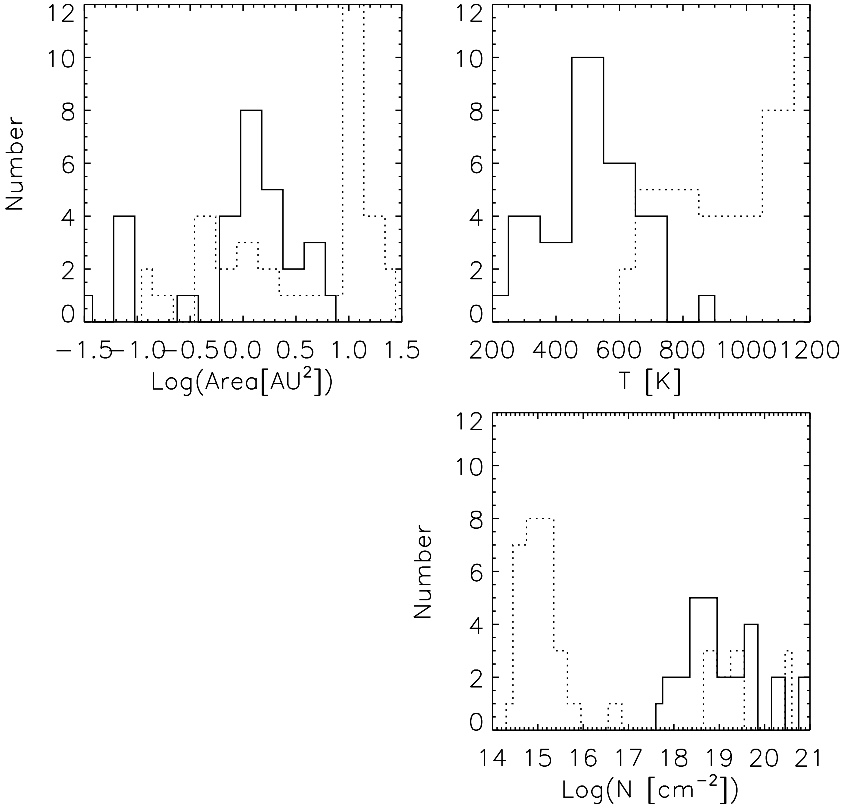

Figure 6.8: Histogram of H_2O (solid lines) and OH (dashed lines) model-fit parameters

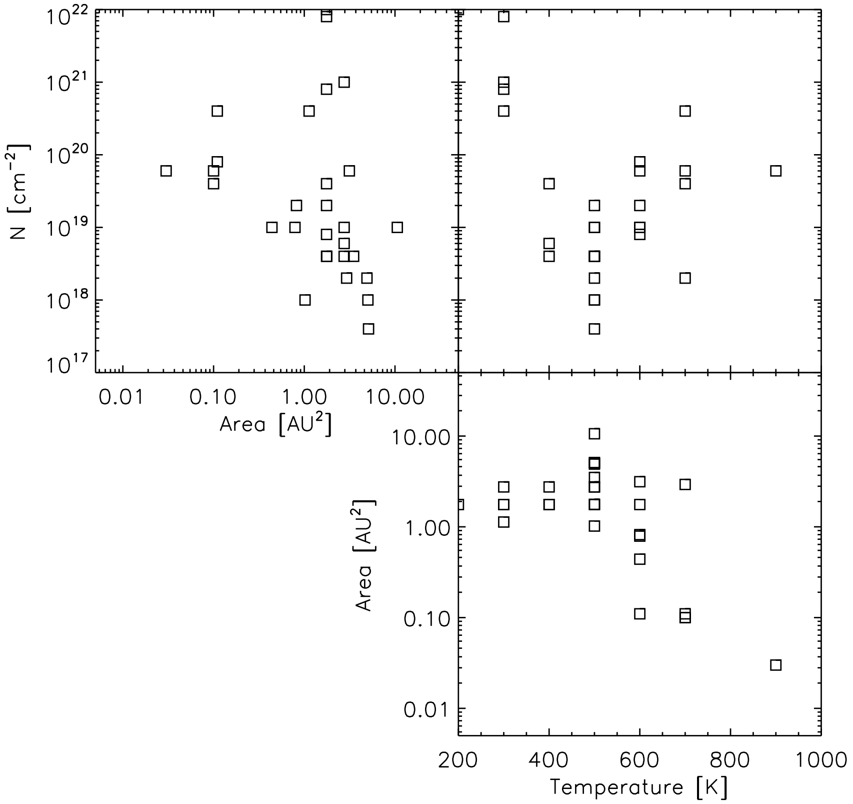

Figure 6.9: Correlations between H_2O model-fit parameters. Note that emitting areas are typically a few AU^2, and temperatures are typically 400–600 K, suggesting that the H_2O resides in the inner disk. Also note the strong anti-correlation between temperature and emitting area.

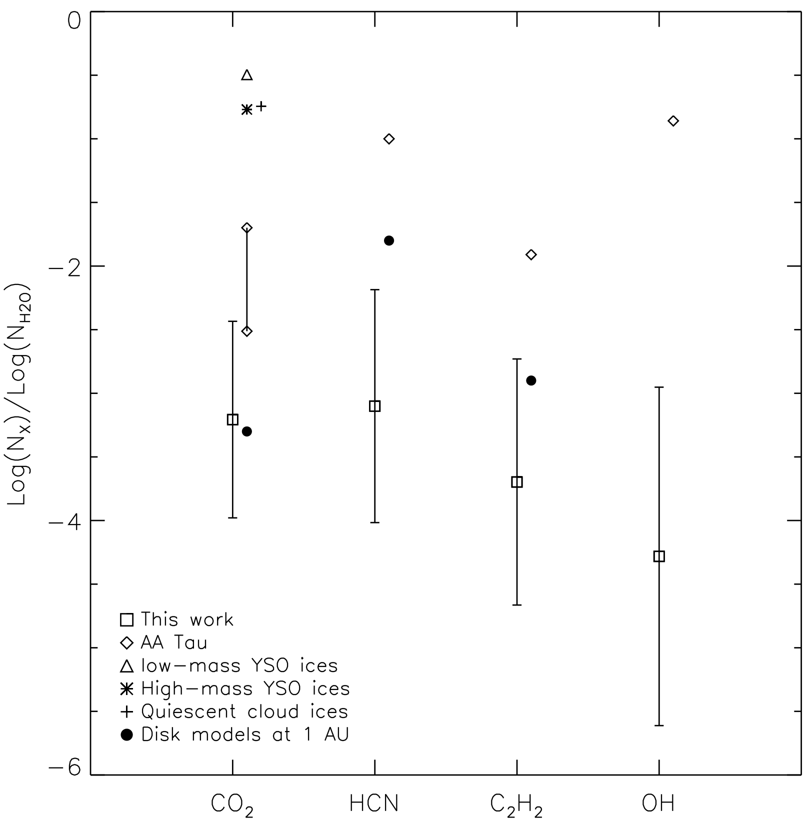

Figure 6.10: Molecular ratios from this work, compared to previous results and other environments. References are: for AA Tau, (Carr and Najita, 2008), low-mass YSO ices (Pontoppidan et al., 2008b), high-mass YSO ices (Gerakines et al., 1999), and quiescent cloud ices (Whittet et al., 2007).

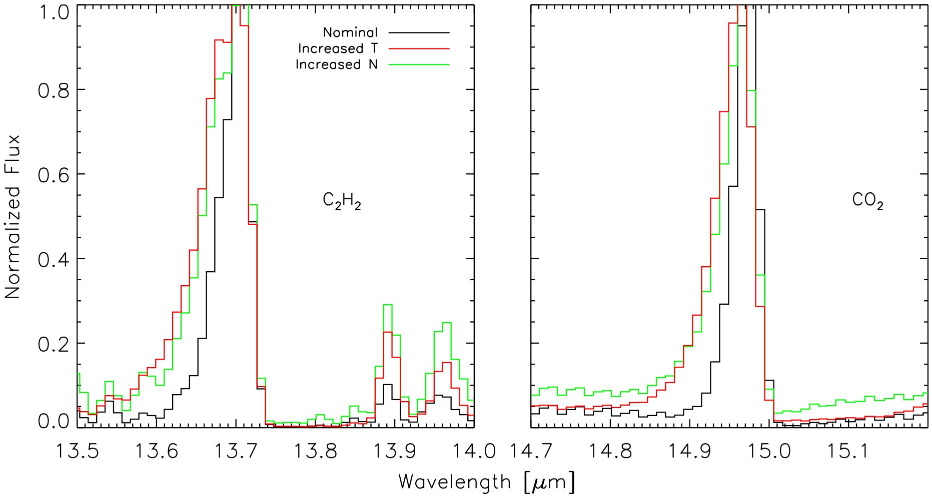

Figure 6.11: Sample model results for CO_2 and C_2H_2. Note that increased temperatures and column densities affect the model output in similar ways. For both molecules the nominal model has $T = 400\,K$, and the high-T model has $T = 900$ K. For C_2H_2, N is increased by a factor of 60 for the high-N model, while for CO_2 it is increased by a factor of 6000.

Table 6.1: Stellar Parameters

Star	d [pc]	SpT	ref	Lx [^{1}]	ref	$M_\star$ [$M_\odot$]	ref	$L_\star$ [$L_\odot$]	ref	A_V	ref
AA Tau	140	K7	6,23	1.24	26	0.67	12	0.98	12	1.75	23
AS 205 A	160	K5	44	···	···	1.50	44	7.10	44	2.90	44
AS 353 A	200	K3	22	···	···	···	···	···	···	2.10	44
BF Ori	400	A5–F6	36	···	···	···	···	···	···	0.55	55
BP Tau	140	K7	6,23	1.36	26	···	12	0.95	12	1.00	23
CHXR 30	178	K7–M1	38	1.91	4	···	···	···	···	···	···
CI Tau	140	K7	6,23	0.20	26	0.70	12	0.87	12	2.00	23
CoKu Tau/4	140	M1.5	6,23	<0.21	42	0.43	56	0.68	56	3.00	23
CS Cha	178	K4	3	1.00	21	1.20	21	1.10	21	0.85	55
CW Tau	140	K3	6,23	2.84	26	1.40	12	1.10	12	2.75	23
CY Tau	140	M1	6,23	0.19	26	0.48	12	0.50	12	1.70	23
DE Tau	140	M1–M2	6,23	<0.29	42	0.44	12	1.21	12	1.20	23
DG Tau	140	K5–M0	27	0.25	26	0.56	12	1.70	12	1.60	23
DK Tau	140	K7	6,23	0.92	26	0.65	12	1.30	12	1.30	23
DL Cha	178	M6	36	···	···	···	···	···	···	···	···
DL Tau	140	K7	6,23	<0.31	42	0.76	33	0.77	12	1.50	23
DM Tau	140	M1	6,23	0.18	26	0.62	12	0.30	12	0.72	23
Do Ar 24E	160	K7–M0	25	0.50	15	0.47	41	1.26	41	2.90	25
Do Ar 25	160	K3–M0	10	0.25	15	0.49	41	1.35	41	2.90	7
DO Tau	140	M0	6,23	···	···	0.57	12	1.38	12	2.05	23
DP Tau	140	M0	6,23	0.10	26	0.60	12	0.20	12	0.60	23
DR Tau	140	K7	6,23	<0.64	42	0.55	12	2.50	12	1.20	23
EC 82	260	M0	36	···	···	···	···	···	···	···	···
EX Lup	150	M0	30	···	···	0.59	30	0.39	30	0.00	55
FN Tau	140	M5	35	< 0.37	42	0.11	35	1.00	12	1.35	23
FT Tau	140	cont	6,23	<0.22	42	···	···	1.30	56	···	···
FX Tau	140	M1	6,23	0.50	26	0.44	12	1.02	12	2.00	23
FZ Tau	140	M0	6,23	0.64	26	0.57	56	1.08	56	3.70	23
GI Tau	140	K7	23	0.83	26	0.91	12	1.00	12	2.30	23
GK Tau	140	K7	6,23	1.47	26	0.57	12	1.40	12	1.15	23
GM Aur	140	K7	6,23	<0.55	42	0.72	12	0.70	12	1.21	23
GQ Lup	150	K7–M0	30	···	···	0.80	48	0.80	48	0.50	48
GW Lup	100	M2–M4	30	···	···	0.46	30	0.23	30	0.00	55
Haro 1-16	125	K2–K3	36	···	···	···	···	···	···	···	···
Haro 1-17	125	M2.5	36	···	···	···	···	···	···	···	···
Haro 1-1	125	K5–K7	36	···	···	···	···	···	···	1.70	55
Haro 1-4	125	K6–K7	36	···	···	···	···	···	···	···	···
Haro 6-13	149	M0	6,23	0.80	26	0.55	12	2.10	12	11.90	23
HD 101412	160	B9.5	36	···	···	···	···	···	···	0.56	55
HD 135344	84	A0–F4	36	···	···	1.50	24	8.00	24	0.30	24
HD 98922	540	B9	24	···	···	5.00	24	···	24	0.30	24
HK Tau	140	M0.5–M	6,23	0.08	26	0.55	12	0.56	12	2.70	23
HN Tau	140	K5	6,23	0.15	26	0.59	12	0.25	12	1.50	23
HQ Tau	140	···	···	5.32	26	···	···	5.37	12	···	···
HT Lup	145	K2	30	···	···	1.57	30	1.45	30	1.45	55
IM Lup	140	M0	30	···	···	1.00	43	1.30	30	0.98	55
IQ Tau	140	G0–M0	6,23	0.42	26	0.54	12	0.88	12	1.44	23
LkCa 8	140	M0	36	···	···	···	···	···	···	···	···
LkHa 270	250	K2.5	22	···	···	···	···	···	···	···	···
LkHa 326	250	G-M0	36	···	···	···	···	···	···	···	···
LkHa 330	250	G2–G3	22	···	···	···	···	···	···	···	···
LkHa 348	260	cont	22	···	···	···	···	···	···	···	···
RNO 15	250	···	···	···	···	···	···	···	···	···	···
RNO 90	140	G5	36	···	···	···	···	···	···	···	···
RNO 91	140	···	···	···	···	···	···	···	···	···	···
ROXs 42C	125	M	36	···	···	···	···	···	···	···	···
ROXs 43A	125	G0–G8	36	···	···	···	···	···	···	···	···
RR Tau	160	B8–A5	36	···	···	2.50	24	37.00	24	1.10	24
RU Lup	140	K7–M0	30,28	···	···	1.00	28	0.42	28	0.10	28
RW Aur	140	K1–K3	56,22	···	···	1.34	56	1.70	56	0.50	23

Continued on Next Page…

Table 6.1 – Continued

Star	d	SpT	ref	Lx	ref	$M_\star$	ref	$L_\star$	ref	A_V	ref
RY Lup	150	K0–K4	30	···	···	1.19	30	1.30	30	0.65	55
SR 9	125	K4–M2	25	2.51	15	0.60	41	1.90	41	2.50	25
St 34	140	M3	31	···	···	0.37 [2]	57	···	···	···	···
SU Aur	140	G1–G2	6,23	9.46	26	2.65	12	9.90	12	0.90	23
SX Cha	178	M0.5	36	< 0.32	21	0.80	21	0.30	21	1.12	21
SY Cha	178	M0	36	0.16	21	0.80	21	0.30	21	0.21	21
Sz 18	178	M2.5	37	···	···	···	···	···	···	···	···
Sz 50	178	M3	36	3.02	4	···	···	···	···	···	···
T Cha	66	G2-G8	36	···	···	···	···	···	···	···	···
TW Cha	178	M0	36	1.00	21	1.00	21	0.90	21	2.99	21
TW Hya	56	K7	10	2.00	10	0.77	28	0.17	28	0.00	55
UX Tau A	140	K2	6,23	0.95	42	1.49	12	2.70	12	0.70	23
UY Aur	140	···	···	···	···	···	···	···	···	···	···
V1331 Cyg	500	A8-G5	40	···	···	···	···	···	···	2.40	40
V710 Tau	140	M0.5	6,23	1.38	26	0.42	56	1.10	56	1.90	23
V853 Oph	125	M1.5	36	···	···	0.42	41	1.05	41	···	···
VV Ser	260	B1–A3	36	···	···	3.10	24	85.00	24	3.10	24
VW Cha	178	M0.5	36	9.33	21	0.60	21	3.31	21	2.39	21
VZ Cha	178	M0	36	1.26	21	0.90	21	0.30	21	0.47	21
Wa Oph 6	140	K6	7	···	···	···	···	···	···	3.50	7
WX Cha	178	K7	36	1.48	21	0.80	21	0.85	53	2.14	21
XX Cha	178	M2	36	< 28.60	46	0.70	21	0.10	21	0.61	21

---

[1] 10^{30}erg s^{-1}

[2] For each member of a spectroscopic binary

Table 6.2: Disk Parameters

Star	EW$_{H\alpha}$ [Å]	ref	$\log \dot{M}$ [$10^{-8} M_{\odot}\mathrm{yr}^{-1}$]	ref	M_d [$M_{\odot}$]	ref	i_d [°]	ref	ID*
AA Tau	37	12	-8.48/-8.19	7	0.03	6	75	33	3
AS 205 A	55–155	22,32	-6.14/-6.14	7	0.0330	8	47	7	1
AS 353 A	15–17	22	···	···	···	···	···	···	3
BF Ori	6–11	32	···	···	···	···	···	···	2
BP Tau	40–76	12,22	-7.88/-7.54	26	0.0200	6	20	50	3
CHXR 30	···	···	···	···	···	···	···	···	4
CI Tau	102	12	-7.59/-7.19	7	0.0400	6	46	7	1
CoKu Tau/4	1–2	32	< -11.00	17	0.0005	6	···	···	2,4
CS Cha	13	21	-7.92/-7.92	20	···	···	···	···	4
CW Tau	135–140	12	-8.80/-7.99	27	0.002	6	···	···	1
CY Tau	70	12	-8.86/-8.12	26	0.006	6	47	50	1
DE Tau	54	12	-7.59/-7.59	39	0.005	6	···	···	1
DG Tau	113	12	-8.40/-6.13	27,28	0.0200	6	70	16	3
DK Tau	19	12	-7.42/-7.42	26	0.005	6	···	···	3
DL Cha	···	···	···	···	···	···	···	···	2
DL Tau	105	12	-7.73/-7.17	7	0.1	6	35	7	1
DM Tau	140	12	-8.70/-8.67	7	0.014	6	32	7	4
Do Ar 24E	···	···	-8.46/-8.46	41	0.008	8	···	···	1
Do Ar 25	2	10	< -9.24	7	0.1	9	62	7	2
DO Tau	109	12	-6.85/-6.85	39	0.007	6	42	34	3
DP Tau	86	12	-8.50/-6.92	27	<0.0005	6	···	···	1
DR Tau	87	12	-6.50/-6.25	7	0.01	6	72	7	1
EC 82	5–11	32	···	···	···	···	···	···	1
EX Lup	31–43	32	···	···	···	···	···	···	1
FN Tau	16–25	12,35	···	···	0.007	35	20	35	2
FT Tau	189	31	···	···	0.05	6	60	7	1
FX Tau	10–15	26	-8.65/-8.65	26	0.0009	6	···	···	2
FZ Tau	204	12	-7.70/-7.70	56	0.002	6	···	···	1
GI Tau	15–21	26	-8.08/-8.08	26	···	···	···	···	3
GK Tau	15–35	26	-8.19/-8.19	26	0.002	6	···	···	3
GM Aur	97	12	-8.18/-8.02	7	0.057	6	54	47	4
GQ Lup	31–39	32	-8.00/-7.00	48	···	···	51	48	1
GW Lup	90–98	32	···	···	···	···	···	···	2
Haro 1-16	59–76	32	···	···	···	···	···	···	1
Haro 1-17	15	32	···	···	···	···	···	···	2
Haro 1-1	···	···	···	···	···	···	···	···	2
Haro 1-4	···	···	···	···	···	···	···	···	2
Haro 6-13	34–88	26	-7.54/-7.54	26	0.01	6	···	···	1
HD 101412	14–20	32	···	···	···	···	···	···	2
HD 135344	17	32	-8.30/-8.30	24	···	···	46	18	2
HD 98922	27	32	-5.76/-5.76	24	···	···	···	···	2
HK Tau	29–54	26	-7.65/-7.65	26	0.004	6	84	52	1
HN Tau	138–163	26	-8.60/-8.60	56	0.0008	6	···	···	1
HQ Tau	···	···	···	···	0.0005	6	···	···	1
HT Lup	3–7	32	···	···	···	···	···	···	1
IM Lup	4–8	32	···	···	0.1	43	50	43	1
IQ Tau	8	12	-8.32/-7.55	26	0.02	6	79	33	1
LkCa 8	···	···	···	···	···	···	···	···	2
LkHa 270	92	22	···	···	···	···	···	···	2
LkHa 326	···	···	···	···	···	···	···	···	1
LkHa 330	11–20	22	-8.80/-8.80	22	···	···	40	14	1
LkHa 348	301–324	22	···	···	···	···	···	···	2
RNO 15	116	32	···	···	···	···	···	···	2
RNO 90	76	32	···	···	0.0047	8	···	···	1
RNO 91	···	···	···	···	0.01	5	···	···	1
ROXs 42C	···	···	···	···	<0.005	5	···	···	2
ROXs 43A	···	···	···	···	<0.005	5	···	···	2
RR Tau	21–50	32	-6.90/-6.90	24	···	···	···	···	2
RU Lup	136-216	32	-7.70/-7.70	28	···	···	···	···	1
RW Aur	52-122	22	-7.50/-6.50	56	0.004	56	···	···	3

Continued on Next Page. . .

Table 6.2 – Continued

Star	$EW_{H\alpha}$	ref	$\log \dot{M}$	ref	M_d	ref	i_d	ref	ID
RY Lup	7	32	...	...	...	...	...	...	2
SR 9	6–14	32	-8.26/-8.26	41	0.0019	8	...	...	2
St 34	78	31	-9.6/-9.6	57	<0.0005	6	...	...	4
SU Aur	2– 6	26	-8.30/-8.20	26	<0.0009	6	52	1	1
SX Cha	26	21	...	...	...	...	...	...	1
SY Cha	24–64	21	...	...	...	...	...	...	1
Sz 18	...	...	...	...	...	...	...	...	4
Sz 50	46	32	-10.30/-10.30	51	...	...	...	...	1
T Cha	2–10	32	...	...	...	...	...	...	2
TW Cha	26	21	...	...	...	...	...	...	1
TW Hya	194–220	10	-8.80/-8.80	28	...	...	7	45	2,4
UX Tau A	4	12	-9.00/-9.00	39	0.005	6	...	...	4
UY Aur	...	...	...	...	...	...	...	...	3
V1331 Cyg	41–59	22	...	...	0.5	40	...	...	3
V710 Tau	34–89	26	...	...	0.007	6	...	...	2
V853 Oph	41	49	-8.31/-8.31	41	...	...	...	...	2
VV Ser	22–90	22	-6.34/-6.34	24	...	...	81	19	2
VW Cha	60–147	21	...	...	...	...	...	...	1
VZ Cha	58–71	21	...	...	...	...	...	...	1
Wa Oph 6	35	49	-6.64/-6.64	7	0.081	8	41	7	1
WX Cha	65	21	...	...	...	...	...	...	1
XX Cha	133	21	...	...	...	...	...	...	1

References — (1) Akeson et al. 2005a (2) Akeson et al. 2005b (3) Alcala et al. 1995 (4) Alcala et al. 2000 (5) Andre et al. 1994 (6) Andrews & Williams 2005 (7) Andrews & Williams 2007a (8) Andrews & Williams 2007b (9) Andrews & Williams 2008 (10) Bary et al. 2003 (11) Barsony et al. 2005 (12) Beckwith et al. 1990 (13) Bontemps et al. 2001 (14) Brown et al. 2008 (15) Casanova et al. 1995 (16) Colavita et al. 2003 (17) D'Alessio et al. 2005 (18) Doucet et al. 2006 (19) Eisner et al. 2003 (20) Espaillat et al. 2007 (21) Feigelson et al. 1993 (22) Fernandez et al. 1995 (23) Furlan et al. 2006 (24) Garcia Lopez et al. 2006 (25) Greene & Meyer 1995 (26) Gudel et al. 2007a (27) Gudel et al. 2007b (28) Herczeg et al. 2008 (29) Hiramatsu et al. 2007 (30) Hughes et al. 1994 (31) Kenyon & Hartmann 1995 (32) Kessler-Silacci et al. 2006 (33) Kitamura et al. 2002 (34) Koerner & Sargent 1995 (35) Kudo et al. 2008 (36) Lahuis et al. 2007 (37) Luhman et al. 2004 (38) Luhman et al. 2007 (39) Najita et al. 2007 (40) Najita et al. 2009 (41) Natta et al. 2006 (42) Neuhauser et al. 1995 (43) Pinte et al. 2008 (44) Prato et al. 2003 (45) Qi et al. 2004 (46) Robrade et al. 2007 (47) Schneider et al. 2003 (48) Seperuelo Duarte et al. 2008 (49) Shevchenko et al. 1998 (50) Simon et al. 2001 (51) Spezzi et al. 2008 (52) Stapelfeldt et al. 1998 (53) Stelzer et al. 2004 (54) Thi et al. 2002 (55) Valenti et al. 2003 (56) Watson et al. 2009 (57) White et al. 2005

* Program ID: 1=Program 50641, 2=c2d, 3=Program 20363, 4=Program 30300

Table 6.3. Detection Statistics

	All [a]	No trans [b]	Trans [c]	P-value [d]
H I	0.53	0.51	0.67	0.19
H_2O	0.35	0.40	0.00	0.02
OH	0.49	0.55	0.00	0.00
HCN	0.46	0.51	0.00	0.00
C_2H_2	0.43	0.49	0.00	0.01
CO_2	0.47	0.53	0.00	0.00
[Ne II]	0.41	0.38	0.67	0.08
[Ar III]	0.46	0.54	0.00	0.00
H_2	0.30	0.33	0.11	0.15
Error	0.06	0.06	0.17	

[a] Fraction of disks with molecular/atomic detection (if wavelength region was observed)

[b] Fraction of non-transitional disks with molecular/atomic detection

[c] Fraction of transitional disks with molecular/atomic detection

[d] Probability of randomly sampling 8 disks with detection fraction given in column 4, assuming the population has the detection fraction given in column 2

[e] Error here and elsewhere assumes $\sigma = 1/(2\sqrt{N})$ where N is the number of objects observed in the sample.

Note. — Transitional disk subsample taken to be: CoKu Tau/4, CS Cha, DM Tau, GM Aur, HD 135344, LkHα 330, T Cha and UX Tau A.

Table 6.4. Parameter–Detection Statistics Correlations

	Hα	L$_X$	$\dot{M}$	$M_\star$	M_d	i	$L_\star$	H I	H_2O	OH	HCN	C_2H_2	CO_2	[Ne II]	[Ar III]	H_2
H I	**0.02**	0.34	0.06	0.03	0.39	-0.40	0.19	···	0.24	0.14	0.14	0.28	0.21	0.51	0.97	0.44
H_2O	0.15	-0.58	0.22	-0.16	-0.23	0.51	-0.18	0.23	···	**0.00**	**0.00**	**0.00**	**0.00**	0.71	**0.00**	**0.02**
OH	0.07	-0.57	0.23	-0.06	0.48	0.53	-0.08	0.15	**0.00**	···	**0.00**	**0.00**	**0.00**	0.61	**0.00**	**0.03**
HCN	0.13	-0.42	0.69	-0.07	-0.32	0.38	-0.11	0.14	**0.00**	**0.00**	···	**0.00**	**0.00**	0.97	**0.00**	**0.01**
C_2H_2	0.44	-0.27	0.06	**-0.02**	-0.57	0.57	-0.11	0.28	**0.00**	**0.00**	**0.00**	···	**0.00**	0.74	**0.00**	**0.02**
CO_2	0.08	-0.61	0.53	-0.09	-0.28	0.17	-0.13	0.21	**0.00**	**0.00**	**0.00**	**0.00**	···	0.26	**0.01**	0.15
[Ne II]	0.31	0.87	-0.48	-0.42	0.91	0.58	-0.23	0.51	-0.71	0.62	-0.97	0.74	0.26	···	0.17	0.43
[Ar III]	0.72	-0.94	0.63	-0.30	-0.40	0.27	-0.26	0.94	**0.00**	**0.00**	**0.00**	**0.00**	**0.00**	-0.18	···	**0.01**
H_2	0.62	-0.69	0.86	-0.21	0.20	0.58	-0.29	0.41	**0.01**	**0.02**	**0.01**	**0.01**	0.12	0.38	**0.00**	···

Note. — The absolute values of the numbers at upper right are the p-value associated with the slope of a linear regression of the two parameters. (There is a probability p of getting a slope at least that extreme by chance alone.) The sign gives the sense of the correlation (positive or negative). Lower-left quadrant shows the p-value associated with a chi-squared value for the two parameters (see text for details). p-values are bolded if ≤ 0.02.

Table 6.5: Colors

Star	n_{6-13}	n_{6-30}	n_{13-30}	Ref
AA Tau	-0.87	-0.73	-0.25	2, 4
AS 205 A	-0.37	-0.36	-0.35	1
AS 353 A	···	···	-0.65	1
BF Ori	-0.60	···	···	1
BP Tau	-0.67	-0.65	-0.34	2, 4
CHXR 30	···	···	-0.25	2, 4
CI Tau	-0.95	-0.56	-0.16	2, 4
CoKu Tau/4	-0.60	0.81	2.54	2, 4
CS Cha	···	···	2.95	1
CW Tau	-1.26	-0.77	-0.66	2, 4
CY Tau	-1.45	-1.20	-1.16	2, 4
DE Tau	-0.87	-0.49	0.01	2, 4
DG Tau	-0.20	-0.03	0.38	2, 4
DK Tau	-1.00	-0.80	-0.59	3
DL Cha	···	···	···	1
DL Tau	-0.78	-0.73	-0.68	2, 4
DM Tau	-0.11	0.60	1.40	2, 4
Do Ar 24E	2.26	0.89	-0.50	1
Do Ar 25	-1.45	···	···	1
DO Tau	-0.56	-0.33	-0.18	2, 4
DP Tau	-0.43	-0.41	-0.27	2, 4
DR Tau	-0.88	-0.63	-0.37	2, 4
EC 82	-0.26	0.11	0.49	1
EX Lup	2.13	0.69	-0.75	1
FN Tau	-0.29	-0.17	-0.01	2, 4
FT Tau	-0.62	-0.50	-0.32	2, 4
FX Tau	-1.05	-0.75	···	2, 4
FZ Tau	-1.14	···	-0.89	2
GI Tau	-0.55	-0.60	-0.70	2, 4
GK Tau	-0.45	-0.44	-0.28	2, 4
GM Aur	-0.91	0.48	1.95	2, 4
GQ Lup	-1.32	-0.74	-0.15	1
GW Lup	-0.56	···	···	1
Haro 1-16	-0.89	-0.02	0.85	1
Haro 1-17	-0.68	···	···	1
Haro 1-1	1.33	1.09	0.84	1
Haro 1-4	···	···	···	1
Haro 6-13	-0.56	0.08	0.55	2, 4
HD 101412	-0.67	···	···	1
HD 135344	···	···	1.67	1
HD 98922	···	···	-1.30	1
HK Tau	-0.72	0.06	1.03	2, 4
HN Tau	-0.70	-0.59	-0.58	2, 4
HQ Tau	-0.76	-0.66	-0.45	2, 4
HT Lup	0.10	-0.18	-0.47	1
IM Lup	-0.30	-0.29	-0.28	1
IQ Tau	-1.30	···	-0.59	2
LkCa 8	···	···	···	1
LkHa 270	-0.94	···	···	1
LkHa 326	-0.74	-0.29	0.17	1
LkHa 330	-1.51	0.21	1.96	1
LkHa 348	-1.13	-1.59	-2.05	1
RNO 15	-0.17	···	···	1
RNO 90	-0.88	-0.66	-0.44	1
RNO 91	···	0.13	···	1
ROXs 42C	-0.94	···	···	1
ROXs 43A	···	···	···	1
RR Tau	-0.84	···	···	1
RU Lup	0.74	0.09	-0.56	1
RW Aur	-0.67	-0.60	-0.47	2, 4
RY Lup	-1.04	···	···	1

Continued on Next Page...

Star	n_{6-13}	n_{6-30}	n_{13-30}	Ref
SR 9	-0.94	···	···	1
St 34	···	···	-0.52	1
SU Aur	-0.32	···	0.86	2
SX Cha	···	···	-0.47	2
SY Cha	···	···	-0.15	2
Sz 18	···	···	2.88	2
Sz 50	-0.49	-0.26	-0.03	1
T Cha	···	···	1.60	1
TW Cha	···	···	-0.10	1
TW Hya	0.37	0.54	0.72	3
UX Tau A	-1.99	-0.07	1.83	2, 4
UY Aur	···	···	-0.19	2, 4
V1331 Cyg	···	···	0.34	2, 4
V710 Tau	-1.07	-0.88	···	2, 4
V853 Oph	-1.41	···	···	1
VV Ser	-1.04	···	···	1
VW Cha	···	···	-0.11	1
VZ Cha	···	···	-1.05	1
Wa Oph 6	-1.00	-0.69	-0.38	1
WX Cha	···	···	-0.99	1
XX Cha	···	···	-0.25	1

References: (1) Evans et al. 2003 (2) Furlan et al. 2006 (3) Hartmann et al. 2005 (4) Watson et al. 2009

Table 6.6. Settling–Detection Statistics

	Region 1[a]	Region 2 [b]
H I	0.79	0.43
H_2O	0.79	0.19
OH	0.83	0.38
HCN	0.79	0.29
C_2H_2	0.71	0.14
CO_2	0.67	0.38
[Ne II]	0.42	0.52
[Ar III]	0.58	0.33
H_2	0.38	0.24
Error	0.20	0.22

[a] Detection fraction for Region 1 sources, with $n_{6-13} < -0.5$ and $n_{13-30} < 1$. Also see Figure 6.6.

[b] Detection fraction for Region 2 sources, with h $n_{6-13} > -0.5$ or $n_{13-30} > 1$

Table 6.7: Equivalent Widths

Star	H I (12.37)	H_2O (16.1)	H_2O (33)	OH (27.6)	HCN	C_2H_2	CO_2	[Ne II]	[Ar III]	H_2 (12.279)
AA Tau	21 ± 3	33 ± 3	168 ± 16	24 ± 17	82 ± 3	18 ± 2	35 ± 3	33 ± 3	16 ± 2	24 ± 3
AS 205 A	0 ± 0	8 ± 1	70 ± 7	2 ± 8	17 ± 2	6 ± 1	20 ± 1	0 ± 0	6 ± 1	0 ± 0
AS 353 A	20 ± 1	0 ± 0	0 ± 0	37 ± 10	0 ± 0	0 ± 0	15 ± 1	12 ± 1	0 ± 0	15 ± 1
BF Ori	27 ± 3	0 ± 0	⋯	⋯	0 ± 0	0 ± 0	0 ± 0	19 ± 3	⋯	0 ± 0
BP Tau	25 ± 3	30 ± 2	213 ± 15	26 ± 14	78 ± 3	10 ± 2	0 ± 0	0 ± 0	19 ± 1	8 ± 2
CHXR 30	0 ± 0	0 ± 0	0 ± 0	0 ± 0	0 ± 0	0 ± 0	0 ± 0	0 ± 0	0 ± 0	0 ± 0
CI Tau	24 ± 3	24 ± 2	102 ± 12	29 ± 13	32 ± 3	11 ± 2	17 ± 2	14 ± 2	0 ± 0	10 ± 2
CoKu Tau/4	0 ± 0	0 ± 0	0 ± 0	0 ± 0	0 ± 0	0 ± 0	0 ± 0	0 ± 0	0 ± 0	0 ± 0
CS Cha	116 ± 9	0 ± 0	0 ± 0	0 ± 0	0 ± 0	0 ± 0	0 ± 0	427 ± 7	0 ± 0	0 ± 0
CW Tau	28 ± 3	36 ± 2	197 ± 16	43 ± 17	24 ± 3	0 ± 0	25 ± 2	0 ± 0	17 ± 1	0 ± 0
CY Tau	19 ± 4	24 ± 4	107 ± 31	0 ± 0	34 ± 4	30 ± 2	21 ± 4	0 ± 0	0 ± 0	0 ± 0
DE Tau	0 ± 0	23 ± 2	24 ± 6	24 ± 7	14 ± 2	6 ± 1	9 ± 2	0 ± 0	0 ± 0	0 ± 0
DG Tau	0 ± 0	0 ± 0	0 ± 0	33 ± 7	0 ± 0	0 ± 0	0 ± 0	35 ± 1	0 ± 0	0 ± 0
DK Tau	32 ± 4	52 ± 3	279 ± 25	70 ± 24	41 ± 4	8 ± 2	13 ± 3	0 ± 0	15 ± 2	10 ± 3
DL Cha	0 ± 0	0 ± 0	⋯	⋯	0 ± 0	0 ± 0	44 ± 1	0 ± 0	⋯	0 ± 0
DL Tau	30 ± 2	0 ± 0	0 ± 0	24 ± 8	0 ± 0	23 ± 1	13 ± 2	17 ± 2	9 ± 1	0 ± 0
DM Tau	0 ± 0	0 ± 0	0 ± 0	0 ± 0	0 ± 0	0 ± 0	0 ± 0	100 ± 5	0 ± 0	61 ± 6
Do Ar 24E	0 ± 0	25 ± 2	96 ± 12	27 ± 13	37 ± 2	16 ± 1	15 ± 2	0 ± 0	7 ± 1	0 ± 0
Do Ar 25	0 ± 0	0 ± 0	⋯	⋯	89 ± 3	21 ± 2	0 ± 0	0 ± 0	⋯	141 ± 2
DO Tau	25 ± 2	0 ± 0	0 ± 0	37 ± 11	0 ± 0	0 ± 0	0 ± 0	0 ± 0	0 ± 0	0 ± 0
DP Tau	19 ± 3	24 ± 2	138 ± 16	32 ± 15	20 ± 3	2 ± 2	12 ± 2	18 ± 2	11 ± 1	19 ± 2
DR Tau	23 ± 2	20 ± 2	91 ± 8	12 ± 9	32 ± 2	6 ± 1	15 ± 2	0 ± 0	19 ± 1	0 ± 0
EC 82	0 ± 0	0 ± 0	0 ± 0	0 ± 0	0 ± 0	0 ± 0	0 ± 0	18 ± 2	0 ± 0	21 ± 2
EX Lup	22 ± 2	0 ± 0	0 ± 0	30 ± 10	0 ± 0	0 ± 0	0 ± 0	0 ± 0	11 ± 1	0 ± 0
FN Tau	0 ± 0	0 ± 0	0 ± 0	0 ± 0	0 ± 0	0 ± 0	0 ± 0	0 ± 0	0 ± 0	0 ± 0
FT Tau	26 ± 3	25 ± 3	121 ± 14	23 ± 15	39 ± 3	13 ± 2	27 ± 2	25 ± 2	13 ± 1	25 ± 3
FX Tau	0 ± 0	0 ± 0	⋯	⋯	0 ± 0	0 ± 0	0 ± 0	0 ± 0	⋯	0 ± 0
FZ Tau	27 ± 3	37 ± 3	221 ± 25	33 ± 26	26 ± 3	7 ± 2	44 ± 3	0 ± 0	34 ± 2	8 ± 2
GI Tau	0 ± 0	24 ± 2	182 ± 18	36 ± 17	38 ± 3	8 ± 2	0 ± 0	14 ± 2	15 ± 1	17 ± 2
GK Tau	0 ± 0	32 ± 3	121 ± 11	37 ± 9	0 ± 0	0 ± 0	0 ± 0	0 ± 0	9 ± 1	0 ± 0
GM Aur	142 ± 9	0 ± 0	0 ± 0	0 ± 0	0 ± 0	0 ± 0	0 ± 0	88 ± 7	0 ± 0	0 ± 0
GQ Lup	31 ± 3	28 ± 3	154 ± 11	25 ± 11	53 ± 3	9 ± 2	17 ± 3	0 ± 0	14 ± 1	0 ± 0
GW Lup	0 ± 0	0 ± 0	⋯	⋯	0 ± 0	29 ± 2	76 ± 3	0 ± 0	⋯	0 ± 0
Haro 1-16	35 ± 5	29 ± 3	70 ± 9	22 ± 9	26 ± 5	0 ± 0	0 ± 0	0 ± 0	0 ± 0	0 ± 0
Haro 1-17	0 ± 0	0 ± 0	⋯	⋯	0 ± 0	0 ± 0	0 ± 0	0 ± 0	⋯	51 ± 5
Haro 1-1	43 ± 4	0 ± 0	0 ± 0	0 ± 0	48 ± 4	0 ± 0	0 ± 0	0 ± 0	14 ± 1	11 ± 4
Haro 1-4	32 ± 3	0 ± 0	⋯	⋯	38 ± 3	20 ± 2	30 ± 2	13 ± 2	⋯	0 ± 0
Haro 6-13	17 ± 2	0 ± 0	0 ± 0	0 ± 0	0 ± 0	6 ± 1	26 ± 1	13 ± 1	0 ± 0	0 ± 0
HD 101412	9 ± 2	0 ± 0	⋯	⋯	0 ± 0	6 ± 1	23 ± 1	0 ± 0	⋯	0 ± 0
HD 135344	28 ± 1	0 ± 0	0 ± 0	0 ± 0	0 ± 0	0 ± 0	0 ± 0	0 ± 0	0 ± 0	0 ± 0
HD 98922	9 ± 1	0 ± 0	0 ± 0	0 ± 0	0 ± 0	0 ± 0	0 ± 0	0 ± 0	0 ± 0	0 ± 0
HK Tau	0 ± 0	0 ± 0	0 ± 0	0 ± 0	0 ± 0	0 ± 0	24 ± 2	20 ± 2	0 ± 0	13 ± 2
HN Tau	10 ± 2	26 ± 2	57 ± 6	7 ± 7	11 ± 2	0 ± 0	8 ± 2	16 ± 2	0 ± 0	0 ± 0
HQ Tau	0 ± 0	0 ± 0	0 ± 0	0 ± 0	0 ± 0	0 ± 0	0 ± 0	0 ± 0	0 ± 0	0 ± 0
HT Lup	0 ± 0	0 ± 0	0 ± 0	0 ± 0	0 ± 0	0 ± 0	24 ± 1	0 ± 0	0 ± 0	0 ± 0
IM Lup	0 ± 0	0 ± 0	0 ± 0	0 ± 0	0 ± 0	0 ± 0	26 ± 2	20 ± 2	0 ± 0	0 ± 0
IQ Tau	0 ± 0	18 ± 3	132 ± 12	4 ± 12	63 ± 4	16 ± 2	0 ± 0	27 ± 3	14 ± 1	0 ± 0
LkCa 8	69 ± 6	0 ± 0	⋯	⋯	0 ± 0	0 ± 0	0 ± 0	55 ± 5	⋯	0 ± 0
LkHa 270	0 ± 0	0 ± 0	⋯	⋯	0 ± 0	0 ± 0	42 ± 2	40 ± 2	⋯	27 ± 3
LkHa 326	0 ± 0	21 ± 2	36 ± 8	18 ± 9	12 ± 2	0 ± 0	23 ± 2	14 ± 2	6 ± 1	0 ± 0
LkHa 330	18 ± 2	0 ± 0	0 ± 0	0 ± 0	0 ± 0	0 ± 0	0 ± 0	0 ± 0	0 ± 0	0 ± 0
LkHa 348	27 ± 2	0 ± 0	0 ± 0	0 ± 0	0 ± 0	0 ± 0	0 ± 0	0 ± 0	0 ± 0	0 ± 0
RNO 15	0 ± 0	0 ± 0	⋯	⋯	0 ± 0	9 ± 1	0 ± 0	10 ± 1	⋯	0 ± 0
RNO 90	30 ± 3	18 ± 2	249 ± 17	26 ± 17	78 ± 3	14 ± 2	22 ± 2	0 ± 0	20 ± 1	13 ± 2
RNO 91	⋯	⋯	0 ± 0	22 ± 6	⋯	⋯	⋯	⋯	0 ± 0	⋯
ROXs 42C	0 ± 0	0 ± 0	⋯	⋯	0 ± 0	0 ± 0	0 ± 0	0 ± 0	⋯	0 ± 0
ROXs 43A	0 ± 0	0 ± 0	⋯	⋯	0 ± 0	0 ± 0	0 ± 0	0 ± 0	⋯	0 ± 0
RR Tau	4 ± 2	0 ± 0	⋯	⋯	0 ± 0	0 ± 0	0 ± 0	0 ± 0	⋯	0 ± 0
RU Lup	26 ± 2	0 ± 0	0 ± 0	16 ± 5	22 ± 2	0 ± 0	17 ± 2	14 ± 2	0 ± 0	0 ± 0
RW Aur	36 ± 3	32 ± 3	147 ± 15	28 ± 15	39 ± 3	14 ± 2	35 ± 3	0 ± 0	18 ± 1	22 ± 3

Continued on Next Page . . .

Star	H I (12.37)	H_2O (16.1)	H_2O (33)	OH (27.6)	HCN	C_2H_2	CO_2	[Ne II]	[Ar III]	H_2 (12.279)
RY Lup	0 ± 0	0 ± 0	···	···	0 ± 0	0 ± 0	0 ± 0	0 ± 0	···	0 ± 0
SR 9	0 ± 0	0 ± 0	···	···	0 ± 0	0 ± 0	0 ± 0	0 ± 0	···	28 ± 4
St 34	0 ± 0	0 ± 0	0 ± 0	0 ± 0	0 ± 0	0 ± 0	0 ± 0	0 ± 0	0 ± 0	0 ± 0
SU Aur	17 ± 2	0 ± 0	0 ± 0	0 ± 0	0 ± 0	0 ± 0	0 ± 0	12 ± 2	0 ± 0	0 ± 0
SX Cha	0 ± 0	19 ± 2	148 ± 16	21 ± 16	13 ± 2	−0 ± 1	0 ± 0	0 ± 0	11 ± 1	0 ± 0
SY Cha	0 ± 0	0 ± 0	0 ± 0	23 ± 14	30 ± 2	12 ± 1	29 ± 2	20 ± 2	10 ± 1	0 ± 0
Sz 18	0 ± 0	0 ± 0	0 ± 0	0 ± 0	0 ± 0	0 ± 0	0 ± 0	0 ± 0	0 ± 0	0 ± 0
Sz 50	0 ± 0	0 ± 0	0 ± 0	21 ± 8	32 ± 3	0 ± 0	43 ± 2	0 ± 0	7 ± 1	0 ± 0
T Cha	0 ± 0	0 ± 0	0 ± 0	0 ± 0	0 ± 0	0 ± 0	0 ± 0	24 ± 2	0 ± 0	0 ± 0
TW Cha	0 ± 0	41 ± 3	380 ± 30	36 ± 29	82 ± 4	22 ± 3	0 ± 0	0 ± 0	33 ± 2	24 ± 3
TW Hya	76 ± 3	0 ± 0	0 ± 0	0 ± 0	0 ± 0	0 ± 0	0 ± 0	48 ± 3	0 ± 0	0 ± 0
UX Tau A	92 ± 7	0 ± 0	0 ± 0	0 ± 0	0 ± 0	0 ± 0	0 ± 0	37 ± 5	0 ± 0	0 ± 0
UY Aur	19 ± 2	0 ± 0	0 ± 0	19 ± 11	29 ± 2	8 ± 1	28 ± 1	0 ± 0	9 ± 1	22 ± 2
V1331 Cyg	22 ± 2	0 ± 0	0 ± 0	29 ± 9	0 ± 0	0 ± 0	0 ± 0	0 ± 0	0 ± 0	14 ± 2
V710 Tau	90 ± 5	0 ± 0	···	···	95 ± 6	42 ± 3	59 ± 5	0 ± 0	···	0 ± 0
V853 Oph	0 ± 0	0 ± 0	···	···	29 ± 2	20 ± 1	21 ± 2	25 ± 2	···	0 ± 0
VV Ser	31 ± 2	0 ± 0	···	···	0 ± 0	0 ± 0	0 ± 0	0 ± 0	···	0 ± 0
VW Cha	51 ± 3	32 ± 2	163 ± 15	61 ± 16	34 ± 3	9 ± 2	22 ± 3	30 ± 3	12 ± 1	8 ± 3
VZ Cha	0 ± 0	40 ± 4	253 ± 30	40 ± 29	41 ± 4	15 ± 2	10 ± 4	0 ± 0	26 ± 2	0 ± 0
Wa Oph 6	5 ± 2	18 ± 2	63 ± 11	20 ± 12	14 ± 2	2 ± 1	17 ± 2	12 ± 2	0 ± 0	0 ± 0
WX Cha	43 ± 4	34 ± 4	457 ± 41	56 ± 38	67 ± 4	16 ± 2	27 ± 4	0 ± 0	27 ± 3	18 ± 3
XX Cha	0 ± 0	31 ± 3	145 ± 11	19 ± 12	43 ± 3	24 ± 2	41 ± 3	28 ± 3	19 ± 1	22 ± 3

Table 6.8. Parameter–Equivalent Width Correlations

	Hα	L$_X$ [a]	log $\dot{M}$[b]	$M_\star$	M_d	i	$L_\star$	H I[c]	H$_2$O [d]	H$_2$O [e]	OH	HCN[f]	C$_2$H$_2$ [f]	CO$_2$[g]	[Ne II][h]	[Ar III]	H$_2$ [i]
Hα	···	···	···	···	···	···	···	0.03	-0.01	-0.15	-0.14	-0.39	-0.01	0.19	0.29	0.23	0.01
L$_X$	···	···	···	···	···	···	···	0.27	0.47	0.43	0.25	0.05	-0.02	0.44	0.13	-0.04	-0.04
log $\dot{M}$	···	···	···	···	···	···	···	-0.34	-0.36	-0.19	-0.18	-0.21	**-0.58**	-0.03	-0.45	-0.01	**-0.69**
$M_\star$	···	···	···	···	···	···	···	-0.16	-0.02	0.21	-0.08	-0.10	-0.18	0.18	-0.17	0.05	0.05
M_d	···	···	···	···	···	···	···	-0.06	-0.39	-0.31	-0.02	0.29	0.22	0.04	-0.15	-0.40	-0.11
i	···	···	···	···	···	···	···	-0.13	-0.05	-0.15	-0.31	0.20	0.09	0.45	-0.26	0.17	-0.20
$L_\star$	···	···	···	···	···	···	···	-0.13	-0.40	-0.22	-0.12	-0.13	-0.39	-0.02	-0.20	-0.27	-0.31
H I	0.85	0.38	-0.08	-0.46	-0.82	-0.62	-0.54	···	0.46	0.51	0.37	0.35	0.38	0.33	**0.92**	0.13	-0.27
H$_2$O	-0.97	0.06	-0.12	-0.94	-0.11	-0.90	-0.05	0.07	···	**0.61**	**0.76**	0.32	0.22	0.19	0.66	**0.53**	-0.09
H$_2$O	-0.45	0.09	-0.44	0.35	-0.22	-0.67	-0.29	0.04	**0.00**	···	**0.63**	**0.66**	0.28	0.26	0.61	**0.76**	0.01
OH	-0.41	0.32	-0.42	-0.69	-0.94	-0.33	-0.54	0.09	**0.00**	**0.00**	···	0.23	-0.01	-0.05	0.17	0.32	-0.45
HCN	-0.03	0.83	-0.39	-0.62	0.23	0.55	-0.51	0.13	0.10	**0.00**	0.20	···	**0.48**	0.29	**0.71**	**0.49**	0.15
C$_2$H$_2$	-0.94	-0.95	**-0.01**	-0.39	0.39	0.78	-0.05	0.12	0.31	0.20	-0.98	**0.01**	···	0.33	0.45	0.22	0.50
CO$_2$	0.32	0.10	-0.91	0.40	0.86	0.20	-0.94	0.15	0.40	0.24	-0.81	0.13	0.10	···	**0.68**	0.20	0.42
[Ne II]	0.12	0.68	-0.06	-0.46	-0.61	-0.40	-0.37	**0.00**	0.03	0.05	0.52	**0.00**	0.10	**0.00**	···	0.62	**0.92**
[Ar III]	0.28	-0.88	-0.96	0.84	-0.16	0.69	-0.21	0.65	**0.01**	**0.00**	0.10	**0.01**	0.32	0.40	0.06	···	-0.08
H$_2$	0.95	-0.90	**-0.02**	0.88	-0.73	-0.71	-0.24	-0.36	-0.75	0.98	-0.07	0.59	0.06	0.11	**0.00**	-0.78	···

Note. — Upper-right quadrant shows the correlation coefficient, R, between the two parameters. Lower-left quadrant shows the p-value, p, associated with the slope of a linear regression of the two parameters. Both R and p are bolded if $p \leq 0.02$.

[a] Outliers VW Cha and SU Aur excluded

[b] Outlier Sz 50 excluded

[c] Outliers VW Cha, WX Cha and V710 Tau excluded

[d] 16.1 μm

[e] 33 μm

[f] Outlier V710 Tau excluded

[g] Outliers V710 Tau and GW Lup excluded

[h] Outlier CS Cha excluded

[i] Outlier DoAr 25 excluded

Table 6.9. Color–Equivalent Width Relationships

	H I	H_2O	H_2O	OH	HCN	C_2H_2	CO_2	[Ne II]	[Ar III]	H_2
n_{6-13}	-0.56	-0.32	-0.42	-0.50	-0.13	-0.06	-0.86	0.98	-0.03	-0.25
n_{13-30}	**0.00**	-0.40	-0.03	-0.25	-0.74	-0.04	0.58	**0.00**	-0.05	0.03
n_{6-30}	0.04	**-0.02**	**-0.00**	-0.20	**-0.01**	-0.04	-0.65	**0.00**	**-0.00**	**0.01**

Note. — Absolute values shown are p-value associated with the slope of a linear regression of the two parameters. Signs show whether the correlation is positive or negative.

Table 6.10. Model Fit Parameters

Source	T [K]	Area [AU^2]	N$_{H_2O}$ [cm^{-2}]	N$_{CO_2}$ [cm^{-2}]	N$_{HCN}$ [cm^{-2}]	$N_{C_2H_2}$ [cm^{-2}]	T [K]	Area [AU^2]	N$_{OH}$ [cm^{-2}]
AA Tau	400	1.76	4.E+18	8.E+15	2.E+16	2.E+15	1100	11.00	4.E+14
AS 205 A	600	3.14	6.E+19	2.E+16	4.E+16	8.E+15	1200	12.57	4.E+15
AS 353 A	···	···	···	2.E+16	···	···	800	0.63	1.E+19
BP Tau	500	5.03	1.E+18	···	1.E+16	1.E+15	1000	31.42	6.E+14
CI Tau	600	0.44	1.E+19	1.E+16	2.E+16	4.E+15	1100	11.00	6.E+14
CW Tau	500	3.50	4.E+18	8.E+15	8.E+15	···	1100	13.98	2.E+15
CY Tau	900	0.03	6.E+19	4.E+16	4.E+16	4.E+16	0	0.00	···
DE Tau	600	0.11	8.E+19	2.E+16	4.E+16	1.E+16	1200	11.00	2.E+14
DG Tau	···	···	···	···	···	···	1200	13.98	8.E+15
DK Tau	500	2.75	4.E+18	4.E+15	1.E+16	2.E+15	1000	11.00	2.E+15
DL Cha	···	···	···	1.E+21	···	···	···	···	···
DL Tau	···	···	···	···	···	2.E+16	600	0.44	4.E+20
Do Ar 24E	500	2.75	1.E+19	1.E+16	2.E+16	8.E+15	1200	11.00	2.E+15
Do Ar 25	···	···	···	···	2.E+16	4.E+15	···	···	···
DO Tau	···	···	···	···	···	···	800	1.26	1.E+19
DP Tau	400	1.76	4.E+19	6.E+15	8.E+15	1.E+15	1100	11.00	1.E+15
DR Tau	600	1.76	8.E+18	1.E+16	2.E+16	4.E+15	1200	11.00	1.E+15
EX Lup	···	···	···	···	···	···	800	1.13	2.E+19
FT Tau	300	1.13	4.E+20	1.E+16	2.E+16	2.E+15	1200	3.14	1.E+15
FZ Tau	500	1.76	2.E+19	1.E+16	8.E+15	2.E+15	800	11.00	2.E+15
GI Tau	400	2.75	6.E+18	···	1.E+16	2.E+15	1200	2.75	2.E+15
GK Tau	300	1.76	8.E+21	···	···	···	1200	11.00	8.E+14
GQ Lup	500	5.11	4.E+17	4.E+15	6.E+15	1.E+15	1200	5.11	2.E+15
GW Lup	···	···	···	1.E+16	···	4.E+15	···	···	···
Haro 1-16	300	2.75	1.E+21	···	1.E+16	···	1200	11.00	8.E+14
Haro 1-1	···	···	···	···	4.E+16	···	···	···	···
Haro 1-4	···	···	···	2.E+16	2.E+16	8.E+15	···	···	···
Haro 6-13	···	···	···	6.E+16	···	1.E+16	···	···	···
HD 101412	···	···	···	1.E+17	···	2.E+16	···	···	···
HK Tau	···	···	···	8.E+15	···	···	···	···	···
HN Tau	700	0.11	4.E+20	1.E+17	6.E+16	···	1100	11.00	6.E+14
HT Lup	···	···	···	2.E+17	···	···	···	···	···
IM Lup	···	···	···	2.E+16	···	···	···	···	···
IQ Tau	700	0.10	6.E+19	···	8.E+16	2.E+16	700	9.82	8.E+14
LkHa 270	···	···	···	2.E+16	···	···	···	···	···
LkHa 326	700	0.10	4.E+19	2.E+16	1.E+16	···	600	0.88	8.E+16
RNO 15	···	···	···	···	···	1.E+16	···	···	···
RNO 90	700	2.93	2.E+18	6.E+15	2.E+16	4.E+15	1100	11.70	4.E+15
RNO 91	···	···	···	···	···	···	900	1.13	4.E+20
RU Lup	···	···	···	6.E+17	2.E+18	···	900	0.59	4.E+19
RW Aur	500	10.60	1.E+19	2.E+16	2.E+16	4.E+15	1000	42.41	2.E+15
SX Cha	300	1.76	8.E+20	···	6.E+15	2.E+14	1200	11.00	4.E+14
SY Cha	···	···	···	6.E+15	8.E+15	2.E+15	700	0.11	4.E+19
Sz 50	···	···	···	1.E+16	1.E+16	···	700	0.11	4.E+19
TW Cha	500	1.02	1.E+18	···	6.E+15	1.E+15	1100	1.82	2.E+15
UY Aur	···	···	···	2.E+17	4.E+17	6.E+16	900	0.99	1.E+19
V1331 Cyg	···	···	···	···	···	···	800	0.44	2.E+19
V710 Tau	···	···	···	1.E+16	1.E+16	4.E+15	···	···	···
V853 Oph	···	···	···	1.E+16	2.E+16	6.E+15	700	0.20	6.E+20
VW Cha	500	4.91	2.E+18	6.E+15	8.E+15	2.E+15	900	19.63	4.E+15
VZ Cha	600	0.79	1.E+19	8.E+15	2.E+16	6.E+15	1200	19.63	4.E+14
Wa Oph 6	600	0.82	2.E+19	2.E+16	1.E+16	2.E+15	1100	20.42	8.E+14
WX Cha	500	1.77	4.E+18	6.E+15	1.E+16	2.E+15	1000	19.63	4.E+14
XX Cha	200	1.76	1.E+22	2.E+16	6.E+16	2.E+16	700	11.00	8.E+14

Chapter 7

Final Thoughts and Future Work

Molecular emission is a common, and nearly ubiquitous, feature of the spectra of circumstellar disks. We now know that, as expected, the planet-forming regions of circumstellar disks are gas-rich, with upper atmospheres sufficiently heated to produce infrared emission from a variety of molecules, including CO, H_2O, OH, HCN, C_2H_2, and CO_2. Transitional disks, in which the inner disks have been partially depleted of small dust grains, are also gas-rich, although they do not show evidence for molecules besides CO, and, perhaps, H_2, in the 4.5–30 μm range. Preliminary results show that the strength of emission lines in classical circumstellar disks depends on such factors as disk structure, dust settling, and spectral type. Disk structure and dust settling have an effect on the total column of gas visible to the observer, while all three can determine the type and strength of radiation to which the gas is exposed.

The results presented here have inspired many new projects, and several are already underway. L-band (3 μm) surveys for H_2O in disks are being pursued with NIRSPEC, on the Keck telescope, as well as with CRIRES—a high-resolution spectrograph on the Very Large Telescope. The advantage of these ground-based studies is that the lines are spectrally resolved, and so can better constrain the emitting location. The shorter wavelength spectra also complement the Spitzer-IRS results, as they probe vibrational transitions with higher excitation energies than the purely rotational lines observed with the IRS (for water and OH). In Figure 7.1, we plot H_2O and OH emission from a few circumstellar disks (as well as a photospheric template star) that have been observed with NIRSPEC. Note that line:continuum ratios are significantly higher for CO than for H_2O (and were adjusted to display on the same scale), but appear correlated for any given source. Additional emission lines are also being investigated, including HCN, which has been identified in one source thus far (Figure 7.2). If several molecules are detected, it may be possible to detect differences in line shapes due to the different locations of each molecule's condensation radius, and hence test various disk models (e.g., Dodson-Robinson et al., 2009). Very high spectral resolution data are required to be sensitive to Keplerian velocities at several AU, where the molecules condense, so such a project would best be pursued with instruments such as TEXES or CRIRES.

M-band veiling measurements of transitional disks have produced some curious results (see Figure 3.7) that are not yet understood—the continuum emission seems to be too high at 5 μm. Is this a statistical fluke, or is infrared continuum emission not well-fit by a single blackbody? And if not, what are the emission components? Does this discrepancy hold for classical disks, as well as transitional? This mystery will be pursued by measuring J, H and K-band veiling for a larger sample of transitional disks with TripleSpec on the Palomar 200" telescope, or SpeX on the IRTF, and combining these with veiling measurements derived from our M- and L-band surveys.

The Pfβ (4.6538 μm, n=7→5) hydrogen recombination line was serendipitously covered in our survey for CO rovibrational emission from circumstellar disks (see, for example, Figure 7.1). By relating the Pfβ line luminosity to accretion luminosity, accretion rates can be estimated for our entire sample of over 100 circumstellar disks. Because Pfβ is a high-energy transition, it is likely to be optically thin, and thus a good tracer of the total accretion column. Since the emission is at a significantly longer wavelength than some of the more commonly used tracers, it may provide accretion rates for disks obscured by a significant amount of extinction. Additionally, these data provide contemporaneous measures of CO emission and accretion rate, the latter of which is known to be highly variable in some disks. Preliminary results (shown in Figure 7.3) show that Pfβ luminosities are well-correlated with accretion luminosity, albeit with the ~ 1 order of magnitude scatter typical for these types of correlations (e.g., Herczeg and Hillenbrand, 2008).

The true nature of transitional disks is still not known, but several images (Hughes et al., 2007; Brown et al., 2008; Dutrey et al., 2008) have already confirmed that SED-based interpretations are correct—the inner disks really are depleted of small dust grains. Observations are now being pushed a step further with CARMA, which has implemented a new antenna 'buddy-system' that uses small antennas alongside the main array to correct for atmospheric phase fluctuations (Perez-Muñoz et al., in prep). This system allows CARMA to produce sharper images in its longest baseline configurations, and has already resulted in images of transitional disk clearings with sub-arcsecond resolution and much improved image fidelity.

One of the most exciting elements of this work is that the rich Spitzer-IRS high S/N dataset (discussed in Chapter 6) has only begun to be explored. Radiative transfer models are currently being created to model the disk emission in more detail than the slab models presented here (Meijerink et al., in prep). Preliminary results for H_2O suggest that creation of emission lines may depend crucially on having a gas kinetic temperature in excess of the local dust temperature. Also, non-LTE excitation is important, especially for the strongest emission lines, so these effects need to be included to properly compute gas column densities. An interesting dichotomy between transitional disks and classical disks was unearthed, but is still not understood. Why is CO prevalent in transitional disks, but not H_2O? An investigation into the effects of photodissociation on both molecules, in both kinds of disks, might provide the answer, as CO is expected to self-shield, while many other molecules do not. Evidence for CO self-shielding could lend support to its possible role in the creation of the varying oxygen isotope ratios found in solar-system materials. Finally, the IRS dataset can also be used to measure the ortho-para ratio of disk atmosperic water vapor. This ratio equilibrates to 3 at high temperatures, but would be lower than 3 if the observed vapor derived from sublimated icy grains or planetesimals.

In the coming years, the 3.5 meter Herschel space telescope promises to provide a new window into circumstellar disks and planet formation, and hopefully some exciting new results. Launched successfully on 14 May 2009, it consists of a high-resolution heterodyne spectrometer (HIFI), and two photometer/mid-resolution spectrometers (PACS and SPIRE). It will observe dust and gas from circumstellar disks at wavelengths from 55–672 μm over its 3.5 year lifetime—covering a region in-between the wavelengths covered by Spitzer and most ground-based instruments, both infrared observatories such as Keck or the VLT and (sub-)millimeter wavelength facilities such as SMA, CARMA, and IRAM. Most importantly, like Spitzer, Herschel is not subject to the absorption and blurring of light caused by the Earth's atmosphere.

On a longer timescale, the Stratospheric Observatory For Infrared Astronomy (SOFIA), the James Webb Space Telescope (JWST), the Atacama Large Millimeter Array (ALMA) and a new generation of 30-meter-class telescopes promise to create breakthroughs in the study of disks and planet formation. SOFIA, a 2.5 meter telescope set to begin science observations in Fall 2009, has a suite of infrared imagers and spectrometers covering the near- to far-infrared, and will reside above the bulk of the Earth's atmosphere. The instrument most relevant to the work presented here is EXES—the first high-resolution (up to R $\sim$ 100,000) infrared spectrometer to be situated above the Earth's atmosphere. JWST, a 6.5 meter space telescope scheduled for launch in 2013, includes a mid-infrared imager/spectrograph (MIRI). Covering 5–27μm, it will overlap with the wavelengths observed by Spitzer, but provide higher resolution (R $\sim$ 3000) and greater sensitivity.

ALMA, set to be fully constructed by 2012, is perhaps the most ambitious astronomical project in history—an array of 80 antennas located in the Atacama desert, created by an international collaboration between scientific partners in Asia, Europe, and North America. Its 80 antennas provide a large collecting area, and excellent uv-coverage, and the stable, dry Atacama air allows for baselines as large as 10 km. Thus, this array should produce phenomenal images of circumstellar disks, and, potentially, of actively forming young planets, with a continuum resolution down to $\sim$ 1 AU for nearby star-forming regions. Finally, 30-meter-class telescopes, such as the Thirty Meter Telescope (TMT) and the European Extremely Large Telescope (E-ELT), are planned for $\sim$ 2018. These facilities will offer unprecedented spatial resolution and collecting areas for infrared observations.

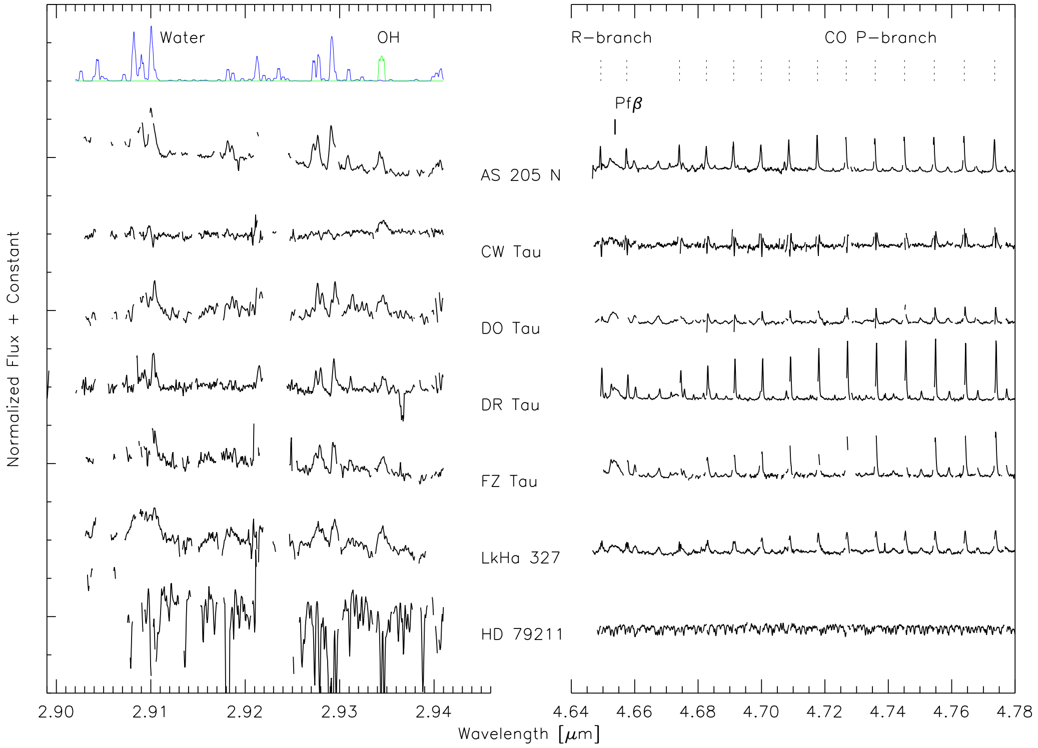

Figure 7.1: Spectra for a sample of circumstellar disks, and a photospheric standard star, in the L- and M-bands. Spectra have been normalized by the continuum, and multiplied by factors of 7 and 0.5 for the L- and M-bands, respectively. Above the spectra are plotted a water + OH emission model, and labels for the CO P- and R-branches.

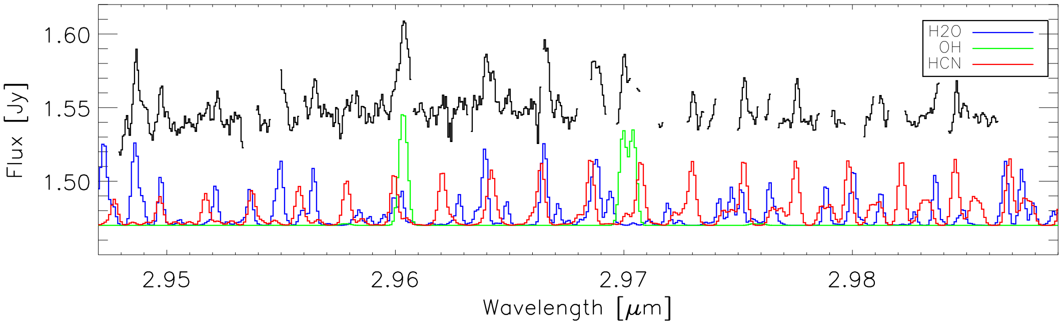

Figure 7.2: NIRSPEC spectrum of a circumstellar disk showing evidence for H_2O, OH, and HCN. Black lines show data, with emission models of H_2O, OH, and HCN shown below.

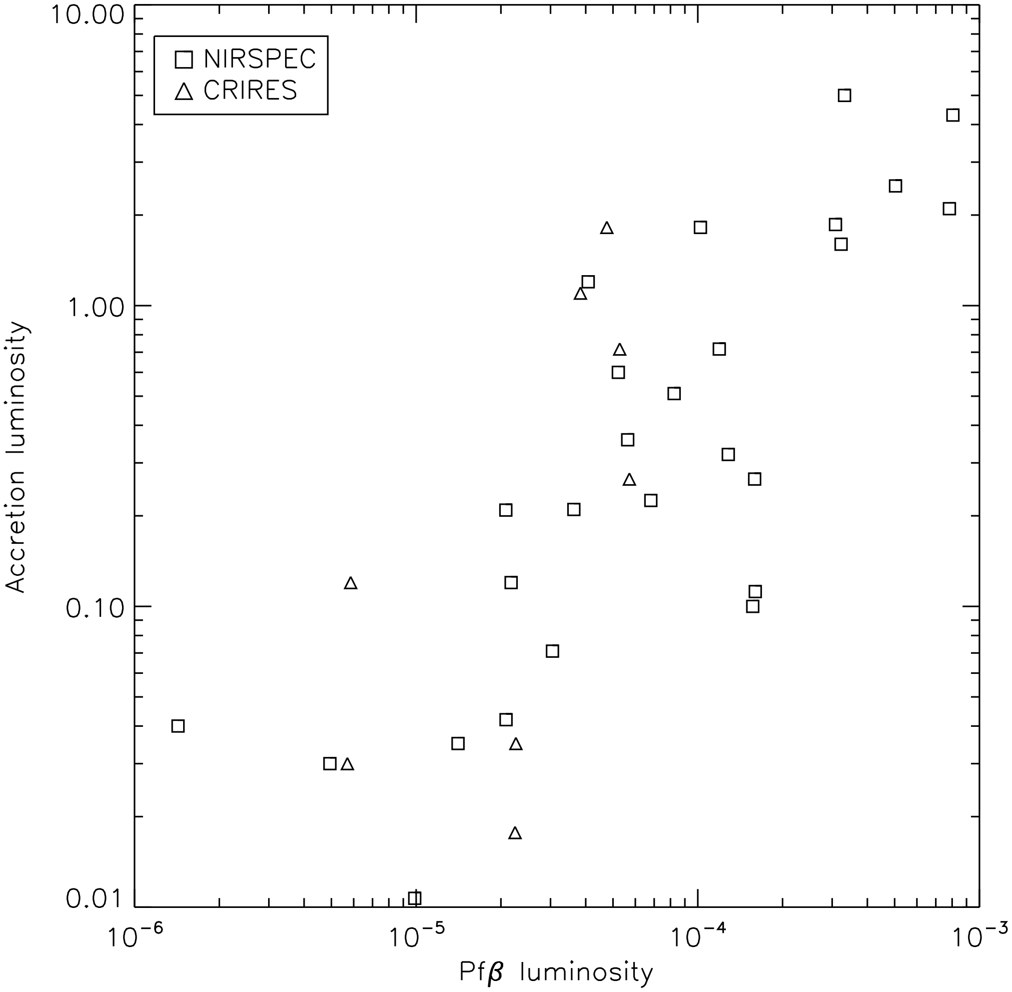

Figure 7.3: Accretion luminosity plotted against Pfβ line luminosity. Pfβ spectra were obtained with Keck-NIRSPEC and VLT-CRIRES.

Bibliography

B. Acke, M. E. van den Ancker, C. P. Dullemond, R. van Boekel, and L. B. F. M. Waters. Correlation between grain growth and disk geometry in Herbig Ae/Be systems. *Astronomy and Astrophysics*, 422:621–626, August 2004. doi: 10.1051/0004-6361:20040197.

B. Acke, M. E. van den Ancker, and C. P. Dullemond. [O I] 6300 Å emission in Herbig Ae/Be systems: Signature of Keplerian rotation. *Astronomy and Astrophysics*, 436:209–230, June 2005. doi: 10.1051/0004-6361:20042484.

R. L. Akeson, D. R. Ciardi, G. T. van Belle, and M. J. Creech-Eakman. Constraints on Circumstellar Disk Parameters from Multiwavelength Observations: T Tauri and SU Aurigae. *Astrophysical Journal*, 566:1124–1131, February 2002. doi: 10.1086/338229.

R. L. Akeson, A. F. Boden, J. D. Monnier, R. Millan-Gabet, C. Beichman, J. Beletic, N. Calvet, L. Hartmann, L. Hillenbrand, C. Koresko, A. Sargent, and A. Tannirkulam. Keck Interferometer Observations of Classical and Weak-line T Tauri Stars. *Astrophysical Journal*, 635:1173–1181, December 2005a. doi: 10.1086/497436.

R. L. Akeson, C. H. Walker, K. Wood, J. A. Eisner, E. Scire, B. Penprase, D. R. Ciardi, G. T. van Belle, B. Whitney, and J. E. Bjorkman. Observations and Modeling of the Inner Disk Region of T Tauri Stars. *Astrophysical Journal*, 622:440–450, March 2005b. doi: 10.1086/427770.

J. M. Alcala, J. Krautter, J. H. M. M. Schmitt, E. Covino, R. Wichmann, and R. Mundt. A study of the Chamaeleon star forming region from the ROSAT all-sky survey. I. X-ray observations and optical identifications. *Astronomy and Astrophysics, Supplement*, 114:109–134, November 1995.

J. M. Alcalá, E. Covino, M. F. Sterzik, J. H. M. M. Schmitt, J. Krautter, and R. Neuhäuser. A ROSAT pointed observation of the Chamaeleon II dark cloud. *Astronomy and Astrophysics*, 355:

629–638, March 2000.

R. D. Alexander and P. J. Armitage. Dust dynamics during protoplanetary disc clearing. *Monthly Notices of the RAS*, 375:500–512, February 2007. doi: 10.1111/j.1365-2966.2006.11341.x.

P. André. Observations of protostars and protostellar stages. In T. Montmerle, C. J. Lada, I. F. Mirabel, and J. Tran Thanh van, editors, *The Cold Universe*, page 179, 1994.

S. M. Andrews and J. P. Williams. Submillimeter Array Observations of Disks in the SR 24 Multiple Star System. *Astrophysical Journal, Letters*, 619:L175–L178, February 2005. doi: 10.1086/427325.

S. M. Andrews and J. P. Williams. A Submillimeter View of Circumstellar Dust Disks in ρ Ophiuchi. *Astrophysical Journal*, 671:1800–1812, December 2007a. doi: 10.1086/522885.

S. M. Andrews and J. P. Williams. High-Resolution Submillimeter Constraints on Circumstellar Disk Structure. *Astrophysical Journal*, 659:705–728, April 2007b. doi: 10.1086/511741.

S. M. Andrews, A. M. Hughes, D. J. Wilner, and C. Qi. The Structure of the DoAr 25 Circumstellar Disk. *Astrophysical Journal, Letters*, 678:L133–L136, May 2008. doi: 10.1086/588730.

Y. Andrillat, M. Jaschek, and C. Jaschek. The infrared spectrum of HD 141569. *Astronomy and Astrophysics*, 233:474–476, July 1990.

P. Artymowicz and S. H. Lubow. Mass Flow through Gaps in Circumbinary Disks. *Astrophysical Journal, Letters*, 467:L77–L80, August 1996. doi: 10.1086/310200.

M. Barsony, M. E. Ressler, and K. A. Marsh. A Mid-Infrared Imaging Survey of Embedded Young Stellar Objects in the ρ Ophiuchi Cloud Core. *Astrophysical Journal*, 630:381–399, September 2005. doi: 10.1086/431351.

J. S. Bary, D. A. Weintraub, and J. H. Kastner. Detections of Rovibrational H_2 Emission from the Disks of T Tauri Stars. *Astrophysical Journal*, 586:1136–1147, April 2003. doi: 10.1086/367719.

S. V. W. Beckwith, A. I. Sargent, R. S. Chini, and R. Guesten. A survey for circumstellar disks around young stellar objects. *Astronomical Journal*, 99:924–945, March 1990. doi: 10.1086/115385.

E. Bergin, N. Calvet, P. D'Alessio, and G. J. Herczeg. The Effects of UV Continuum and Lyα Radiation on the Chemical Equilibrium of T Tauri Disks. *Astrophysical Journal, Letters*, 591:

L159–L162, July 2003. doi: 10.1086/377148.

G. A. Blake and A. C. A. Boogert. High-Resolution 4.7 Micron Keck/NIRSPEC Spectroscopy of the CO Emission from the Disks Surrounding Herbig Ae Stars. *Astrophysical Journal, Letters*, 606:L73–L76, May 2004. doi: 10.1086/421082.

A. F. Boden, A. I. Sargent, R. L. Akeson, J. M. Carpenter, G. Torres, D. W. Latham, D. R. Soderblom, E. Nelan, O. G. Franz, and L. H. Wasserman. Dynamical Masses for Low-Mass Pre-Main-Sequence Stars: A Preliminary Physical Orbit for HD 98800 B. *Astrophysical Journal*, 635: 442–451, December 2005. doi: 10.1086/497328.

B. P. Bonev, M. J. Mumma, M. A. DiSanti, N. Dello Russo, K. Magee-Sauer, R. S. Ellis, and D. P. Stark. A Comprehensive Study of Infrared OH Prompt Emission in Two Comets. I. Observations and Effective g-Factors. *Astrophysical Journal*, 653:774–787, December 2006. doi: 10.1086/508452.

S. Bontemps, P. André, A. A. Kaas, L. Nordh, G. Olofsson, M. Huldtgren, A. Abergel, J. Blommaert, F. Boulanger, M. Burgdorf, C. J. Cesarsky, D. Cesarsky, E. Copet, J. Davies, E. Falgarone, G. Lagache, T. Montmerle, M. Pérault, P. Persi, T. Prusti, J. L. Puget, and F. Sibille. ISOCAM observations of the rho Ophiuchi cloud: Luminosity and mass functions of the pre-main sequence embedded cluster. *Astronomy and Astrophysics*, 372:173–194, June 2001. doi: 10.1051/0004-6361:20010474.

A. C. A. Boogert, G. A. Blake, and A. G. G. M. Tielens. High-Resolution 4.7 Micron Keck/NIRSPEC Spectra of Protostars. II. Detection of the ^{13}CO Isotope in Icy Grain Mantles. *Astrophysical Journal*, 577:271–280, September 2002. doi: 10.1086/342176.

A. C. A. Boogert, K. M. Pontoppidan, F. Lahuis, J. K. Jørgensen, J.-C. Augereau, G. A. Blake, T. Y. Brooke, J. Brown, C. P. Dullemond, N. J. Evans, II, V. Geers, M. R. Hogerheijde, J. Kessler-Silacci, C. Knez, P. Morris, A. Noriega-Crespo, F. L. Schöier, E. F. van Dishoeck, L. E. Allen, P. M. Harvey, D. W. Koerner, L. G. Mundy, P. C. Myers, D. L. Padgett, A. I. Sargent, and K. R. Stapelfeldt. Spitzer Space Telescope Spectroscopy of Ices toward Low-Mass Embedded Protostars. *Astrophysical Journal, Supplement*, 154:359–362, September 2004. doi: 10.1086/422556.

J. Bouvier. Rotation in T Tauri stars. II - Clues for magnetic activity. *Astronomical Journal*, 99:

946–964, March 1990. doi: 10.1086/115386.

J. Bouvier and I. Appenzeller. A magnitude-limited spectroscopic and photometric survey of Rho Ophiuchus X-ray sources. *Astronomy and Astrophysics, Supplement*, 92:481–516, February 1992.

J. Bouvier, E. Covino, O. Kovo, E. L. Martin, J. M. Matthews, L. Terranegra, and S. C. Beck. COYOTES II: SPOT properties and the origin of photometric period variations in T Tauri stars. *Astronomy and Astrophysics*, 299:89–107, July 1995.

S. D. Brittain, T. W. Rettig, T. Simon, C. Kulesa, M. A. DiSanti, and N. Dello Russo. CO Emission from Disks around AB Aurigae and HD 141569: Implications for Disk Structure and Planet Formation Timescales. *Astrophysical Journal*, 588:535–544, May 2003. doi: 10.1086/373987.

S. D. Brittain, T. W. Rettig, T. Simon, and C. Kulesa. CO Line Emission and Absorption from the HL Tauri Disk-Where Is All the Dust? *Astrophysical Journal*, 626:283–291, June 2005. doi: 10.1086/429310.

S. D. Brittain, T. Simon, J. R. Najita, and T. W. Rettig. Warm Gas in the Inner Disks around Young Intermediate-Mass Stars. *Astrophysical Journal*, 659:685–704, April 2007. doi: 10.1086/511255.

J. M. Brown. Submillimeter observations of transitional disks. (in preparation).

J. M. Brown, G. A. Blake, C. P. Dullemond, B. Merín, J. C. Augereau, A. C. A. Boogert, N. J. Evans, II, V. C. Geers, F. Lahuis, J. E. Kessler-Silacci, K. M. Pontoppidan, and E. F. van Dishoeck. Cold Disks: Spitzer Spectroscopy of Disks around Young Stars with Large Gaps. *Astrophysical Journal, Letters*, 664:L107–L110, August 2007. doi: 10.1086/520808.

J. M. Brown, G. A. Blake, C. Qi, C. P. Dullemond, and D. J. Wilner. LkHα 330: Evidence for Dust Clearing through Resolved Submillimeter Imaging. *Astrophysical Journal, Letters*, 675:L109–L112, March 2008. doi: 10.1086/533464.

N. Calvet and P. D'Alessio. YSO Disk Structure and Planetary Signatures. In A. Wootten, editor, *Science with the Atacama Large Millimeter Array*, volume 235 of *Astronomical Society of the Pacific Conference Series*, pages 205–214, 2001.

N. Calvet, L. Hartmann, and S. E. Strom. Evolution of Disk Accretion. *Protostars and Planets IV*, pages 377–399, May 2000.

N. Calvet, P. D'Alessio, L. Hartmann, D. Wilner, A. Walsh, and M. Sitko. Evidence for a Developing Gap in a 10 Myr Old Protoplanetary Disk. *Astrophysical Journal*, 568:1008–1016, April 2002. doi: 10.1086/339061.

N. Calvet, J. Muzerolle, C. Briceño, J. Hernández, L. Hartmann, J. L. Saucedo, and K. D. Gordon. The Mass Accretion Rates of Intermediate-Mass T Tauri Stars. *Astronomical Journal*, 128:1294–1318, September 2004. doi: 10.1086/422733.

N. Calvet, P. D'Alessio, D. M. Watson, R. Franco-Hernández, E. Furlan, J. Green, P. M. Sutter, W. J. Forrest, L. Hartmann, K. I. Uchida, L. D. Keller, B. Sargent, J. Najita, T. L. Herter, D. J. Barry, and P. Hall. Disks in Transition in the Taurus Population: Spitzer IRS Spectra of GM Aurigae and DM Tauri. *Astrophysical Journal, Letters*, 630:L185–L188, September 2005. doi: 10.1086/491652.

J. M. Carpenter, L. A. Hillenbrand, and M. F. Skrutskie. Near-Infrared Photometric Variability of Stars toward the Orion A Molecular Cloud. *Astronomical Journal*, 121:3160–3190, June 2001. doi: 10.1086/321086.

J. S. Carr and J. R. Najita. Organic Molecules and Water in the Planet Formation Region of Young Circumstellar Disks. *Science*, 319:1504–1506, March 2008. doi: 10.1126/science.1153807.

J. S. Carr, A. T. Tokunaga, and J. Najita. Hot H_2O Emission and Evidence for Turbulence in the Disk of a Young Star. *Astrophysical Journal*, 603:213–220, March 2004. doi: 10.1086/381356.

S. Casanova, T. Montmerle, E. D. Feigelson, and P. Andre. ROSAT X-ray sources embedded in the rho Ophiuchi cloud core. *Astrophysical Journal*, 439:752–770, February 1995. doi: 10.1086/175214.

E. Chiang and R. Murray-Clay. Inside-out evacuation of transitional protoplanetary discs by the magneto-rotational instability. *Nature Physics*, 3:604–608, September 2007. doi: 10.1038/nphys661.

E. I. Chiang and P. Goldreich. Spectral Energy Distributions of T Tauri Stars with Passive Circumstellar Disks. *Astrophysical Journal*, 490:368–376, November 1997. doi: 10.1086/304869.

F. J. Ciesla and J. N. Cuzzi. The evolution of the water distribution in a viscous protoplanetary disk. *Icarus*, 181:178–204, March 2006. doi: 10.1016/j.icarus.2005.11.009.

L. A. Cieza, J. E. Kessler-Silacci, D. T. Jaffe, P. M. Harvey, and N. J. Evans, II. Evidence for J- and H-Band Excess in Classical T Tauri Stars and the Implications for Disk Structure and Estimated Ages. *Astrophysical Journal*, 635:422–441, December 2005. doi: 10.1086/497325.

C. J. Clarke and J. Bouvier. A comparison of the rotational properties of T Tauri stars in Orion and Taurus. *Monthly Notices of the RAS*, 319:457–466, December 2000. doi: 10.1046/j.1365-8711.2000.03855.x.

L. M. Close, F. Roddier, M. J. Northcott, C. Roddier, and J. E. Graves. Adaptive Optics 0"-4.25pt.+1.25pt2 Resolution Infrared Images of HL Tauri: Direct Images of an Active Accretion Disk around a Protostar. *Astrophysical Journal*, 478:766–777, March 1997. doi: 10.1086/303813.

M. Cohen and L. V. Kuhi. Observational studies of pre-main-sequence evolution. *Astrophysical Journal, Supplement*, 41:743–843, December 1979. doi: 10.1086/190641.

M. Cohen, J. P. Emerson, and C. A. Beichman. A reexamination of luminosity sources in T Tauri stars. I - Taurus-Auriga. *Astrophysical Journal*, 339:455–473, April 1989. doi: 10.1086/167310.

M. Colavita, R. Akeson, P. Wizinowich, M. Shao, S. Acton, J. Beletic, J. Bell, J. Berlin, A. Boden, A. Booth, R. Boutell, F. Chaffee, D. Chan, J. Chock, R. Cohen, S. Crawford, M. Creech-Eakman, G. Eychaner, C. Felizardo, J. Gathright, G. Hardy, H. Henderson, J. Herstein, M. Hess, E. Hovland, M. Hrynevych, R. Johnson, J. Kelley, R. Kendrick, C. Koresko, P. Kurpis, D. Le Mignant, H. Lewis, E. Ligon, W. Lupton, D. McBride, B. Mennesson, R. Millan-Gabet, J. Monnier, J. Moore, C. Nance, C. Neyman, A. Niessner, D. Palmer, L. Reder, A. Rudeen, T. Saloga, A. Sargent, E. Serabyn, R. Smythe, P. Stomski, K. Summers, M. Swain, P. Swanson, R. Thompson, K. Tsubota, A. Tumminello, G. van Belle, G. Vasisht, J. Vause, J. Walker, K. Wallace, and U. Wehmeier. Observations of DG Tauri with the Keck Interferometer. *Astrophysical Journal, Letters*, 592:L83–L86, August 2003. doi: 10.1086/377704.

I. M. Coulson and D. M. Walther. SAO 206462 — a solar-type star with a dusty, organically rich environment. *Monthly Notices of the RAS*, 274:977–986, June 1995.

M. Cuttela and A. E. Ringuelet. A Model for the Ae-Star with Detected Magnetic Field HD190073. *Monthly Notices of the RAS*, 246:20–28, September 1990.

P. D'Alessio, L. Hartmann, N. Calvet, R. Franco-Hernández, W. J. Forrest, B. Sargent, E. Furlan, K. Uchida, J. D. Green, D. M. Watson, C. H. Chen, F. Kemper, G. C. Sloan, and J. Najita. The Truncated Disk of CoKu Tau/4. *Astrophysical Journal*, 621:461–472, March 2005. doi: 10.1086/427490.

R. de la Reza and G. Pinzón. On the Rotation of Post-T Tauri Stars in Associations. *Astronomical Journal*, 128:1812–1824, October 2004. doi: 10.1086/423439.

N. dello Russo, M. A. Disanti, K. Magee-Sauer, E. L. Gibb, M. J. Mumma, R. J. Barber, and J. Tennyson. Water production and release in Comet 153P/Ikeya-Zhang (C/2002 C1): accurate rotational temperature retrievals from hot-band lines near 2.9-μm. *Icarus*, 168:186–200, March 2004. doi: 10.1016/j.icarus.2003.11.004.

W. R. F. Dent, J. S. Greaves, and I. M. Coulson. CO emission from discs around isolated HAeBe and Vega-excess stars. *Monthly Notices of the RAS*, 359:663–676, May 2005. doi: 10.1111/j.1365-2966.2005.08938.x.

E. Di Folco, F. Thévenin, P. Kervella, A. Domiciano de Souza, V. Coudé du Foresto, D. Ségransan, and P. Morel. VLTI near-IR interferometric observations of Vega-like stars. Radius and age of α PsA, β Leo, β Pic, ϵ Eri and τ Cet. *Astronomy and Astrophysics*, 426:601–617, November 2004. doi: 10.1051/0004-6361:20047189.

S. E. Dodson-Robinson, K. Willacy, P. Bodenheimer, N. J. Turner, and C. A. Beichman. Ice lines, planetesimal composition and solid surface density in the solar nebula. *Icarus*, 200:672–693, April 2009. doi: 10.1016/j.icarus.2008.11.023.

C. Doucet, E. Pantin, P. O. Lagage, and C. P. Dullemond. Mid-infrared imaging of the circumstellar dust around three Herbig Ae stars: HD 135344, CQ Tau, and HD 163296. *Astronomy and Astrophysics*, 460:117–124, December 2006. doi: 10.1051/0004-6361:20054371.

C. P. Dullemond, C. Dominik, and A. Natta. Passive Irradiated Circumstellar Disks with an Inner Hole. *Astrophysical Journal*, 560:957–969, October 2001. doi: 10.1086/323057.

C. P. Dullemond, G. J. van Zadelhoff, and A. Natta. Vertical structure models of T Tauri and Herbig Ae/Be disks. *Astronomy and Astrophysics*, 389:464–474, July 2002. doi: 10.1051/0004-

6361:20020608.

C. P. Dullemond, D. Hollenbach, I. Kamp, and P. D'Alessio. Models of the Structure and Evolution of Protoplanetary Disks. In B. Reipurth, D. Jewitt, and K. Keil, editors, *Protostars and Planets V*, pages 555–572, 2007.

S. K. Dunkin, M. J. Barlow, and S. G. Ryan. High-resolution spectroscopy of Vega-like stars - II. Age indicators, activity and circumstellar gas. *Monthly Notices of the RAS*, 290:165–185, September 1997.

A. Dutrey, S. Guilloteau, V. Piétu, E. Chapillon, F. Gueth, T. Henning, R. Launhardt, Y. Pavlyuchenkov, K. Schreyer, and D. Semenov. Cavities in inner disks: the GM Aurigae case. *Astronomy and Astrophysics*, 490:L15–L18, November 2008. doi: 10.1051/0004-6361:200810732.

S. Edwards, P. Hartigan, L. Ghandour, and C. Andrulis. Spectroscopic evidence for magnetospheric accretion in classical T Tauri stars. *Astronomical Journal*, 108:1056–1070, September 1994. doi: 10.1086/117134.

S. Edwards, W. Fischer, L. Hillenbrand, and J. Kwan. Probing T Tauri Accretion and Outflow with 1 Micron Spectroscopy. *Astrophysical Journal*, 646:319–341, July 2006. doi: 10.1086/504832.

D. Ehrenreich, G. Hébrard, A. Lecavelier des Etangs, D. K. Sing, J.-M. Désert, F. Bouchy, R. Ferlet, and A. Vidal-Madjar. A Spitzer Search for Water in the Transiting Exoplanet HD 189733b. *Astrophysical Journal, Letters*, 668:L179–L182, October 2007. doi: 10.1086/522792.

C. Eiroa, R. D. Oudmaijer, J. K. Davies, D. de Winter, F. Garzón, J. Palacios, A. Alberdi, R. Ferlet, C. A. Grady, A. Cameron, H. J. Deeg, A. W. Harris, K. Horne, B. Merín, L. F. Miranda, B. Montesinos, A. Mora, A. Penny, A. Quirrenbach, H. Rauer, J. Schneider, E. Solano, Y. Tsapras, and P. R. Wesselius. On the simultaneous optical and near-infrared variability of pre-main sequence stars. *Astronomy and Astrophysics*, 384:1038–1049, March 2002. doi: 10.1051/0004-6361:20020096.

J. A. Eisner, B. F. Lane, R. L. Akeson, L. A. Hillenbrand, and A. I. Sargent. Near-Infrared Interferometric Measurements of Herbig Ae/Be Stars. *Astrophysical Journal*, 588:360–372, May 2003. doi: 10.1086/373923.

J. A. Eisner, B. F. Lane, L. A. Hillenbrand, R. L. Akeson, and A. I. Sargent. Resolved Inner Disks around Herbig Ae/Be Stars. *Astrophysical Journal*, 613:1049–1071, October 2004. doi: 10.1086/423314.

J. A. Eisner, L. A. Hillenbrand, R. J. White, R. L. Akeson, and A. I. Sargent. Observations of T Tauri Disks at Sub-AU Radii: Implications for Magnetospheric Accretion and Planet Formation. *Astrophysical Journal*, 623:952–966, April 2005. doi: 10.1086/428828.

J. A. Eisner, E. I. Chiang, and L. A. Hillenbrand. Spatially Resolving the Inner Disk of TW Hydrae. *Astrophysical Journal, Letters*, 637:L133–L136, February 2006. doi: 10.1086/500689.

J. A. Eisner, L. A. Hillenbrand, R. J. White, J. S. Bloom, R. L. Akeson, and C. H. Blake. Near-Infrared Interferometric, Spectroscopic, and Photometric Monitoring of T Tauri Inner Disks. *Astrophysical Journal*, 669:1072–1084, November 2007. doi: 10.1086/521874.

J. A. Eisner, J. R. Graham, R. L. Akeson, and J. Najita. Spatially Resolved Spectroscopy of Sub-AU-Sized Regions of T Tauri and Herbig Ae/Be Disks. *Astrophysical Journal*, 692:309–323, February 2009. doi: 10.1088/0004-637X/692/1/309.

C. Espaillat, N. Calvet, P. D'Alessio, J. Hernández, C. Qi, L. Hartmann, E. Furlan, and D. M. Watson. On the Diversity of the Taurus Transitional Disks: UX Tauri A and LkCa 15. *Astrophysical Journal, Letters*, 670:L135–L138, December 2007. doi: 10.1086/524360.

C. Espaillat, N. Calvet, K. L. Luhman, J. Muzerolle, and P. D'Alessio. Confirmation of a Gapped Primordial Disk around LkCa 15. *Astrophysical Journal, Letters*, 682:L125–L128, August 2008. doi: 10.1086/591270.

N. J. Evans, II, L. E. Allen, G. A. Blake, A. C. A. Boogert, T. Bourke, P. M. Harvey, J. E. Kessler, D. W. Koerner, C. W. Lee, L. G. Mundy, P. C. Myers, D. L. Padgett, K. Pontoppidan, A. I. Sargent, K. R. Stapelfeldt, E. F. van Dishoeck, C. H. Young, and K. E. Young. From Molecular Cores to Planet-forming Disks: An SIRTF Legacy Program. *Publications of the ASP*, 115:965–980, August 2003. doi: 10.1086/376697.

F. Favata, G. Micela, S. Sciortino, and F. D'Antona. The evolutionary status of activity-selected solar-type stars and of T Tauri stars as derived from HIPPARCOS parallaxes: evidence for long-lived T Tauri disks? *Astronomy and Astrophysics*, 335:218–226, July 1998.

E. D. Feigelson, S. Casanova, T. Montmerle, and J. Guibert. ROSAT X-Ray Study of the Chamaeleon I Dark Cloud. I. The Stellar Population. *Astrophysical Journal*, 416:623–646, October 1993. doi: 10.1086/173264.

M. Fernandez, E. Ortiz, C. Eiroa, and L. F. Miranda. Hα emission from pre-main sequence stars. *Astronomy and Astrophysics, Supplement*, 114:439–464, December 1995.

D. F. M. Folha and J. P. Emerson. High veiling at near infrared wavelengths in classical T Tauri stars. *Astronomy and Astrophysics*, 352:517–531, December 1999.

E. Furlan, L. Hartmann, N. Calvet, P. D'Alessio, R. Franco-Hernández, W. J. Forrest, D. M. Watson, K. I. Uchida, B. Sargent, J. D. Green, L. D. Keller, and T. L. Herter. A Survey and Analysis of Spitzer Infrared Spectrograph Spectra of T Tauri Stars in Taurus. *Astrophysical Journal, Supplement*, 165:568–605, August 2006. doi: 10.1086/505468.

E. Furlan, B. Sargent, N. Calvet, W. J. Forrest, P. D'Alessio, L. Hartmann, D. M. Watson, J. D. Green, J. Najita, and C. H. Chen. HD 98800: A 10 Myr Old Transition Disk. *Astrophysical Journal*, 664:1176–1184, August 2007. doi: 10.1086/519301.

R. Garcia Lopez, A. Natta, L. Testi, and E. Habart. Accretion rates in Herbig Ae stars. *Astronomy and Astrophysics*, 459:837–842, December 2006. doi: 10.1051/0004-6361:20065575.

P. A. Gerakines, D. C. B. Whittet, P. Ehrenfreund, A. C. A. Boogert, A. G. G. M. Tielens, W. A. Schutte, J. E. Chiar, E. F. van Dishoeck, T. Prusti, F. P. Helmich, and T. de Graauw. Observations of Solid Carbon Dioxide in Molecular Clouds with the Infrared Space Observatory. *Astrophysical Journal*, 522:357–377, September 1999. doi: 10.1086/307611.

M. Goto, T. Usuda, C. P. Dullemond, T. Henning, H. Linz, B. Stecklum, and H. Suto. Inner Rim of a Molecular Disk Spatially Resolved in Infrared CO Emission Lines. *Astrophysical Journal*, 652: 758–762, November 2006. doi: 10.1086/506582.

C. A. Grady, D. Devine, B. Woodgate, R. Kimble, F. C. Bruhweiler, A. Boggess, J. L. Linsky, P. Plait, M. Clampin, and P. Kalas. STIS Coronagraphic Imaging of the Herbig AE Star: HD 163296. *Astrophysical Journal*, 544:895–902, December 2000. doi: 10.1086/317222.

J. S. Greaves, V. Mannings, and W. S. Holland. The Dust and Gas Content of a Disk around the Young Star HR 4796A. *Icarus*, 143:155–158, January 2000. doi: 10.1006/icar.1999.6244.

T. Greene. Protostars. *American Scientist*, 89:316–325, August 2001. doi: 10.1511/2001.4.316.

T. P. Greene and M. R. Meyer. An Infrared Spectroscopic Survey of the rho Ophiuchi Young Stellar Cluster: Masses and Ages from the H-R Diagram. *Astrophysical Journal*, 450:233–244, September 1995. doi: 10.1086/176134.

M. Güdel, K. R. Briggs, K. Arzner, M. Audard, J. Bouvier, E. D. Feigelson, E. Franciosini, A. Glauser, N. Grosso, G. Micela, J.-L. Monin, T. Montmerle, D. L. Padgett, F. Palla, I. Pillitteri, L. Rebull, L. Scelsi, B. Silva, S. L. Skinner, B. Stelzer, and A. Telleschi. The XMM-Newton extended survey of the Taurus molecular cloud (XEST). *Astronomy and Astrophysics*, 468:353–377, June 2007a. doi: 10.1051/0004-6361:20065724.

M. Güdel, A. Telleschi, M. Audard, S. L. Skinner, K. R. Briggs, F. Palla, and C. Dougados. X-rays from jet-driving protostars and T Tauri stars. *Astronomy and Astrophysics*, 468:515–528, June 2007b. doi: 10.1051/0004-6361:20065736.

E. Guenther and F. V. Hessman. The spectral variability of DR Tauri. *Astronomy and Astrophysics*, 268:192–200, February 1993.

E. W. Guenther, M. Esposito, R. Mundt, E. Covino, J. M. Alcalá, F. Cusano, and B. Stecklum. Pre-main sequence spectroscopic binaries suitable for VLTI observations. *Astronomy and Astrophysics*, 467:1147–1155, June 2007. doi: 10.1051/0004-6361:20065686.

E. Gullbring, L. Hartmann, C. Briceno, and N. Calvet. Disk Accretion Rates for T Tauri Stars. *Astrophysical Journal*, 492:323–341, January 1998. doi: 10.1086/305032.

E. Gullbring, N. Calvet, J. Muzerolle, and L. Hartmann. The Structure and Emission of the Accretion Shock in T Tauri Stars. II. The Ultraviolet-Continuum Emission. *Astrophysical Journal*, 544:927–932, December 2000. doi: 10.1086/317253.

P. Hartigan, L. Hartmann, S. Kenyon, R. Hewett, and J. Stauffer. How to unveil a T Tauri star. *Astrophysical Journal, Supplement*, 70:899–914, August 1989. doi: 10.1086/191361.

L. Hartmann, R. Hewett, and N. Calvet. Magnetospheric accretion models for T Tauri stars.

1: Balmer line profiles without rotation. *Astrophysical Journal*, 426:669–687, May 1994. doi: 10.1086/174104.

L. Hartmann, N. Calvet, E. Gullbring, and P. D'Alessio. Accretion and the Evolutiion of T Tauri Disks. *Astrophysical Journal*, 495:385–400, March 1998. doi: 10.1086/305277.

L. Hartmann, S. T. Megeath, L. Allen, K. Luhman, N. Calvet, P. D'Alessio, R. Franco-Hernandez, and G. Fazio. IRAC Observations of Taurus Pre-Main-Sequence Stars. *Astrophysical Journal*, 629:881–896, August 2005. doi: 10.1086/431472.

M. Hayashi, N. Ohashi, and S. M. Miyama. A Dynamically Accreting Gas Disk around HL Tauri. *Astrophysical Journal, Letters*, 418:L71–L74, December 1993. doi: 10.1086/187119.

G. H. Herbig. The properties and problems of T Tauri stars and related objects. *Advances in Astronomy and Astrophysics*, 1:47–103, 1962.

G. H. Herbig and K. R. Bell. *Catalog of emission line stars of the orion population:3:1988*. *Lick Observatory Bulletin*, Santa Cruz: Lick Observatory, 1988.

G. J. Herczeg and L. A. Hillenbrand. UV Excess Measures of Accretion onto Young Very Low Mass Stars and Brown Dwarfs. *Astrophysical Journal*, 681:594–625, July 2008. doi: 10.1086/586728.

J. Hernández, N. Calvet, C. Briceño, L. Hartmann, and P. Berlind. Spectral Analysis and Classification of Herbig Ae/Be Stars. *Astronomical Journal*, 127:1682–1701, March 2004.

F. V. Hessman and E. W. Guenther. The highly veiled T Tauri stars DG Tau, DR Tau, and DI Cep. *Astronomy and Astrophysics*, 321:497–512, May 1997.

L. A. Hillenbrand, S. E. Strom, F. J. Vrba, and J. Keene. Herbig Ae/Be stars - Intermediate-mass stars surrounded by massive circumstellar accretion disks. *Astrophysical Journal*, 397:613–643, October 1992. doi: 10.1086/171819.

K. H. Hinkle, R. D. Blum, R. R. Joyce, N. Sharp, S. T. Ridgway, P. Bouchet, N. S. van der Bliek, J. Najita, and C. Winge. The Phoenix Spectrograph at Gemini South. In P. Guhathakurta, editor, *Society of Photo-Optical Instrumentation Engineers (SPIE) Conference Series*, volume 4834, pages 353–363, February 2003. doi: 10.1117/12.457666.

M. Hiramatsu, T. Hayakawa, K. Tatematsu, K. Kamegai, T. Onishi, A. Mizuno, N. Yamaguchi, and T. Hasegawa. ASTE Submillimeter Observations of a Young Stellar Object Condensation in Cederblad 110. *Astrophysical Journal*, 664:964–974, August 2007. doi: 10.1086/519269.

M. Hogerheijde. *The molecular environment of low-mass protostars*. PhD thesis, Dept. of Astronomy, University of California, Campbell Hall, Berkeley, CA 94720, USA, 1998.

D. Hollenbach, D. Johnstone, S. Lizano, and F. Shu. Photoevaporation of disks around massive stars and application to ultracompact H II regions. *Astrophysical Journal*, 428:654–669, June 1994. doi: 10.1086/174276.

K. Horne and T. R. Marsh. Emission line formation in accretion discs. *Monthly Notices of the RAS*, 218:761–773, February 1986.

J. R. Houck, T. L. Roellig, J. Van Cleve, W. J. Forrest, T. L. Herter, C. R. Lawrence, K. Matthews, H. J. Reitsema, B. T. Soifer, D. M. Watson, D. Weedman, M. Huisjen, J. R. Troeltzsch, D. J. Barry, J. Bernard-Salas, C. Blacken, B. R. Brandl, V. Charmandaris, D. Devost, G. E. Gull, P. Hall, C. P. Henderson, S. J. U. Higdon, B. E. Pirger, J. Schoenwald, G. C. Sloan, K. I. Uchida, P. N. Appleton, L. Armus, M. J. Burgdorf, S. B. Fajardo-Acosta, C. J. Grillmair, J. G. Ingalls, P. W. Morris, and H. I. Teplitz. The infrared spectrograph on the Spitzer Space Telescope. In J. C. Mather, editor, *Society of Photo-Optical Instrumentation Engineers (SPIE) Conference Series*, volume 5487, pages 62–76, October 2004. doi: 10.1117/12.550517.

N. Huélamo, P. Figueira, X. Bonfils, N. C. Santos, F. Pepe, M. Gillon, R. Azevedo, T. Barman, M. Fernández, E. di Folco, E. W. Guenther, C. Lovis, C. H. F. Melo, D. Queloz, and S. Udry. TW Hydrae: evidence of stellar spots instead of a Hot Jupiter. *Astronomy and Astrophysics*, 489: L9–L13, October 2008. doi: 10.1051/0004-6361:200810596.

A. M. Hughes, D. J. Wilner, N. Calvet, P. D'Alessio, M. J. Claussen, and M. R. Hogerheijde. An Inner Hole in the Disk around TW Hydrae Resolved in 7 mm Dust Emission. *Astrophysical Journal*, 664:536–542, July 2007. doi: 10.1086/518885.

J. Hughes, P. Hartigan, J. Krautter, and J. Kelemen. The stellar population of the Lupus clouds. *Astronomical Journal*, 108:1071–1090, September 1994. doi: 10.1086/117135.

M. J. Ireland and A. L. Kraus. The Disk Around CoKu Tauri/4: Circumbinary, Not Transitional.

Astrophysical Journal, Letters, 678:L59–L62, May 2008. doi: 10.1086/588216.

R. Jayawardhana, L. Hartmann, G. Fazio, R. S. Fisher, C. M. Telesco, and R. K. Piña. A Disk Census for the Nearest Group of Young Stars: Mid-Infrared Observations of the TW Hydrae Association. *Astrophysical Journal, Letters*, 521:L129–L132, August 1999. doi: 10.1086/312200.

C. M. Johns-Krull and G. Basri. The Spectral Variability of the T Tauri Star DF Tauri. *Astrophysical Journal*, 474:433–454, January 1997. doi: 10.1086/303460.

C. M. Johns-Krull and A. D. Gafford. New Tests of Magnetospheric Accretion in T Tauri Stars. *Astrophysical Journal*, 573:685–698, July 2002. doi: 10.1086/340898.

C. M. Johns-Krull and J. A. Valenti. New Infrared Veiling Measurements and Constraints on Accretion Disk Models for Classical T Tauri Stars. *Astrophysical Journal*, 561:1060–1073, November 2001. doi: 10.1086/323257.

C. M. Johns-Krull, J. A. Valenti, and J. L. Linsky. A Short Wavelength IUE Atlas of Pre-Main-Sequence Stars. In R. A. Donahue and J. A. Bookbinder, editors, *Cool Stars, Stellar Systems, and the Sun*, volume 154 of *Astronomical Society of the Pacific Conference Series*, pages 1724–1734, 1998.

M. Jura, B. Zuckerman, E. E. Becklin, and R. C. Smith. Constraints on the Evolution of Remnant Protostellar Dust Debris around HR 4796. *Astrophysical Journal, Letters*, 418:L37–L40, November 1993. doi: 10.1086/187110.

M. Jura, M. Malkan, R. White, C. Telesco, R. Pina, and R. S. Fisher. A Protocometary Cloud around HR 4796A? *Astrophysical Journal*, 505:897–902, October 1998. doi: 10.1086/306184.

P. Kalas, J. R. Graham, E. Chiang, M. P. Fitzgerald, M. Clampin, E. S. Kite, K. Stapelfeldt, C. Marois, and J. Krist. Optical Images of an Exosolar Planet 25 Light-Years from Earth. *Science*, 322:1345–1348, November 2008. doi: 10.1126/science.1166609.

I. Kamp and C. P. Dullemond. The Gas Temperature in the Surface Layers of Protoplanetary Disks. *Astrophysical Journal*, 615:991–999, November 2004. doi: 10.1086/424703.

S. J. Kenyon and L. Hartmann. Pre-Main-Sequence Evolution in the Taurus-Auriga Molecular Cloud. *Astrophysical Journal, Supplement*, 101:117–171, November 1995. doi: 10.1086/192235.

J. Kessler-Silacci, J.-C. Augereau, C. P. Dullemond, V. Geers, F. Lahuis, N. J. Evans, II, E. F. van Dishoeck, G. A. Blake, A. C. A. Boogert, J. Brown, J. K. Jørgensen, C. Knez, and K. M. Pontoppidan. c2d Spitzer IRS Spectra of Disks around T Tauri Stars. I. Silicate Emission and Grain Growth. *Astrophysical Journal*, 639:275–291, March 2006. doi: 10.1086/499330.

Y. Kitamura, M. Momose, S. Yokogawa, R. Kawabe, M. Tamura, and S. Ida. Investigation of the Physical Properties of Protoplanetary Disks around T Tauri Stars by a 1 Arcsecond Imaging Survey: Evolution and Diversity of the Disks in Their Accretion Stage. *Astrophysical Journal*, 581:357–380, December 2002. doi: 10.1086/344223.

D. W. Koerner, A. I. Sargent, and S. V. W. Beckwith. A rotating gaseous disk around the T Tauri star GM Aurigae. *Icarus*, 106:2–10, November 1993. doi: 10.1006/icar.1993.1154.

D. W. Koerner, C. J. Chandler, and A. I. Sargent. Aperture Synthesis Imaging of the Circumstellar Dust Disk around DO Tauri. *Astrophysical Journal, Letters*, 452:L69–L72, October 1995. doi: 10.1086/309705.

D. W. Koerner, M. E. Ressler, M. W. Werner, and D. E. Backman. Mid-Infrared Imaging of a Circumstellar Disk around HR 4796: Mapping the Debris of Planetary Formation. *Astrophysical Journal, Letters*, 503:L83–L86, August 1998. doi: 10.1086/311525.

D. W. Koerner, E. L. N. Jensen, K. L. Cruz, T. B. Guild, and K. Gultekin. A Single Circumbinary Disk in the HD 98800 Quadruple System. *Astrophysical Journal, Letters*, 533:L37–L40, April 2000. doi: 10.1086/312593.

J. Kominami and S. Ida. The Effect of Tidal Interaction with a Gas Disk on Formation of Terrestrial Planets. *Icarus*, 157:43–56, May 2002. doi: 10.1006/icar.2001.6811.

M. J. Kuchner. A Minimum-Mass Extrasolar Nebula. *Astrophysical Journal*, 612:1147–1151, September 2004. doi: 10.1086/422577.

T. Kudo, M. Tamura, Y. Kitamura, M. Hayashi, E. Kokubo, M. Fukagawa, S. S. Hayashi, M. Ishii, Y. Itoh, S. Mayama, M. Momose, J. Morino, Y. Oasa, T.-S. Pyo, and H. Suto. Discovery of a Scattering Disk around the Low-Mass T Tauri Star FN Tauri. *Astrophysical Journal, Letters*, 673: L67–L70, January 2008. doi: 10.1086/527474.

R. L. Kurucz. Model Atmospheres (Kurucz, 1979). *VizieR Online Data Catalog*, 6039:0, October 1993.

J. H. Lacy, R. Knacke, T. R. Geballe, and A. T. Tokunaga. Detection of absorption by H2 in molecular clouds: A direct measurement of the H2:CO ratio. *Astrophysical Journal, Letters*, 428: L69–L72, June 1994. doi: 10.1086/187395.

C. J. Lada, A. A. Muench, K. L. Luhman, L. Allen, L. Hartmann, T. Megeath, P. Myers, G. Fazio, K. Wood, J. Muzerolle, G. Rieke, N. Siegler, and E. Young. Spitzer Observations of IC 348: The Disk Population at 2–3 Million Years. *Astronomical Journal*, 131:1574–1607, March 2006. doi: 10.1086/499808.

F. Lahuis and J. E. Kessler-Silacci. *c2d Spectroscopy Explanatory Supplement*, November 2006.

F. Lahuis, E. F. van Dishoeck, G. A. Blake, N. J. Evans, II, J. E. Kessler-Silacci, and K. M. Pontoppidan. c2d Spitzer IRS Spectra of Disks around T Tauri Stars. III. [Ne II], [Fe I], and H_2 Gas-Phase Lines. *Astrophysical Journal*, 665:492–511, August 2007. doi: 10.1086/518931.

M. Lecar, M. Podolak, D. Sasselov, and E. Chiang. On the Location of the Snow Line in a Protoplanetary Disk. *Astrophysical Journal*, 640:1115–1118, April 2006. doi: 10.1086/500287.

C. Leinert, R. van Boekel, L. B. F. M. Waters, O. Chesneau, F. Malbet, R. Köhler, W. Jaffe, T. Ratzka, A. Dutrey, T. Preibisch, U. Graser, E. Bakker, G. Chagnon, W. D. Cotton, C. Dominik, C. P. Dullemond, A. W. Glazenborg-Kluttig, A. Glindemann, T. Henning, K.-H. Hofmann, J. de Jong, R. Lenzen, S. Ligori, B. Lopez, J. Meisner, S. Morel, F. Paresce, J.-W. Pel, I. Percheron, G. Perrin, F. Przygodda, A. Richichi, M. Schöller, P. Schuller, B. Stecklum, M. E. van den Ancker, O. von der Lühe, and G. Weigelt. Mid-infrared sizes of circumstellar disks around Herbig Ae/Be stars measured with MIDI on the VLTI. *Astronomy and Astrophysics*, 423:537–548, August 2004. doi: 10.1051/0004-6361:20047178.

D. N. C. Lin and J. Papaloizou. On the structure of circumbinary accretion disks and the tidal evolution of commensurable satellites. *Monthly Notices of the RAS*, 188:191–201, July 1979.

M. Lombardi, C. J. Lada, and J. Alves. Hipparcos distance estimates of the Ophiuchus and the Lupus cloud complexes. *Astronomy and Astrophysics*, 480:785–792, March 2008. doi: 10.1051/0004-

6361:20079110.

S. H. Lubow, M. Seibert, and P. Artymowicz. Disk Accretion onto High-Mass Planets. *Astrophysical Journal*, 526:1001–1012, December 1999. doi: 10.1086/308045.

K. L. Luhman. A Census of the Chamaeleon I Star-forming Region. *Astrophysical Journal*, 602: 816–842, February 2004. doi: 10.1086/381146.

K. L. Luhman. The Stellar Population of the Chamaeleon I Star-forming Region. *Astrophysical Journal, Supplement*, 173:104–136, November 2007. doi: 10.1086/520114.

D. Lynden-Bell and J. E. Pringle. The evolution of viscous discs and the origin of the nebular variables. *Monthly Notices of the RAS*, 168:603–637, September 1974.

K. Malfait, C. Waelkens, L. B. F. M. Waters, B. Vandenbussche, E. Huygen, and M. S. de Graauw. The spectrum of the young star HD 100546 observed with the Infrared Space Observatory. *Astronomy and Astrophysics*, 332:L25–L28, April 1998.

A. M. Mandell, M. J. Mumma, G. A. Blake, B. P. Bonev, G. L. Villanueva, and C. Salyk. Discovery of OH in Circumstellar Disks around Young Intermediate-Mass Stars. *Astrophysical Journal, Letters*, 681:L25–L28, July 2008. doi: 10.1086/590180.

V. Mannings and A. I. Sargent. High-Resolution Studies of Gas and Dust around Young Intermediate-Mass Stars. II. Observations of an Additional Sample of Herbig AE Systems. *Astrophysical Journal*, 529:391–401, January 2000. doi: 10.1086/308253.

G. Marcy, R. P. Butler, D. Fischer, S. Vogt, J. T. Wright, C. G. Tinney, and H. R. A. Jones. Observed Properties of Exoplanets: Masses, Orbits, and Metallicities. *Progress of Theoretical Physics Supplement*, 158:24–42, 2005. doi: 10.1143/PTPS.158.24.

A. J. Markwick, M. Ilgner, T. J. Millar, and T. Henning. Molecular distributions in the inner regions of protostellar disks. *Astronomy and Astrophysics*, 385:632–646, April 2002. doi: 10.1051/0004-6361:20020050.

C. Marois, B. Macintosh, T. Barman, B. Zuckerman, I. Song, J. Patience, D. Lafrenière, and R. Doyon. Direct Imaging of Multiple Planets Orbiting the Star HR 8799. *Science*, 322:1348–1352, November 2008. doi: 10.1126/science.1166585.

K. A. Marsh, M. D. Silverstone, E. E. Becklin, D. W. Koerner, M. W. Werner, A. J. Weinberger, and M. E. Ressler. Mid-Infrared Images of the Debris Disk around HD 141569. *Astrophysical Journal*, 573:425–430, July 2002. doi: 10.1086/340488.

R. D. Mathieu. Pre-Main-Sequence Binary Stars. *Annual Review of Astron and Astrophys*, 32: 465–530, 1994. doi: 10.1146/annurev.aa.32.090194.002341.

M. Mayor, S. Udry, D. Naef, F. Pepe, D. Queloz, N. C. Santos, and M. Burnet. The CORALIE survey for extrasolar planets. XII (Mayor+, 2004). *VizieR Online Data Catalog*, 341:50391, February 2004.

C. McCabe, A. M. Ghez, L. Prato, G. Duchêne, R. S. Fisher, and C. Telesco. Investigating Disk Evolution: A High Spatial Resolution Mid-Infrared Survey of T Tauri Stars. *Astrophysical Journal*, 636:932–951, January 2006. doi: 10.1086/498207.

I. S. McLean, E. E. Becklin, O. Bendiksen, G. Brims, J. Canfield, D. F. Figer, J. R. Graham, J. Hare, F. Lacayanga, J. E. Larkin, S. B. Larson, N. Levenson, N. Magnone, H. Teplitz, and W. Wong. Design and development of NIRSPEC: a near-infrared echelle spectrograph for the Keck II telescope. In A. M. Fowler, editor, *Society of Photo-Optical Instrumentation Engineers (SPIE) Conference Series*, volume 3354, pages 566–578, August 1998.

G. Meeus, L. B. F. M. Waters, J. Bouwman, M. E. van den Ancker, C. Waelkens, and K. Malfait. ISO spectroscopy of circumstellar dust in 14 Herbig Ae/Be systems: Towards an understanding of dust processing. *Astronomy and Astrophysics*, 365:476–490, January 2001. doi: 10.1051/0004-6361:20000144.

B. Merín, B. Montesinos, C. Eiroa, E. Solano, A. Mora, P. D'Alessio, N. Calvet, R. D. Oudmaijer, D. de Winter, J. K. Davies, A. W. Harris, A. Cameron, H. J. Deeg, R. Ferlet, F. Garzón, C. A. Grady, K. Horne, L. F. Miranda, J. Palacios, A. Penny, A. Quirrenbach, H. Rauer, J. Schneider, and P. R. Wesselius. Study of the properties and spectral energy distributions of the Herbig AeBe stars HD 34282 and HD 141569. *Astronomy and Astrophysics*, 419:301–318, May 2004. doi: 10.1051/0004-6361:20034561.

B. Merín, J. Jørgensen, L. Spezzi, J. M. Alcalá, N. J. Evans, II, P. M. Harvey, T. Prusti, N. Chapman,

T. Huard, E. F. van Dishoeck, and F. Comerón. The Spitzer c2d Survey of Large, Nearby, Interstellar Clouds. XI. Lupus Observed with IRAC and MIPS. *Astrophysical Journal, Supplement*, 177:551–583, August 2008. doi: 10.1086/588042.

R. Millan-Gabet, F. P. Schloerb, W. A. Traub, F. Malbet, J. P. Berger, and J. D. Bregman. Sub-Astronomical Unit Structure of the Near-Infrared Emission from AB Aurigae. *Astrophysical Journal, Letters*, 513:L131–L134, March 1999. doi: 10.1086/311926.

R. Millan-Gabet, F. P. Schloerb, and W. A. Traub. Spatially Resolved Circumstellar Structure of Herbig AE/BE Stars in the Near-Infrared. *Astrophysical Journal*, 546:358–381, January 2001. doi: 10.1086/318239.

J. D. Monnier and R. Millan-Gabet. On the Interferometric Sizes of Young Stellar Objects. *Astrophysical Journal*, 579:694–698, November 2002. doi: 10.1086/342917.

J. D. Monnier, R. Millan-Gabet, R. Billmeier, R. L. Akeson, D. Wallace, J.-P. Berger, N. Calvet, P. D'Alessio, W. C. Danchi, L. Hartmann, L. A. Hillenbrand, M. Kuchner, J. Rajagopal, W. A. Traub, P. G. Tuthill, A. Boden, A. Booth, M. Colavita, J. Gathright, M. Hrynevych, D. Le Mignant, R. Ligon, C. Neyman, M. Swain, R. Thompson, G. Vasisht, P. Wizinowich, C. Beichman, J. Beletic, M. Creech-Eakman, C. Koresko, A. Sargent, M. Shao, and G. van Belle. The Near-Infrared Size-Luminosity Relations for Herbig Ae/Be Disks. *Astrophysical Journal*, 624:832–840, May 2005. doi: 10.1086/429266.

J. Muzerolle, L. Hartmann, and N. Calvet. Emission-Line Diagnostics of T Tauri Magnetospheric Accretion. I. Line Profile Observations. *Astronomical Journal*, 116:455–468, July 1998. doi: 10.1086/300428.

J. Muzerolle, N. Calvet, C. Briceño, L. Hartmann, and L. Hillenbrand. Disk Accretion in the 10 MYR Old T Tauri Stars TW Hydrae and Hen 3-600A. *Astrophysical Journal, Letters*, 535:L47–L50, May 2000. doi: 10.1086/312691.

J. Muzerolle, N. Calvet, L. Hartmann, and P. D'Alessio. Unveiling the Inner Disk Structure of T Tauri Stars. *Astrophysical Journal, Letters*, 597:L149–L152, November 2003. doi: 10.1086/379921.

J. Muzerolle, L. Adame, P. D'Alessio, N. Calvet, K. L. Luhman, A. A. Muench, C. J. Lada, G. H.

Rieke, N. Siegler, D. E. Trilling, E. T. Young, L. Allen, L. Hartmann, and S. T. Megeath. 24 μm Detections of Circum(sub)stellar Disks in IC 348: Grain Growth and Inner Holes? *Astrophysical Journal*, 643:1003–1010, June 2006. doi: 10.1086/503271.

J. Najita, J. S. Carr, and R. D. Mathieu. Gas in the Terrestrial Planet Region of Disks: CO Fundamental Emission from T Tauri Stars. *Astrophysical Journal*, 589:931–952, June 2003. doi: 10.1086/374809.

J. R. Najita, S. E. Strom, and J. Muzerolle. Demographics of transition objects. *Monthly Notices of the RAS*, 378:369–378, June 2007. doi: 10.1111/j.1365-2966.2007.11793.x.

J. R. Najita, G. W. Doppmann, J. S. Carr, J. R. Graham, and J. A. Eisner. High-Resolution K-Band Spectroscopy of MWC 480 and V1331 Cyg. *Astrophysical Journal*, 691:738–748, January 2009. doi: 10.1088/0004-637X/691/1/738.

A. Natta, T. Prusti, R. Neri, D. Wooden, V. P. Grinin, and V. Mannings. A reconsideration of disk properties in Herbig Ae stars. *Astronomy and Astrophysics*, 371:186–197, May 2001. doi: 10.1051/0004-6361:20010334.

A. Natta, L. Testi, J. Muzerolle, S. Randich, F. Comerón, and P. Persi. Accretion in brown dwarfs: An infrared view. *Astronomy and Astrophysics*, 424:603–612, September 2004. doi: 10.1051/0004-6361:20040356.

A. Natta, L. Testi, and S. Randich. Accretion in the ρ-Ophiuchi pre-main sequence stars. *Astronomy and Astrophysics*, 452:245–252, June 2006. doi: 10.1051/0004-6361:20054706.

R. Neuhaeuser, M. F. Sterzik, J. H. M. M. Schmitt, R. Wichmann, and J. Krautter. ROSAT survey observation of T Tauri stars in Taurus. *Astronomy and Astrophysics*, 297:391–417, May 1995.

I. Pascucci, D. Apai, K. Luhman, T. Henning, J. Bouwman, M. R. Meyer, F. Lahuis, and A. Natta. The Different Evolution of Gas and Dust in Disks around Sun-Like and Cool Stars. *Astrophysical Journal*, 696:143–159, May 2009. doi: 10.1088/0004-637X/696/1/143.

C. Pinte, D. L. Padgett, F. Ménard, K. R. Stapelfeldt, G. Schneider, J. Olofsson, O. Panić, J. C. Augereau, G. Duchêne, J. Krist, K. Pontoppidan, M. D. Perrin, C. A. Grady, J. Kessler-Silacci, E. F. van Dishoeck, D. Lommen, M. Silverstone, D. C. Hines, S. Wolf, G. A. Blake, T. Henning, and B. Stecklum. Probing dust grain evolution in IM Lupi's circumstellar disc. Multi-wavelength observations and modelling of the dust disc. *Astronomy and Astrophysics*, 489:633–650, October 2008. doi: 10.1051/0004-6361:200810121.

M. A. Pogodin, G. A. P. Franco, and D. F. Lopes. Spectroscopic behaviour of the unusual Ae star HD 190073. *Astronomy and Astrophysics*, 438:239–250, July 2005. doi: 10.1051/0004-6361:20034290.

K. M. Pontoppidan, F. L. Schöier, E. F. van Dishoeck, and E. Dartois. Bright CO ro-vibrational emission lines in the class I source GSS 30 IRS1. Probing the inner disk of a young embedded star. *Astronomy and Astrophysics*, 393:585–595, October 2002. doi: 10.1051/0004-6361:20021056.

K. M. Pontoppidan, G. A. Blake, E. F. van Dishoeck, A. Smette, M. J. Ireland, and J. Brown. Spectroastrometric Imaging of Molecular Gas within Protoplanetary Disk Gaps. *Astrophysical Journal*, 684:1323–1329, September 2008a. doi: 10.1086/590400.

K. M. Pontoppidan, A. C. A. Boogert, H. J. Fraser, E. F. van Dishoeck, G. A. Blake, F. Lahuis, K. I. Öberg, N. J. Evans, II, and C. Salyk. The c2d Spitzer Spectroscopic Survey of Ices around Low-Mass Young Stellar Objects. II. CO_2. *Astrophysical Journal*, 678:1005–1031, May 2008b. doi: 10.1086/533431.

L. Prato, A. M. Ghez, R. K. Piña, C. M. Telesco, R. S. Fisher, P. Wizinowich, O. Lai, D. S. Acton, and P. Stomski. Keck Diffraction-limited Imaging of the Young Quadruple Star System HD 98800. *Astrophysical Journal*, 549:590–598, March 2001. doi: 10.1086/319061.

L. Prato, T. P. Greene, and M. Simon. Astrophysics of Young Star Binaries. *Astrophysical Journal*, 584:853–874, February 2003. doi: 10.1086/345828.

J. E. Pringle. Accretion discs in astrophysics. *Annual Review of Astron and Astrophys*, 19:137–162, 1981. doi: 10.1146/annurev.aa.19.090181.001033.

C. Qi, P. T. P. Ho, D. J. Wilner, S. Takakuwa, N. Hirano, N. Ohashi, T. L. Bourke, Q. Zhang, G. A. Blake, M. Hogerheijde, M. Saito, M. Choi, and J. Yang. Imaging the Disk around TW Hydrae with the Submillimeter Array. *Astrophysical Journal, Letters*, 616:L11–L14, November 2004. doi: 10.1086/421063.

T. Ratzka, C. Leinert, T. Henning, J. Bouwman, C. P. Dullemond, and W. Jaffe. High spatial resolution mid-infrared observations of the low-mass young star TW Hydrae. *Astronomy and Astrophysics*, 471:173–185, August 2007. doi: 10.1051/0004-6361:20077357.

K. Regenauer-Lieb, D. A. Yuen, and J. Branlund. The Initiation of Subduction: Criticality by Addition of Water? *Science*, 294:578–581, October 2001.

B. Reipurth, A. Pedrosa, and M. T. V. T. Lago. Hα emission in pre-main sequence stars. I. an atlas of line profiles. *Astronomy and Astrophysics, Supplement*, 120:229–256, December 1996.

T. W. Rettig, J. Haywood, T. Simon, S. D. Brittain, and E. Gibb. Discovery of CO Gas in the Inner Disk of TW Hydrae. *Astrophysical Journal, Letters*, 616:L163–L166, December 2004. doi: 10.1086/426433.

W. K. M. Rice, K. Wood, P. J. Armitage, B. A. Whitney, and J. E. Bjorkman. Constraints on a planetary origin for the gap in the protoplanetary disc of GM Aurigae. *Monthly Notices of the RAS*, 342:79–85, June 2003. doi: 10.1046/j.1365-8711.2003.06515.x.

J. Robrade and J. H. M. M. Schmitt. A deep XMM-Newton X-ray observation of the Chamaeleon I dark cloud. *Astronomy and Astrophysics*, 461:669–678, January 2007. doi: 10.1051/0004-6361:20066250.

R. A. Rossiter. Fourth list of new southern double stars found at the Lamont-Hussey Observatory of the University of Michigan, at Bloemfontein, Orange Free State, South Africa. *Publications of Michigan Observatory*, 8:133–140, 1943.

L. S. Rothman, R. R. Gamache, R. H. Tipping, C. P. Rinsland, M. A. H. Smith, D. C. Benner, V. M. Devi, J.-M. Flaud, C. Camy-Peyret, and A. Perrin. The HITRAN molecular data base—Editions of 1991 and 1992. *Journal of Quantitative Spectroscopy and Radiative Transfer*, 48:469–507, 1992. doi: 10.1016/0022-4073(92)90115-K.

L. S. Rothman, D. Jacquemart, A. Barbe, D. Chris Benner, M. Birk, L. R. Brown, M. R. Carleer, C. Chackerian, K. Chance, L. H. Coudert, V. Dana, V. M. Devi, J.-M. Flaud, R. R. Gamache, A. Goldman, J.-M. Hartmann, K. W. Jucks, A. G. Maki, J.-Y. Mandin, S. T. Massie, J. Orphal, A. Perrin, C. P. Rinsland, M. A. H. Smith, J. Tennyson, R. N. Tolchenov, R. A. Toth, J. Vander Auwera, P. Varanasi, and G. Wagner. The HITRAN 2004 molecular spectroscopic database.

Journal of Quantitative Spectroscopy and Radiative Transfer, 96:139–204, December 2005. doi: 10.1016/j.jqsrt.2004.10.008.

S. M. Rucinski and J. Krautter. TW Hya—A T Tauri star far from any dark cloud. *Astronomy and Astrophysics*, 121:217–225, May 1983.

S. P. Ruden. The Formation of Planets. In C. J. Lada and N. D. Kylafis, editors, *NATO ASIC Proc. 540: The Origin of Stars and Planetary Systems*, pages 643–678, 1999.

C. Salyk, G. A. Blake, A. C. A. Boogert, and J. M. Brown. High-Resolution 5μm Spectroscopy of Transitional Disks. *Astrophysical Journal*, 1999, (in press).

C. Salyk, G. A. Blake, A. C. A. Boogert, and J. M. Brown. Molecular Gas in the Inner 1 AU of the TW Hya and GM Aur Transitional Disks. *Astrophysical Journal, Letters*, 655:L105–L108, February 2007. doi: 10.1086/512012.

C. Salyk, K. M. Pontoppidan, G. A. Blake, F. Lahuis, E. F. van Dishoeck, and N. J. Evans, II. H_2O and OH Gas in the Terrestrial Planet-forming Zones of Protoplanetary Disks. *Astrophysical Journal, Letters*, 676:L49–L52, March 2008. doi: 10.1086/586894.

B. Sargent, W. J. Forrest, P. D'Alessio, A. Li, J. Najita, D. M. Watson, N. Calvet, E. Furlan, J. D. Green, K. H. Kim, G. C. Sloan, C. H. Chen, L. Hartmann, and J. R. Houck. Dust Processing in Disks around T Tauri Stars. *Astrophysical Journal*, 645:395–415, July 2006. doi: 10.1086/504283.

G. Schneider, K. Wood, M. D. Silverstone, D. C. Hines, D. W. Koerner, B. A. Whitney, J. E. Bjorkman, and P. J. Lowrance. NICMOS Coronagraphic Observations of the GM Aurigae Circumstellar Disk. *Astronomical Journal*, 125:1467–1479, March 2003. doi: 10.1086/367596.

E. Seperuelo Duarte, S. H. P. Alencar, C. Batalha, and D. Lopes. Spectrophotometric analysis of the T Tauri star GQ Lupi A. *Astronomy and Astrophysics*, 489:349–357, October 2008. doi: 10.1051/0004-6361:20078275.

J. Setiawan, T. Henning, R. Launhardt, A. Müller, P. Weise, and M. Kürster. A young massive planet in a star-disk system. *Nature*, 451:38–41, January 2008. doi: 10.1038/nature06426.

V. S. Shevchenko and W. Herbst. The Search for Rotational Modulation of T Tauri Stars in the Ophiuchus Dark Clouds. *Astronomical Journal*, 116:1419–1431, September 1998. doi: 10.1086/300496.

F. Shu, J. Najita, E. Ostriker, F. Wilkin, S. Ruden, and S. Lizano. Magnetocentrifugally driven flows from young stars and disks. 1: A generalized model. *Astrophysical Journal*, 429:781–796, July 1994. doi: 10.1086/174363.

M. Simon, A. Dutrey, and S. Guilloteau. Dynamical Masses of T Tauri Stars and Calibration of Pre-Main-Sequence Evolution. *Astrophysical Journal*, 545:1034–1043, December 2001. doi: 10.1086/317838.

M. F. Skrutskie, R. M. Cutri, R. Stiening, M. D. Weinberg, S. Schneider, J. M. Carpenter, C. Beichman, R. Capps, T. Chester, J. Elias, J. Huchra, J. Liebert, C. Lonsdale, D. G. Monet, S. Price, P. Seitzer, T. Jarrett, J. D. Kirkpatrick, J. E. Gizis, E. Howard, T. Evans, J. Fowler, L. Fullmer, R. Hurt, R. Light, E. L. Kopan, K. A. Marsh, H. L. McCallon, R. Tam, S. Van Dyk, and S. Wheelock. The Two Micron All Sky Survey (2MASS). *Astronomical Journal*, 131:1163–1183, February 2006. doi: 10.1086/498708.

L. Spezzi, J. M. Alcalá, E. Covino, A. Frasca, D. Gandolfi, I. Oliveira, N. Chapman, N. J. Evans, II, T. L. Huard, J. K. Jørgensen, B. Merín, and K. R. Stapelfeldt. The Young Population of the Chamaeleon II Dark Cloud. *Astrophysical Journal*, 680:1295–1318, June 2008. doi: 10.1086/587931.

K. R. Stapelfeldt, J. E. Krist, F. Menard, J. Bouvier, D. L. Padgett, and C. J. Burrows. An Edge-On Circumstellar Disk in the Young Binary System HK Tauri. *Astrophysical Journal, Letters*, 502: L65–L68, July 1998. doi: 10.1086/311479.

B. Stelzer, G. Micela, and R. Neuhäuser. XMM-Newton probes the stellar population in Chamaeleon I South. *Astronomy and Astrophysics*, 423:1029–1044, September 2004. doi: 10.1051/0004-6361:20040202.

D. J. Stevenson and J. I. Lunine. Rapid formation of Jupiter by diffuse redistribution of water vapor in the solar nebula. *Icarus*, 75:146–155, July 1988. doi: 10.1016/0019-1035(88)90133-9.

K. M. Strom, S. E. Strom, S. Edwards, S. Cabrit, and M. F. Skrutskie. Circumstellar material associated with solar-type pre-main-sequence stars—A possible constraint on the timescale for planet building. *Astronomical Journal*, 97:1451–1470, May 1989. doi: 10.1086/115085.

H. Tanaka, Y. Himeno, and S. Ida. Dust Growth and Settling in Protoplanetary Disks and Disk Spectral Energy Distributions. I. Laminar Disks. *Astrophysical Journal*, 625:414–426, May 2005. doi: 10.1086/429658.

H. Terada, A. T. Tokunaga, N. Kobayashi, N. Takato, Y. Hayano, and H. Takami. Detection of Water Ice in Edge-on Protoplanetary Disks: HK Tauri B and HV Tauri C. *Astrophysical Journal*, 667:303–307, September 2007. doi: 10.1086/520951.

W. F. Thi, E. F. van Dishoeck, G. A. Blake, G. J. van Zadelhoff, J. Horn, E. E. Becklin, V. Mannings, A. I. Sargent, M. E. van den Ancker, A. Natta, and J. Kessler. H_2 and CO Emission from Disks around T Tauri and Herbig Ae Pre-Main-Sequence Stars and from Debris Disks around Young Stars: Warm and Cold Circumstellar Gas. *Astrophysical Journal*, 561:1074–1094, November 2001. doi: 10.1086/323361.

W. F. Thi, K. M. Pontoppidan, E. F. van Dishoeck, E. Dartois, and L. d'Hendecourt. Detection of abundant solid CO in the disk around ¡ASTROBJ¿CRBR 2422.8-3423¡/ASTROBJ¿. *Astronomy and Astrophysics*, 394:L27–L30, November 2002. doi: 10.1051/0004-6361:20021353.

W.-F. Thi, G.-J. van Zadelhoff, and E. F. van Dishoeck. Organic molecules in protoplanetary disks around T Tauri and Herbig Ae stars. *Astronomy and Astrophysics*, 425:955–972, October 2004. doi: 10.1051/0004-6361:200400026.

J. Tonry and M. Davis. A survey of galaxy redshifts. I—Data reduction techniques. *Astronomical Journal*, 84:1511–1525, October 1979. doi: 10.1086/112569.

D. E. Trilling, D. W. Koerner, J. W. Barnes, C. Ftaclas, and R. H. Brown. Near-Infrared Coronagraphic Imaging of the Circumstellar Disk around TW Hydrae. *Astrophysical Journal, Letters*, 552:L151–L154, May 2001. doi: 10.1086/320332.

K. I. Uchida, N. Calvet, L. Hartmann, F. Kemper, W. J. Forrest, D. M. Watson, P. D'Alessio, C. H. Chen, E. Furlan, B. Sargent, B. R. Brandl, T. L. Herter, P. Morris, P. C. Myers, J. Najita, G. C. Sloan, D. J. Barry, J. Green, L. D. Keller, and P. Hall. The State of Protoplanetary Material 10 Million years after Stellar Formation: Circumstellar Disks in the TW Hydrae Association. *Astrophysical Journal, Supplement*, 154:439–442, September 2004. doi: 10.1086/422888.

J. A. Valenti, A. A. Fallon, and C. M. Johns-Krull. An IUE Atlas of Pre-Main-Sequence Stars. III. Co-added Final Archive Spectra from the Long-Wavelength Cameras. *Astrophysical Journal, Supplement*, 147:305–336, August 2003. doi: 10.1086/375445.

R. van Boekel, M. Min, L. B. F. M. Waters, A. de Koter, C. Dominik, M. E. van den Ancker, and J. Bouwman. A 10 μm spectroscopic survey of Herbig Ae star disks: Grain growth and crystallization. *Astronomy and Astrophysics*, 437:189–208, July 2005. doi: 10.1051/0004-6361:20042339.

M. E. van den Ancker, D. de Winter, and H. R. E. Tjin A Djie. HIPPARCOS photometry of Herbig Ae/Be stars. *Astronomy and Astrophysics*, 330:145–154, February 1998.

E. F. van Dishoeck and J. H. Black. The photodissociation and chemistry of interstellar CO. *Astrophysical Journal*, 334:771–802, November 1988. doi: 10.1086/166877.

E. F. van Dishoeck, B. Jonkheid, and M. C. van Hemert. Photoprocesses in protoplanetary disks. *ArXiv e-prints*, May 2008.

J. S. Vink, J. E. Drew, T. J. Harries, and R. D. Oudmaijer. Probing the circumstellar structure of Herbig Ae/Be stars. *Monthly Notices of the RAS*, 337:356–368, November 2002. doi: 10.1046/j.1365-8711.2002.05920.x.

W. R. Ward. Protoplanet Migration by Nebula Tides. *Icarus*, 126:261–281, April 1997. doi: 10.1006/icar.1996.5647.

D. M. Watson, J. M. Leisenring, E. Furlan, C. J. Bohac, B. Sargent, W. J. Forrest, N. Calvet, L. Hartmann, J. T. Nordhaus, J. D. Green, K. H. Kim, G. C. Sloan, C. H. Chen, L. D. Keller, P. d'Alessio, J. Najita, K. I. Uchida, and J. R. Houck. Crystalline Silicates and Dust Processing in the Protoplanetary Disks of the Taurus Young Cluster. *Astrophysical Journal, Supplement*, 180: 84–101, January 2009. doi: 10.1088/0067-0049/180/1/84.

R. A. Webb, B. Zuckerman, I. Platais, J. Patience, R. J. White, M. J. Schwartz, and C. McCarthy. Discovery of Seven T Tauri Stars and a Brown Dwarf Candidate in the Nearby TW Hydrae Association. *Astrophysical Journal, Letters*, 512:L63–L67, February 1999. doi: 10.1086/311856.

A. J. Weinberger, E. E. Becklin, G. Schneider, B. A. Smith, P. J. Lowrance, M. D. Silverstone, B. Zuckerman, and R. J. Terrile. The Circumstellar Disk of HD 141569 Imaged with NICMOS.

Astrophysical Journal, Letters, 525:L53–L56, November 1999. doi: 10.1086/312334.

A. J. Weinberger, E. E. Becklin, B. Zuckerman, G. Schneider, and M. D. Silverstone. A Stellar Association Near HD 141569? In R. Jayawardhana and T. Greene, editors, *Young Stars Near Earth: Progress and Prospects*, volume 244 of *Astronomical Society of the Pacific Conference Series*, pages 75–80, 2001.

R. J. White and A. M. Ghez. Observational Constraints on the Formation and Evolution of Binary Stars. *Astrophysical Journal*, 556:265–295, July 2001. doi: 10.1086/321542.

R. J. White and L. A. Hillenbrand. A Long-lived Accretion Disk around a Lithium-depleted Binary T Tauri Star. *Astrophysical Journal, Letters*, 621:L65–L68, March 2005. doi: 10.1086/428752.

D. C. B. Whittet, S. S. Shenoy, E. A. Bergin, J. E. Chiar, P. A. Gerakines, E. L. Gibb, G. J. Melnick, and D. A. Neufeld. The Abundance of Carbon Dioxide Ice in the Quiescent Intracloud Medium. *Astrophysical Journal*, 655:332–341, January 2007. doi: 10.1086/509772.